

**Simulation of Separating Flows in the X2
Expansion Tube Over Bluff Aerocapture Vehicles**

Adriaan Window

A thesis submitted for the degree of Master of Philosophy at

The University of Queensland in October 2008

School of Engineering



© 2008

Adriaan Window

All Rights Reserved

Declaration by author

This thesis is composed of my original work, and contains no material previously published or written by another person except where due reference has been made in the text. I have clearly stated the contribution by others to jointly-authored works that I have included in my thesis.

I have clearly stated the contribution of others to my thesis as a whole, including statistical assistance, survey design, data analysis, significant technical procedures, professional editorial advice, and any other original research work used or reported in my thesis. The content of my thesis is the result of work I have carried out since the commencement of my research higher degree candidature and does not include a substantial part of work that has been submitted to qualify for the award of any other degree or diploma in any university or other tertiary institution. I have clearly stated which parts of my thesis, if any, have been submitted to qualify for another award.

I acknowledge that an electronic copy of my thesis must be lodged with the University Library and, subject to the General Award Rules of The University of Queensland, immediately made available for research and study in accordance with the Copyright Act 1968.

I acknowledge that copyright of all material contained in my thesis resides with the copyright holder(s) of that material.

Statement of Contributions to Jointly Authored Works Contained in the Thesis

No jointly-authored works.

Statement of Contributions by Others to the Thesis as a Whole

No contributions by others.

Statement of Parts of the Thesis Submitted to Qualify for the Award of Another Degree

None.

Published Works by the Author Incorporated into the Thesis

None.

Additional Published Works by the Author Relevant to the Thesis but not Forming Part of it

None.

Keywords

computational fluid dynamics, hypersonic, heat transfer, near wake, thin film, heat transfer, Mars Pathfinder, impulse, shock tube, expansion tube

Australian and New Zealand Standard Research Classifications

(ANZSRC)

090107 Hypersonic Propulsion and Hypersonic Aerodynamics 60%

091501 Computational Fluid Dynamics 20%

091505 Heat and Mass Transfer Operations 20%

Abstract

Blunt-nosed sphere-cone aeroshell vehicles have played an integral part in space exploration to date and their use is set to continue into the next decade and beyond. While these vehicles have been flight proven with four decades of heritage, design uncertainties in aft body thermal protection systems in the order of 300-400% exist due to the as yet unpredictable flowfield characteristics of the near-wake region of these vehicles at hypersonic speeds. Attempts have been made to reduce this uncertainty but current technology in the field of computational fluid dynamics (CFD) still requires phenomenological models to be developed that accurately predict base heating rates.

Expansion tube experimental facilities have the potential for aiding in the reduction of this design uncertainty. However, it is not known whether the X2 or X3 expansion tubes at the University of Queensland can be employed to obtain data for assisting the development of CFD modelling techniques.

A survey of the current best practices in CFD modelling techniques is presented. Preliminary CFD models have been developed to resolve the macroscopic features of the wake flows around the Mars Pathfinder aeroshell geometry. A series of experiments have been performed and the duration of time average steady heating is documented. Results of experimentation indicated that the X2 impulse machine operating in expansion tube mode is capable of generating a sufficient length of steady flow for the study of near-wake phenomena. This is documented in flow conditions using CO₂ to simulate Martian flight conditions. It was also demonstrated that flow speeds and model dimensions must be matched appropriately to allow for sufficient test time. A method for the sizing of experimental models is also presented for the study of heat transfer in near-wake flow fields. Example model geometries are prescribed for a variety of flow conditions for the X2 expansion tube.

Acknowledgements

I would like to thank my supervisors Dr Peter Jacobs and Prof. Richard Morgan for the guidance and technical assistance you have both provided over the last few years. It has been a long road and without you as my navigation system telling me to go back and have another look I would still be stuck at the beginning. Also, thanks to Richard for arranging financial support along the way. And Peter, thank you for constant reassurance and validation of my work.

To my family, thank you for the patience and the nagging. I may have dismissed a lot of it at the time but it kept me honest about my progress and milestones.

Thank you to my colleagues and fellow post-graduate students for your support over the years. Special thanks to Rowan Gollan, Dan Potter, Carolyn Jacobs, Troy Eichmann, Andrew Dann, Matthew Green, Zane Smith, Michael Kearney and Brendan O'Flaherty.

I would also like to thank my current employer, Bassett Consulting Engineers and specifically Dr Nathan Groenhout and Mike Dagnall for their support. Without their understanding and flexibility the final hurdles would have been a great deal harder to jump. Mike, you have re-instilled the quality of perfectionism and this thesis would not be the same without it.

Finally, I wish to thank my wonderful partner Kathryn. Without her assistance and life providing nourishment I might not be alive to have finished this. Thank you for your patience and support.

Nomenclature

Alphabetical

a	local speed of sound
C_D	coefficient of drag
C_H	Stanton number
D	diameter
F_D	drag force
h	enthalpy
H	total enthalpy
L	reference length
L_f	flow lengths
M	Mach number
P	pressure
q	heat flux
R	radius
Re	Reynolds number
s	cell spacing
S	projected drag/lift area
S	chord length S/R_b
t	time
T	temperature
U	x -component of velocity
y	distance normal to model wall

Greek

μ	viscosity
ν	expansion angle
ρ	density
τ_P	pressure establishment time
τ_Q	heat transfer establishment time
σ	root-mean-squared value

Subscripts

0, 2	post-shock conditions
298	conditions at temperature of 298K
b	body (overall)
e	edge of free-shear-layer
P	pressure
Q	heat transfer
ref	reference
s	sting
tr	point of transition to turbulence
w	denotes value at the wall
∞	denotes freestream conditions

Acronyms

c.g.	center of gravity
CFD	Computational Fluid Dynamics
LAURA	Langley Aerothermodynamic Upwind Relaxation Algorithm
MBCNS2	Multi-Block Compressible Navier Stokes v2
NASA	National Aeronautics and Space Administration
SST	Shear-Stress Transport
TPS	Thermal Protection System

Contents

Abstract	iii
Acknowledgements	iv
Nomenclature	v
1 Introduction	2
1.1 Motivation and Scope	3
1.2 Thesis Outline	6
2 Near-Wake Flow Region Studies	8
2.1 Establishment Times in Hypersonic Flow Facilities	8
2.2 Physics of wake flow around bluff bodies	17
3 Computational Study	26
3.1 Overview	26
3.2 Grid Preparation	27
3.2.1 Valliammai Cluster Function	29
3.2.2 Block and Grid Layouts	31
3.3 Grid Dependence Study	31
3.4 Near Wake Flow Field Characteristics	38
3.5 Wake Flow Establishment	43
4 Experimental Study	52
4.1 Overview	52
4.2 Experimental Objectives	53
4.3 Description and Operation of the X2 Expansion Tube	54

4.4	Measurement Techniques in High Speed Flows	56
4.4.1	Pressure Measurement	56
4.4.2	Heat Transfer Measurement	59
4.5	Model Construction and Instrumentation	59
4.5.1	Aeroshell Models	60
4.5.2	Measurement and Instrumentation	60
4.6	Calibration of thin-film heat gauges	62
4.7	Experimental Flow Conditions	64
4.8	Experimental Results	64
4.8.1	Mars Condition 2 - Langley condition	67
4.8.2	Mars Condition 1 - Low-speed aerocapture	74
4.8.3	Discussion of Results	80
4.9	Experimental Design	83
5	Conclusions	86
A	CFD Governing Equations	A-90
A.1	Governing Equations	A-92
A.2	Axisymmetric Geometries	A-94
A.3	Discretised Equations and Flux Calculation	A-95
B	Code Listings	B-97
B.1	Final CFD Model Generation Scripts	B-97
B.1.1	x2-pathfinder-base.py	B-97
B.1.2	bezier_from_points.py	B-106
B.1.3	hollis_control_points.py	B-107
B.2	Experimental Post-Processing Scripts	B-109
B.2.1	makefile	B-109
B.2.2	runpostexp.py	B-110
B.2.3	postexp.pyx	B-111
C	Supplementary CFD Data	C-116
C.1	Heat transfer time history plots	C-116
C.1.1	Low-speed aerocapture flow condition	C-116

C.1.2	Direct entry flow condition	C-121
C.2	Instantaneous heat transfer plots along model sting	C-127
C.2.1	Low-speed aerocapture condition	C-127
C.2.2	Direct entry condition	C-130
D	Model Schematics	D-134
E	Gauge Calibration	E-140
E.1	Calibration Oven Settings	E-140
E.2	Calibration Data - Before model installation	E-143
E.3	Calibration Data - After model installation	E-145
F	Experimental Data	F-148
	Bibliography	182

Introduction

Interplanetary probes have played a large role in the exploration of our Solar System to date. Use of robotic probes is set to continue into the future with human exploration missions suffering continuous funding and technical setbacks. Recent history suggests that space agencies such as the National Aeronautics and Space Administration (NASA) will return to flight the crew capsules harking back to the days of the Apollo program rather than more complex vehicles such as the Space Shuttle. With these capsule type vehicles comes the inability and/or impracticability to transport both crew and cargo in the same capsule, thus there will be an increase in the number of these capsules in flight through the variety of atmospheres in our Solar System.

Aeroshell designs are driven by the need for a vehicle that is capable of safely delivering a payload through a ballistic atmospheric flight trajectory. The primary design requirements and operating principles are to provide deceleration from orbital or super-orbital speeds and dissipate the large quantities of thermal energy generated in this process.

The process of deceleration is determined by the force of drag which acts along the vector opposite that of the velocity. The amount of drag is determined by Equation 1.1

$$F_D = \frac{1}{2} \rho_\infty U_\infty^2 S C_D \quad (1.1)$$

where S is the projected drag area, C_D is the coefficient of drag and ρ_∞ and U_∞ are the freestream density and velocity respectively. Hence, the amount of deceleration is directly proportional to the projected drag area of the vehicle. Also, the amount

of convective heat transfer is inversely proportional to the radius of curvature. In general terms, this promotes a design that is blunt and oblate. Figure 1.1 illustrates some of the more famous and typical geometries.

While these unmanned probes have been highly successful (more than two dozen exploration missions launched since June 1967 and hundreds of Discoverer/Corona intelligence gathering missions) there are still some design uncertainties to resolve. For example, the thermal protection system (TPS) designs have in some cases more than 300% margin [27] due mainly to unpredictable heating conditions on the aft body in hypersonic flow fields. The implications of the magnitude of such safety factors will play a major part in determining the feasibility of many exploration missions in the future.

Therefore, there is great need to accurately predict the aerothermodynamic loading during such flights to reduce design uncertainties. Current technology and theory is inadequate in its ability to model the near-wake flowfield conditions to a high level of confidence. In fact, until recently, the magnitude of uncertainty was not considered large, but rather unknown [26].

Experimental facilities such as the X2 and X3 superorbital expansion tubes show the greatest potential in the simulation of hypersonic flowfield conditions. However, due to the operating principles of these machines the duration of tests are short and the duration over which steady time averaged heat transfer measurements can be acquired is even shorter.

1.1 Motivation and Scope

Given that expansion tubes generate transient, impulsive flow conditions, it is not certain that these facilities can be used to obtain accurate data on large separated flows that exist in the near wake region of typical aeroshell models. A better understanding of the physical processes occurring during these short duration experiments is required in order to determine the effectiveness of these facilities for the study of these types of flows. Specifically, it is of interest to determine the time required for the aft flowfield to develop to the point where major features are steady and consistent.

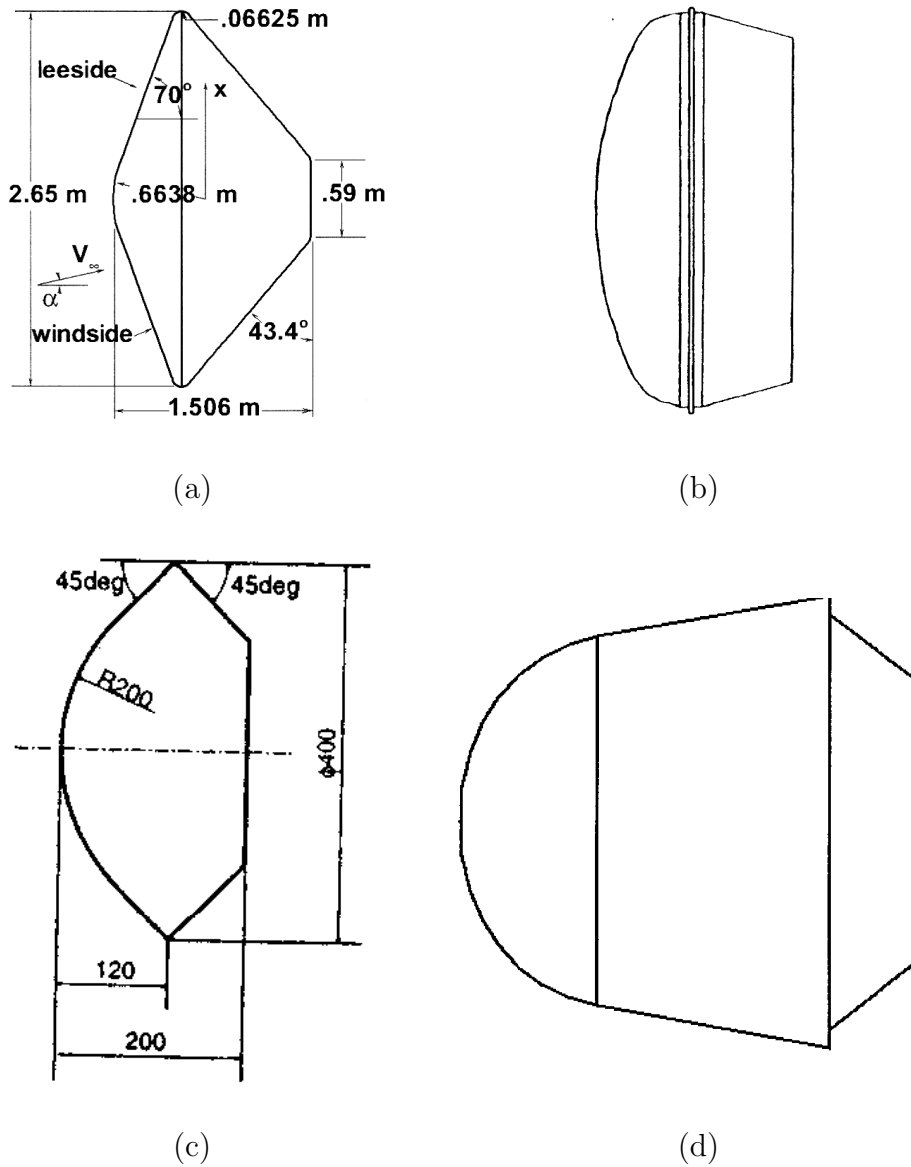


Figure 1.1: Aeroshell geometries used in various missions since June 1967. Flow direction from the left. (a) Mars Pathfinder [5], (b) ESA's Huygens Titan probe [2], (c) Japanese MUSES-C capsule [24] and (d) Corona spy satellite return capsule and potential geometry for NASA Crew Exploration Vehicle Command Module.

Unlike the study conducted by Hollis [8] (described in the following section) which focused on one flow condition specific to a given mission, this study will look at multiple flow conditions for different types of exploratory probe missions. Studying the effects of flow velocity, density and temperature on wake flow formation can provide better insight into the capability of the ground-based hypersonic experimental facilities at the University of Queensland.

The scope of this thesis was the characterisation of near wake region flow fields around blunt body aeroshell vehicles as simulated in the X2 expansion tube. This scope was met by:

1. Reviewing literature relevant to the field of rearward facing flows and wake flow establishment;
2. The selection of appropriate and relevant flow conditions as summarised in Table 1.1;
3. Gaining understanding and engineering approximations of the flow field using computational fluid dynamics (CFD);
4. Evaluating the potential for the X2 expansion tube in simulating these flows for the purposes of acquiring steady time averaged heat transfer data in the near-wake region;
5. Determining the correlation between geometry length scales and wake flow establishment time at a fixed angle-of-attack;
6. Building upon existing computational methods to enable more convenient analyses of the aeroshell flows, specifically by providing an enhancement to the grid generation capability of the in-house codes.

Table 1.1: Flow conditions selected for simulation and experimentation in this study.

Experimental flow condition identifier	Condition description	Nominal freestream velocity U_∞ (m/s)
MC1	Low-speed Mars aerocapture profile	6,500
MC2	Direct Mars entry condition (also known as the “Langley” condition)	4,700

1.2 Thesis Outline

Chapter 2 reviews the relevant literature regarding wake flow physics and wake establishment times in hypersonic flows. This review examines work involving many types of flow simulation facilities, model geometries and gas properties and the findings presented by each study with regards to the time required for wake establishment. Also reviewed are the current best practices with regards to data acquisition in hypersonic flows. This section also outlines the physics of the near-wake flow field structure and the current gaps in understanding and modelling these physical phenomena.

Chapter 3 presents the process and findings of the computational fluid dynamics portion of this study. This chapter aims to provide understanding of the wake flow structure in the specific flow conditions examined in this thesis and associated time and length scales. The methodology and results presented are intended to provide engineering approximations to assist in the experimental portion of the study.

Chapter 4 details the experimental aspect of this study. The experimental facilities are described including the manufacturing, instrumentation and calibration processes of the scale model used in these experiments. The conditions for the experiments are presented as well as general observations of the experimental investigation overall. The results of each test series are analysed and compared to the CFD analysis of the previous chapter. A complete record of results from individual tests can also be found in Appendix F.

Chapter 5 provides an overview of the study and presents conclusions with regards to the motivation and scope of this thesis.

Near-Wake Flow Region Studies

Two areas of research provide the bulk of literature relevant to the current study. This section looks at these fields and discusses the implications for this investigation.

2.1 Establishment Times in Hypersonic Flow Facilities

Much work has been done in this particular area in a range of experimental facilities around the world and at various flow conditions. While the flow conditions in most of the studies are not in the same range as those of interest to users of the X2 and X3 expansion tubes at the University of Queensland, the results and conclusions are relevant. To provide some basis for comparison, a sample set of flow conditions used in X3 are shown in Table 2.1. Figure 2.1 illustrates the established flow field in the wake of the Pathfinder aeroshell. It is this flow field structure that influences near-wake heating and is the basis for the current investigation.

Brian Hollis [8] conducted a study entitled the “Experimental and Computational Aerothermodynamics of a Mars Entry Vehicle”. This study resulted in the production of an aerothermodynamic database of the Pathfinder vehicle at hypersonic speeds.

At the time of the study (1996) the Mars Pathfinder mission was of great interest to researchers and Hollis conducted his study by examining the hypersonic flow fields around several parametrically related geometries based on the Viking/Pathfinder aeroshell as illustrated in Figure 2.2. Hollis included the parametric geometries to observe the effects of the shoulder radii on wake flow structure and for the same

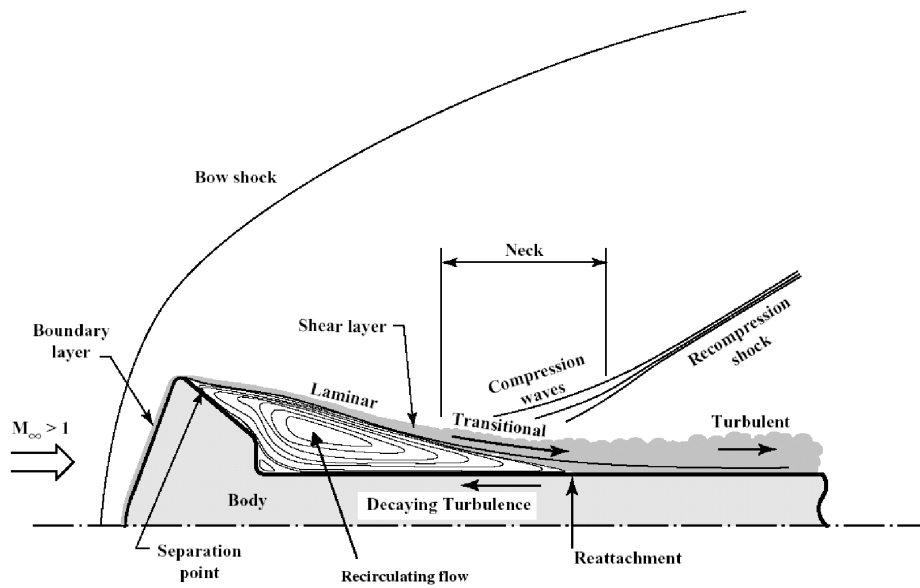


Figure 2.1: Diagram of the flow structure in the wake of the Pathfinder aeroshell on a sting mount [8].

Table 2.1: Typical flow conditions for the X3 expansion tube [9].

Property	Finite-rate CFD	Equil. CFD	Exp.	JUMP
Density, kg/m ³	2.826 x10 ⁻³	1.410 x10 ⁻³	-	1.836 x10 ⁻³
Velocity, m/s	8230	8551	-	8284
Shock velocity, m/s	8059	8324	7868 - 8320	8284
Mach number	12.0	9.7	11.2	10.8
Static pressure, kPa	0.967	0.934	0.8 - 0.95	0.762
Static temperature, K	1036	2282	-	1168
Total enthalpy, MJ/kg	36.9	39.1	-	40.3
Pitot pressure, kPa	150	107	100 - 130	126
Unit Reynolds number, m ⁻¹	549203	157660	-	325668
Ratio of specific heats	1.384	1.295	-	1.408
Specific gas constant, J/(kg-K)	330	290	-	355
N ₂ mass fraction	0.7674	0.7483	-	0.7183
N mass fraction	0.0	0.0	-	0.0534
O ₂ mass fraction	0.0450	0.2123	-	0.0011
O mass fraction	0.1608	0.0113	-	0.1982
NO mass fraction	0.0268	0.0145	-	0.0191

reason also incorporated smaller scale models.

Hollis conducted the experimental component of his research in the HYPULSE expansion tube facility (previously known as the Langley 6-inch Expansion Tube). This facility produces nominal test periods on the order of 200-300 μs .

Instrumentation was placed along the entire length of the symmetry line, including the mounting sting with a total of 37 gauges per model. Thin-film temperature resistance gauges were selected due to their rapid response time ($< 1 \mu\text{s}$) and their high sensitivity compared to other gauge types, allowing for measurements of wake flow temperatures which are relatively cooler than that experienced over the forebody.

The aeroshell models were constructed from a glass-ceramic called Macor. This material was used as opposed to metals due to its comparatively low thermal conductivity and thermal diffusivity. With the high incident temperatures over the forebody such material characteristics would yield a “larger and more easily measurable surface temperature rise than would occur in higher conductivity materials” [8].

The mounting stings were, however, constructed from hardened steel, suitable to withstand several tube shots. It was found that after several runs the models or mounts needed replacement due to excess surface damage and therefore unreliable data measurement.

Test gases of Air and Carbon dioxide were primarily used with a limited number of Helium-based runs also. Table 2.2 details the test conditions and error bounds. Using a $\pm 5\%$ variation on the average pressure as the criteria for steady flow, the HYPULSE tube delivered test windows of 146 μs and 122 μs for the CO_2 and Air conditions respectively.

It was also determined that flow establishment time can be defined in a non-dimensional form in Equation 2.1, where y_{ref} is a characteristic length and L_f is the number of flow lengths (the symbol τ was used by Hollis). The characteristic length employed by Hollis was the difference between the radius of the aeroshell model at the shoulder and the radius of the supporting sting mount. For the MP-1 model used in that study this length was 15 mm. It has been shown that for separated flows in CO_2 , 40-70 flow lengths are required for the flow to fully establish [8] with a mean value of 51. Hollis also employed time history plots of measured heat transfer against

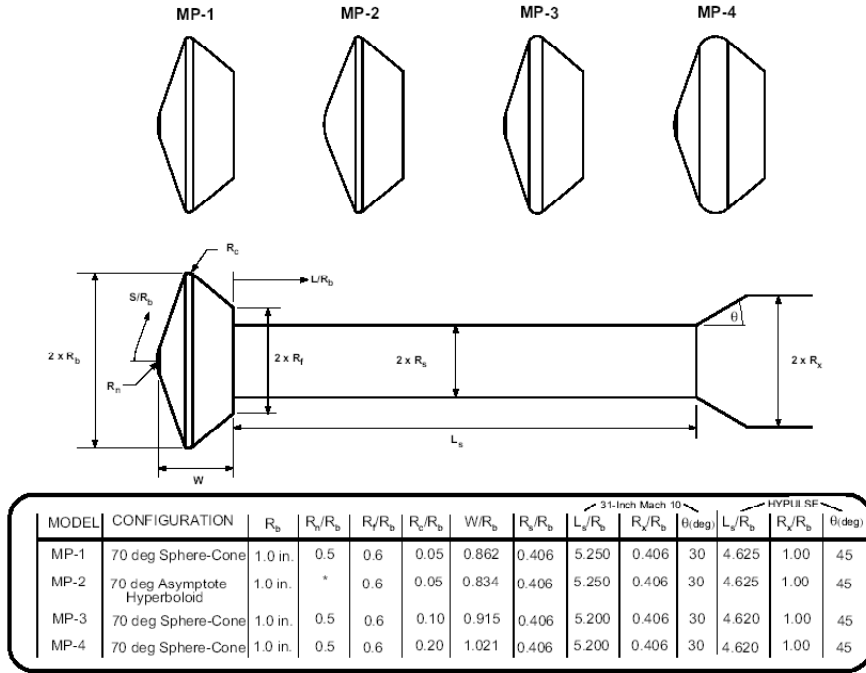


Figure 2.2: Vehicle geometry configurations used by Hollis [8].

Table 2.2: Test conditions used by Hollis in HYPULSE [8].

Parameter	Air	CO ₂	He
P_∞ (Pa)	1824 ± 9.9%	1191 ± 10.8%	1511
T_∞ (K)	1113 ± 9.3%	1088 ± 8.7%	302
ρ_∞ (kg/m ³)	$5.712 \times 10^{-3} \pm 1.8\%$	$5.789 \times 10^{-3} \pm 3.1\%$	2.416×10^{-3}
U_∞ (m/s)	5162 ± 0.9%	4772 ± 1.1%	6170
M_∞	7.93 ± 4.1%	9.71 ± 4.1%	6.04
Re_∞ (1/m)	$0.668 \times 10^6 \pm 3.9\%$	$0.660 \times 10^6 \pm 4.9\%$	0.70×10^6
$P_{0,2}$ (kPa)	147.2 ± 1.3%	129.6 ± 1.8%	81.7
$T_{0,2}$ (K)	6028 ± 0.8%	3703 ± 0.9%	3968
$H_{0,2} - H_{298}$ (MJ/kg)	14.18 ± 1.4%	12.25 ± 2.1%	19.0
$\frac{\rho_2}{\rho_\infty}$	18.98 ± 1.0%	10.98 ± 0.7%	3.70

gauge location to visually qualify flow establishment but suggested this method was still arbitrary.

$$L_f = \frac{U_\infty \Delta t_{est}}{y_{ref}} \quad (2.1)$$

Hollis preferred a mathematical model to determine the establishment time from recorded data, using a normalised heat transfer residual. This residual is defined as:

$$\sigma(t) = \frac{\Delta q(t)}{q(t)} \quad (2.2)$$

where:

$$\Delta q = \frac{\delta q}{\delta t} \Delta t \quad (2.3)$$

The time-history heat transfer measurements are collected into a single value by calculating a root-mean-squared (RMS) quantity, as given by Equation 2.4 from individual gauge time-histories.

$$\hat{\sigma}(t) = \sqrt{\frac{1}{n} (\sigma_1^2 + \sigma_2^2 + \dots + \sigma_n^2)} \quad (2.4)$$

Figure 2.3 shows a pressure-time trace for a HYPULSE run. It can be seen in Figure 2.4 that the heat transfer residual reaches a minima toward the end of the steady flow test window, as defined by pressure trace data. Hollis showed that this mathematically-based analysis method is in good agreement with that suggested by Holden [7], yielding an average value of 51 flow lengths.

It was also suggested that data recorded from sensors that were overly noisy due to degradation or faulty connections was not be included in the RMS calculation so as not to skew the results. The criterion that Hollis developed from this method was that the wake establishment had occurred when the RMS value fell below 0.02.

Finally, all experimental heat transfer results were presented in non-dimensional format in terms of the Stanton number:

$$C_H = \frac{q}{\rho_\infty U_\infty (h_0 - h_w)} \quad (2.5)$$

In this form the data was in a form readily comparable given any fluctuation in free

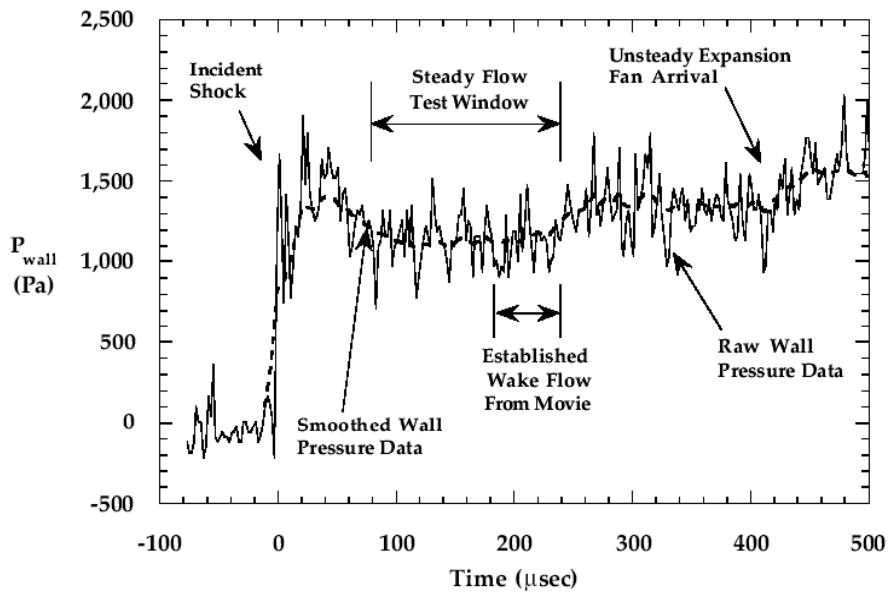


Figure 2.3: Wall pressure time-history from Hollis' Run 749 [8].

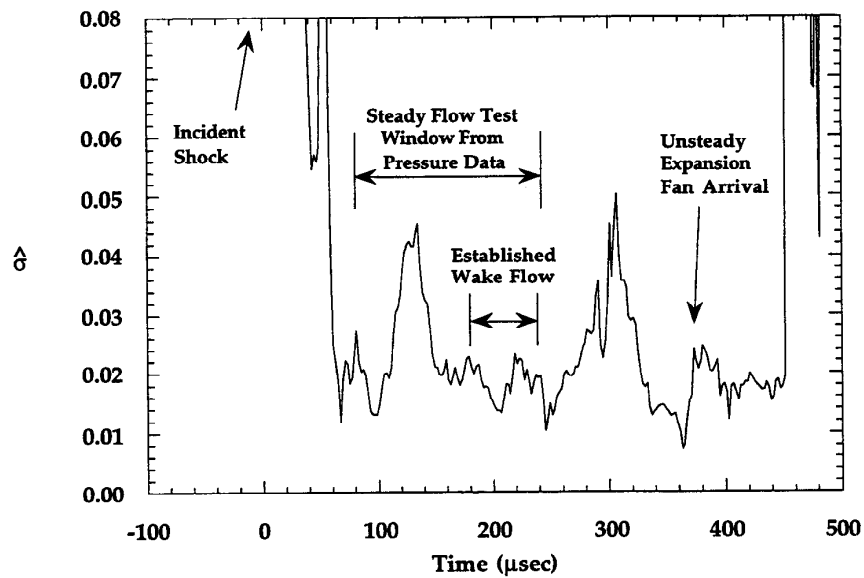


Figure 2.4: Wake RMS time-history from Hollis' Run 749 [8].

stream conditions.

In the paper “Establishment time of laminar separated flows”, Holden [7] suggested a correlation for flow establishment times in shock facilities using measurements taken from the Cornell Aeronautical Laboratory (CAL) shock tunnel. While the test times from shock facilities are an order of magnitude longer than those in X2, X3 and HYPULSE machines, the results presented are still relevant.

Holden recorded pressure and heat transfer data over spheres of diameters between 2 and 12 inches, unit Reynolds numbers from 2×10^6 to $9 \times 10^6/\text{ft}$ and Mach numbers of 6 to 8.5. It was determined that flows were considered to be established once pressure and heat transfer data reached levels equal to 98% of their steady mean level.

Figure 2.5 illustrates the results of the non-dimensionalised flow establishment time given by Equation 2.1 where y_{ref} is defined as the sphere diameter, D . Holden derived a correlation to the data as given by the line fit in Equation 2.6.

$$\tau_P = \frac{t_P U_\infty}{D} = \frac{27.5[2.28]}{[M_e \sqrt{Re_D}]^{1/16}} \quad (2.6)$$

It was documented that less than 30 flow lengths ($\frac{\tau_P U_\infty}{D} = 27.9$) of flow were required before the flow could be considered established based on pressure observations and 70 flow lengths as determined by heat transfer measurements.

Lee and Lewis [12] built on the work of Holden by conducting numerical simulations of unsteady hypersonic viscous flows over a variety of geometries. Similarly to Holden, they chose to set the 98% level as the indication for flow establishment. However, rather than having separate times for both pressure (τ_P) and heat transfer (τ_Q), they maintained only one time, τ_{est} . Table 2.3 details the results of this study. It is interesting to note that flow establishment around the circular cylinder required almost twice as much time as the spheres studied by Holden in order for the flow to establish in the wake region.

The results presented by Holden, Lee and Lewis and Hollis have been reproduced in Figure 2.6 using the same format as that presented by Holden (Figure 2.5). It should be noted that the data from Hollis represents both CO₂ and Air results at both angles of attack $\alpha = 0^\circ$ and $\alpha = -4^\circ$. For each angle of attack the establishment

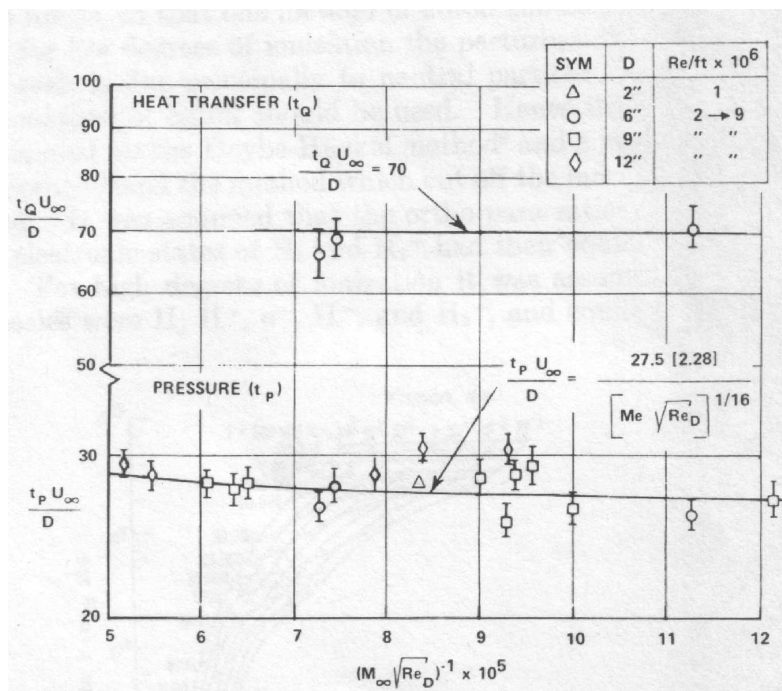


Figure 2.5: Experimental data as presented by Holden [7].

Table 2.3: Establishment time data for various geometries as measured by Lee [12].

Models	τ_p (msec)	$\frac{\tau_p U_\infty}{L}$
flat plate	0.3	3
bi-convex airfoil	1.0	9
thin double wedge	1.5	14
thick double wedge	3.0	28
circular cylinder	5.0	46

time in Air was longer than that in CO₂ and at $\alpha = 0^\circ$ the establishment time in air of 65 flow lengths is in good agreement with that found by Holden using spheres as the test geometries. From this chart it is apparent that the establishment time for a wake flow is quite dependent on the shape of the object creating said wake.

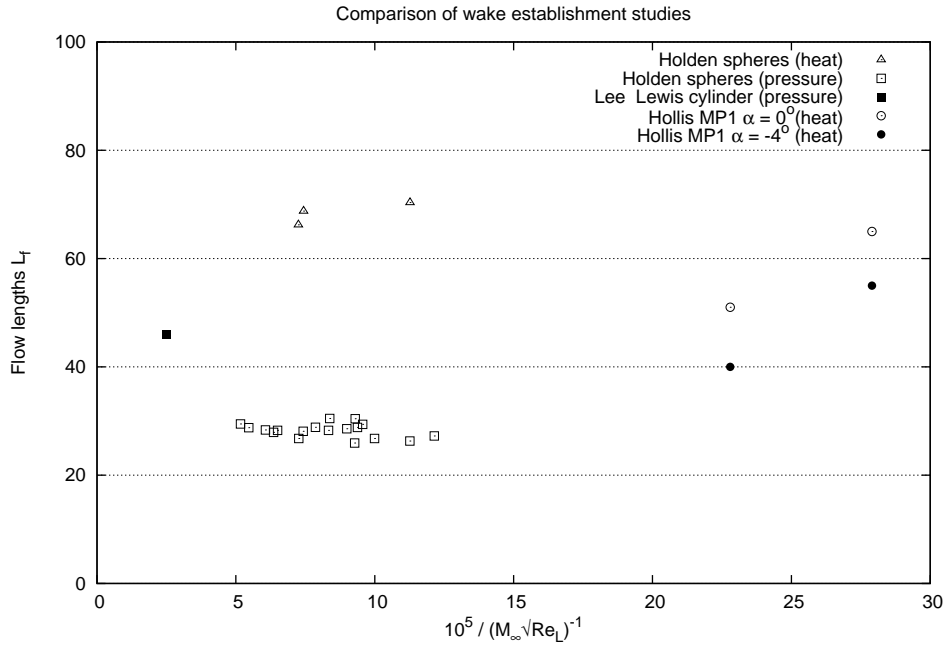


Figure 2.6: Non-dimensionalised flow length time for a variety of blunt geometries and flow conditions from Hollis [8], Lee and Lewis [12] and Holden [7]. Two types of data are presented based on the flow property (pressure or heat transfer) observed to determine establishment. Reynold’s number values were calculated in units of 1/ft to match the original data presented by Holden.

2.2 Physics of wake flow around bluff bodies

Understanding the physical processes that occur during the formation of the wake flow structure is critical to the success of accurately modelling these features computationally. While much progress has been made in this area there is still some uncertainty in our ability to predict the base heating. This section discusses the current state-of-the-art in computational modelling.

Wright [27] states that the current inability to accurately predict base heating rates has resulted in the necessity for some 200-300% design margin in the afterbody thermal protection system. Such a degree of margin significantly influences the selection of materials, mass of the overall aft body TPS and hence the position of the centre of gravity (c.g.) of the vehicle, for example. An elementary analysis of forces and moments on a probe capsule demonstrates that the position of the centre of gravity relative to the centre of pressure can cause dynamic instabilities of the capsule in flight, leading to a mission failure. Wright suggests that in some cases the effect of the TPS on vehicle design often necessitates the addition of ballast to

compensate for this effect.

Current methodology in the analysis of afterbody flows makes several assumptions:

- flow is laminar,
- flow is fully catalytic, and
- the afterbody surface is non-ablating.

With these assumptions in mind it can be stated that, for the most part, the design margin takes into account the increased levels of heating following the transition to turbulence and the unmodelled material response.

Another reason for concern is the scarcity of flight data. Wright states that the majority of available data stems from the days of the Apollo program and perhaps a few other European and American missions. The Mars Pathfinder mission carried only one thermocouple on the aft heat shield and the Viking Landers carried two. While the engineering community supports the addition of instrumentation to heat shields, mission management dismisses these proposals from a cost perspective.

In all data recorded from experimental facilities, such as shock and expansion tunnels, the necessity of the sting mount for the test models interferes with the wake flow structure and provides flow attachment as a method of wake closure. This is evident when comparing simulations of the Mars Pathfinder aeroshell, as shown in Figure 2.7. The image on the left represents an axisymmetric flow solution at angle-of-attack, $\alpha = 0^\circ$, which shows evidence of a disc shock in the wake. However, the second image showing the solution of a 3D simulation at $\alpha = 1^\circ$ demonstrates a completely different flow structure and no disc shock. Clearly, then, there is some question as to whether this phenomena is merely artificial or truly exists. Conventional Schlieren images cannot resolve the presence of this weak shock and so further work needs to be done in this area.

In all this uncertainty some things are known such as the basic physical process of wake structure formation. It is known that in most circumstances the flow will undergo the transition to turbulence following the expansion around the shoulder (or some angle) of the bluff body. This process begins in the far wake region and propagates upstream (further with increasing freestream Reynolds number). It is

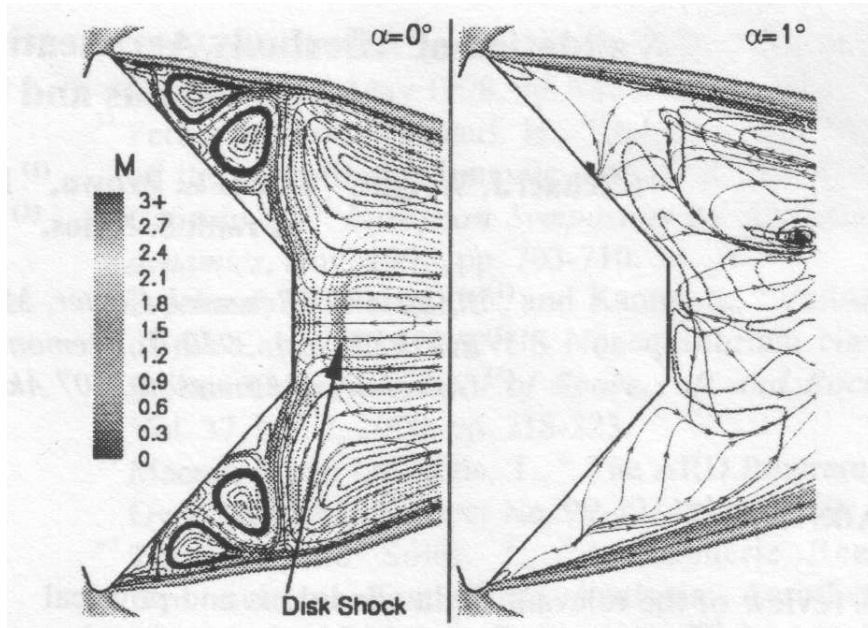


Figure 2.7: Computed Mach number contours and streamlines in the wake region of the symmetry plane of the Mars Pathfinder entry probe [27].

stopped at the neck by the adverse pressure gradients. The separation shear layer causes the transition in the base region.

Lees [13] suggested a Reynolds number based correlation to predict the transition to turbulence for use with two-dimensional or axisymmetric flows, as given in Equation 2.7.

$$Re_{tr} = \frac{\rho_e U_e L}{\mu_e} \quad (2.7)$$

where L is the length of the shear layer from the separation point and the other parameters are taken from the outer edge of the shear layer. The values of Re_{tr} are in the range of 2×10^4 and 5×10^6 at Mach 2 and 5 respectively.

Wright also noted that for low Re_∞ the wake flow was steadier with fewer and larger vortices while at higher Re_∞ the flow structure included more separation and a more complex vortex pattern. Considering this phenomenon, Wright [27] suggests that a non-equilibrium gas model is needed in computational studies. Ionisation and dissociation effects are present due to the high temperature flow and shock structure. Furthermore, the differing characteristic relaxation times for the thermal and chemical processes affect the flow simulation. As the flow expands into the the near-wake region the slower processes are frozen but faster processes such as chemical relaxation continue at a finite rate.

A review of the current turbulence modelling techniques was conducted by Wright which included:

- Baldwin-Lomax with compressibility correction,
- One-equation Spalart-Allmaras,
- Two-equation Wilcox $k-\omega$ model, and
- Menter's two-equation SST $k-\omega$ model [14].

It was shown that flow simulated with the laminar assumption or the Baldwin-Lomax model under predicted heat rates up to a factor of three. The Spalart-Allmaras and Wilcox models also under-predicted the rates but the amount was not specified. Menter's SST $k-\omega$ model accurately predicted the base heating rates. Sample results from this survey are shown in Figure 2.8.

Computational fluid dynamics formed the basis of the analysis that Hollis [8] conducted. Table 2.4 details the control points used to defined the Mars Pathfinder vehicle geometry and Figure 2.2 shows the critical dimensions. The baseline grid for Hollis' study, comprised of 125 streamwise points and 90 normal points, was generated via an elliptical grid generation algorithm. While higher wall resolution was desired, spacings of 10^{-5} were specified. Test computations revealed that the change in heat transfer rates was minimal for wall cell spacing less than this value and so extra computational time was not deemed worthwhile. Evaluations of the cell Reynolds number as per Equation 2.8 yielded values of 10 or less.

$$Re_{wall} = \frac{\rho a \Delta s}{\mu} \quad (2.8)$$

Grid adaptation was employed to improve grid resolution in regions of high gradients. Initially the adaptation included holding steady the local Reynolds number (Eq. 2.8) but this led to excess cell growth in the afterbody region. A solution adaptive scheme to fit the grid to the shock and adjust the normal spacing near the wall was employed. Figure 2.9 illustrates the differences between the initial grid and the result of solution adaptation.

Wright [27] also indicated the need for careful generation of computational grids. He suggested that it was critical to have the grid aligned with the major flow features

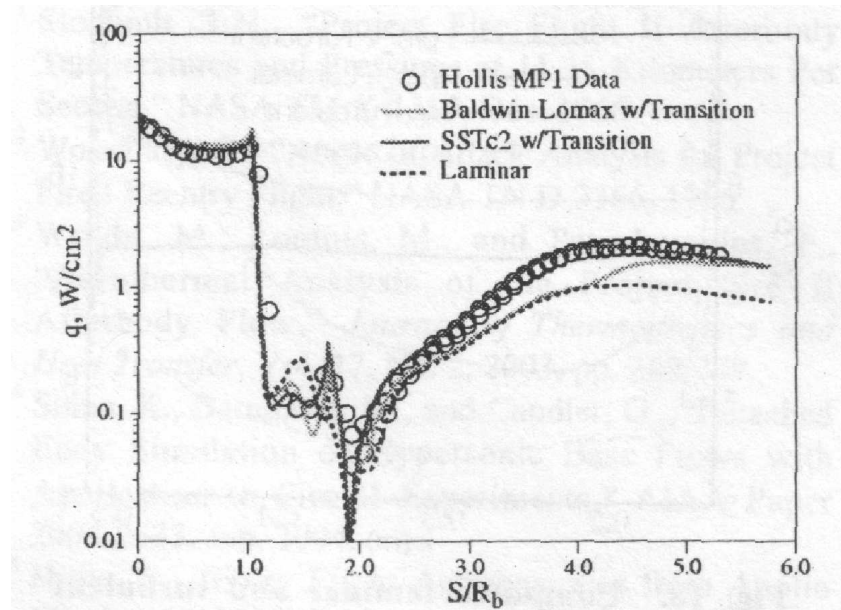


Figure 2.8: Results of a turbulence model survey over the Mars Pathfinder aeroshell geometry [27].

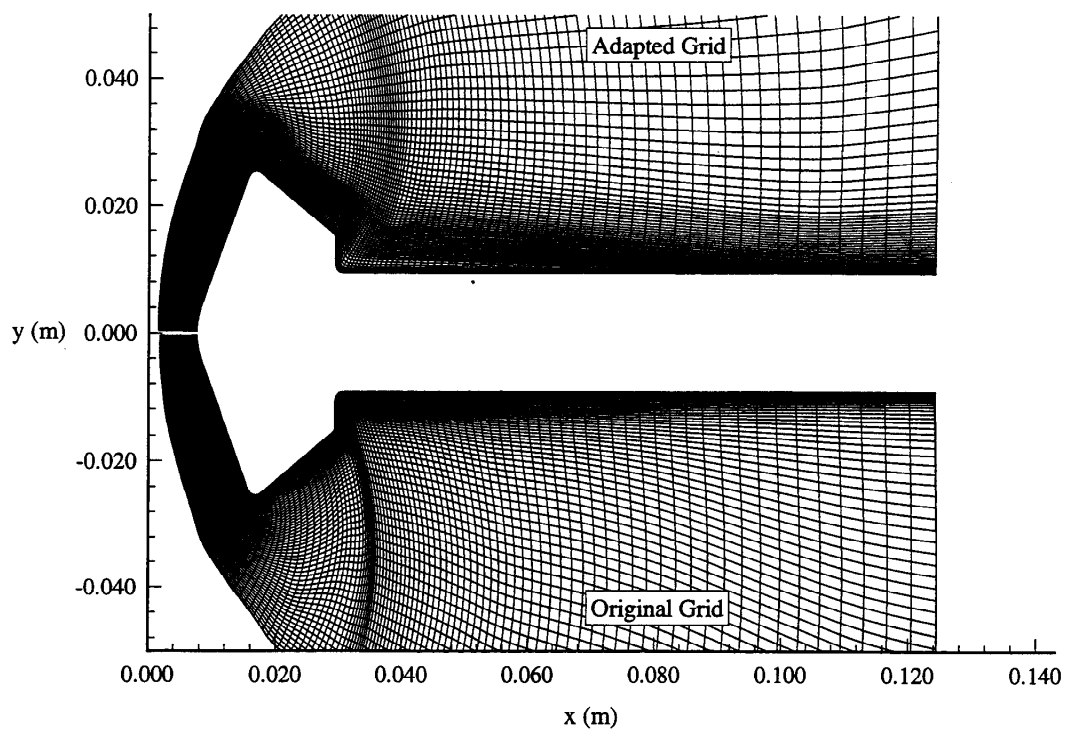
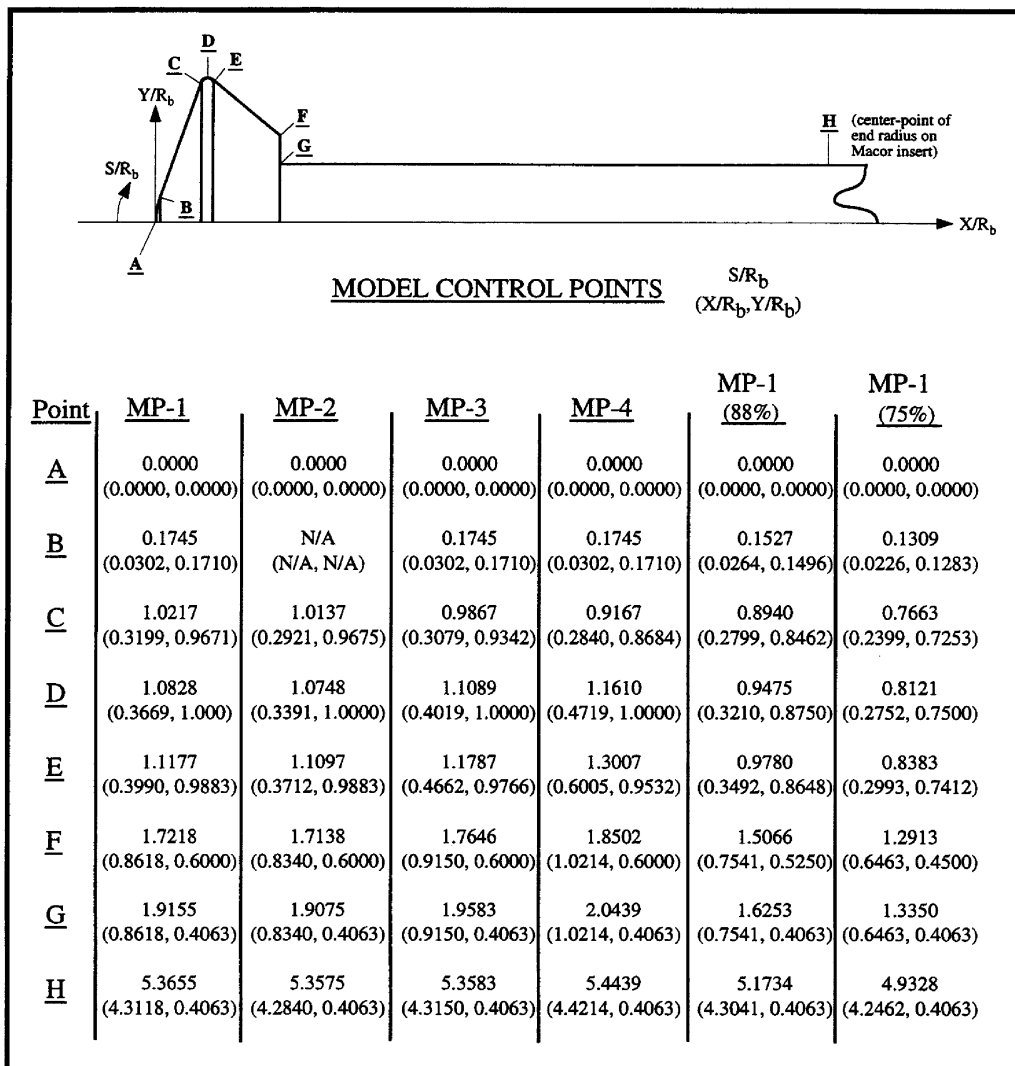


Figure 2.9: Example of a solution adaptive grid [8].

Table 2.4: Control points used to define computational models [8]. The notation MP stands for Mars Pathfinder.



and to ensure sufficient points were placed around areas of flow expansion and separation. Hollis' adapted grid is an example of this.

Mitcheltree and Gnoffo [15] performed CFD simulations using LAURA (Langley Aerothermodynamic Upwind Relaxation Algorithm) based on the Mars Pathfinder vehicle and conditions taken at two critical points in the entry trajectory: maximum heating and maximum deceleration. The conditions at these points are detailed in Table 2.5 with the calculated values for the maximum convective heat flux on the aft body and corresponding pressure with percentages of forebody stagnation values in parentheses. This data can be used for comparison to the current computational capabilities of the in-house Multi-Block Compressible Navier-Stokes (MBCNS2) code.

The geometry of the Pathfinder (as used by the authors) is a 70° sphere cone forebody with a 0.6625m nose radius and overall vehicle diameter of 2.64m. The 49.7° aft body cone is connected to the forebody by a shoulder of radius 0.06625m.

Mitcheltree and Gnoffo used a similarly refined grid to Hollis with cell spacing at the wall of 1×10^{-5} m, which gave a Reynolds number of $Re = 3$ at the stagnation point. They sized the flow domain to include a distance of 7.5 radii downstream of the vehicle. They found that a mesh with 136 streamwise and 80 normal points was adequate for resolving the heating rates when compared to a 136×160 grid.

Results showed that for the flight condition at the point of maximum heating a strong recirculation vortex extended downstream to the free-shear-layer stagnation point 5.17 m ($x/R_b = 3.92$) from the nose. However, at the flight condition of the point of maximum deceleration this vortex was much smaller and the shear-layer stagnation point was at 4.41 m ($x/R_b = 3.34$) from the nose.

Current best practices in CFD for simulation of separated hypersonic flows around bluff aeroshells are unable to provide accurate predictions of base heat-

Table 2.5: Flow conditions used by Mitcheltree and Gnoffo [15].

Quantity	Max. Heating	Max. Deceleration
Altitude (km)	40.7	28.5
Velocity (m.s ⁻¹)	6592	4862
Density (kg.m ⁻³)	3.24×10^{-4}	1.161×10^{-3}
Temperature (K)	162	176.8
Reynolds No.	0.64×10^6	1.53×10^6
Max. q_w (W.cm ⁻¹)	6.7 (5.9%)	7.0 (10%)
Aft body pressure (Pa)	154 (1.1%)	371.55 (1.4%)

ing rates. The Baldwin-Lomax turbulence model is a good tool for engineering estimates but lacks the accuracy of the SST $k-\omega$ model. Solution adaptive grid generation techniques have been suggested in order to correct alignment of the grid to the major wake flow features. Sufficient volume must be specified downstream of the vehicle geometry in order to capture the formation of wake flow features.

Computational Study

3.1 Overview

Computational fluid dynamics (CFD) has been used in this study to provide insight into the flow structure behind the Mars Pathfinder aeroshell geometry under the flow conditions of interest, outlined previously in Table 1.1. The objectives of this CFD study are:

- To provide insight into the flow structure behind a model of the Pathfinder aeroshell geometry;
- To determine the size of the expected separated recirculation zone behind the model and the location of flow reattachment;
- To estimate the time required for wake flow establishment.

To meet these objectives a computer generated model was created and the flow field solved using an in-house code named Multi-block Compressible Navier-Stokes v2 (MBCNS2) developed by Jacobs [11]. A description of the governing equations can be found in Appendix A. It should be noted that turbulence was not included in any computer models as part of this study.

Following the discussion of the previous chapter, CFD techniques are currently unable to predict base heating rates accurately. This portion of the present study does not aim to improve upon these techniques. Rather, this computational exercise was undertaken to provide insight that would assist in the subsequent experiments and to evaluate the use of expansion tubes as a means for studying the phenomena.

3.2 Grid Preparation

Formation of a suitable solution grid is an essential part of any CFD study. The discretisation of the flow field plays an important part because the Navier-Stokes equations are solved at any given point in the flow domain by using flow properties around that point. Poor spatial structure and inadequate resolution can lead to numerical inaccuracies driven by false flow gradients. Prior to any attempt at grid generation, a review of similar work was conducted to examine what would provide the best basis for calculation.

Solution adaptive grid generation was considered but it was deemed too computationally expensive and superfluous to the aims of the study. This type of simulation requires constant runtime analysis of the flow features which then adapts the grid to provide a better spatial basis for solving the Navier-Stokes equations. However, the expensive technique of solution adaptive grid generation is not required for this study designed to provide insight into the near-wake flow field. As such, a simple grid dependence study was conducted to aid in the selection of a suitable computational grid.

To this end, basis grids for the Pathfinder capsule geometry were constructed from a generic template as shown in Figure 3.1. The flow domain around the forebody was generated by applying the Billig correlation [3] relating the bow shock standoff distance to the freestream Mach number and the radius of the body. This domain allowed for some margin of error for capturing the bow shock and a rudimentary attempt at aligning the grid with the shock to aid in better spatial resolution of the shock itself. The grid in the aft flow region was designed to capture the full length of the instrumented model support sting and a portion of the sting mount apparatus as used in the experiments discussed in the next chapter. The computer generated model only accounts for a two-dimensional cross-section through the flow domain around the geometry and as such an axisymmetric condition is applied during the solution process.

Grid resolution around the bluff body and in the vicinity of anticipated flow features was taken into consideration during the design. Cell clustering was implemented to increase cell density near walls and the near-wake region behind the capsule. Hollis [8] determined that a spacing of $S/R_b = 4 \times 10^{-7}$ m was sufficient

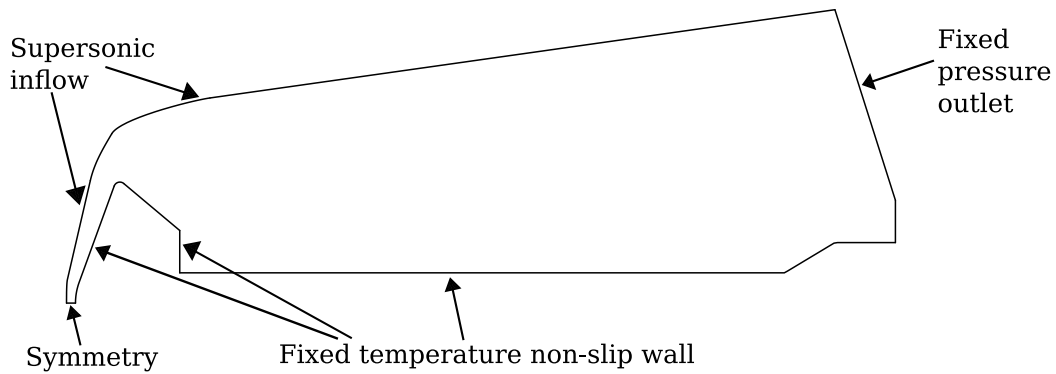


Figure 3.1: Computer generated flow domain with boundary condition types marked.

to resolve heat transfer on the model walls. For cell heights smaller than this the “heat transfer rates were nearly invariant” [8].

In order to maximise computational efficiency and ensure the flow field is solved as accurately as possible, grids are arranged so that more nodes are present in regions where the flow gradients are expected to be large, and conversely less nodes in regions of relatively small gradients. For example, the bow shock across the forebody of an aeroshell creates a large pressure gradient in that region of the flow. Therefore, more grid nodes are placed around and behind the shock than upstream of the shock where the flow is stable. This technique is known as clustering and can be achieved by many methods.

Prior to this investigation, the MBCNS2 software contained only one such method in the form of a geometric cell growth function by Roberts [21]. The practical limitations of a simple geometric growth function are two-fold. Firstly, whilst this function could provide the desired spacing around a feature it would be by trial-and-error by varying the growth factor and number of nodes along the interval. Secondly, the implementation within MBCNS2 imposes constraints on surrounding grid patches because the clustering is either one-sided or symmetrical over the interval. An alternative node clustering method has been implemented providing more flexibility and control of the mesh generation process.

3.2.1 Valliammai Cluster Function

Valliammai et. al. [25] demonstrated a versatile function for distributing points along a discretised interval, described in Equation 3.1

$$x(t) = \frac{\exp(\alpha t) - 1}{\exp(\alpha) - 1} \quad (3.1)$$

where α is a scalar and $0 < t < 1$ is a fraction denoting the position of the n th discrete portion of a curve. The cell spacing, $x(t_n) - x(t_{n-1})$, at the end of a discretised interval is found by solving the value of the scalar α from the following difference.

$$x(t_n) - x(t_{n-1}) = \frac{\exp(\alpha t_n) - 1}{\exp(\alpha) - 1} - \frac{\exp(\alpha t_{n-1}) - 1}{\exp(\alpha) - 1} \quad (3.2)$$

The function is then applied to an interval of known length. In theory, this function allows for spacing of any magnitude to be specified to either end of the interval. The implementation of this function for MBCNS2 improves the process of maintaining cell aspect ratios across block boundaries when the same spacing is applied on each side of the block boundary. In practice the spacing at the end of the interval is limited by the number of nodes requested, the length of the interval and the desired spacing required by the user.

The comparison of the Valliammai cluster function to the Roberts cluster function is best described by the illustrations in Figures 3.2a and 3.2b. The figures show the same domain separated in three distinct patches with a grid applied using the Roberts function (Fig. 3.2a) and the Valliammai function (Fig. 3.2b). In this example, the grid has been refined around each of the boundaries of the centre block to better resolve an arbitrary flow field at those locations. A different level of refinement is required at each location, so the centre block must provide a suitable mechanism at each boundary to match the cell spacing in the adjacent blocks. For the purposes of demonstration, the left interface of the centre block required a high density of nodes where the interface on the right required no clustering. By comparing the figures, it is evident that the implementation of the Valliammai function was able to apply a different clustering density on each side of the central block thus meeting the requirements and maintaining a smooth cell aspect ratio across the boundary. However, the built-in Roberts clustering was limited by its symmet-

ric constraint. The interface to the right of the central block in Figure 3.2a shows a non-smooth aspect ratio transition across the boundary.

Furthermore, the Valliammai function provides a big improvement to grid generation efficiency. Typically the grid generation process is one of the most time intensive aspects of any CFD based study. Given that the grid has a major impact on the solution this time is justified. However, the Valliammai function can yield considerable time savings in the grid generation stage over the existing cluster functions within MBCNS2. The Roberts function uses a geometric growth factor which is used to determine the spacing of the nodes. Ergo, the positioning of the nodes along any given interval is dependent on the interval length and the number of nodes. Should either parameter change, the spacing at the end of the interval will also change. The implementation of the Valliammai function for MBCNS2 fixes the cell length at the end of the interval and therefore, changes to these parameters do not impact the cell spacing at the interval ends (within practical limitations). Given that grid generation is always an iterative design process with many variations implemented before a suitable grid is selected, this implementation of the Valliammai function proves to be more efficient and more flexible than the MBCNS2 built-in Roberts function.

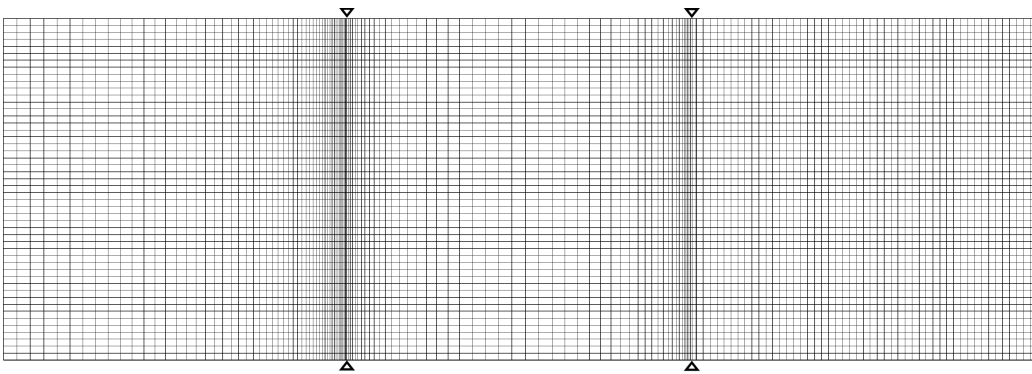


Figure 3.2a: Example of multi-block cell clustering using the Roberts function. Arrows indicate block interface locations.

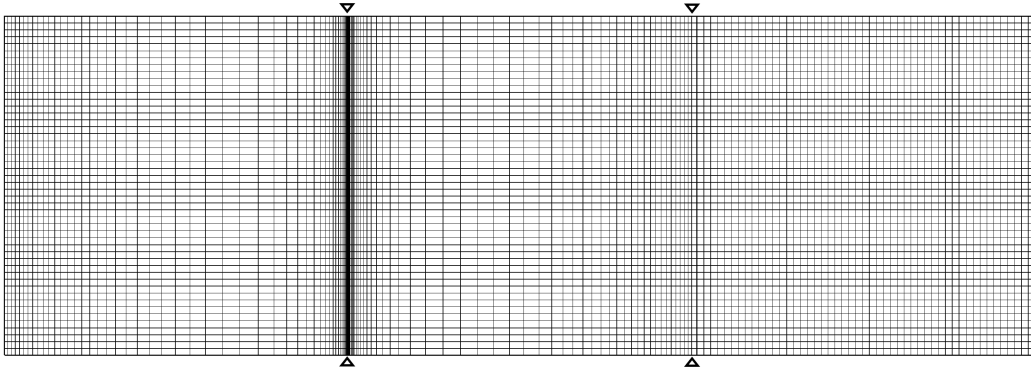


Figure 3.2b: Example of multi-block cell clustering using the Valliammai function. Arrows indicate block interface locations.

3.2.2 Block and Grid Layouts

Depicted in Figure 3.3 is the block layout used for the MBCNS2 CFD calculations for the Mars Pathfinder capsule. The flow domain is subdivided into what are classified as “superblocks”. The boundaries of the superblocks are discretised using the methods described in the previous section. Prior to solving, the flow the grid is determined using Transfinite Interpolation (TFI) based on the on the discretised boundaries of the superblocks. These superblocks are then subdivided (shown with dashed lines) after grid generation in preparation for parallelisation. The subdivision is done such that each sub-block has an equal number of cells to any other sub-block in a given superblock. This facilitates a basic load sharing system for solving the flow using cluster or parallel computing facilities.

With a base grid designed a grid dependence study was conducted for the selection of a suitable grid for the purposes of providing engineering estimates for this investigation.

3.3 Grid Dependence Study

A study was conducted to ensure that the computationally derived results were not compromised by an inappropriately discretised mesh. This process involves the generation of a base grid and refining this grid in stages. Refinement can include both adding nodes and changing the clustering conditions in certain regions of the flow domain. At each stage of refinement the fluid flow is solved and the solution compared to that at other refinements. An ideal grid will yield an acceptable solu-

tion and at the lowest computational cost whilst also demonstrating minimal change between grid refinements. That is, the ideal grid will generate the same solution as a more refined grid, within acceptable tolerances, and take the least amount of computational time to solve. For this grid dependence study, the solution comparison criteria were the location of the flow reattachment to the sting and the heat transfer distribution over the experimental model sting after a set amount of time.

A starting point was defined for this process. The base geometry is shown in Figure 3.3 and Table 3.1. The design basis for this grid was to have wall cell spacing in the order of $S/R_b = 4 \times 10^{-7}\text{m}$ as determined by Hollis [8] to resolve the heat transfer rates. This value was not improved on in this study as attempts to do so increased the required computational time by several orders of magnitude. The refinement process used in this study was aimed at improving the spatial accuracy of the two criteria listed above. Ergo, the number of cells along the model body was refined both in the streamwise direction and normal to the wall.

The *Base* grid design included the use of both the Roberts and Valliammai clustering functions for the streamwise and normal cell positioning, respectively. However, the cell transition across the boundaries between blocks proved to be unsatisfactory and therefore Valliammai clustering was adopted in refinements *Base+1* and *Base+2*. Furthermore, the resolution of cells along the wall of the model was too coarse resulting in large errors, numeric instability and a false solution. In comparison to the refined grids, the error in flow attachment location was in the order of 100% and levels of heat transfer were four orders of magnitude greater. Wall profiles for pressure and velocity along the sting are shown in Figures 3.4 and 3.5 respectively. These plots clearly indicate the discrepancy between the *Base* grid and its refined counterparts.

The refinement options in meshes *Base+1* and *Base+2* yielded better results. Figure 3.6 depicts the flow attachment time history from the solutions of the *Base+1* and *Base+2* grids. The comparison between the solutions generated with grids *Base+1* and *Base+2* indicates only minor improvements between the two refinements. The results from the *Base* solution contained too much numerical noise to obtain a smooth line representation of the flow attachment history. However, several points were manually extracted at intervals of every ten flow lengths. The location

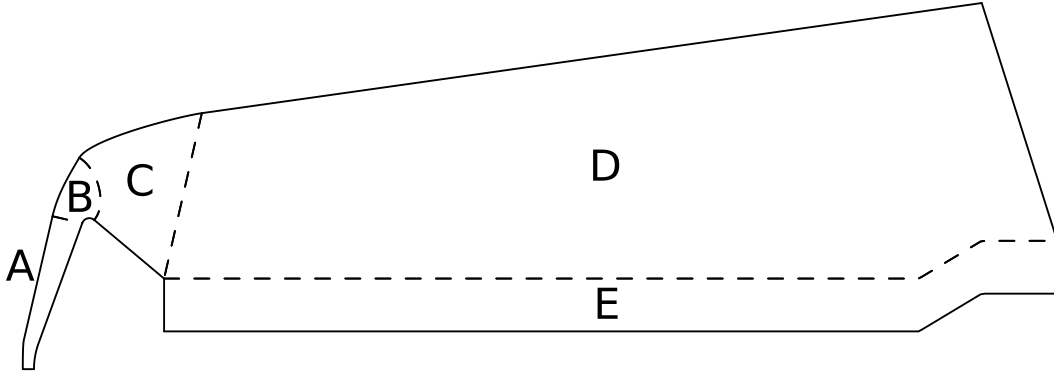


Figure 3.3: Base CFD model block layout for the Mars Pathfinder experimental scale model geometry.

Table 3.1: CFD block refinement parameters.

Block	Cell quantity (Streamwise \times Normal)	Wall normal cell height [m]
<i>Base grid</i>		
A	100×50	1.40×10^{-5}
B	30×50	1.05×10^{-5}
C	50×50	1.55×10^{-5}
D	100×50	-
E	100×100	2.20×10^{-4} (base) 1.36×10^{-5} (sting)
<i>Base+1 refinement grid</i>		
A	100×50	1.40×10^{-5}
B	30×50	1.10×10^{-5}
C	50×50	1.49×10^{-5}
D	200×50	-
E	200×40	1.04×10^{-5} (base) 1.48×10^{-5} (sting)
<i>Base+2 refinement grid</i>		
A	100×75	1.30×10^{-5}
B	30×75	1.01×10^{-5}
C	75×75	1.32×10^{-5}
D	200×75	-
E	200×60	1.04×10^{-5} (base) 1.28×10^{-5} (sting)

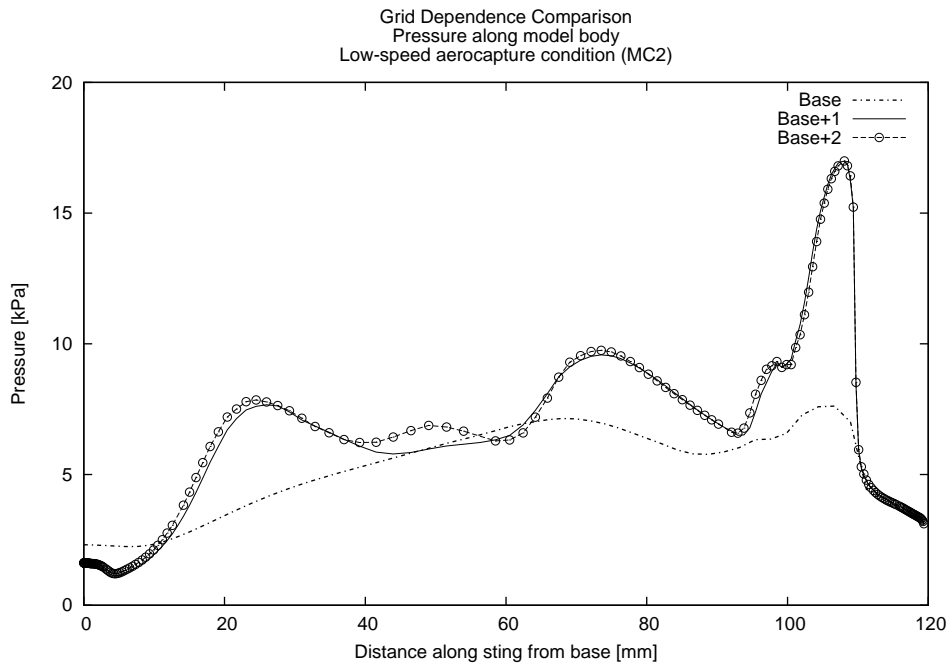


Figure 3.4: Grid dependence study grid comparison - pressure profile along the sting.

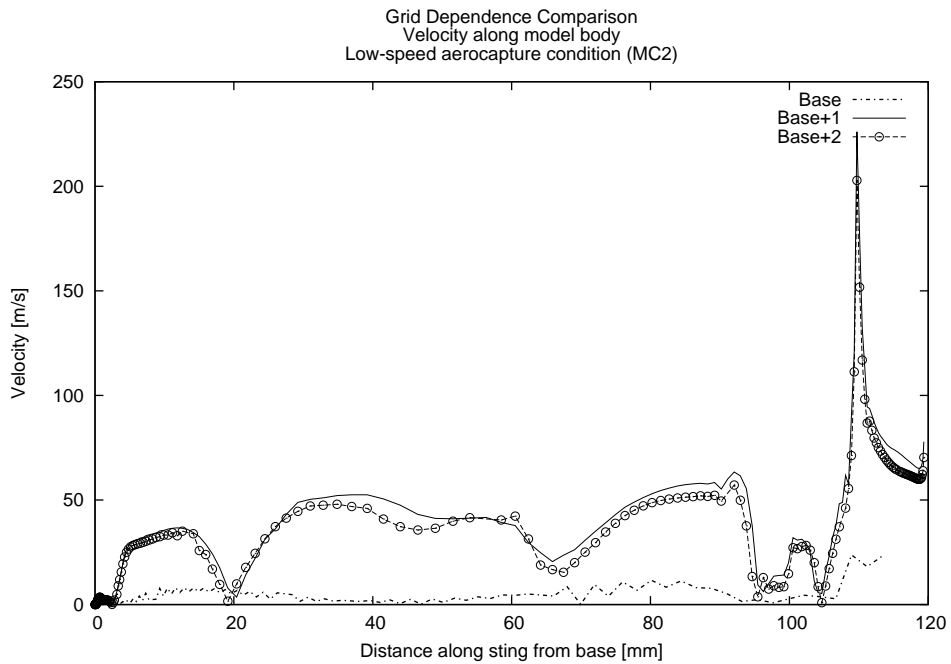


Figure 3.5: Grid dependence study grid comparison - velocity profile along the sting.

resolved by the solution on this grid is vastly different to that determined by the more refined meshes. Further indication that this grid was inadequate can be observed in Figure 3.7 where the flow attachment location is plotted against the cell height at the wall along the sting.

Figure 3.8 illustrates the heat transfer distribution as solved on the refined grids. The heat transfer distribution along the sting appears to be smoother in the solution from grid *Base+2* suggesting that this refinement induces less artificial gradients in the flow at the wall and indeed throughout the flow domain given the structured nature of the discretisation. The computational time for the generation of this solution was not significantly greater than that of grid refinement *Base+1* and therefore grid *Base+2* was selected as the nominal grid for all further flow simulations.

Further refinements were attempted with a focus to reducing the cell height along the aeroshell body and sting. However, when the normal cell count was increased and therefore cell height reduced, the required computational time increased greatly. The driving factor behind the increase in computational time was the viscous terms in the flow equations. The time step associated with viscous terms is directly proportional to square of the cell size. Thus, if the cell size in an arbitrary reference mesh was reduced by a factor of 2, say in the streamwise direction, the time step would decrease by a factor of 4 (observed for the *Base+1* and *Base+2* meshes). If the cell size was halved again, perhaps in the normal direction, the time step would decrease by a factor of 16 over the reference mesh.

These changes in time step lead to a very significant change in computational cost. As such, attempts to obtain solutions on further refined meshes fell outside the scope of this work. However, it is recognised that further computational work would require additional studies in this area including the investigation of adaptive mesh techniques.

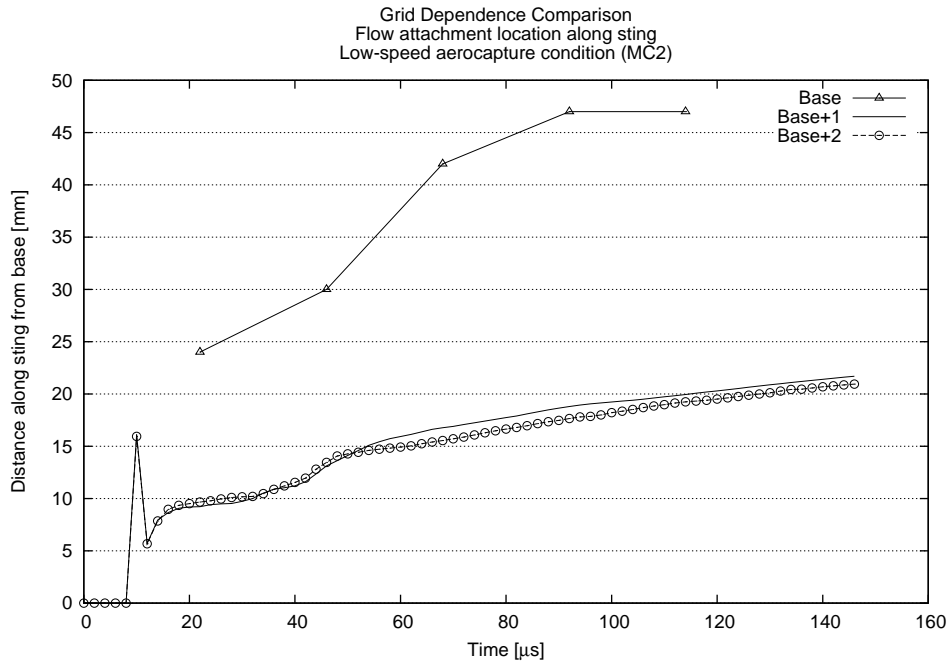


Figure 3.6: Grid dependence study grid comparison - flow attachment location along sting.

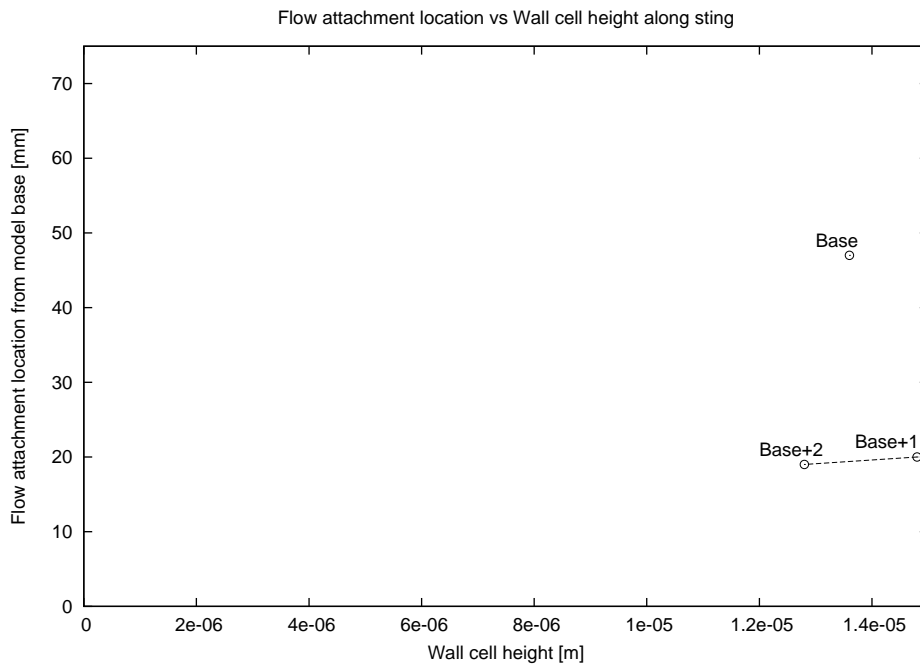


Figure 3.7: Grid dependence study grid comparison - flow attachment location after 50 flow lengths along sting for each grid solution plotted against the cell height along the sting wall.

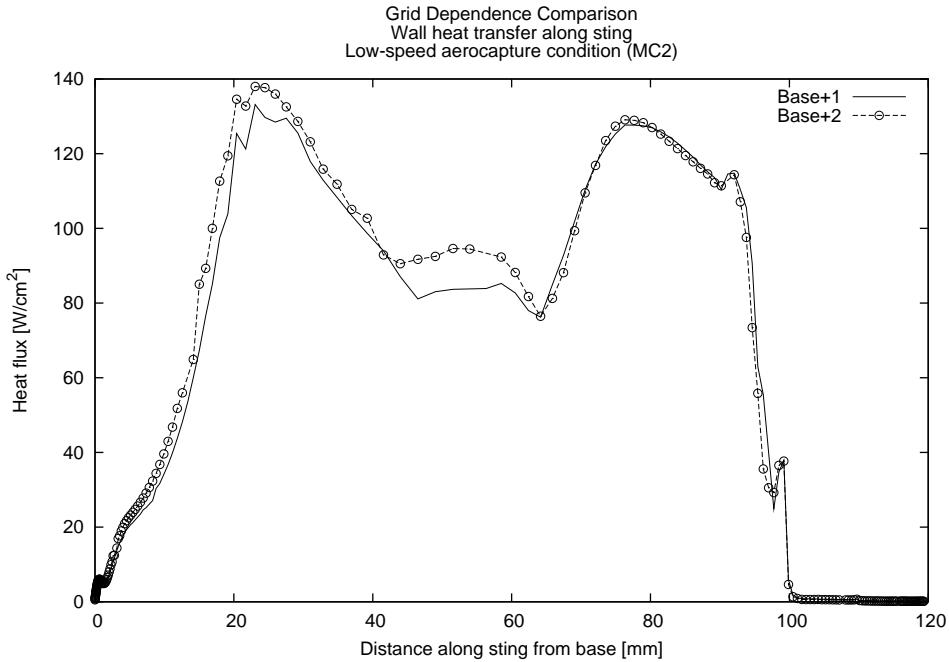


Figure 3.8: Grid dependence study grid comparison - heat transfer distribution along sting.

3.4 Near Wake Flow Field Characteristics

The flow field examined in this study is inherently transient by virtue of the short test durations of ground-based impulse facilities. For the purposes of providing a point of comparison to the experimental portion of this study and insight into this region of the flow field, a snapshot has been taken at a selected point in time. The selection of this point in time was derived from the work of Hollis [8]. The determination of that study was that between 40 and 70 flow lengths were required for wake establishment with an average requirement of 51 flow lengths in CO₂ flows at speeds of 4,700 m/s using a characteristic length of $y_{ref} = 15$ mm.

Recapping the discussion of Section 2.1, a flow length, denoted as L_f , is a non-dimensional parameter that quantifies the number of slugs of gas at freestream velocity covering some characteristic length in a given amount of time and is described by Equation 2.1. In the present study, the characteristic length has been selected as the step height defined by the radius at the shoulder of the aeroshell less the radius of the mounting sting. This step height is $y_{ref} = 15$ mm which is illustrated in Figure 3.9. Based on the average flow length requirement from Hollis' study, the wake establishment times for the model employed in this study are presented in Table 3.2.

From the flow solutions obtained at each flow condition, velocity data was captured along the sting in order to determine the flow reattachment point. The time history of the location of the reattachment point is shown in Figures 3.10 and 3.11 for flow conditions MC1 and MC2 respectively. It is clearly evident from these charts that the size of the recirculation zone continues to grow at a linear rate after 50 flow

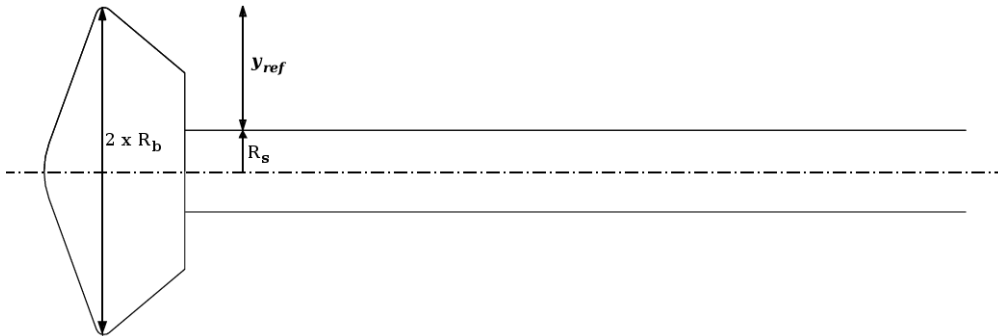


Figure 3.9: Reference length for the Mars Pathfinder geometry.

Table 3.2: Predicted wake establishment times based on findings by Hollis ($L_f = 51$) and characteristic length of 15 mm.

Experimental flow condition identifier	Condition description	Nominal freestream velocity U_∞ (m/s)	Wake establishment time (μs)
MC1	Low-speed Mars aerocapture profile	6,500	118
MC2	Direct Mars entry condition (also known as the “Langley” condition)	4,700	163

lengths of gas at constant conditions. In addition to these time-based plots, a series streamline plots were generated to examine the formation of the wake flow structure. For condition MC1 these plots are depicted in Figure 3.14 and in Figure 3.15 for the MC2 flow condition.¹

The size of the recirculation zone in the Langley flow conditions is notably smaller than that determined by Hollis, as depicted in Figure 3.18. This is thought to be because the solution produced by Hollis is much more advanced in time, possibly to the point of being a steady-state solution. It is clearly evident that the flow field in Hollis’ simulations appears to have separated at the shoulder and the recirculation zone covers the entire length along the aft cone frustum. Conversely, in the current study the most time advanced solution at 150 μs shows that the vortex has extended part way along the aft cone and that the flow remains attached from the shoulder along the majority of the frustum. Streamlines presented from a steady-state solution provide a false impression of the wake flow structure in comparison to what may be observed in ground-based testing given the very short experimentation times. In a flight-based context the wake flow structure has an abundance of time to develop more fully and so the steady-state solution is a reasonable approximation of the size of the vortex in flight.

¹It should be noted that the available visualisation software is unable to correctly interpret the grid structure and as a result places small triangular artefacts throughout the domain. These artefacts also impede the computation of the stream functions which terminate when encountering these artefacts. However, these visual glitches in no way compromise the process of solving the Navier-Stokes equations.

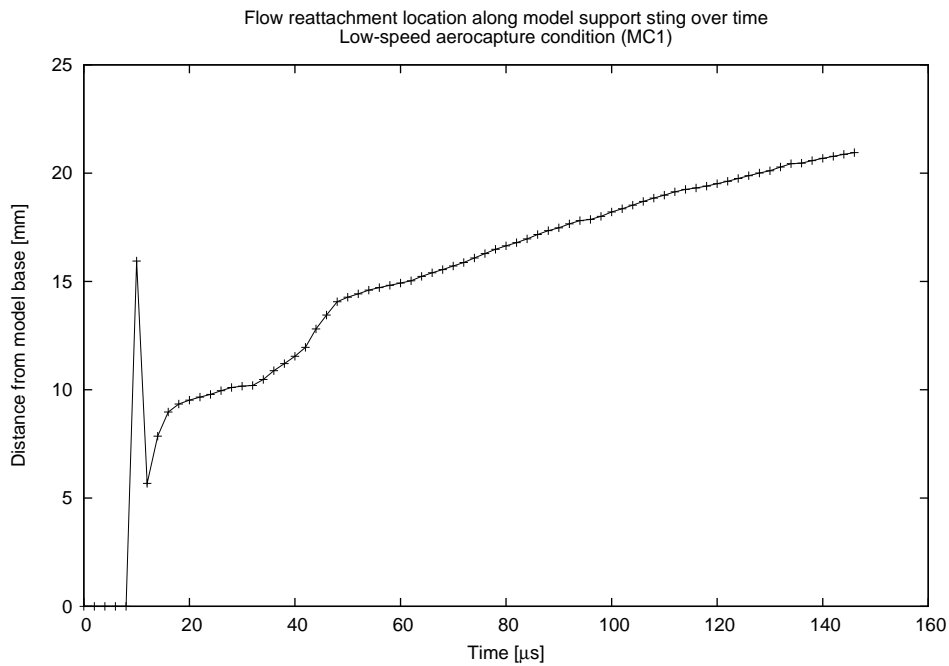


Figure 3.10: Wake flow attachment location time history for the low-speed aerocapture condition (free stream velocity $U_\infty = 6,500$ m/s).

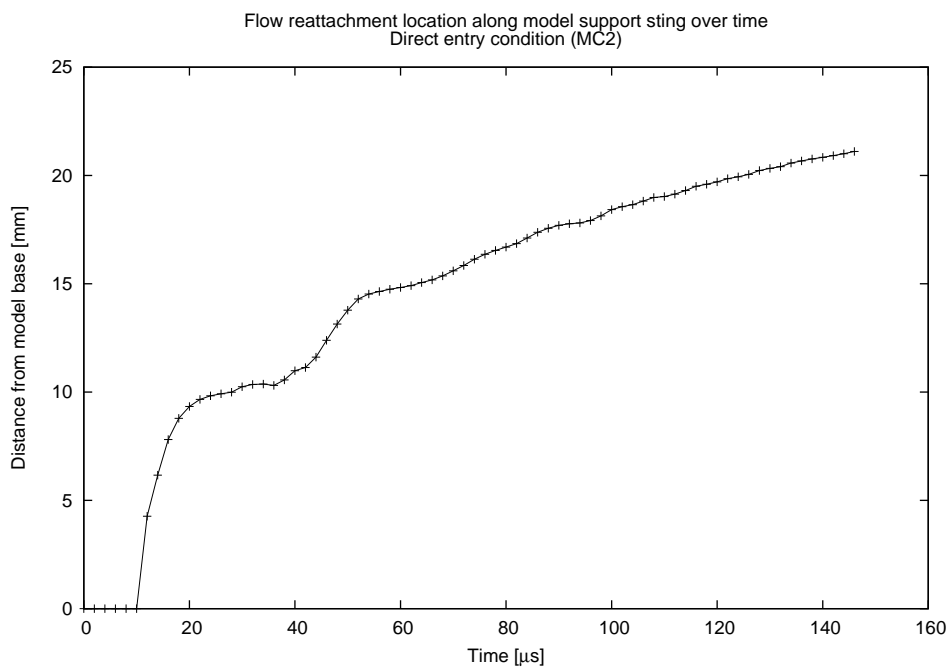


Figure 3.11: Wake flow attachment location time history for the direct entry condition (free stream velocity $U_\infty = 4,700$ m/s).

Heat transfer data along the model sting mount was also extracted from the solution at a time of 50 flow lengths and is presented in Figures 3.12 and 3.13 for flow conditions MC1 and MC2, respectively. It is evident from these charts that the peak heating point closest to the base of the aeroshell body occurs near to heat gauge location F. This is in reasonable agreement with the streamline plots and the flow attachment point time history. Additional plots for instantaneous heat transfer rates along the sting at time intervals of 10 flow lengths are located in Appendix C.

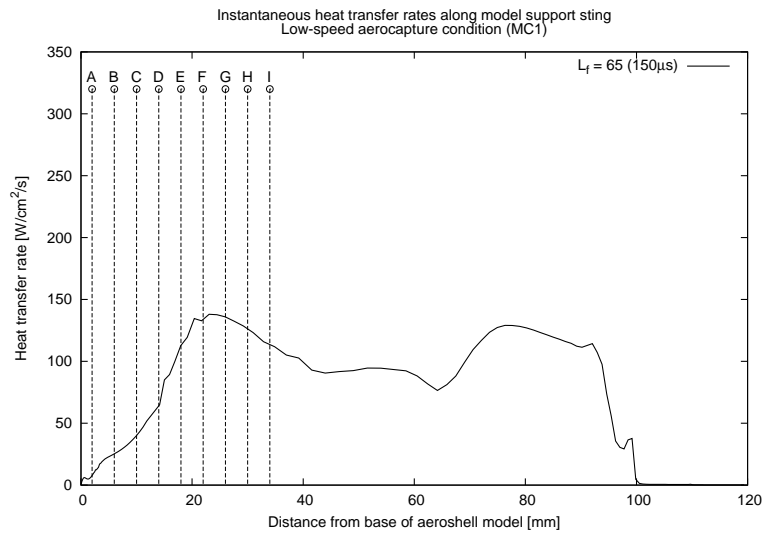


Figure 3.12: Instantaneous heat transfer after 65 flow lengths for the low-speed aerocapture condition (free stream velocity $U_\infty = 6,500$ m/s). Relative positions of heat gauges is shown.

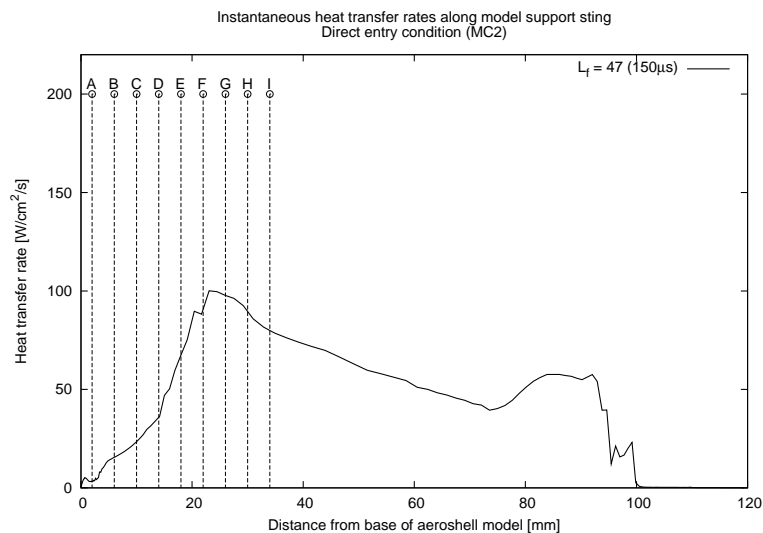


Figure 3.13: Instantaneous heat transfer after 50 flow lengths for the direct entry condition (free stream velocity $U_\infty = 4,700$ m/s). Relative positions of heat gauges is shown.

3.5 Wake Flow Establishment

Based on this spatial reasoning alone it could be concluded that the wake flow does not achieve steady-state within the time frame given by Hollis, being on average 51 flow lengths of the characteristic length $y_{ref} = 15$ mm. There is an important distinction between the terms *steady-state* and *established wake flow* in the context of this and other investigations. Steady-state is used to describe the state of the flow in which the flow field is unchanging from one time step to the next. Hollis quantified the point at which the wake flow had become established as the time at which stable time-averaged heat transfer was observed. As demonstrated by the CFD study, the flow field is still evolving beyond the point at which Hollis declared that the wake flow was established. Despite the flow field not being in steady-state, the work of Hollis suggests that the time-averaged heat transfer measurements are stable.

Moreover, streamline plots do provide some insight into the evolution of the wake flow field with respect to the thin-film heat gauges installed in the experimental model. The construction and instrumentation of the model is discussed in more detail in Chapter 4. It should be noted however that early in the wake establishment process the flow attachment point is seen to move further from the base of the aeroshell as time progresses.

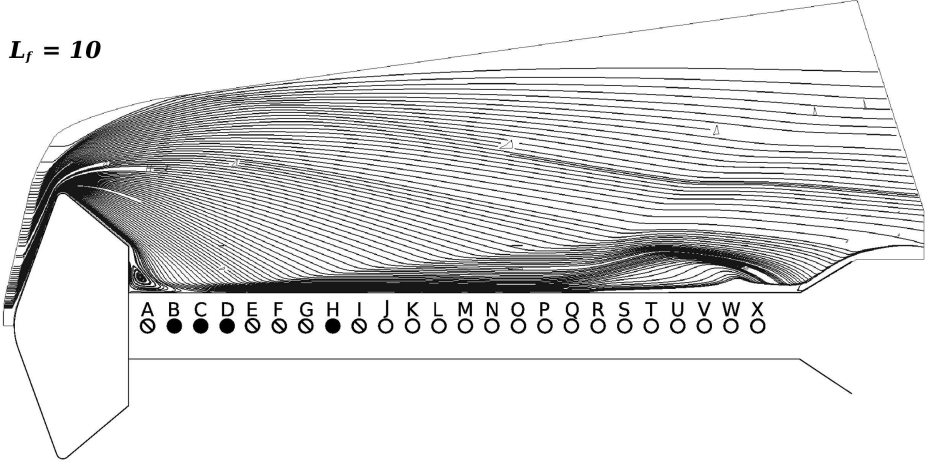
To investigate the stability of heat transfer in the computed flow solutions, data was extracted along the surface of the sting behind the aeroshell where thin-film heat gauges were mounted for the experimental portion of this study (as discussed in Section 4.5.2). The simulated level of heat transfer has been extracted as a function of time at gauge mounting positions A through I, as denoted in Figure 3.14 and Figure 3.15 for each of the flow conditions. The time history of heat transfer rates for the aerocapture condition MC1 is presented in Figure 3.16 and in Figure 3.17 for the Langley MC2 flow condition. These charts depict heat transfer at multiple locations for the convenience of comparison. The individual heat transfer plots can be found in Appendix C.

For both flow conditions the first 20 flow lengths can be considered to be consumed in the start up processes behind the aeroshell, as the wake flow structure takes a more steady form. Following this period of unsteadiness the heat transfer

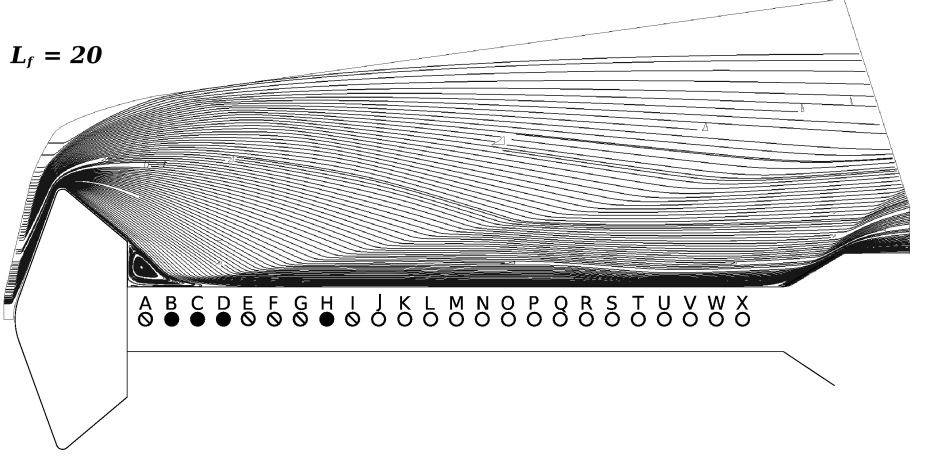
rates approach a more stable level. After 50 flow lengths the wake flow field in both flow conditions could be described as stable. Arguably the heat transfer at some locations reaches a stable level before others. However, in the same way that Hollis evaluated wake flow establishment by combining heat transfer rates at all gauge positions into a single averaged metric, the wake flow field produced in both flow conditions can be classified as established after 50 flow lengths. Despite this, the flow field in the near-wake region is not in steady-state at this point. That is, the heat transfer rate at most gauge locations has reached a steady level and only those closest to the still moving flow attachment point are in a state of relatively slow change.

The flow attachment location can be observed from the heat transfer time history plots. As evident in Figures 3.16 and 3.17 after a period of approximately 23 flow lengths the flow structure is fairly established. That is, the heat transfer at each gauge location relative to each other is established. However, the flow attachment point is still in a state of change. At approximately 23 flow lengths the heat transfer is greatest near gauge location E. The heating level at location E drops off as the flow attachment point moves closer to gauge location F at which point it becomes the point with the highest heat transfer. This pattern can also be seen to occur for gauge locations G and H.

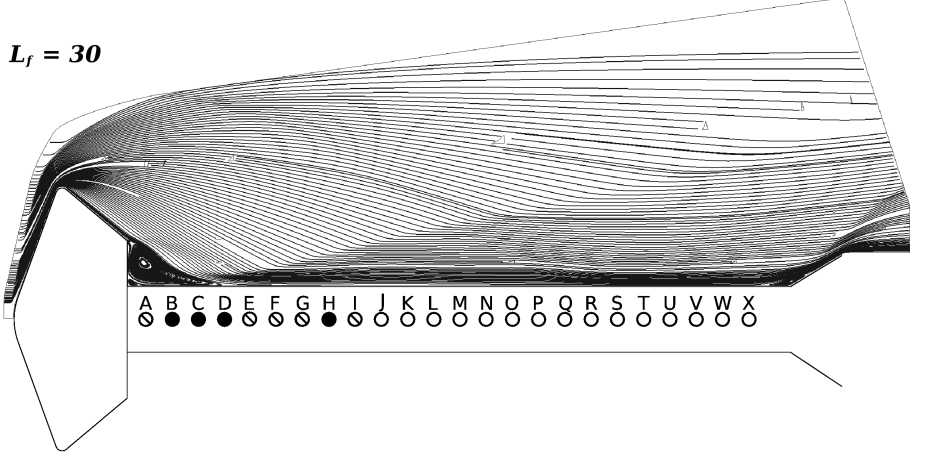
$L_f = 10$



$L_f = 20$



$L_f = 30$



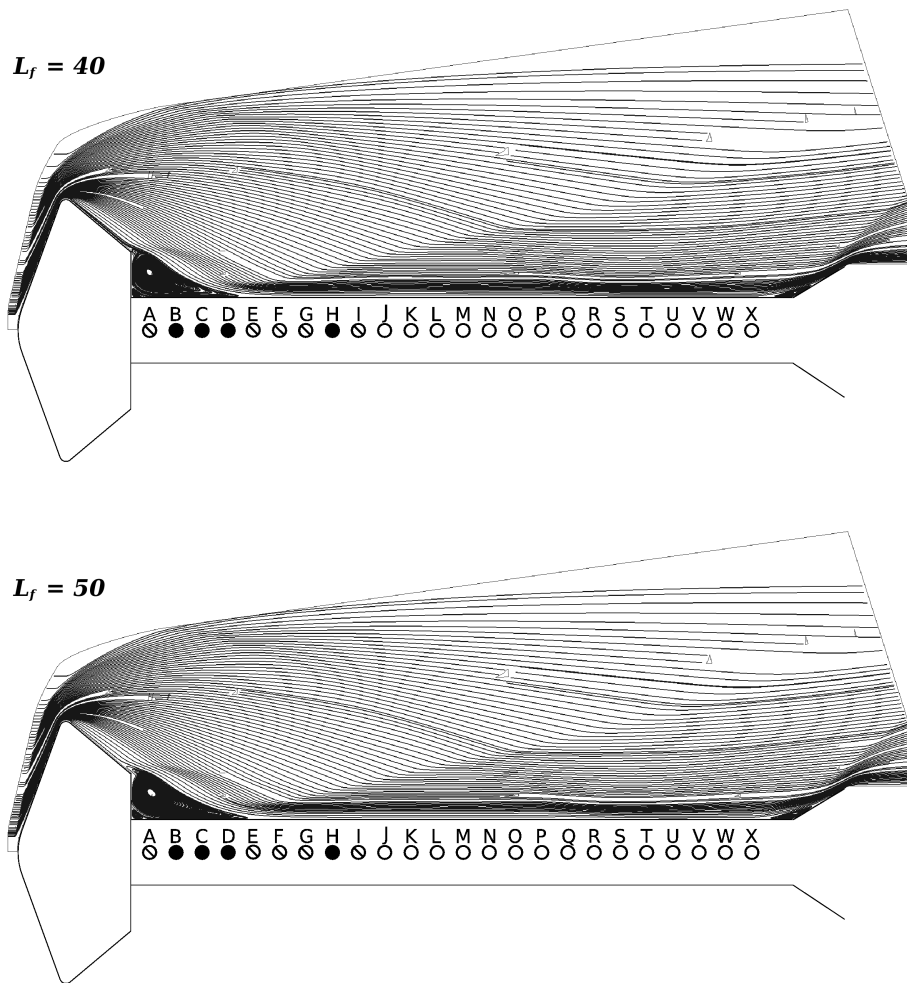
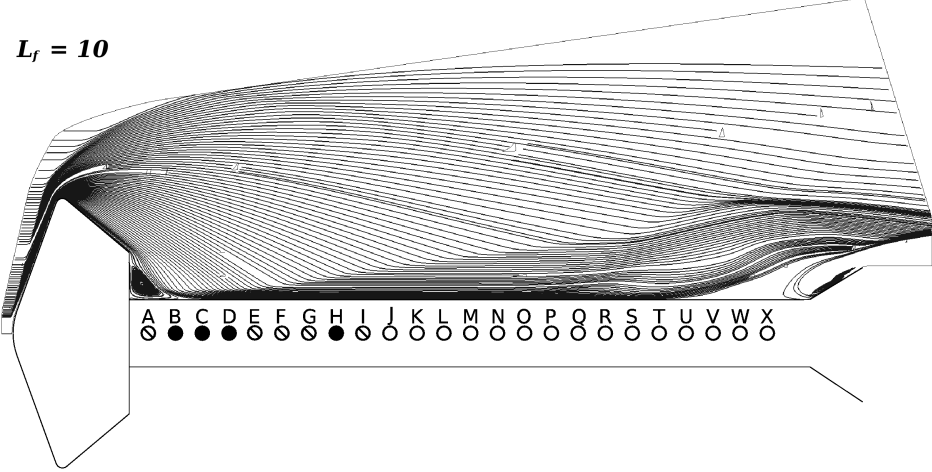
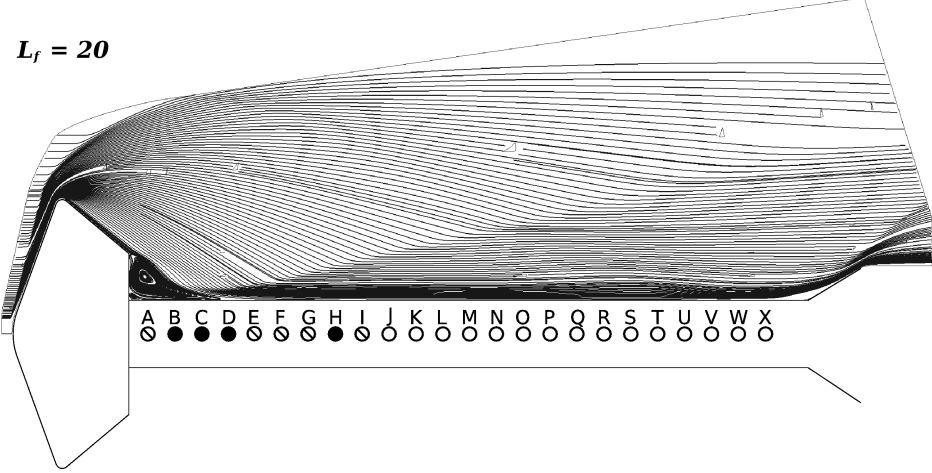


Figure 3.14: Flow streamlines at regular flow length intervals for the low-speed aerocapture condition (free stream velocity $U_\infty = 6,500$ m/s). Thin-film heat gauges are labelled alphabetically and marked based on working status. Solid circles indicate operational gauges. Struck-out circles indicate failed gauges. Open circles indicated blank positions. Refer to Section 4.5.2.

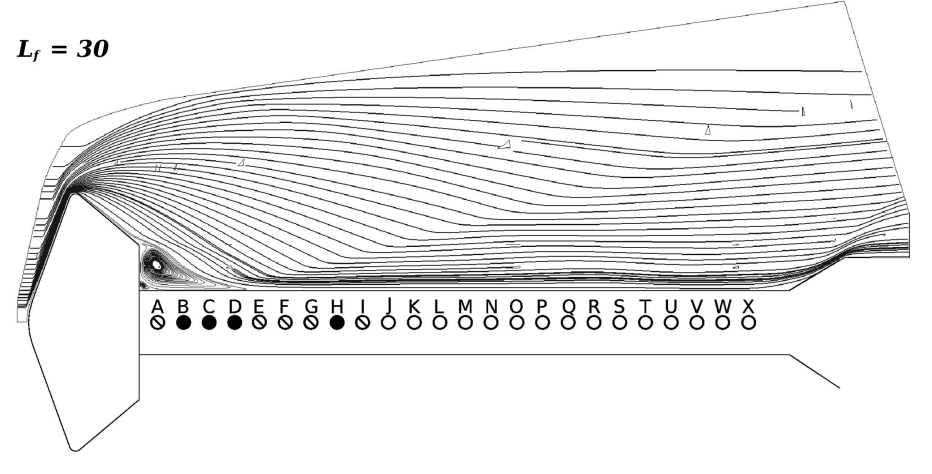
$L_f = 10$



$L_f = 20$



$L_f = 30$



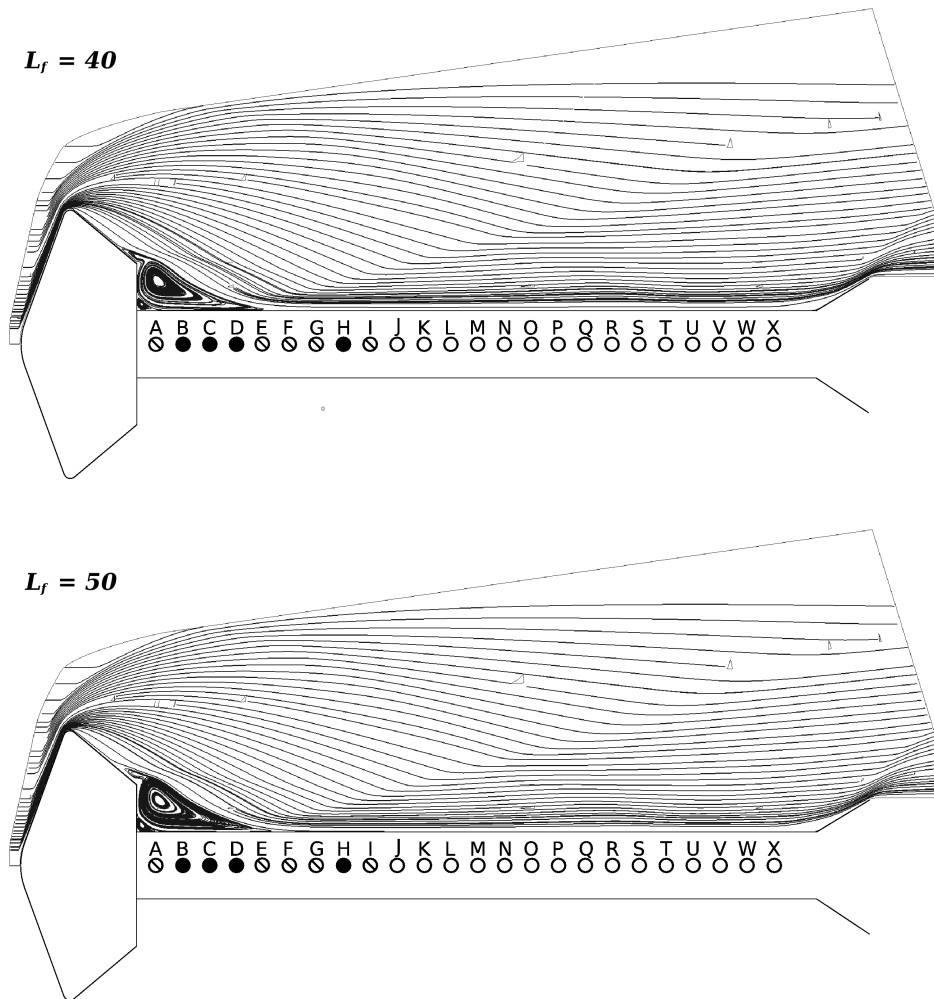


Figure 3.15: Flow streamlines at regular flow length intervals for the direct entry condition (free stream velocity $U_\infty = 4,700$ m/s). Thin-film heat gauges are labelled alphabetically and marked based on working status. Solid circles indicate operational gauges. Struck-out circles indicate failed gauges. Open circles indicated blank positions. Refer to Section 4.5.2.

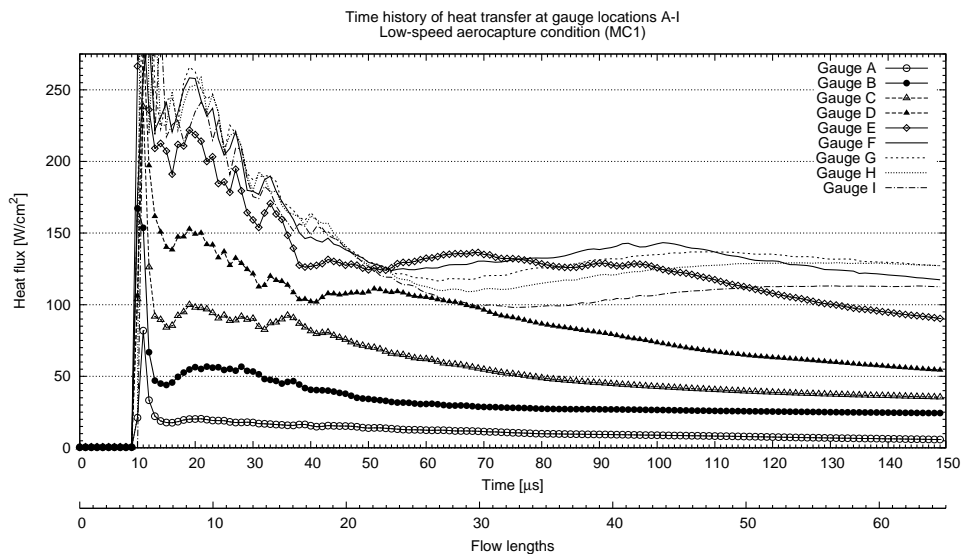


Figure 3.16: Heat transfer time history for the low-speed aerocapture condition (MC1, free stream velocity $U_\infty = 6,500$ m/s). Data sampled at heat gauge locations A through I.

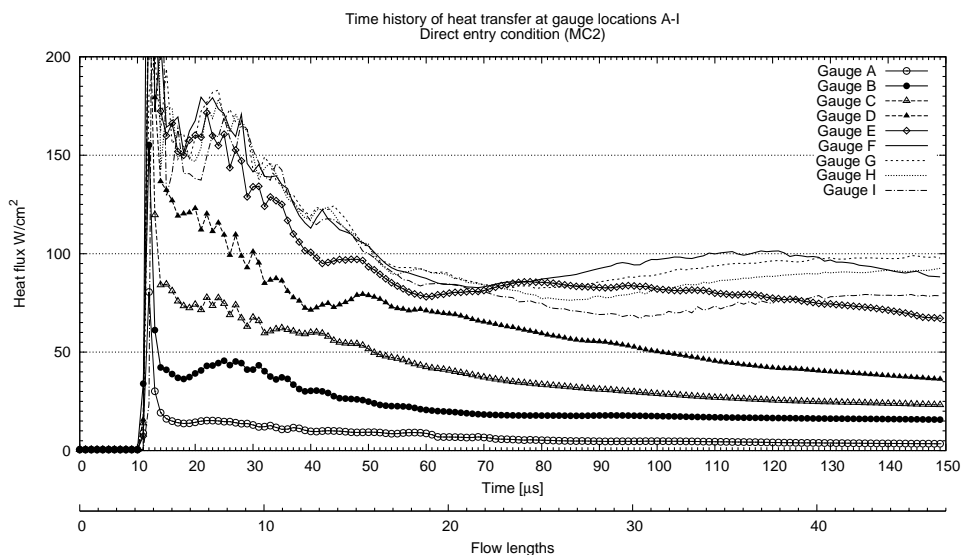


Figure 3.17: Heat transfer time history for the direct entry condition (MC2, free stream velocity $U_\infty = 4,700$ m/s). Data sampled at heat gauge locations A through I.

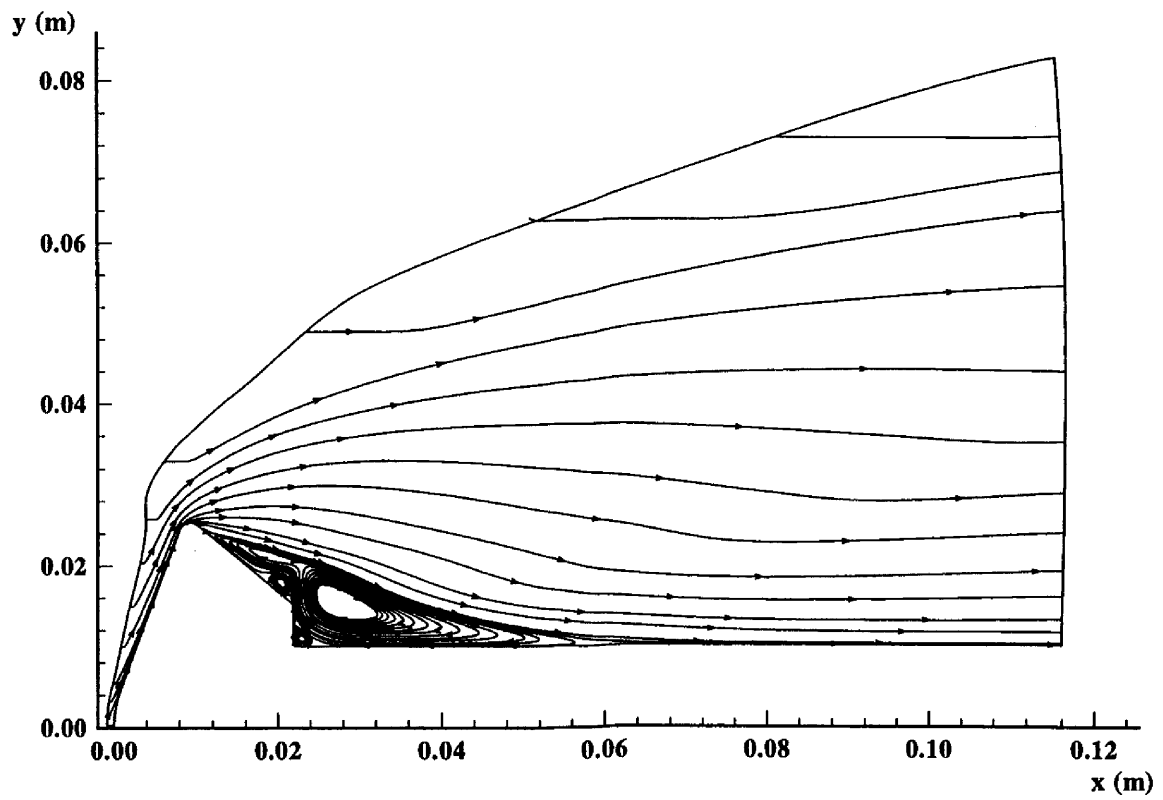


Figure 3.18: Plot of streamlines for a Mars Pathfinder geometry with sting ($R_b = 25$ mm) in CO_2 gas with a free stream velocity of $U_\infty = 4,700$ m/s [8].

Experimental Study

4.1 Overview

Ground-based experimentation is the only cost effective means of physically testing materials and collecting data concerning aerothermodynamic phenomenon in the current political and economic climate. In a world where aerospace missions and research programs are driven by cost rather than goals, on-board instrumentation not related to payload performance is often the first item to get scratched due to budget and mass constraints.

As a result of the immense quantities of energy associated with hypersonic flows, ground based experimental facilities are generally only able to generate test flows matching some of the properties of real flight-based flow conditions. For the testing of materials in arc-jet facilities, the enthalpy of the flow is matched at a reduced supersonic flow speed in a continuous, long duration gas stream. Expansion tube facilities generate flows that match flight-based speeds and thus total temperatures, though only for short durations. As such, expansion tubes are part of the family of impulse facilities. At the University of Queensland four such impulse facilities exist ranging in size and operating profiles. The X2 and X3 expansion tubes are able to generate superorbital flow speeds and are ideal for producing the flow field conditions equivalent to a Martian atmospheric entry and aerocapture flights.

The purpose of the experimental portion of this study is to provide data for future work involving heat measurement in hypersonic flows around aeroshell geometries. Heat-transfer measurements in the near-wake flow region will provide details regarding the time required for wake flow establishment. This information can then be used in the design of future hypersonic ground based experiments.

The X2 superorbital expansion tube has been employed to complete the experimental portion of this investigation.

4.2 Experimental Objectives

The aim of this experimental investigation was to determine the capability of the X2 expansion tube to facilitate the study of aerothermodynamics in near-wake flow fields behind bluff body aeroshell geometries. In order to obtain useful heat transfer data from a ground-based impulse facility it must first be determined if the machine is capable of generating a stable flow field at the rear of the aeroshell at a given nominal flow condition. Impulse facilities are known to be able to generate steady forebody flowfields well within the typical steady flow test times, providing sufficient time to gather data. However, as shown in the computational part of this study, the flow field behind an aeroshell geometry takes significantly longer to stabilise which therefore limits the potential of impulse facilities for these types of studies.

Whilst flow fields in real flight conditions are transient, ground-based facilities are limited to simulating a single, nominated condition in any given experiment. The steady-state flow structure is illustrated in Figure 4.1. After passing through the bow shock, the flow along the face of the forebody expands as it moves around the shoulder of the aeroshell geometry and separates from the body. As a result, a shear layer is formed and the flow reattaches to the wall along the aeroshell model sting mount downstream of the aeroshell base. As time progresses, the attachment point moves downstream along the sting causing the recirculation zone to expand until it reaches a steady-state form.

The steady-state flow structure is indicative of a flow field that is much more advanced in time than that typically achievable in impulse facility experiments. Forebody flow fields establish very quickly due to the length scales involved. The shock standoff distance and forebody boundary layer thickness are much smaller than length scales associated with near-wake flow structures such as the aeroshell shoulder radius. Furthermore, near-wake flows over bluff bodies exhibit recirculation at much lower speeds, increasing the residence time of any given flow particle. Thus, near-wake flows have a much longer starting process. Given sufficient time the

simulated flow around the entire vehicle will reach steady-state.

To achieve the objectives of this study, data was collected for static flow pressure in the experimental flow and the heat transfer rate behind the aeroshell geometry. This data was used to determine how much time is required for the establishment of the near-wake flow field. In this work, this metric is referred to as the *wake flow establishment* time. As discussed in the following section, the gas that flows over the model in the X2 expansion tube during a single shot is not all at the desired test conditions. A normal shock precedes the test gas over the model and unsteady expansion waves follow the test gas. However, the initial flow prior to the test gas begins the startup processes of wake flow establishment. Therefore, the wake establishment time includes all gas and flow conditions preceding the desired test conditions.

With the determination of the wake establishment time and the amount of steady test time at a given flow condition, observations regarding the quality and quantity of suitable heat-transfer observation time can be made. Information of this nature is useful to experimenters wishing to explore phenomenon in the near-wake region with regards to sizing of models, selection of facilities and flow conditions to simulate.

4.3 Description and Operation of the X2 Expansion Tube

Figure 4.2 illustrates the X2 tube and an ideal $x - t$ diagram for operation in expansion mode. This diagram describes the state of gas as it travels down the tube in both time and spatial dimensions. When configured for expansion mode, the X2 expansion tube comprises a driver gas reservoir, a single piston inside the compression tube, a shock tube, an acceleration tube with an expansion nozzle and a test chamber and dump tank. The alternative mode of operation is the non-reflecting shock tube mode. For use in this study however, the X2 machine was configured in expansion mode.

The process of executing a single shot starts with the installation of a primary diaphragm at the capstan nut, securing the shock tube to the the compression tube, and a secondary diaphragm at the capstan nut between the shock tube and

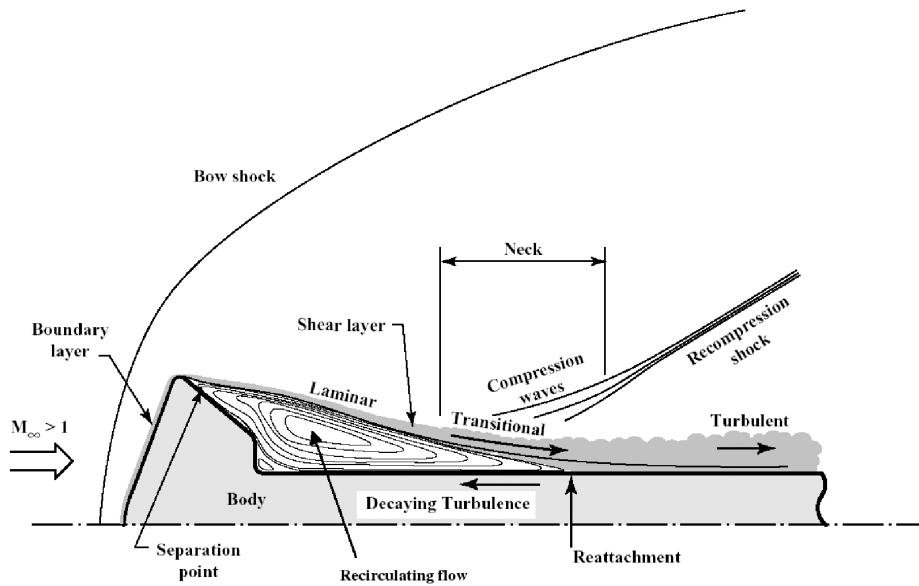


Figure 4.1: Diagram of the flow structure in the wake of the Pathfinder aeroshell on a sting mount [8].

acceleration tube. The dump tank, expansion nozzle and acceleration tube are then evacuated to as close to vacuum as possible. When a good vacuum is attained the shock tube is filled with the desired test gas - carbon dioxide in this instance will simulate the Martian atmosphere. The final preparatory step is filling the main reservoir (upstream of the piston) with air to a high pressure. The reservoir fill pressure and shock tube test gas pressure are determined prior to experimentation through computational techniques and tweaked over a series of flow condition survey experiments.

With the shock tube and driver section filled and ready to fire, a valve is opened allowing the high pressure air in the reservoir to fill behind the piston thereby “firing” the piston and executing the shot. Upon firing of the piston the gas in the driver section is compressed until the point at which the primary diaphragm bursts. At this point ($t = 0$ in Figure 4.2) the driver gas accelerates down the shock tube section compressing and accelerating the test gas. The shock tube is separated from the acceleration tube with only a very thin Mylar diaphragm and upon rupturing of this membrane the test gas expands into the acceleration tube. The acceleration tube allows the shock compressed test gas to expand to the correct flow conditions prior to its contact with the model ensuring the longest test times possible. The

addition of an expansion nozzle to the acceleration tube serves to increase the test time and core flow diameter as verified in the nozzle design and optimisation study by Scott [23].

4.4 Measurement Techniques in High Speed Flows

Due to the high speed and high enthalpy of gas flows in expansion tubes, special techniques are needed to measure properties of the simulated flows. For this particular study two flow parameters were recorded and used to estimate the functional range of the X2 for studying heat transfer rates in near-wake flow fields. These parameters are static pressure and heat transfer.

4.4.1 Pressure Measurement

The X2 expansion tube was fitted with a number of static pressure transducers mounted into the tube wall which determine the static pressure in the flow as it travels down the tunnel towards the test chamber. Following the rupture of the primary diaphragm the arrival of the shock at each static pressure transducer creates a spike in the local static pressure which can be seen in the recorded data. Based on the shock arrival time at each transducer and the known location of each transducer relative to the primary diaphragm and each other, the speed of the shock can be estimated within $\pm 2.5\%$ as determined by Hayne [6].

At the end of the nozzle two static pressure transducers have been mounted which also measure static pressure of the flow at the nozzle exit. These transducers provide the best characterisation of the flow and duration of steady test gas flow over the model. Figure 4.3 illustrates a typical pressure data trace from an X2 shot in the expansion mode of operation. The arrival of the secondary shock is marked by a sharp increase in pressure gradient. The signal drops off following the interface gas between the test and acceleration gas slugs. Pressure measurements stabilise relatively fast as the test gas flows past the transducers. The test time ends on the arrival of the unsteady expansion gas whereupon the pressure begins to rise and fluctuate in magnitude. Determination of test time from pressure data traces is rather subjective and, as such, error bands are difficult to quantify.

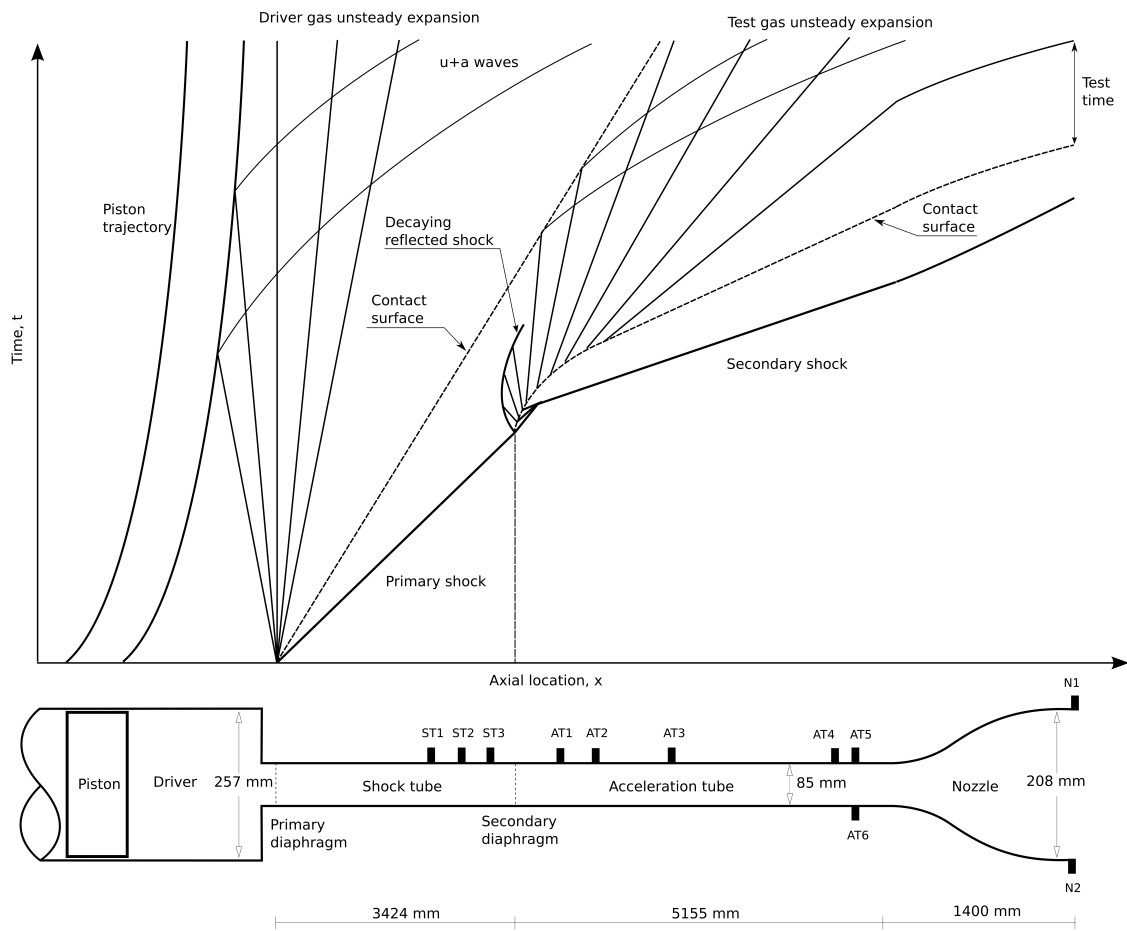


Figure 4.2: An $x-t$ diagram of the X2 expansion tube operation (*top*), and a schematic of the X2 expansion tube [20].

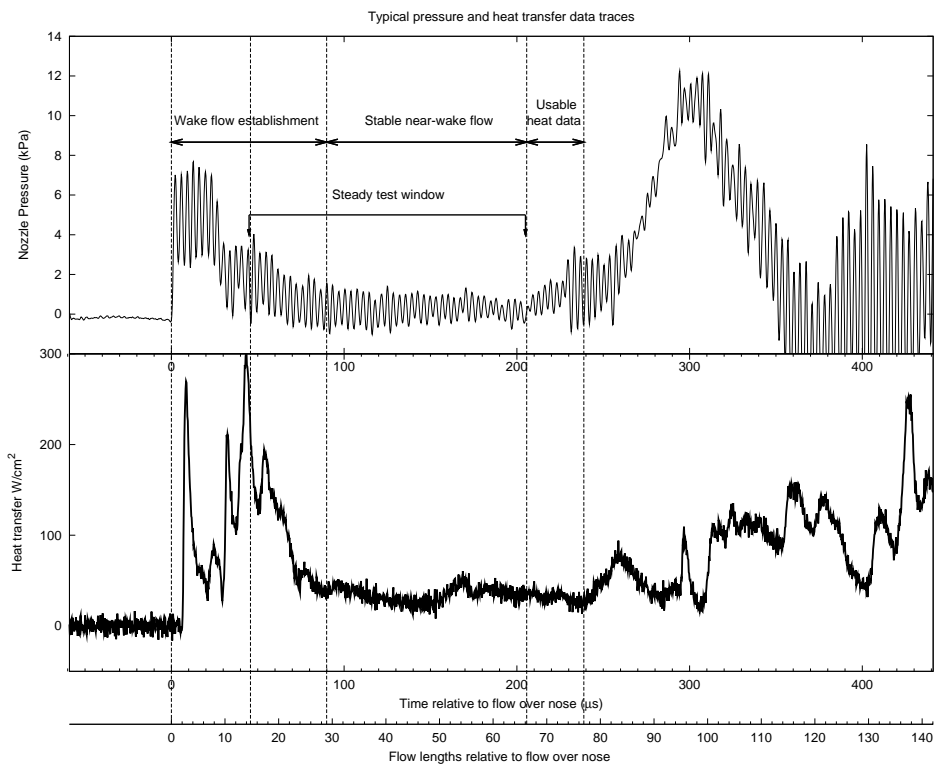


Figure 4.3: Typical pressure and heat transfer data for an X2 shot. The steady test window is observed when flow pressure is relatively stable. Heat transfer measurements were taken in a rear-ward facing flow behind a blunt body aeroshell in this example.

4.4.2 Heat Transfer Measurement

Ground-based hypersonic test facilities originated from the need to characterise the flow field around high-speed planetary entry vehicles. In particular the temperature and heat transfer to the forebody of the vehicles are of interest regarding the design and manufacture of thermal protection systems (TPS). Measurement of heat transfer in high speed impulse facilities requires devices with very fast response times and to this end thin-film heat gauges have been employed for this purpose. Thin-film gauges have an extensive history of use in impulse facilities [22].

Thin-film heat gauges make use of the semi-infinite heat transfer theorem which assumes that the support slab to which the sensing strip is mounted is in effect infinitely thick compared with the sensing strip. Given that high-speed impulse facilities generally run for periods in the order of 0.5 ms the semi-infinite theory allows the assumption that this support slab is isothermal. As a result, thin-film heat gauges permit the experimenter to fabricate test models from common and durable materials such as steel and brass.

The gauges used in this study were fabricated using the process developed by Schultz and Jones [22] and adapted by Hayne [6]. The gauges consist of a nickel strip that is vacuum deposited on the polished surface of a cylindrical quartz substrate. The metallic strip was coated with a thin layer of silicone dioxide for protection from erosion and the effects of ionisation. Electrical connection to the metallic strip is facilitated by contacts made by gold paint to which enamelled output wires are soldered. The gauges were then baked at high temperature to age them and reduce hysteresis.

4.5 Model Construction and Instrumentation

The model used in this investigation was initially constructed by Richard Poole for similar experiments that were never completed. There are two main parts to the models: the aeroshell capsule geometry and the mounting sting. Figure 4.4 illustrates the models with the mounting stings attached.

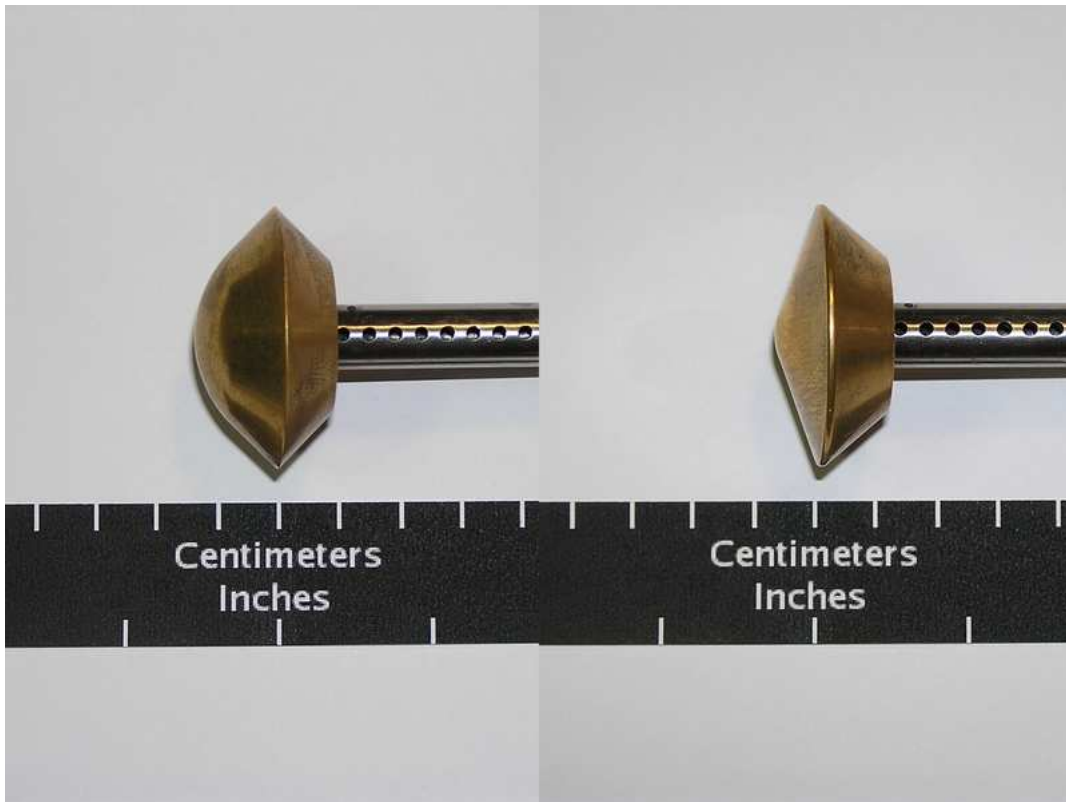


Figure 4.4: Test models based on US Mars Pathfinder and Japanese MUSES-C aeroshell geometries. Images show only part of the support sting.

4.5.1 Aeroshell Models

The model design is based on NASA's Mars Pathfinder. This geometry was selected for use in this investigation given its prolific usage in the current robotic exploration programs and with its usage slated to continue into the future. The model was fabricated from brass for ease of machining, avoidance of rust, and low cost. The schematics for the aeroshell model can be found in Appendix D. The model includes an M10 threaded hole for attachment to a mounting sting for installation into the test chamber of the X2 expansion tube.

4.5.2 Measurement and Instrumentation

To meet the objectives of this study heat flux measurements from the gas in the near-wake region were acquired. This was achieved by mounting thin-film heat transfer gauges in a purpose built sting mount. Given that the sting is located in the wake of the bluff forebody geometry it is the most suitable position for gauges to be located, removing the need for additional infrastructure.

The sting was constructed from stainless steel and was fashioned as a cylindrical tube comprised of two halves split longitudinally. The cylinder has an outer diameter of 12 mm and inner bore diameter of 6 mm. The top half of the sting was modified to allow the thin-film heat gauges to be mounted flush with the exterior surface. A total of 25 holes with diameter 2 mm were made along the main axis of the tube with a centre-to-centre spacing of 4 mm. The first hole closest to the aeroshell model is 2 mm from the base of the model when the sting is installed into the aeroshell model. The sting is threaded with M10 threads at both ends to enable attachment to the aeroshell model and to the X2 mounting adaptor piece. The X2 mounting adaptor piece was designed to fit with pre-existing X2 test chamber mounting brackets and to allow for housing of internal cabling from the heat gauges.

A total of ten gauges were installed into the model. The positioning of these sensors was determined based on the results of the CFD study. CFD results showed that the recirculation region would be best characterised by locating gauges in positions A through to I. The remaining 15 of the total 25 locations were filled with elastomeric silicone gel. This served to block the unused holes and protect internal cabling. The thin-film heat gauges were secured in place with cyanoacrylate adhesive. The adhesive also ensured electric isolation from the sting itself.

Due to unknown reasons, six of the gauges failed during either the gauge installation process, the calibration of the gauges post-installation or during the pre-experimental installation of the model into the expansion tube. Unfortunately, due to the high relative cost of the gauges and their fabrication and short supply, the faulty gauges were not replaced. The distribution of functioning gauges in the sting is illustrated in Figure 4.5.

In hindsight, the design was flawed from an instrumentation point of view, but served its purpose. Improvements in the design could have included an electrical transfer point. This point would be fixed relative to the mounting sting and act as an anchor for the thin, delicate output wires from the thin-film gauges. A transfer point would eliminate damage due to handling and assembly of the instrumentation and could have possibly prevented the loss of some of the gauges in this experiment. Heavy duty wires would conduct the data signals from the transfer point through to the facility's data acquisition system. If these connections became severed the repair

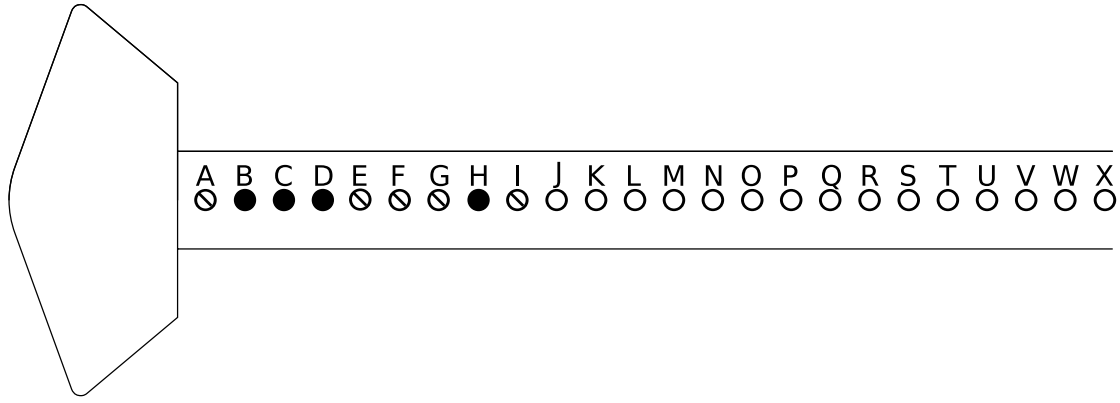


Figure 4.5: Heat gauge instrumentation positions along the aeroshell model mounting sting. Solid circles indicate operational gauges. Struck-out circles indicate failed gauges. Open circles indicated blank positions.

would be less time consuming and minimise the chance of putting other gauges at risk of failure.

4.6 Calibration of thin-film heat gauges

Calibration of the sensor suite was performed on the thin-film heat gauges at several stages during the apparatus setup. The first stage of the calibration was conducted with only the gauges themselves. This was as much a calibration of the sensors as it was a test of their performance and suitability for the experiment. The gauges were connected to the calibration board via the output wires and placed in a purpose built calibration oven. Appendix E details the settings used for the calibration oven.

For each gauge, the variation of resistance with the change in temperature ($\frac{\delta\Omega}{\delta T}$) was recorded. This value is the calibration constant for each thin-film heat gauge. The gauge sensitivity (α_R) was then found by dividing the calibration constant by the gauge resistance. Table 4.1 details these values for the first stage of calibration. Calibration plots are presented in Appendix E.

Another series of calibrations was conducted after the sensors were installed into the model itself. The same calibration settings were used and the results of these tests are shown in Table 4.2. At this stage it should be noted that gauges denoted E, F and I were defunct. Following the installation of the model into the expansion tube, gauges A and G were also found to have failed. For the gauges still functional

Table 4.1: Thin-film gauge calibration results prior to installation into the mounting sting.

Gauge Number	Gradient (Ω/K)	Resistance (Ω)	α_{R} (K^{-1})
A	0.1468	41.6	3.52×10^{-3}
B	0.0386	25.0	1.54×10^{-3}
C	0.1965	83.8	2.45×10^{-3}
D	0.0877	40.8	2.15×10^{-3}
E	0.1489	118.6	1.26×10^{-3}
F	0.3540	107.6	3.29×10^{-3}
G	0.1200	33.6	3.57×10^{-3}
H	0.0573	32.5	1.76×10^{-3}
I	0.1839	136.4	1.35×10^{-3}

Table 4.2: Thin-film gauge calibration results after installation into the mounting sting.

Gauge Number	Gradient (Ω/K)	Resistance (Ω)	α_{R} (K^{-1})
A	-	-	-
B	0.0444	22.8	1.95×10^{-3}
C	0.1934	83.0	2.33×10^{-3}
D	0.0896	42.1	2.13×10^{-3}
E	-	-	-
F	-	-	-
G	-	-	-
H	0.0766	43.5	1.76×10^{-3}
I	-	-	-

at this stage in positions B, C, D and H the results showed little variance between the calibrations. This indicates that the installation of these gauges was a success and that they were properly isolated from the model both thermally and electrically.

4.7 Experimental Flow Conditions

Given the current and ongoing interest in Mars exploration, flow conditions have been chosen to reflect those experienced in past, current and potential future missions. Two conditions that represented two very different types of atmospheric flight were selected. The first of these is a low-speed aerocapture flow condition, relevant to future robotic and potentially human exploration missions to Mars. This condition is labeled as Mars Condition 1 (MC1) in this study. The second condition is commonly known in the aerothermodynamic scientific community as the *Langley* condition which is labeled in this study as Mars condition 2 (MC-2).

The flow properties of these test conditions are presented in Table 4.3. A total of five experiments at each condition were performed to account for random variation between shots. These conditions were simulated in the X2 expansion tube using the setup parameters outlined in Table 4.4.

4.8 Experimental Results

A total of ten experiments were performed over two flow conditions. The results and a discussion of those shots are presented in this section.

These results are presented in the form of pressure and heat flux traces as illustrated in Figure 4.6. Individual sensor data plots are presented in Appendix F for

Table 4.3: Flow conditions simulated in the X2 expansion tube.

	Direct Entry	Low speed Aerocapture
Relative velocity, U_∞ (m/s)	4,700	6,500
Altitude (km)	NA	50
Freestream density, ρ_∞ (kg/m ³)	NA	1.3×10^{-4}
Scaling parameter, ρL (kg/m ²)	2.3×10^{-4}	3.5×10^{-4}

Table 4.4: Setup parameters for the X2 expansion tube facility used in this study (provided by Potter [19]).

	Direct Entry	Low speed Aerocapture
Reservoir air pressure (MPa)	1.25	1.25
Compression tube pressure (kPa)	30.0	30.0
Driver gas composition	83% Ar, 17%He	40%Ar, 60%He
Primary diaphragm	1.2 mm steel pre-scored	1.2 mm steel pre-scored
Secondary diaphragm	Mylar	Mylar
Shock tube CO ₂ pressure (Pa)	14,000	8,000
Acceleration tube air pressure (Pa)	27	27

each shot. The key factors to be taken from this chart are the times associated with flow structure formation. As previously discussed in Section 4.1, the stability of the wake flow region is determined experimentally through observation of the heat flux traces from the thin-film gauges positioned along the sting mount.

In order to observe flow stability in any region of the flow field, the test gas must exhibit properties with very little instantaneous variance. Shown in Figure 4.3 is the time frame over which the test gas remains relatively steady. This period is determined through examination of the static pressure measurements. Given that the gas expands as it traverses the length of the nozzle, the portion of steady test gas also expands. Therefore pressure measurements taken at the end of the nozzle yield a more accurate representation of the test gas flow length and duration than those at the end of the acceleration tube. To this end, pressure transducers mounted at the end of the nozzle were used to determine the steady flow test window.

Based on these times, inferences can be made regarding the stability of the near-wake flow region and the capabilities of the X2 expansion tube for the study of near-wake flow fields and associated heat transfer.

A total of eleven shots were performed between the two flow conditions - five shots at each condition and one scratched shot. An overview of these shots is presented in Table 4.5. For convenience the MC2 shots were performed first, as the expansion tube data acquisition systems were already configured for this condition. All five MC2 shots - 271 through to 275 - were deemed successful.

The five shots taken at condition MC1 were not as successful however. Shot 276

Table 4.5: Summary of observations from X2 expansion tube experiments.

Shot Number sNNN	Shock Speed (m/s)	Error (m/s)	Shot Notes
268	6,777.0	221.0	Mars Condition #1 pitot survey
269	4,771.0	129.0	Mars Condition #2 pitot survey
270	6,296.8	223.0	Mars Condition #1 pitot survey at higher reservoir pressure
271	4,831.7	132.4	First shot - MC2 with Pathfinder model
272	4,794.2	130.4	
273	4,818.1	131.7	
274	4,873.7	134.7	
275	4,730.0	127.0	
276	–	–	First shot - MC1 / Anomaly in shot due to unknown reason - shot scratched
277	6,198.6	216.2	Sinusoidal noise superimposed over pressure traces - reason unknown
278	6,245.0	219.4	Pressure data not recorded on primary DAQ - backup also failed
279	6,260.1	220.5	As above - problem unresolved
280	6,395.5	230.0	Pressure data not recorded on primary DAQ - Backup data issue resolved
281	6,146.5	212.6	As above

was scratched due to an anomaly in the shot conditions. This anomaly was most likely induced through the rupturing of the primary diaphragm at a higher than expected pressure, resulting in a faster shock speed. Given that the data acquisition system was set to delay data capture for a specific time based on predicted shock speeds associated with the flow condition of interest, the recorded data is a snapshot of the flow after the time of interest. The remaining shots for condition MC1 were only partially successful. The pressure traces from the nozzle transducers were polluted with interference of a sinusoidal form. Also, pressure data from shots 278 and 279 failed to record for unknown reasons. Analysis of these shots was assisted with the inclusion of pressure data from the MC1 pitot rake survey shot 268. The steady flow windows for shots 278 and 279 have been adopted as the average steady test time of shots 277, 280 and 281.

It should be noted at this point that the data obtained from the experimental study forms a small sample set. For the purposes of discussion, averages have been adopted to characterise the results of each experiment but it is conceded that there is significant variation in the data that may invalidate inferences drawn using averaged values. The standard deviation for each value recorded has been calculated to assist the reader in assessing the quality of the data. However, a confidence interval cannot be determined because each data set is too small.

For the purposes of maintaining chronological structure, the results of MC2 will be discussed first.

4.8.1 Mars Condition 2 - Langley condition

A total of five shots were conducted with the test gas flow properties simulating the MC2 Langley condition. The results are shown in Figures 4.6 to 4.10. These charts depict the traces from the thin-film heat gauges denoted B, C, D and H (as illustrated in Figure 4.5). They have been positioned down the page to reflect their spatial position along the sting relative to one another. The data trace from the nozzle pressure transducer is also included positioned underneath for plotting convenience and does not reflect the spatial layout. The pressure trace plot includes data from a MC2 pitot survey shot 269 as a point of comparison.

Data from both sensor types has been translated along the time axis. The

zero time mark coincides with the arrival of the shock at the nose of the forebody aeroshell model. In this way, the steady flow characteristics illustrated through the heat transfer traces in the near-wake region can be compared in time relative to the arrival of the steady test gas around the aeroshell model. This provides an excellent point of reference not only for the work in this study but it allows inference to be drawn regarding previous forebody only studies at other flow conditions. For example, if data from a previous experiment regarding the length of the steady test window is known, along with the radius of the forebody model and sting, an inference can be made regarding the wake establishment time and the available time for the observation of stable heat transfer in the near-wake region for that flow condition and that model apparatus.

In each shot three time values have been determined. The values represent the duration of the steady test gas flow, the establishment time for steady wake flowfield formation from the time of arrival of the shock at the aeroshell nose and the duration of steady test flow in the near-wake region of the flow field. The period after the steady test window is also identified to highlight continued stability following the end of the steady test window. The results for the MC2 flow condition are summarised in Table 4.6.

The duration of steady near-wake flow is determined by two factors: the time taken to establish steady flow from the time of arrival of the shock and the length of the slug of steady test gas. The time required for the near-wake region to stabilise is a function of the arrival of the shock and interface gas which in itself is not stable. However, this slug of gas initiates flow around the aeroshell model and increases the pressure in this region from the near vacuum state at the commencement of the shot. Hence, only a small portion of the relatively stable test gas flow is required to complete the flow stabilisation in the near-wake region. The net effect of this is that a large proportion of the steady test window, in the case of the MC2 flow condition, can be used for observation of stable near-wake flow field heating.

The average duration of the steady test window was $148.4 \mu\text{s}$ and this occurred on average $43 \mu\text{s}$ after the arrival of the shock at the nose of the aeroshell. On average, the observation window for stable near-wake region heat transfer as determined from this investigation was $96 \mu\text{s}$ at the MC2 condition. This time equates to 30.9 flow

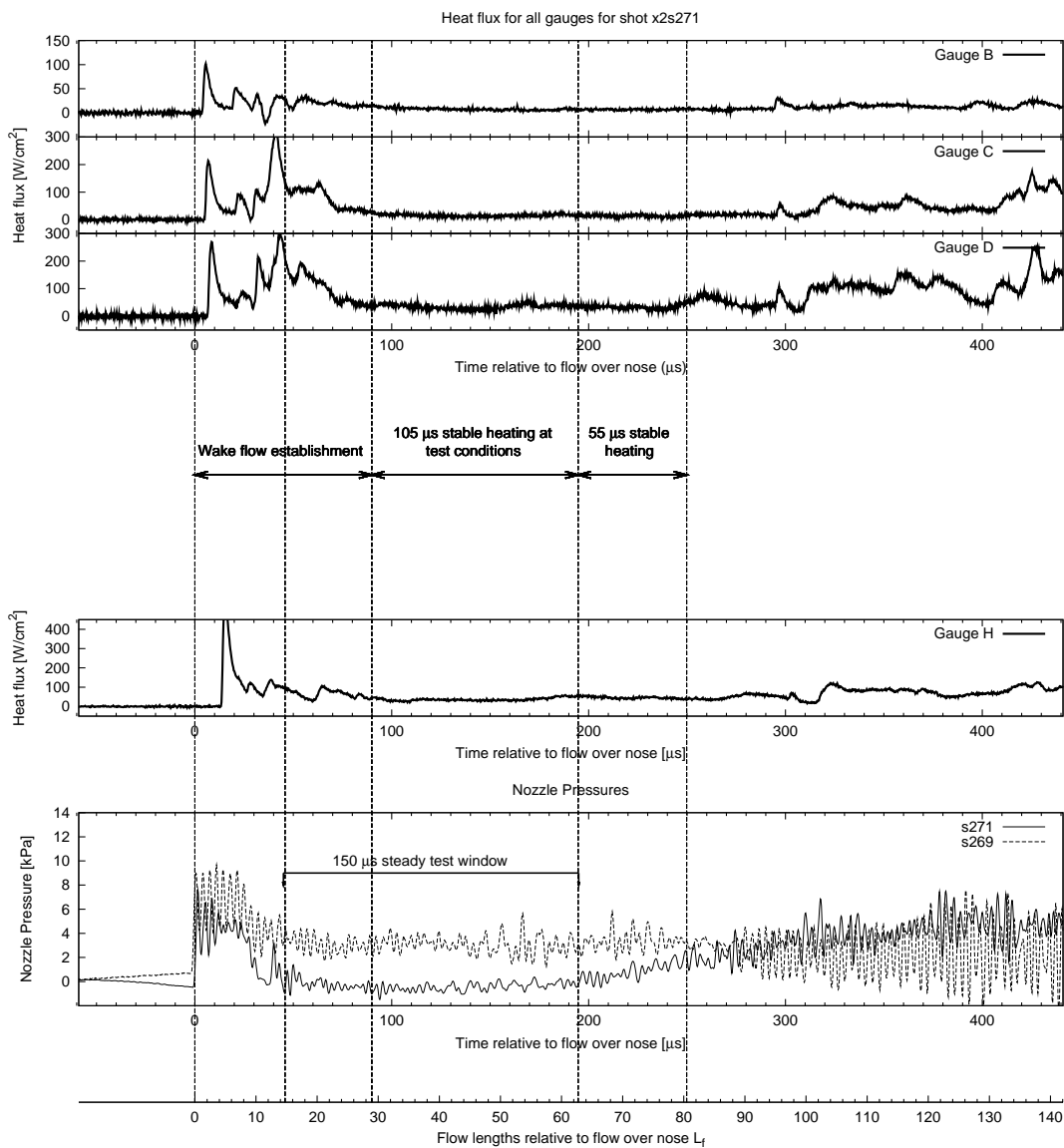


Figure 4.6: Heat and pressure data from X2 shot s271 (MC2).

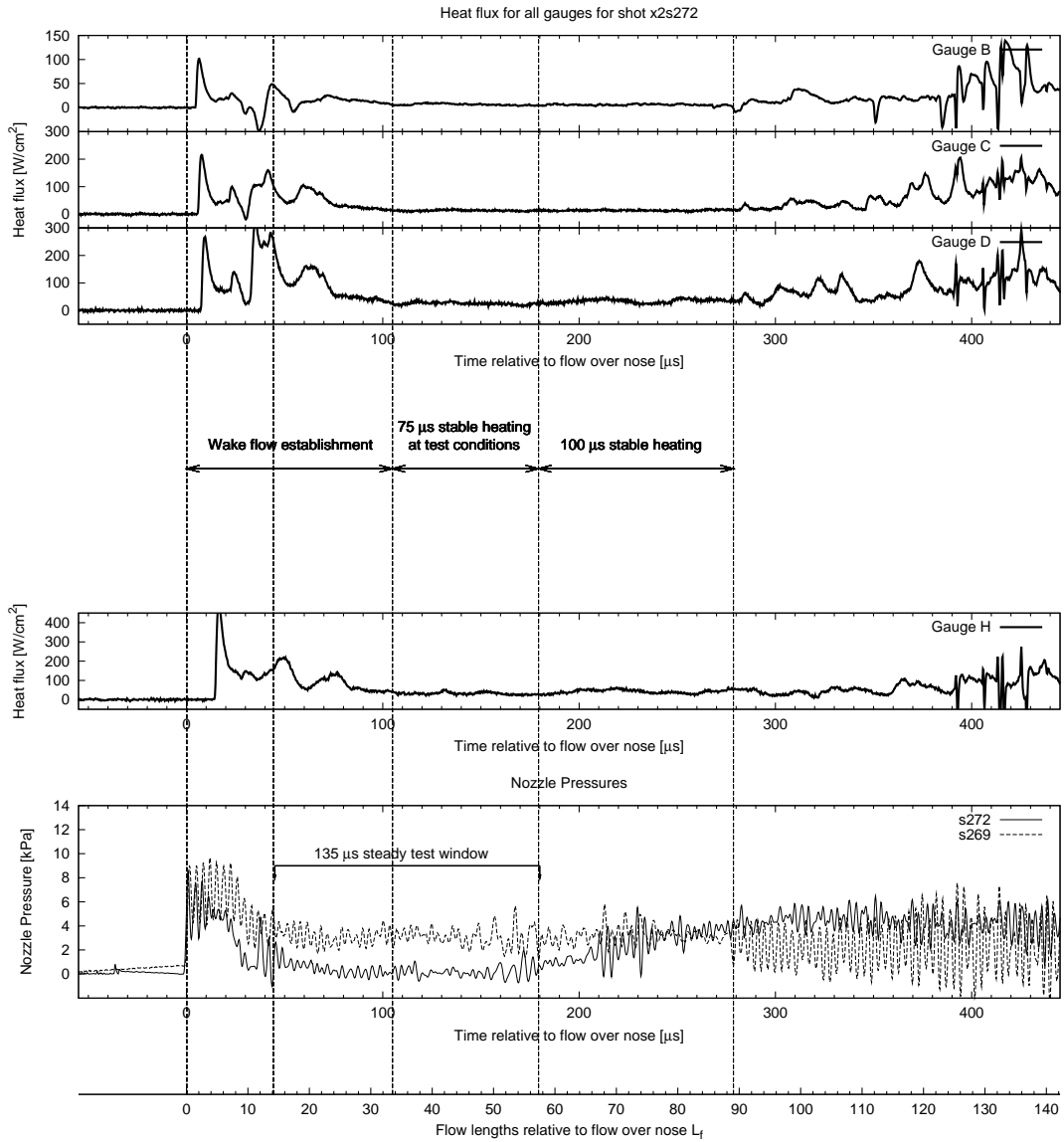


Figure 4.7: Heat and pressure data from X2 shot s272 (MC2).

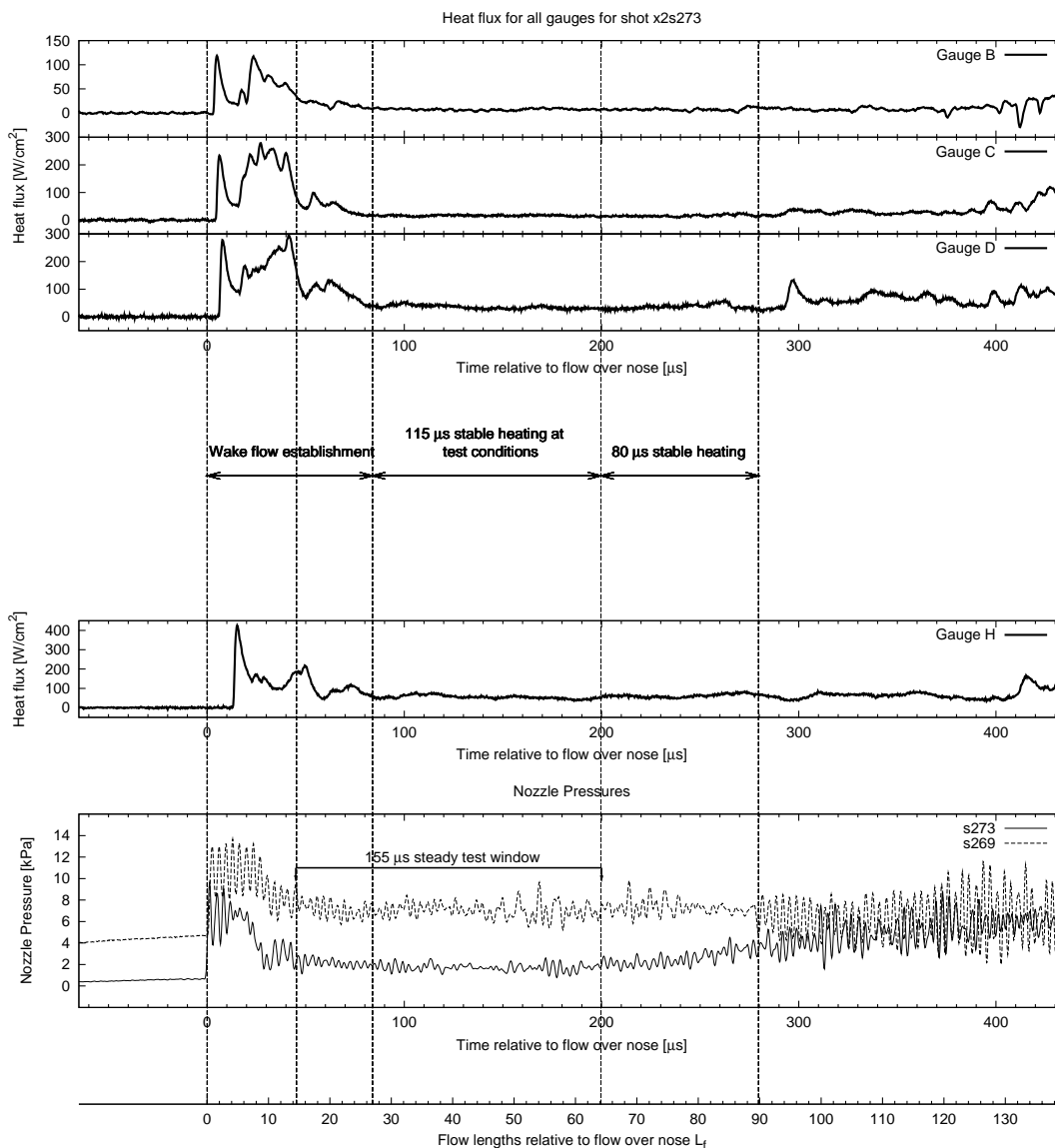


Figure 4.8: Heat and pressure data from X2 shot s273 (MC2).

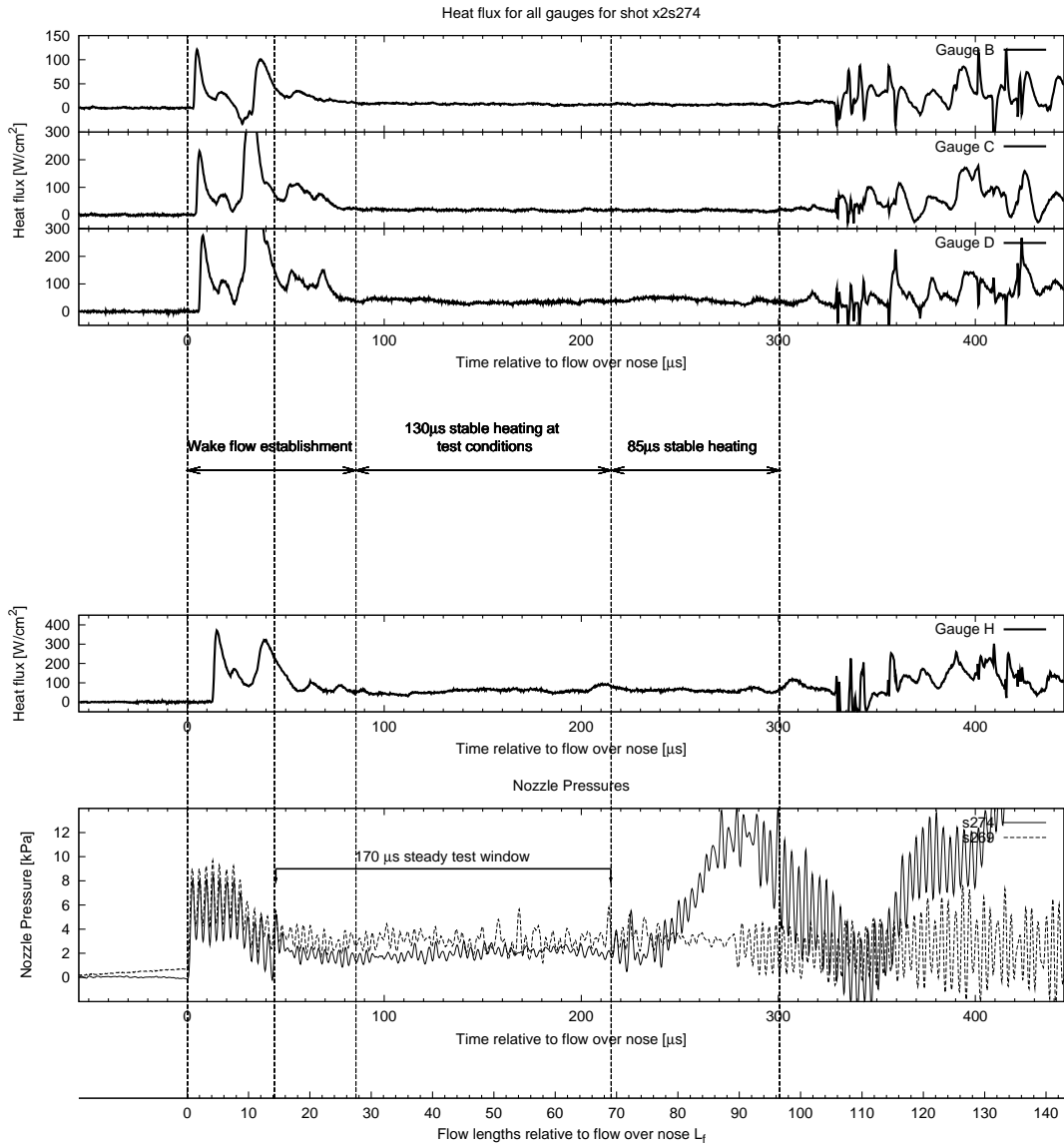


Figure 4.9: Heat and pressure data from X2 shot s274 (MC2).

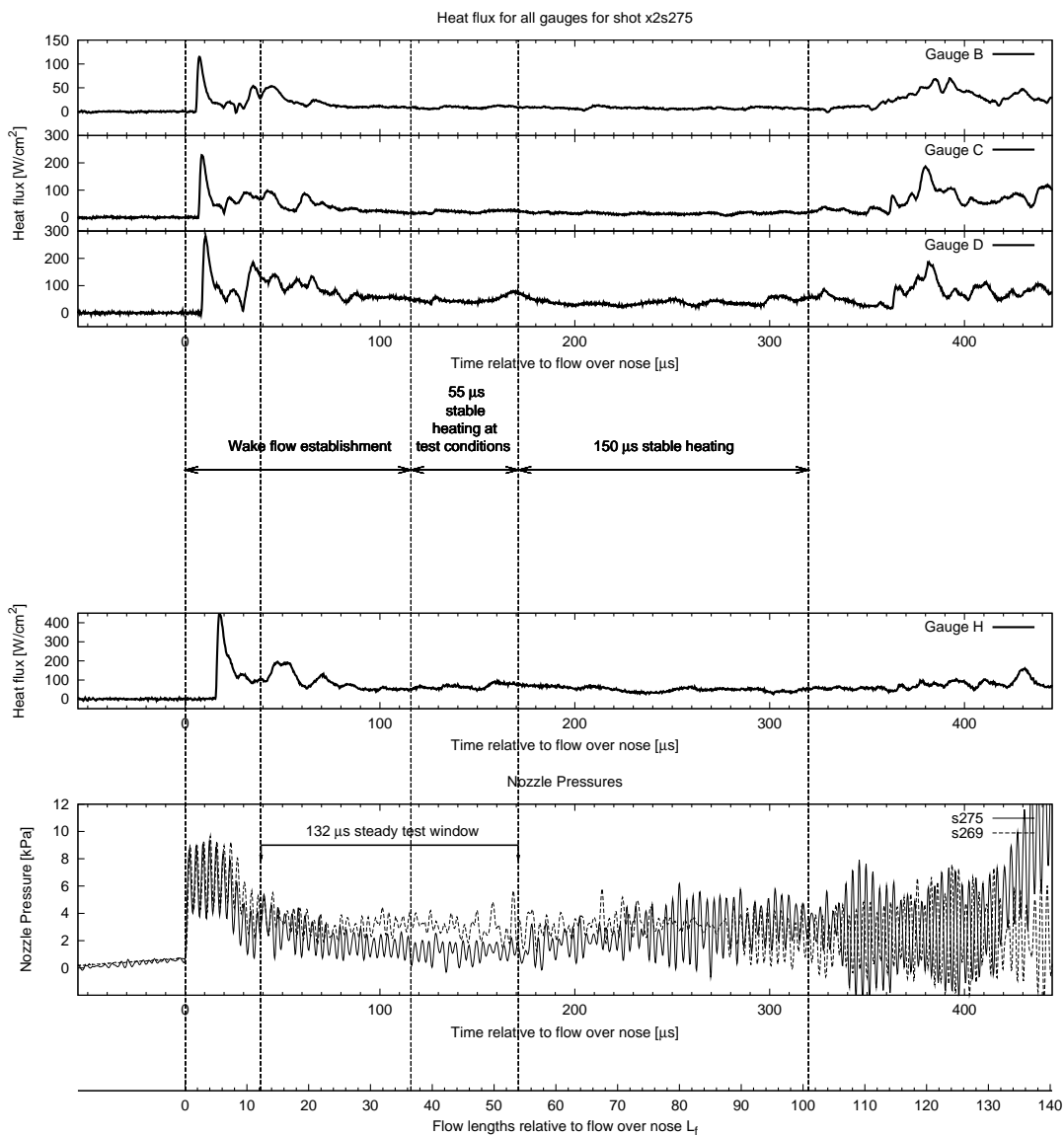


Figure 4.10: Heat and pressure data from X2 shot s275 (MC2).

Table 4.6: Summary of results for MC2 flow condition shots. Values in parentheses are times expressed as flow lengths of gas taken at the shock speed.

Shot No.	Shock Speed m.s ⁻¹	Wake Flow		Stable	
		Establishment μs (L_f)	Steady Test Time μs (L_f)	Near-wake Heating μs (L_f)	Usable heat data μs (L_f)
271	4831	90 (29.0)	150 (48.3)	105 (33.8)	55 (17.7)
272	4794	105 (33.6)	135 (43.2)	75 (24.0)	100 (32.0)
273	4818	85 (27.3)	155 (49.8)	115 (36.9)	80 (25.7)
274	4873	85 (27.6)	170 (55.2)	130 (42.2)	85 (27.6)
275	4730	115 (36.3)	132 (41.6)	55 (17.3)	150 (47.3)
Average	4809.2	96 (30.7)	148.4 (47.6)	96 (30.9)	94 (30.1)
Std Dev	52.7	96 (4.0)	15.5 (5.4)	30.5 (10.1)	35.3 (10.9)

lengths of test gas based on the nominal flow conditions as detailed in Table 4.3 and the model radius step height y_{ref} of 15 mm. For a period of 94 μs following the end of the steady test window, recorded data indicated heat transfer remained relatively stable in the near-wake region.

4.8.2 Mars Condition 1 - Low-speed aerocapture

As with the MC2 condition, five shots were performed to simulate the MC1 flow condition. This flow condition is considerably faster than MC2 and the results are depicted in Figures 4.11 to 4.15. In keeping with the MC2 charts, these figures depict the traces from the thin-film heat gauges positioned down the page to reflect their spatial position along the sting relative to one another. The nozzle pressure transducer data is included underneath for plotting convenience and does not reflect the spatial layout.

Table 4.7 summarises the shots performed using MC1 flow conditions. Pressure data for shots 278 and 279 was not recorded due to an error in the data acquisition setup. However, heat transfer data was recorded and the results for the stable heating window were still determined based on the wake flow establishment and steady test window times taken as the average from shots 277, 280 and 281. The pressure trace plot for shots 278 and 279 include data from a MC1 pitot survey shot 268 as a point of comparison in lieu of recorded data.

Overall, the results from the MC1 flow condition are as expected. The higher

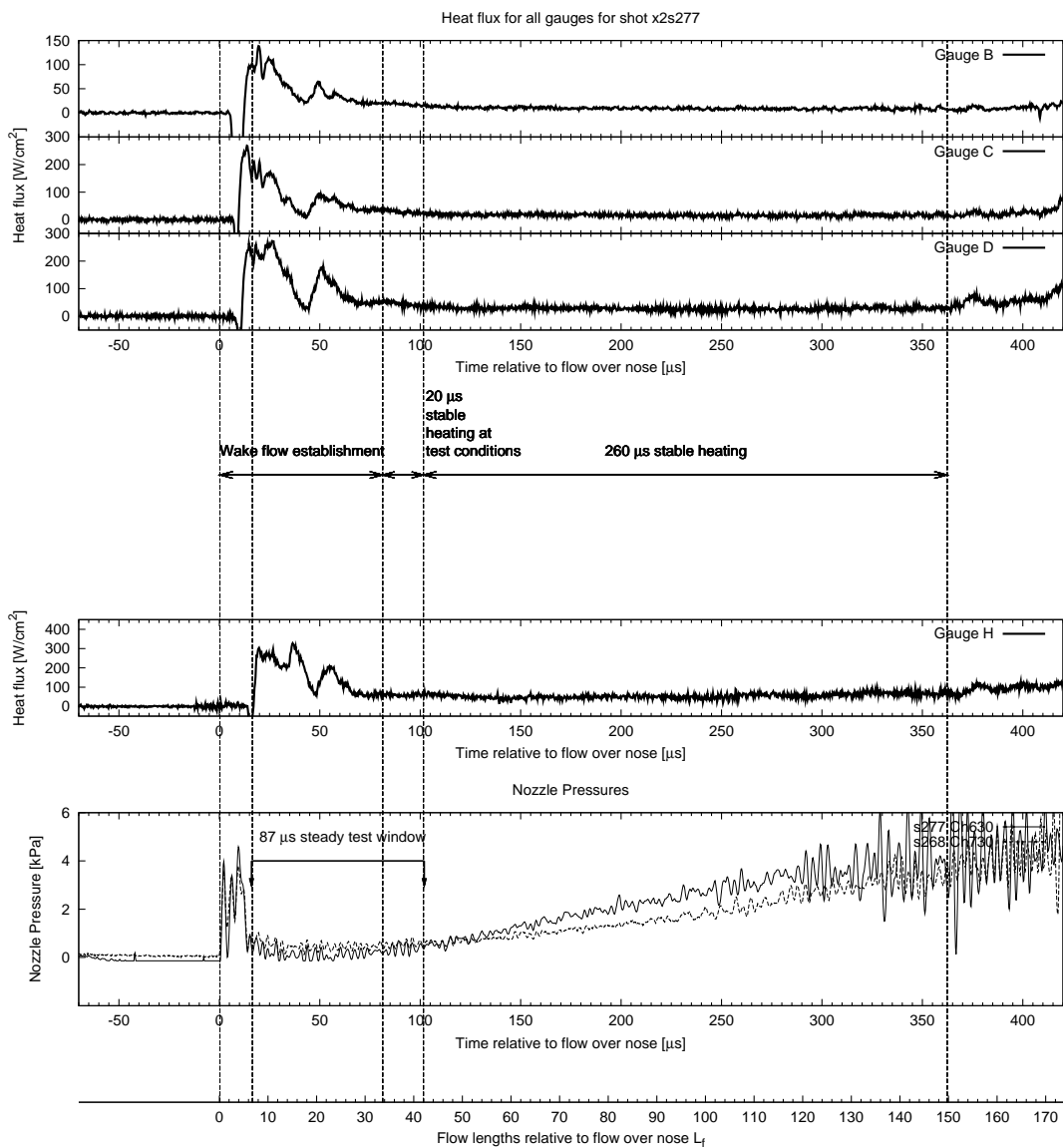


Figure 4.11: Heat and pressure data from X2 shot s277 (MC1).

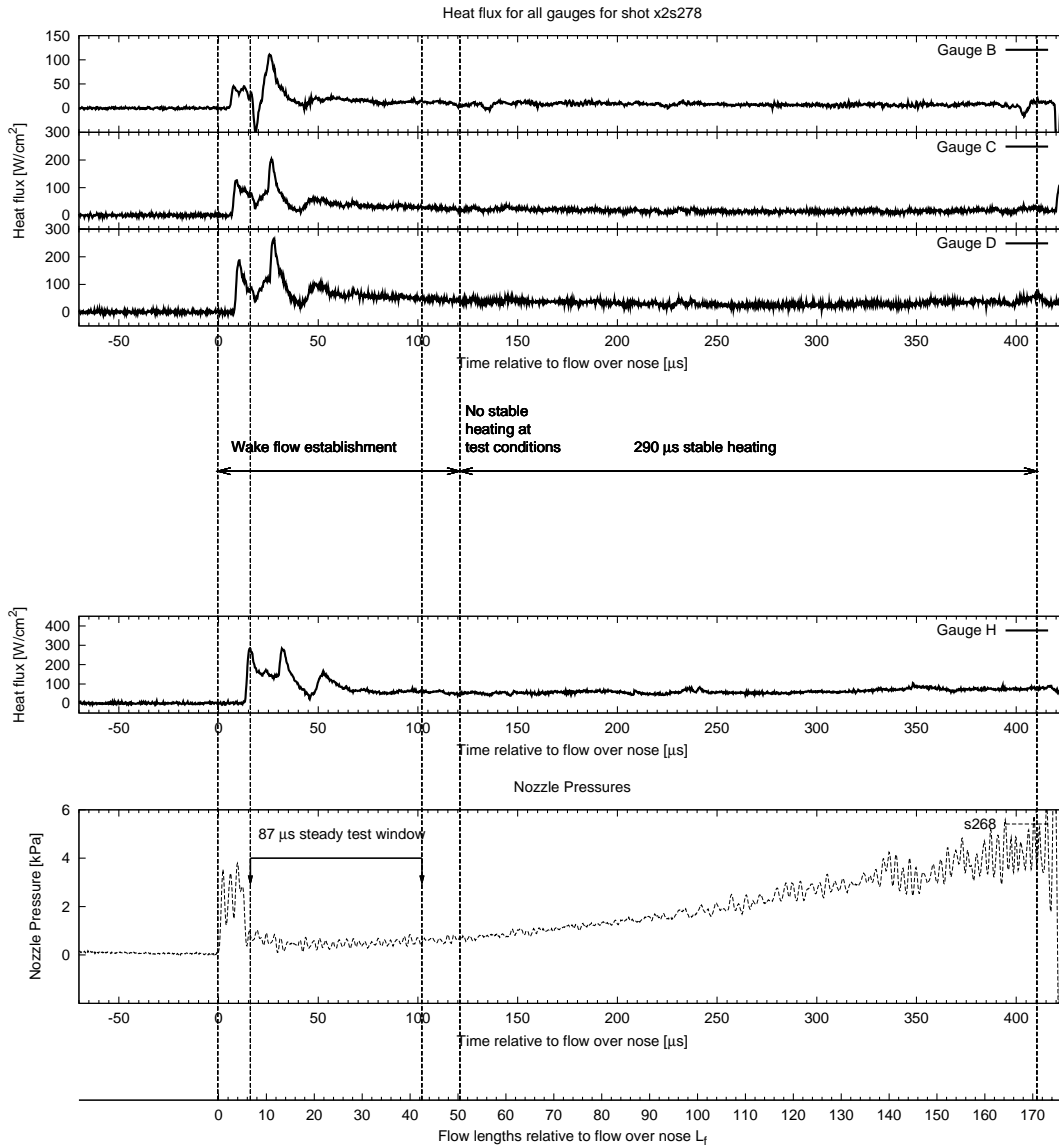


Figure 4.12: Heat and pressure data from X2 shot s278 (MC1).

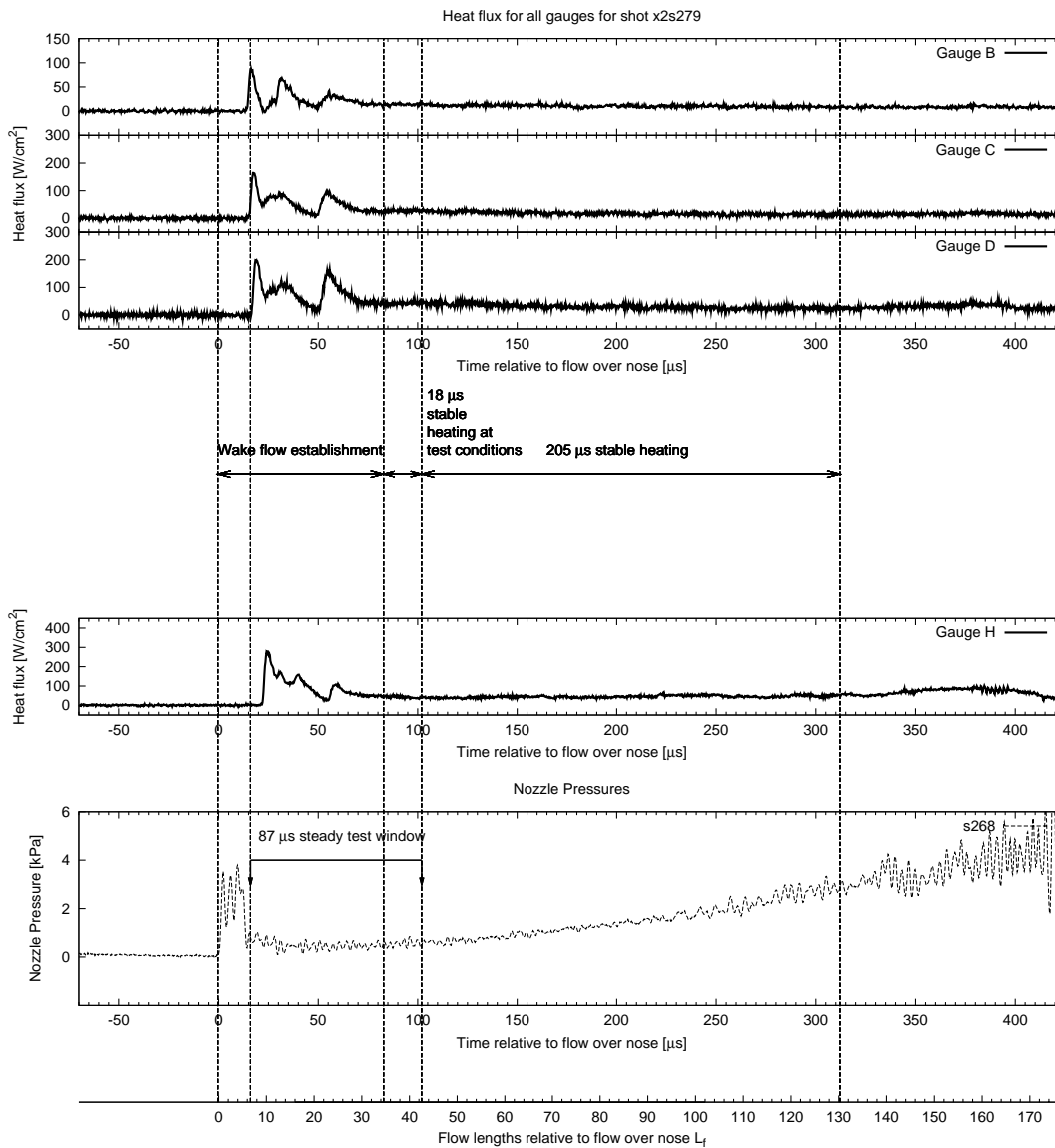


Figure 4.13: Heat and pressure data from X2 shot s279 (MC1).

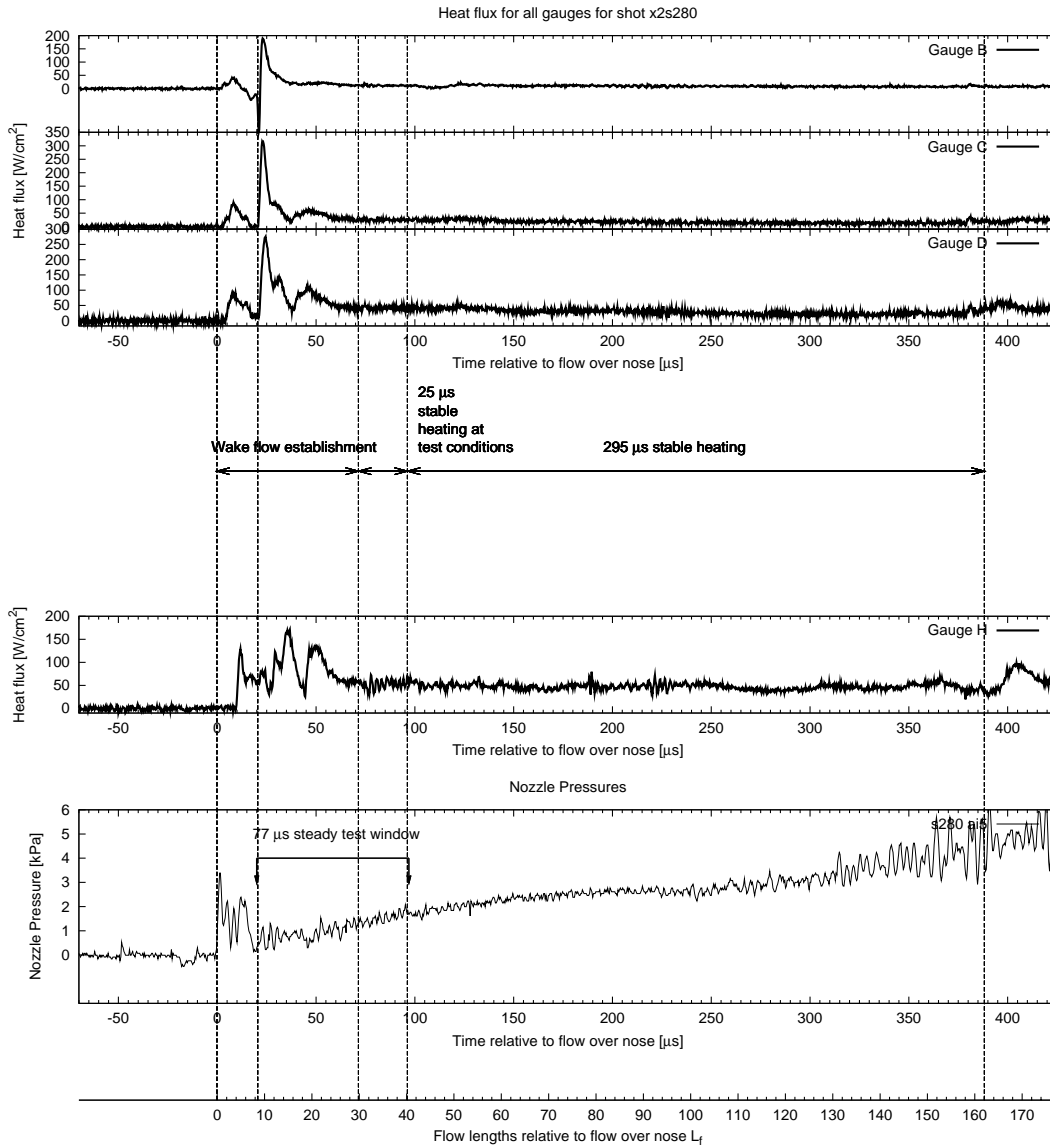


Figure 4.14: Heat and pressure data from X2 shot s280 (MC1).

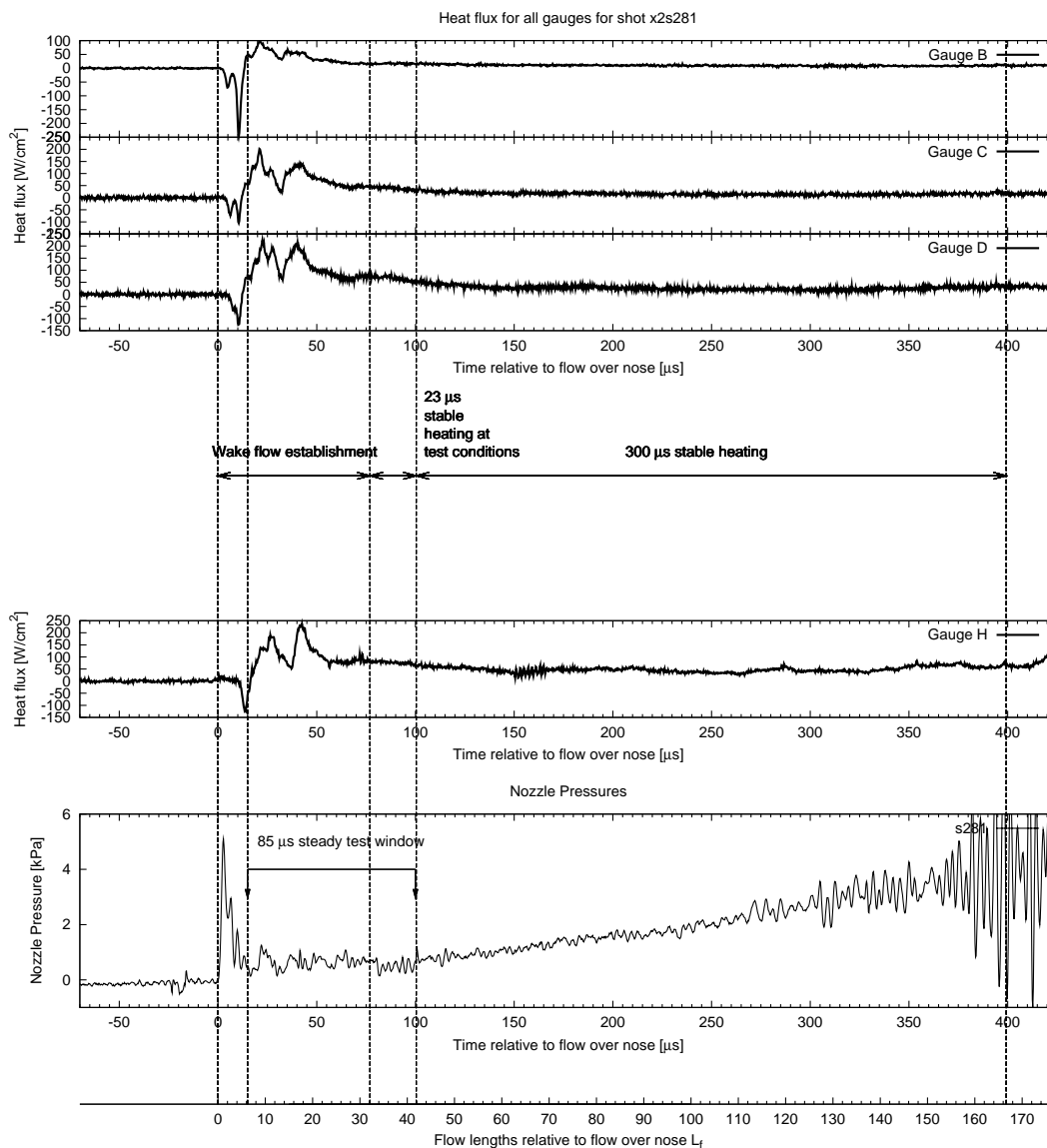


Figure 4.15: Heat and pressure data from X2 shot s281 (MC1).

Table 4.7: Summary of results for MC1 flow condition shots. Values in parentheses are times expressed as flow lengths of gas taken at the shock speed.

Shot No.	Shock Speed m.s ⁻¹	Wake Flow		Stable	
		Establishment μs (L_f)	Steady Test Time μs (L_f)	Near-wake Heating μs (L_f)	Useable heat data μs (L_f)
277	6198	82 (33.9)	87 (36.0)	20 (8.3)	260 (107.4)
278	6245	103 (42.9)	87 (36.2)	0 (0.0)	290 (120.7)
279	6260	83 (34.6)	87 (36.3)	18 (7.5)	205 (85.6)
280	6395	72 (30.7)	77 (32.8)	25 (10.7)	295 (125.8)
281	6146	77 (31.6)	85 (34.8)	23 (9.4)	300 (122.9)
Average	6248.8	83.4 (34.7)	84.6 (35.2)	17.2 (7.2)	270 (112.5)
Std Dev	93.1	11.8 (4.8)	4.3 (1.5)	10.0 (4.2)	39.5 (16.6)

speed flow results in shorter durations for both the steady test window and the stable near-wake heating window. The average duration of the steady test window was 84.6 μs and this occurred on average 17 μs after the arrival of the shock at the nose of the aeroshell. The time required for wake flow establishment was also longer in the higher speed flow. The stability of the flow in the near-wake region can be seen to occur after approximately 83 μs .

On average, the observation window for stable near-wake region heat transfer as determined by this investigation was 17.2 μs in the MC1 flow condition. This time equates to 7.2 flow lengths of test gas based on the nominal flow conditions detailed in Table 4.3 and the model radius step height y_{ref} of 15 mm. It should also be noted that heat transfer measurements from the period after the steady test window exhibit a steady nature and therefore this data could be usable. Indeed, heat transfer recorded at gauges B and C stabilised much sooner than at D and H. Therefore, whilst the holistic analysis of all gauges suggests the near-wake region is not established during the steady test window, analysis on a gauge-by-gauge basis may yield some usable data from some gauges. This point is discussed further below.

4.8.3 Discussion of Results

The results of this investigation have highlighted some key points regarding the flow characteristics of near-wake flow fields in hypersonic flows and the capabilities

of the X2 expansion tube facility.

As discussed in Section 4.2 the wake establishment time is defined as the time between the arrival of the shock at the nose of the aeroshell and the start of stable heat transfer rates in the near-wake region. Figure 4.3 illustrates these times with respect to typical pressure and heat transfer measurements from an X2 shot. Whilst this flow is not solely of test gas composition and known properties, it does contribute to the start up processes around the forebody and near-wake region of the aeroshell. The steady test gas following the shock and interface gas then helps to stabilise the flow structure around the bluff body - first over the forebody and then around the aft.

For both flow conditions examined in this study the results show that the time required for wake flow establishment is of the same order of magnitude. The wake establishment process in the MC1 condition was on average $12.6 \mu\text{s}$ faster than in the MC2 flow condition, however, it was 13% slower in terms of flow lengths. For shots under the MC1 condition, an average of 34.7 flow lengths were required for wake establishment, and 30.7 flow lengths for shots under the MC2 condition. The results of Hollis [8] for shots in CO_2 around a Pathfinder geometry yielded between 40 and 70 flow lengths required for wake establishment with an average of 51 flow lengths. However, the technique used by Hollis for the determination of the wake establishment time differs from that used in the present study. The test model used by Hollis consisted of heat gauges over the back shell of the blunt body as well as along the entire length of the sting. Hollis' technique recorded the time required for all heat gauges on the model and sting to reach a stable level. Given the differences in location and number of gauges between the two studies, comparison for the purposes of validation is not appropriate. However, some insight into the phenomenon of wake flows can be drawn by comparison of the data.

In the present study, the majority of heat gauges were located near the base of the aeroshell with one outlier. It can be said then that the wake flow establishment time represents the time required for heat transfer at those locations to stabilise. Therefore it can be said that results from this study can be used to quantify the time required for flow within the recirculation zone to stabilise whereas those of Hollis more accurately quantify the establishment time of the entire flow system along

the aft facing surface of the model and sting. Following this logic, the difference between the mean wake establishment times found in each study can be understood and deemed acceptable.

The extent of the period of stable heating in the near-wake region is determined by the response of the heat transfer gauges positioned behind the bluff body along the sting mount. After the arrival of the shock and during the wake establishment period the heat transfer in the near-wake region increases as the temperature of the flow field increases. The initial fluctuations observed in the heat transfer traces are due to the time-decay of the gauge response and the changes in temperature gradient as the flow transitions through the flow regimes identified earlier in Figure 4.2. Beyond wake establishment the heat transfer becomes more stable as the near-wake flow stabilises in the steady test window. The extent of the stable near-wake heating window is determined by the end point of the steady test gas window.

The results of the MC1 aerocapture condition demonstrate that the steady test gas window can end before the heat transfer rates have stabilised at all gauges. On average, 17.2 μs of stable heat transfer was achieved before the steady test window closed. In shot 278 the steady test window closed before the heat transfer rates in the near-wake region were able to stabilise. However, it can be observed that the recorded data suggests a long period of relatively stable heat transfer within the near-wake region for on average 270 μs after the steady test window. Although this data is not recorded during a time of steady predictable test gas conditions, it still yields insight into the flow structure behind the blunt forebody geometry. This data is still potentially usable for the heating levels also. With the exception of gauge H, the heating levels remain relatively constant throughout the period defined as “stable heating”. Data from gauge H, however, indicates a break from stability much earlier than gauges B through D which is clearly evident in heat transfer measurements from shots 280 and 281.

The phenomenon can be understood by examining the structure of the wake flow behind a bluff body object with a rearward sting support in a hypersonic flow stream. As depicted in Figure 4.1, the recirculation zone is isolated from the main bulk gas flow by a shear layer. This demarcation inhibits mixing and maintains a laminar flow regime over the recirculation zone until the flow transitions around

the point of flow attachment to the sting mount. The prevention of mixing enables the heat transfer within the recirculation zone to remain relatively constant despite the fact that the gas flowing in the bulk portion of the flow structure is undergoing rapid change from steady test gas flow to unsteady driver gas at much higher static pressures. The net result is that the flow properties within the recirculation zone lag behind those of the bulk flow and remain stable. Gauges B through D are located within the recirculation zone whilst gauge H lies beyond its influence. Despite this lag and apparent continuation of steady heating in the recirculating flow, the stable near-wake heat transfer window is not extended beyond the close of the steady test gas window.

Based on the results of the shots at the MC1 condition, the capabilities of the X2 expansion tube for this type of study appear to have a limit at flow speeds greater than 6,500 m/s based on the Pathfinder model with a reference length $y_{ref} = 15$ mm. At the MC1 condition, measurements from gauges B through D stabilise after the very end of the steady test gas window. This indicates that for this model size and at speeds greater than 6,500 m/s there is most likely insufficient steady test time for the near-wake flow to be classified as established. However, there may be merit in adopting a gauge-by-gauge approach to flow field stabilisation rather than a holistic one. As shown, some gauges reach a stable time average heat transfer level before others in different streamwise locations. Therefore, in certain flow conditions it may only be plausible to obtain stable time average heat transfer data at distinct locations rather than gain a holistic view of flow field stabilisation. As a result, stable heat transfer data could be obtained at higher speed flow conditions at discrete gauge locations despite the flow field not reaching establishment.

4.9 Experimental Design

The results obtained from these experiments can provide guidance for future studies of near-wake flow heat transfer. It has been demonstrated that the amount of time averaged stable heat transfer is dependent on the speed of the flow and the size of the model. This correlation has been described in Equation 2.1 shown here for completeness. The number of flow lengths L_f is directly proportional to

the speed of the flow U_∞ and inversely proportional to the reference length y_{ref} . It has also been demonstrated that the CO₂ flow conditions used in this study as simulated in the X2 expansion tube required in the order of 30 flow lengths for wake establishment.

$$L_f = \frac{U_\infty \Delta t_{est}}{y_{ref}}$$

Based on this information an experimenter must appropriately size the model so that an adequate amount of steady test time is available to determine the time average heat transfer level. Rearranging Equation 2.1 and making substitutions, the reference length y_{ref} for a suitably scaled model can be obtained. This is shown in Equation 4.1,

$$y_{ref} = \frac{U_\infty(a + bf)}{L_f} \quad (4.1)$$

where a is the time between shock arrival at the nose and the start of the steady test window, b is the amount of available steady test time and f is the fraction of the steady test window that the experimenter would like for the time average steady heating window. In the context of these experiments, the reference length is the step height between the shoulder radius of the aeroshell forebody and the radius of the sting mount. Values for a and b can be obtained from prior experimental work at similar conditions or survey shots conducted at the conditions of interest. CFD simulations can also yield these values although, as shown by Scott [23], tend to over estimate the available steady test time.

There are, however, other practical limitations dictating the appropriate size of the model. These limitations include the size of the core flow from the nozzle exit of the X2 machine and the spatial requirements of instrumentation and sensors. Furthermore, the structure of the flow field is greatly affected by the sizing of the model with respect to the sting which is of particular importance when the near-wake flow field is of interest.

The experimental results demonstrate that the model used in this study was appropriately sized for the MC2 flow condition and that a time average stable heat transfer level was observable for on average 65% of the steady test window. However, the model dimensions were less ideal for the MC1 flow condition. On average, only

20% of the steady test window was available for observing a time average stable heat transfer in the near-wake region.

The procedure for sizing the model and sting should begin with selecting the smallest sting radius which will accommodate instrumentation needs. From there the radius of the aeroshell shoulder can be sized based on a suitable step height in order to generate the desired duration of time average steady heat transfer. The largest diameter of the model should then be compared against the diameter of core flow at the the expansion tube nozzle exit. Dimensional changes would be required should the model be too large for the core flow size that the expansion tube is capable of producing at the desired flow conditions.

In the case of the MC1 flow condition used in this study, it was shown that the model was too large compared with the available test time and flow lengths. Applying Equation 4.1 to the results presented in Table 4.7 and setting $f = 0.5$, a step height of 12 mm would be a more appropriate value for y_{ref} . Assuming that the instrumented sting is not replaced (at considerable time and cost), an alternative aeroshell model with a shoulder radius of 17 mm would be required such that the near-wake flow is established at approximately the mid-point of the steady test window. A side effect of resizing the model is that the geometric scales of the backshell relative to the sting radius and the reference height y_{ref} would be different and hence the near-wake flow field would possibly exhibit a slightly different structure. As a result, the flow start-up processes might also be altered. Therefore, Equation 4.1 should be used as a guide only and important features of the model geometry must also be considered during the design of an experiment.

Conclusions

This thesis presents an investigation of the capabilities of the X2 expansion tube in the simulation of separated flows behind the Mars Pathfinder aeroshell. The objective of this study was the determination of the quantity of flow time required for the flow field establishment in the near-wake region. The scope of the study was the characterisation of the X2 machine and determination of its capabilities for this type of simulation in two flow conditions relevant to current and future Mars exploration missions. The first of these flow conditions was based on an aerocapture flight through the Mars atmosphere in a low-speed scenario with a speed of 6,500 m/s. The second condition was based on what is known as the *Langley* condition; a direct entry flight profile with a speed of 4,700 m/s.

Results from the CFD portion of this work were used to gain an understanding of the wake establishment process rather than providing accurate heat transfer data. This simulation data demonstrated that flow separation occurs at the base of the aeroshell vehicle in the early phase of the establishment process with the flow reattaching to the sting. As time progresses the flow attachment location moves further downstream from the base of the aeroshell whilst the flow separation point moves along the rear cone frustum towards the aeroshell shoulder. Streamline plots were used to visualise the flow field for the purpose of determining suitable placement of the thin-film heat transfer gauges for the experimental portion of the study.

Heat transfer data taken from the CFD solutions under both flow conditions studied showed good agreement with wake establishment times derived by Brian Hollis [8]. In a previous study, Hollis had shown that an average of 51 flow lengths of CO₂ were required for wake establishment as determined by experimental heat transfer measurements. Based on the dimensions of the model used in this study the

amount of steady flow time required for establishment in the selected flow conditions was calculated to be $118 \mu\text{s}$ at a freestream speed of $6,500 \text{ m/s}$ and $163 \mu\text{s}$ at $4,700 \text{ m/s}$.

In the experimental portion of this investigation a total of ten successful shots were conducted. Five successful shots were performed at each flow condition to account for statistical error and demonstrate repeatability. Static pressure data taken from pressure transducers mounted on the wall of the nozzle at its exit was used to determine the duration of the steady test gas window. Thin-film heat gauges were employed to measure the heat transfer rate along the model mounting sting in the wake of the aeroshell.

The wake establishment time was defined as the time required for heat transfer measurements to reach a stable time average level from the time of arrival of the shock at the nose of the aeroshell. It was determined that 34.7 flow lengths of gas at a freestream speed of $6,500 \text{ m/s}$ and 30.7 flow lengths of gas at a speed of $4,700 \text{ m/s}$ were required for wake establishment. However, in the low-speed aerocapture condition at a speed of $6,500 \text{ m/s}$ the total steady test window was on average 35.2 flow lengths in duration which resulted in an average of 7.2 flow lengths of steady test gas at the end of the steady test window for which flow in the near-wake region was established. This period was longer in the direct entry condition where the steady test window was 47.6 flow lengths in duration leaving 30.9 flow lengths of steady test gas for which flow in the near-wake region was established.

It was noted that heat transfer measurements recorded after the steady test window had closed remained at the same time average steady level as recorded during the steady test window. This was particularly evident for gauges located within the expected recirculation zone. Whilst the level of heating could not be accurately determined as a stable level during the MC1 flow condition, as opposed to during the MC2 condition, insight was gained into the resilience of the flow structure given the transient and unsteady flow conditions during the experiments. These measurements suggest that, despite the unsteady nature of the driver gas following the steady test time, the shear layer shielded the heat gauges within the recirculation zone and thus maintained a relatively stable time average heat transfer rate. It is possible, therefore, that heat transfer data may still be usable if recorded

on gauges within the recirculation zone and whose record shows that a stable time average heat transfer rate was achieved very soon after the end of the steady test window.

Data collected from this study has shown that the X2 expansion tube at the University of Queensland is capable of generating enough flow time to study the heat transfer in the near-wake regions of aeroshell bodies. The results presented have demonstrated the approximate duration for which heat transfer in the near-wake region remains at a time average steady level for two flow conditions in CO₂ gas simulating the Martian atmosphere. Interpretation of these results has demonstrated that experimenters must appropriately size the scale model in order to maximise the available flow time for the observation of time average stable heat transfer in the steady test window based on the flow condition being investigated. A method for the sizing of models for this type of study was also presented.

For further work in this field, the following recommendations are offered:

- Computational grids used in CFD studies should be refined further with consideration given to adaptive meshing techniques and shock fitting techniques;
- Experimental apparatus design and setup should consider careful placement of thin-film heat gauges and better consideration of the electrical design of the apparatus;
- A larger sample set of experimental data is needed to make proper inferences about the phenomena in the near-wake flowfield, taking into account the implication that multiple shots has on the reliability and deterioration of thin-film heat gauges.

CFD Governing Equations

The contents of this appendix describes the basic governing equations for the MBCNS2 solver, as given by Jacobs [10].

Nomenclature, Units

A	: area, m ²
a	: sound speed, m/s
C_p, C_v	: specific heats, J/(kg.K)
E	: total specific energy, J/kg
e	: specific internal energy, J/kg
\bar{F}	: array of flux terms
f	: species mass fraction
h	: specific enthalpy, J/kg
\hat{i}, \hat{j}	: unit vectors for the cartesian coordinates
k	: coefficient of thermal conductivity
M	: Mach number
n	: direction cosine
\hat{n}, \hat{p}	: unit vectors for the cell interface
P	: point in the (x, y) -plane
p	: pressure, Pa
Q	: array of source terms
q	: heat flux, W/m ²
R	: gas constant, J/(kg.K)
r	: radial coordinate, m
r, s	: normalised coordinates
S	: control surface of the cell
T	: temperature, degree K
t	: time, s; independent parameter for the Bezier curves
U	: array of conserved quantities
u	: velocity, m/s
V	: cell volume, m ³
x, y, z	: cartesian coordinates, m
ρ	: density, kg/m ³
μ, λ	: first and second coefficients of viscosity, Pa.s
γ	: ratio of specific heats

Subscripts, Superscripts

i	: inviscid
is	: species index
L, R	: Left, Right
n	: normal to the cell interface
p	: tangent to the cell interface
v	: viscous
x, y, z	: coordinate directions
*	: intermediate state in the solution of the Riemann problem

A.1 Governing Equations

The starting point for the governing equations encoded within *MB.CNS* is the set Navier-Stokes equations which, in integral form, can be expressed as

$$\frac{\partial}{\partial t} \int_V U dV = - \int_S (\bar{F}_i - \bar{F}_v) \cdot \hat{n} dA + \int_V Q dV \quad , \quad (\text{A.1})$$

where V is the cell's volume, S is the bounding (control) surface and \hat{n} is the outward-facing unit normal of the control surface. For two-dimensional flow, V is the volume per unit depth in the z -direction and A is the area of the cell boundary per unit depth in z . The array of conserved quantities (per unit volume) is

$$U = \begin{bmatrix} \rho \\ \rho u_x \\ \rho u_y \\ \rho E \\ \rho f_{is} \end{bmatrix} . \quad (\text{A.2})$$

These elements represent mass density, x -momentum per volume, y -momentum per volume, total energy per volume and mass density of species is . The flux vector is divided into inviscid and viscous components and the inviscid component, in two

dimensions, is

$$\bar{F}_i = \begin{bmatrix} \rho u_x \\ \rho u_x^2 + p \\ \rho u_y u_x \\ \rho E u_x + p u_x \\ \rho f_{is} u_x \end{bmatrix} \hat{i} + \begin{bmatrix} \rho u_y \\ \rho u_x u_y \\ \rho u_y^2 + p \\ \rho E u_y + p u_y \\ \rho f_{is} u_y \end{bmatrix} \hat{j} . \quad (\text{A.3})$$

The viscous component is

$$\bar{F}_v = \begin{bmatrix} 0 \\ \tau_{xx} \\ \tau_{yx} \\ \tau_{xx} u_x + \tau_{yx} u_y + q_x \\ \rho f_{is} \mu_{x,is} \end{bmatrix} \hat{i} + \begin{bmatrix} 0 \\ \tau_{xy} \\ \tau_{yy} \\ \tau_{xy} u_x + \tau_{yy} u_y + q_y \\ \rho f_{is} \mu_{y,is} \end{bmatrix} \hat{j} , \quad (\text{A.4})$$

where the viscous stresses are

$$\begin{aligned} \tau_{xx} &= 2\mu \frac{\partial u_x}{\partial x} + \lambda \left(\frac{\partial u_x}{\partial x} + \frac{\partial u_y}{\partial y} \right) , \\ \tau_{yy} &= 2\mu \frac{\partial u_y}{\partial y} + \lambda \left(\frac{\partial u_x}{\partial x} + \frac{\partial u_y}{\partial y} \right) , \\ \tau_{xy} = \tau_{yx} &= \mu \left(\frac{\partial u_x}{\partial y} + \frac{\partial u_y}{\partial x} \right) , \end{aligned} \quad (\text{A.5})$$

and the viscous heat fluxes are

$$\begin{aligned} q_x &= k \frac{\partial T}{\partial x} + \rho \sum h_{is} f_{is} \mu_{x,is} , \\ q_y &= k \frac{\partial T}{\partial y} + \rho \sum h_{is} f_{is} \mu_{y,is} . \end{aligned} \quad (\text{A.6})$$

Currently, the code convects species without considering their diffusion (*i.e.* $\mu_{x,is} = 0$, $\mu_{y,is} = 0$). For flow without heat sources or chemical effects, the source terms in Q are set to zero.

The conservation equations are supplemented by the equation of state giving

pressure as a function of density, specific internal energy and species mass fractions

$$p = p(\rho, e, f_{is}) \quad . \quad (\text{A.7})$$

The coefficients of viscosity μ , λ and heat conduction k are also allowed to vary with the fluid state. See Jacobs [10] for a description of the gas models implemented in the code.

A.2 Axisymmetric Geometries

For axisymmetric flow, the geometry is defined such that x -axis is the axis of symmetry and y is the radial coordinate. There are relatively minor changes to the governing equations which include:

- dA is now computed as interface area per radian;
- dV is now cell volume per radian;
- The shear stresses τ_{xx} , τ_{yy} have an extra term so that

$$\begin{aligned} \tau_{xx} &= 2\mu \frac{\partial u_x}{\partial x} + \lambda \left(\frac{\partial u_x}{\partial x} + \frac{\partial u_y}{\partial y} + \frac{u_y}{y} \right) \quad , \\ \tau_{yy} &= 2\mu \frac{\partial u_y}{\partial y} + \lambda \left(\frac{\partial u_x}{\partial x} + \frac{\partial u_y}{\partial y} + \frac{u_y}{y} \right) \quad , \end{aligned} \quad (\text{A.8})$$

- and there is a pressure and shear-stress contribution to the radial momentum equation which can be expressed as an effective source term

$$Q = \begin{bmatrix} 0 \\ 0 \\ (p - \tau_{\theta\theta})A_{xy}/V \\ 0 \\ 0 \end{bmatrix} \quad , \quad (\text{A.9})$$

where A_{xy} is the projected area of the cell in the (x, y) -plane and

$$\tau_{\theta\theta} = 2\mu \frac{u_y}{y} + \lambda \left(\frac{\partial u_x}{\partial x} + \frac{\partial u_y}{\partial y} + \frac{u_y}{y} \right) \quad . \quad (\text{A.10})$$

A.3 Discretised Equations and Flux Calculation

The conservation equations are applied to straight-edged quadrilateral cells for which the boundary, projected onto the (x, y) -plane, consists of four straight lines. These lines (or cell interfaces) are labelled North, East, South and West and the integral equation is approximated as the algebraic expression

$$\frac{dU}{dt} = -\frac{1}{V} \sum_{NESW} (\bar{F}_i - \bar{F}_v) \cdot \hat{n} dA + Q \quad , \quad (\text{A.11})$$

where U and Q now represent cell-averaged values. The code updates the cell-average flow quantities each time step by

1. applying inviscid boundary conditions or exchanging data at boundaries of each block as appropriate;
2. reconstructing (or interpolating) the flow field state on both sides of each interface;
3. computing the inviscid fluxes at interfaces as $(\bar{F}_i \cdot \hat{n})$ using a one-dimensional flux calculator;
4. applying viscous boundary conditions at solid walls;
5. computing the viscous contribution to the fluxes as $(\bar{F}_v \cdot \hat{n})$; and finally
6. updating the cell-average values using equation (A.11).

This whole process will be applied in two stages if predictor-corrector time stepping is used.

When computing the inviscid fluxes at each interface, the velocity field is rotated into a local (n, p) -coordinate system with unit vectors

$$\begin{aligned} \hat{n} &= n_x \hat{i} + n_y \hat{j} \quad , \\ \hat{p} &= p_x \hat{i} + p_y \hat{j} \quad , \end{aligned} \quad (\text{A.12})$$

normal and tangential to the cell interface respectively. We have chosen the tangential direction $p_x = -n_y$ and $p_y = n_x$. The normal and tangential velocity components

$$\begin{aligned} u_n &= n_x u_x + n_y u_y \quad , \\ u_p &= p_x u_x + p_y u_y \quad , \end{aligned} \quad (\text{A.13})$$

are then used, together with the other flow properties either side of the interface, to compute the fluxes

$$\begin{bmatrix} F_{mass} \\ F_{n-momentum} \\ F_{p-momentum} \\ F_{energy} \\ F_{species-is} \end{bmatrix} = \begin{bmatrix} \rho u_n \\ \rho u_n u_n + p \\ \rho u_n u_p \\ \rho u_n E + p u_n \\ \rho u_n f_{is} \end{bmatrix} \quad , \quad (\text{A.14})$$

in the local reference frame. These are then transformed back to the (x, y) -plane as

$$\overline{\mathbf{F}} \cdot \hat{\mathbf{n}} = \begin{bmatrix} F_{mass} \\ F_{x-momentum} \\ F_{y-momentum} \\ F_{energy} \\ F_{species-is} \end{bmatrix} = \begin{bmatrix} F_{mass} \\ F_{n-momentum} n_x + F_{p-momentum} p_x \\ F_{n-momentum} n_y + F_{p-momentum} p_y \\ F_{energy} \\ F_{species-is} \end{bmatrix} \quad . \quad (\text{A.15})$$

Code Listings

B.1 Final CFD Model Generation Scripts

The following input scripts generated the CFD model for use in MBCNS v2. These scripts are fed into MBCNS which interprets them and generates a series of files representing the geometry, solution parameters and initial flow conditions.

B.1.1 x2-pathfinder-base.py

```

## \file x2-pathfinder-base.py
## \brief Hollis's MP1 Pathfinder Aeroshell
## \author Adriaan Window 17-Jul-2005
##
## This file defines a version of the Mars Pathfinder aeroshell geometry
## as defined by the control points specified by Brian Hollis.

## VERSION HISTORY
##
## 30-May-2006 -- File taken from mp1tubemodel/prerun/eqco2/x2model-holls/
##              x2model-hollis.py
##              -- Altered sting geometry to reflect sting adaptor
##              -- Modified block arrangement.
## 08-Jun-2006 -- Added horizontal flat following sting adaptor ramp to fully
##              fully include ramp, yet allow for a pressure b.c. on outlet
## 10-May-2007 -- Changed AdiabaticBC to FixedTBC for heat transfer
## 11-May-2007 -- For rev4 grid, doubled cells on sting longitudinally and
##              doubled subblock count in that direction
## 12-May-2007 -- Increased cell count by 50% in all directions for all blocks
##              with exception of block5 along the sting (radial still
##              changed.
##
##
##
##
## OLD VERSION HISTORY
## 17-Jul-2005 -- File created from mp1trial02.py

```

```
## 17-Jul-2005 -- Manually adjusted global west boundary to better fit shock
## -- Reconfigured boundaries for BLK2&3, fix connection issues
## 19-Jul-2005 -- Moved pylab import to plotting section at end of file and
## -- commented line.
## -- Made upstream flow section larger to fix solution errors -
## -- issue exists were solution is not coming out.
## -- Increased shock factor (initial attempted fix - failed)
## -- Improved clustering and cell sizing over block transitions
## -- Reduced ix cell count in BLK3. Maintained same cell count
## -- in all other blocks from mp1trial02
## 20-Jul-2005 -- Fixed K node location (swapped kx, ky variable calculations)
## 21-Jul-2005 -- Changed clustering along BLK3 South boundary (wall) to
## -- dual 1.05
## 22-Jul-2005 -- Increased BLK3 ix cell count to 80 with NO clustering
## -- (ignore entry from 21-Jul-2005)
## 25-Jul-2005 -- Added direction lists in block definitions as per latest
## -- mb_cns scriptit.py.
##
## 28-Jul-2005 -- File created from mp1trial03.py
## -- Restored block definition order to sequential
## -- Blocks subdivided for extended parallelisation
## 31-Jul-2005 -- Fixed cell distribution in MBLKS 4 & 5
## 01-Aug-2005 -- Corrected minor block-grid alignment issue
## 01-Aug-2005 -- File created from mp1trial04.py
## -- Changed settings from mp1trial04.py (inviscid, perfect CO2)
## -- to viscid with equilibrium CO2
## 02-Aug-2005 -- Reduced number of blocks to increase efficiency of parallel
## -- processor use, improve block-to-block connectivity and
## -- and simplify connectivity.
## -- Increased number of cells in BLOCK4 for better resolution
## -- of wake flow features.
## 06-Sep-2005 -- Changed initial flow conditions u=0.0
## 12-Sep-2005 -- Migrated file to mpleqco2-02.py
## -- Increased grid normal grid resolution to capture b.l.
## 10-Mar-2006 -- Renamed file to mpleqco2-vall01.py
## -- Migrated contents from scriptit to mbcns_prep.py standard
## -- Changed clustering to valliammai type
## 13-Mar-2006 -- File created from mpleqco2-vall01.py
## -- Reverted grid resolution back to mpleqco2-02 standard
## 29-Mar-2006 -- Modified Face2D objects to use AdiabaticBC to allow viscous
## -- effects at the walls. This has been the problem all along.
##
## 10-Apr-2006 -- File created from mpleqco2-vall02.py
## -- Modified body geometry to resemble that of the X2 model but
## -- still uses the Hollis control points, with minor
## -- adjustments.
## -- Flow conditions unaltered from those of Brian Hollis.
## 29-Nov-2006 -- Updated to comply with r927 of mbcns2
## 14-Dec-2006 -- Changed flow conditions to match those of Direct Entry A
## -- as derived by Daniel Potter
## -- Viscous delay flag added to gdata to prevent starting
```

```
##                process instabilities
## 16-Dec-2006    -- After resolving problems with grid in mbcns2, grid dims
##                reset to base values as specified in logbook pg 67
##                -- Superblocks implemented to make clustering and subdivision
##                easier
## 04-Jan-2006    -- File copied from base geometry and conditions updated.
```

```
import sys
import os
sys.path.append(os.path.expandvars("$PWD"))
```

```
from math import *
from hollis_control_points import *
from bezier_from_points import *
from copy import copy
```

```
# -----
# Specify flow conditions
# -----
# note: FlowConditions objects created below
u_inf = 6500.0
T_inf = 2000.0
rho_inf = 4.4e-3
gamma = 1.2
R = 189 # J/kg.K
sound = sqrt(gamma * R * T_inf)
Mach = u_inf / sound
p_inf = rho_inf * sound**2 / gamma
## Rearrangement of Anderson eq. 2.12, pg 36
```

```
# -----
# Begin geometry definition
# -----
# Variables
Rb = 20.0e-3
Rs = 1.0e-3
Rn = 0.5*Rb
Rsting = 5e-3
Lcone = 32.25e-3
Lsting = 100e-3
alpha_sting = 31.0
sting_ramp_h = 5e-3
alpha1 = radians(70.0)
Lback = 13.0e-3
alpha2 = radians(40.0)
# Billig correlation for shock standoff distance.
# Note: The radii specified is the base radius of the geometry and not the
# nose radii. This is done as Billig's correlation took the sphere radii to
# be large relative to the vehicle radii. This is not the case with the
```

```

# Viking/Pathfinder aeroshells and other large half-angle sphere cones.
delta = Rb * 0.143 * exp(3.24/Mach**2)
sf = 0.5
# Was noted that increasing shock standoff by factor of 1.1 and using double
# base radii produced better shock fit for large half-angle sphere cone.
A = 0.143*exp(3.24/Mach**2)*Rb*sf
Rc = 1.143*exp(1.8/(Mach-1)**1.2)*Rb*2
Mangle = radians(5.0) # Mach angle
billigy = array(arange(0,0.4,1e-4),Float)
billigx = - A + Rc*(1/tan(Mangle))**2\
          *((1+billigy**2*tan(Mangle)**2/Rc**2)**0.5 - 1)

# -----
# Node definitions from Hollis control points
# -----
# get hollis points from function MP1 from module hollis_control_points
pts= MP1(Rb)
Z = Node(Rn, 0.0, label="Z")
B = Node(pts[1][0], pts[1][1], label="B")
# node A not pulled from Hollis points due to bad radii precision
A = Node(Z.x-sqrt( (Z.x-B.x)**2 + B.y**2 ), 0.0, label="A")
C = Node(pts[2][0], pts[2][1], label="C")
D = Node(pts[3][0], pts[3][1])#, label="D")
E = Node(pts[4][0], pts[4][1], label="E")
F = Node(pts[5][0], pts[5][1], label="F")
G = Node(pts[6][0], Rsting, label="G")
H = Node(G.x + Lsting, Rsting, label="H")
P = Node(H.x + sting_ramp_h/tan(radians(alpha_sting)), \
        Rsting + sting_ramp_h, label="P")

# -----
# Define flow boundary nodes
# -----
# Want the flow boundary to be smooth without cusps to avoid any grid
# distortions. Will use beziers to do this with control points
# I, I1, I2, J.
# Also, scales the flow domain volume upstream of body with a factor, sf,
# of the analytically calculated shock standoff.
I = Node(-sf*delta, 0.0, label="I")
I1 = Node(I.x, B.y/2.5, label="I1")
jy = B.y+sf*delta*sin(pi/2-alpha1)
jx = billigx[searchsorted(billigy,jy)]
J = Node(jx,jy, label="J")
ky = C.y+sf*1.8*delta*sin(pi/2-alpha1)
kx = billigx[searchsorted(billigy,ky)]
K = Node(kx, ky, label="K")

# gradient of BLK1 flow boundary
mkj = (K.y-J.y)/(K.x-J.x)

```

```

# y-intercept
ckj = J.y-J.x*mkj
I2 = Node(I.x, mkj*I.x+ckj, label="I2" )
K1 = Node(K.x+(sf*2.0*delta*cos(atan(mkj))), \
          K.y+(sf*2.0*delta*sin(atan(mkj))), label="K1")

# locate Node L from Billig correlation
lx = 0.3*Rb
ly = billigy[searchsorted(billigx,lx)]
L = Node(lx,ly, label="L")
M = Node(F.x+0.25*Rb, L.y+tan(20*pi/180)*(F.x+0.25*Rb-L.x), label="M")
nx = P.x
ny = billigy[searchsorted(billigx,nx/6)]
N = Node(nx, ny, label="N")
mlk1 = (L.y-K1.y)/(L.x-K1.x)
clk1 = K1.y-K1.x*mlk1
mmn = (M.y-N.y)/(M.x-N.x)
cmn = N.y-N.x*mmn
L1 = Node(L.x+(sf*2.0*delta*cos(atan(mlk1))), \
          L.y+(sf*2.0*delta*sin(atan(mlk1))), \
          label="L1")
L2 = Node(M.x-(sf*2.0*delta*cos(atan(mmn))), \
          M.y-(sf*2.0*delta*sin(atan(mmn))), \
          label="L2")
K2 = Node(L.x-(sf*2.0*delta*cos(atan(mlk1))), \
          L.y-(sf*2.0*delta*sin(atan(mlk1))), \
          label="K2")
O = Node(P.x, P.y + (F.y-G.y), label="O")
Q = Node(H.x, F.y, label="Q")
R = Node(P.x + 10e-3, P.y, label="R")
S = Node(O.x + 10e-3, O.y, label="S")

# -----
# work out shoulder bezier
linelen = sqrt( (E.x-L.x)**2 + (E.y-L.y)**2 ) / 3.0
x = K2.x - L.x
y = K2.y - L.y
vlen = sqrt(x**2 + y**2)
x = x * linelen/vlen
y = y * linelen/vlen
E2 = Node(-y + L.x, x + L.y, label="E2")

# evaluate bezier point closest to wall
x = E.x - F.x
y = E.y - F.y
vlen = sqrt(x**2 + y**2)
x = x * linelen/vlen
y = y * linelen/vlen
E1 = Node(y + E.x, -x + E.y, label="E1")

```

```
# -----  
# Lines, splines, bezier definitions  
# -----  
ab = Arc(A, B, Z)  
bc = Line(B, C)  
cde = Arc3(C, D, E)  
ef = Line(E, F)  
gf = Line(G, F)  
gh = Line(G, H)  
ij = Bezier([I, I1, I2, J])  
ai = Line(I, A)  
bj = Line(J, B)  
jk = Line(J, K)  
kc = Line(K, C)  
kl = Bezier([K, K1, K2, L])  
el = Bezier([E, E1, E2, L])  
lj = Line(L, J)  
hj = Line(H, J)  
lm = Bezier([L, L1, L2, M])  
fm = Line(F, M)  
mn = Line(M, N)  
fq = Line(F, Q)  
qo = Line(Q, O)  
hp = Line(H, P)  
pr = Line(P, R)  
los = Line(O, S)  
rs = Line(R, S)  
sn = Line(S, N)  
  
# -----  
# Define global parameters  
# -----  
# This section is placed here for convenience, as it uses Rb which is defined  
# above.  
  
job_title = "x2-pathfinder-base EQ CO2 (MP1 Rb="+str(Rb)+")"  
gdata.title = job_title  
gdata.case_id = 0  
gdata.set_gas_model("LUT", "lut.dat")  
gdata.axisymmetric_flag = 1  
gdata.viscous_flag = 1  
gdata.flux_calc = ADAPTIVE  
gdata.max_time = 150.0e-6 #seconds  
gdata.max_step = 50000000  
gdata.cfl = 0.5  
gdata.stringent_cfl = 1  
gdata.dt = 5.0e-12  
gdata.dt_plot = 1.0e-6  
gdata.dt_history = 0.2e-6  
gdata.param_file="x2-pathfinder-base-lowcapture.p"
```

```

# -----
# Definition of flow conditions
# -----
inflow = FlowCondition(p=p_inf, u=u_inf, v=0.0, T=T_inf, mf=[1.0,])
initial = FlowCondition(p=10.0, u=0.0, v=0.0, T=300.0, mf=[1.0,])

# -----
# Define faces
# -----
# Discretisation and cluster parameters
fore_nni = 50
fore_nngrid = fore_nni+10

# Block 0 - forebody
s0 = Polyline([ai,])
e0 = Polyline([ab,bc])
w0 = Polyline([ij,jk])
n0s1 = Polyline([kc,])
patch0 = make_patch(n0s1, e0, s0, w0)
nni0 = 75
nnj0 = 100
bc0 = [AdjacentBC(), FixedTBC(300.0), SlipWallBC(), SupInBC(inflow)]
cf0 = [ValliammaiFunction(1e-5,1e-5,kc.length(),nni0+10),
       ValliammaiFunction(1e-2,1e-5,ab.length()+bc.length(),nnj0+10),
       ValliammaiFunction(1e-5,1e-5,ai.length(),nni0+10),
       ValliammaiFunction(1e-2,1e-5,ij.length()+jk.length(),nnj0+10)]

# Block 1 - shoulder domain
e1 = Polyline([cde,])
w1 = Polyline([kl,])
n1s2 = Polyline([e1,])
n1s2.reverse()
patch1 = make_patch(n1s2, e1, n0s1, w1)
nni1 = 75 #nni0
nnj1 = 30
bc1 = [AdjacentBC(), FixedTBC(300.0), AdjacentBC(), SupInBC(inflow)]
cf1 = [ValliammaiFunction(1e-5,1e-5,e1.length(),nni0+10),
       ValliammaiFunction(1e-5,1e-5,cde.length(),nnj1+10),
       ValliammaiFunction(1e-5,1e-5,kc.length(),nni0+10),
       ValliammaiFunction(1e-5,1e-5,kl.length(),nnj1+10)]

# Block 2 - aft cone frustrum
w2 = Polyline([lm,])
n2s3 = Polyline([fm,])
e2 = Polyline([ef,])

```

```

n2s3.reverse()
patch2 = make_patch(n2s3, e2, n1s2, w2)
nni2 = 75 #nni0
nnj2 = 75
bc2 = [AdjacentBC(), FixedTBC(300.0), AdjacentBC(), SupInBC(inflow)]
cf2 = [ValliammaiFunction(1e-5,1e-5,fm.length(),nni0+10),
       ValliammaiFunction(1e-5,1e-5,ef.length(),nnj2+10),
       ValliammaiFunction(1e-5,1e-5,el.length(),nni0+10),
       ValliammaiFunction(1e-5,1e-5,lm.length(),nnj2+10)]

# Block 3 - mount sting domain - outer
w3 = Polyline([mn,])
n3 = Polyline([sn,])
e3w4 = Polyline([fq,qo,los,])
n3.reverse()
patch3 = make_patch(n3, e3w4, n2s3, w3)
nni3 = 75 #nni0
nnj3 = 200
ns_length = gh.length()+hp.length()+pr.length()
bc3 = [FixedPOutBC(10.0), AdjacentBC(), AdjacentBC(), SupInBC(inflow)]
cf3 = [ValliammaiFunction(1e-5,1e-5,el.length(),nni0+10),
       ValliammaiFunction(1e-5,1e-4,ns_length,nnj3+10),
       ValliammaiFunction(1e-5,1e-5,fm.length(),nni0+10),
       ValliammaiFunction(1e-5,1e-4,mn.length(),nnj3+10)]

# Block 4 - mount sting domain - inner
s4 = Polyline([gf,])
n4 = Polyline([rs,])
e4 = Polyline([gh,hp,pr,])
s4.reverse()
n4.reverse()
patch4 = make_patch(n4, e4, s4, e3w4)
nni4 = 60 #nni0
nnj4 = 200
bc4 = [FixedPOutBC(10.0), FixedTBC(300.0), FixedTBC(300.0), AdjacentBC()]
cf4 = [ValliammaiFunction(1e-5,1e-5,rs.length(),nni4+10),
       ValliammaiFunction(1e-5,1e-4,ns_length,nnj4+10),
       ValliammaiFunction(1e-5,1e-5,gf.length(),nni4+10),
       ValliammaiFunction(1e-5,1e-4,ns_length,nnj4+10)]

```

```
# -----  
# Define blocks  
# -----  
# Order of listing defines which blocks will start first in parallel env  
# NOTE: Block connections must be checked/updated if block subdivision is  
# changed.  
  
# SUPERBLOCK IMPLEMENTATION  
  
sblk0 = SuperBlock2D(patch0, nni=nni0, nnj=nnj0, nbi=2, nbj=4,  
                    bc_list=bc0, cf_list=cf0,  
                    fill_conditions=initial,  
                    label="sblk0")  
  
sblk1 = SuperBlock2D(patch1, nni=nni1, nnj=nnj1, nbi=2, nbj=1,  
                    bc_list=bc1, cf_list=cf1,  
                    fill_conditions=initial,  
                    label="sblk1")  
  
sblk2 = SuperBlock2D(patch2, nni=nni2, nnj=nnj2, nbi=2, nbj=2,  
                    bc_list=bc2, cf_list=cf2,  
                    fill_conditions=initial,  
                    label="sblk2")  
  
sblk3 = SuperBlock2D(patch3, nni=nni3, nnj=nnj3, nbi=2, nbj=8,  
                    bc_list=bc3, cf_list=cf3,  
                    fill_conditions=initial,  
                    label="sblk3")  
  
sblk4 = SuperBlock2D(patch4, nni=nni4, nnj=nnj4, nbi=2, nbj=8,  
                    bc_list=bc4, cf_list=cf4,  
                    fill_conditions=initial,  
                    label="sblk4")  
  
# -----  
# Connect adjacent blocks  
# -----  
identify_block_connections()  
  
# -----  
# Set metapost parameters  
# -----  
mpost.scales(1.0,1.0)  
mpost.xaxis(-0.02,0.4e-1,0.1e-1,-0.01)  
mpost.yaxis(0.0,1.0e-1,0.1e-1,-0.015)  
mpost.origin(0.075,0.05)
```

B.1.2 bezier_from_points.py

```
## \file bezier_from_points.py
## \brief Module that provides functionality to calculate Bezier control
##       points from points on the curve to be modelled by the Bezier.
## \author Adriaan Window 12-May-2005
##

## VERSION HISTORY
##
## 17-Jul-2005          -- File created.

from Numeric import *
from LinearAlgebra import *

def Jb0(t):
    return (1-t)**3

def Jb1(t):
    return 3*t*(1-t)**2

def Jb2(t):
    return 3*t**2*(1-t)

def Jb3(t):
    return t**3

def BezierPoints(t, Px, Py, Xends, Yends):

    A = array([[J1(t[0]),0,J2(t[0]),0],[0,J1(t[0]),0,J2(t[0])],\
               [J1(t[1]),0,J2(t[1]),0],[0,J1(t[1]),0,J2(t[1])]])

    b = array([\
    [Px[0] - Xends[0]*J0(t[0]) - Xends[1]*J3(t[0])],\
    [Py[0] - Yends[0]*J0(t[0]) - Yends[1]*J3(t[0])],\
    [Px[1] - Xends[0]*J2(t[1]) - Xends[1]*J3(t[1])],\
    [Py[1] - Yends[0]*J0(t[1]) - Yends[1]*J3(t[1])]])

    return solve_linear_equations(A,b)
```

B.1.3 hollis_control_points.py

```
# \file hollis_control_points.py
# \author Adriaan Window, 2005
#
# Generates control points for the MP pathfinder models used by
# Brian Hollis, NASA Langley for a given input radius.

# MP1 Geometry

from Numeric import *

def MP1(Rb=1.0):
    """Produces the MP1 geometry as a function of base radius"""
    rat_points = array([[0.0,0.0],\
        [0.0302,0.171],[.3199,.9671],[.3669,1.0],[.399,.9883],\
        [.8618,.600],[.8618,.4063],[4.3118,.4063]])
    return rat_points * Rb

def MP2(Rb=1.0):
    """Produces modifies pathfinder MP2 geometry as a function of base radius"""
    print "Not yet implemented"
    return 0

def MP3(Rb=1.0):
    """Produces the MP3 geometry as a function of base radius"""
    rat_points = array([[0.0,0.0],[.0302,.171],[.3079,.9342],\
        [.4019,1.00],[.4662,.9766],[.9150,.60],\
        [.9150,.4063],[4.315,.4063]])
    return rat_points * Rb

def MP4(Rb=1.0):
    """Produces the MP4 geometry as a function of base radius"""
    rat_points = array([[0.0,0.0],[.0302,.1710],[.2840,.8684],\
        [.4719,1.00],[.6005,.9532],[1.0214,.600],\
        [1.0214,.4063],[4.4214,.4063]])
    return rat_points * Rb

if __name__ == "__main__":

    points = MP1(float(sys.argv[1]))
    print points
```


B.2 Experimental Post-Processing Scripts

The following scripts were used to post-process the raw EMF data from the experimental study. These scripts employ Python language coupled with an extension called Pyrex. Pyrex allows for parts of the script to be compiled using C whilst still benefitting from the easy-to-use pseudo-english Python language. The benefit of compilation means that the program runs up to 80 times faster than if it was just written using Python.

B.2.1 makefile

```
# makefile for pyrex version

postexp.so : postexp.o
    gcc -shared postexp.o -o postexp.so

postexp.o : postexp.c
    gcc -c -O333 -fPIC -I/usr/include/python2.5/
        -I/usr/lib/python2.5/site-packages/numpy/core/include postexp.c

postexp.c : postexp.pyx
    pyrex postexp.pyx
```

B.2.2 runpostexp.py

```

#!/usr/bin/env python

import os
import sys
import time
sys.path.append('/home5/home4/awindow/cfd_bin')
sys.path.append('/home1/adriaan/cfd_bin')
sys.path.append('/home/adriaan/cfd_bin')
sys.path.append('/home/adriaan/Documents/Images/window/')
from string import split,atof,join,atoi
from getopt import getopt
import ConfigParser
import postexp

shortOptions = []
longOptions = ["shot=", "chanlist=", "starttime=", "endtime=", "senslist=", \
               "tflist="]

def print_usage():
    print "runpostexp.py "
    print "--shot=\t\tshot number x2sXXX"
    print "--chanlist=\t\tlist of channels CSV"
    print "--tflist=\t\tlist of thin-film channels CSV"
    print "--senslist=\t\tlist of sensitivities for thin-films CSV"

if __name__ == '__main__':
    if len(sys.argv) == 1:
        print_usage()
        sys.exit(0)
    userOptions = getopt(sys.argv[1:], shortOptions, longOptions)
    uoDict = dict(userOptions[0])

    shotName = uoDict.get("--shot")
    chanlist = split(uoDict.get("--chanlist"),',')
    tflist = split(uoDict.get("--tflist"),',')
    senslist = split(uoDict.get("--senslist"),',')
    starttime = uoDict.get("--starttime",0)
    endtime = uoDict.get("--endtime",0)

    t = time.time()
    postexp.process(shotName, chanlist, tflist, starttime, endtime, senslist)
    print "Elapsed time for channels ", chanlist
    print time.time() - t, " seconds"

```

B.2.3 postexp.pyx

```
#!/usr/bin/env python

## /file postexp.pyx
## /author Adriaan Window
##
## Post processing of X2 experimental data using Python + Pyrex
## Pyrex speeds up the process of integrating the emf data by a factor
## of ~80 over straight Python with Numpy. Enables integration over the
## full 8192 samples taken.
##
##
## VERSION HISTORY
## -----
## 16-July-2007 -- File Created
## 17-July-2007 -- Fixed a bug in computation of total data set
##              -- Improved handling of non-integrated data

import os
import sys
import time
sys.path.append('/home5/home4/awindow/cfd_bin')
sys.path.append('/home1/adriaan/cfd_bin')
sys.path.append('/home/adriaan/cfd_bin')
sys.path.append('/home/adriaan/Documents/Images/window/')
from math import sqrt, pi

cimport c_numpy
cimport c_python

import numpy
from string import split,atof,join,atoi
from getopt import getopt
## import Gnuplot
## from libgas2 import *
import ConfigParser

c_numpy.import_array()

shortOptions = []
longOptions = ["shot=", "chanlist=", "starttime=", "endtime=", "senslist=", \
              "tflist="]
```

```

cdef integrator(shot, channel, double alpha, \
    double rhock, double V0):
    # declare C variables
    cdef char* cemf
    cdef double qdot, qflux, raw, timeInterval
    cdef double ctime[10000]
    cdef int i,j
    cdef c_numpy.ndarray cnumpy_emf
    cdef c_python.Py_intptr_t* stride

    print "Integrating channel ",shot, " : ",channel

    # open input file for reading
    inputfile = open(shot+'A.'+channel,'r')
    data = inputfile.readlines()
    timeInterval = atof(split(data[10])[2])
    datalen = len(data)-23
    emf = numpy.zeros(datalen, float)

    # open output file for writing
    output = open(shot+'.'+channel+'.post','w')

    # read input data and setup time array
    for i in range(datalen):
        ctime[i] = timeInterval * i
        emf[i] = atof(split(data[i+23])[0])

    cnumpy_emf = emf
    cemf = cnumpy_emf.data
    stride = cnumpy_emf.strides

    # integrate data over time
    for i in range(2,datalen):
        qdot = 0.0
        if i >= 1:
            for j in range(1,i):
                qdot = qdot + \
                    ((<double*>(cemf+j*stride[0]))[0] - \
                     (<double*>(cemf+(j-1)*stride[0]))[0]) / \
                    (sqrt(ctime[i] - \
                        ctime[j]) + \
                     sqrt(ctime[i] - \
                        ctime[j-1]))
                qflux = 2*rhock/(sqrt(pi)*alpha*V0) * qdot

            # output the results to file
            raw = (<double*>(cemf+j*stride[0]))[0]

            output.write('%e %e %e\n'%(ctime[j],raw,qflux))
    print "Done "

```

```

def process(shot, chanlist, tflist, starttime, endTime, sensitivity):
    tfcounter = -1
    for i in range(0, len(chanlist)):
        if chanlist[i] not in tflist:
            print "Not in tflist"
            # ungzip data and create input and output file handles
            os.system('gzip -d '+shot+'A.'+chanlist[i]+'.gz')
            inputfile = open(shot+'A.'+chanlist[i], 'r')
            infile = inputfile.readlines()
            output = open(shot+'.'+chanlist[i]+'.post', 'w')

            # determine length of data set and time interval
            dataPoints = len(infile)-23
            timeInterval = atof(split(infile[10])[2])
            totalTime = dataPoints * timeInterval
            print timeInterval

            n = 3
            time = numpy.zeros(dataPoints, float)
            stime = numpy.zeros(dataPoints-n-1, float)
            raw = numpy.zeros(dataPoints, float)
            smoothmf = numpy.zeros(dataPoints-n-1, float)
            ## startTime = int(atof(starttime)/0.25)
            ## stopTime = int(atof(endTime)/0.25)
            # set up time and data arrays
            for j in range(0, dataPoints):
                time[j] = j*timeInterval
                raw[j] = atof(split(infile[j+23])[0])

            for j in range(n, dataPoints-n):
                stime[j-n] = time[j]
                sumraw = 0
                for k in range(-n,n):
                    sumraw = sumraw + raw[j+k]
                smoothmf[j-n] = sumraw/(2*n+1)
                output.write(str(stime[j-n])+ ' '+\
                    str(raw[j-n])+ ' '+\
                    str(smoothmf[j-n])+ '\n')
            output.close()
            inputfile.close()

        else:
            tfcounter = tfcounter + 1
            print "Processing data on channel ", chanlist[i]

            # ungzip data and create input and output file handles
            os.system('gzip -d '+shot+'A.'+chanlist[i]+'.gz')
            inputfile = open(shot+'A.'+chanlist[i], 'r')
            infile = inputfile.readlines()
            output = open(shot+'.'+chanlist[i]+'.post', 'w')

```

```

# determine length of data set and time interval
dataPoints = atoi(split(infile[5])[2])
timeInterval = atof(split(infile[10])[2])
totalTime = dataPoints * timeInterval

rawemf = numpy.zeros(dataPoints, float)
rhock = 1540.0
alpha = atof(sensitivity[tfcouter])
V0 = 1.0

# start integration process
integrator(shot, chanlist[i], alpha, rhock, V0)

# close input and output file handles
output.close()
inputfile.close()

# -----

def print_usage():
    print "runpostexp.py "
    print "--shot=\t\tshot number x2sXXX"
    print "--chanlist=\t\tlist of channels CSV"
    print "--tflist=\t\tlist of thin-film channels CSV"
    print "--senslist=\t\tlist of sensitivities for thin-films CSV"

if __name__ == '__main__':
    if len(sys.argv) == 1:
        print_usage()
        sys.exit(0)
    userOptions = getopt(sys.argv[1:], shortOptions, longOptions)
    uoDict = dict(userOptions[0])

    shotName = uoDict.get("--shot")
    chanlist = split(uoDict.get("--chanlist"),',')
    tflist = split(uoDict.get("--tflist"),',')
    senslist = split(uoDict.get("--senslist"),',')
    starttime = uoDict.get("--starttime",0)
    endtime = uoDict.get("--endtime",0)

    t = time.time()
    process(shotName, chanlist, tflist, starttime, endtime, senslist)
    print "Elapsed time for channels ", chanlist
    print time.time() - t, " seconds"

```

Supplementary CFD Data

C.1 Heat transfer time history plots

C.1.1 Low-speed aerocapture flow condition

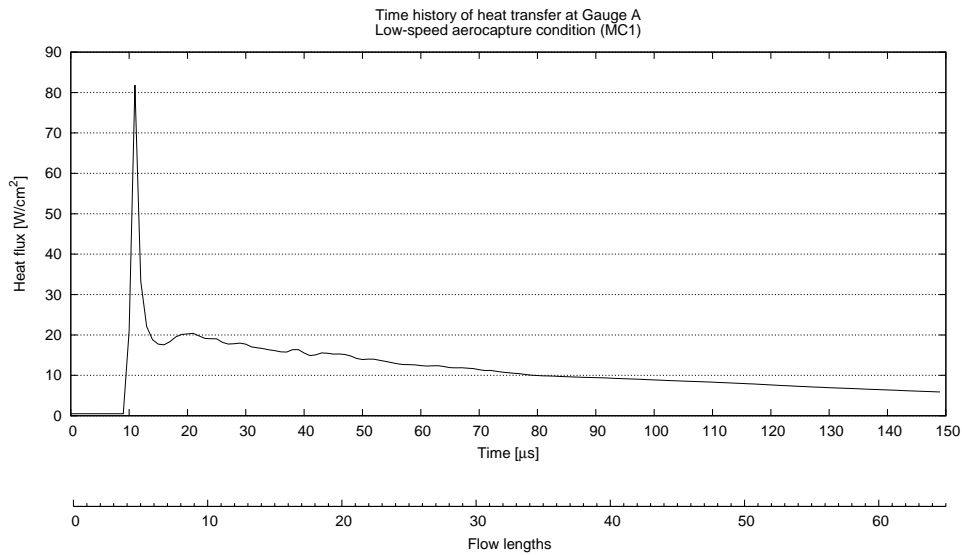


Figure C.1: Heat transfer time history for Gauge A for the low-speed aerocapture condition (free stream velocity $U_\infty = 6,500$ m/s).

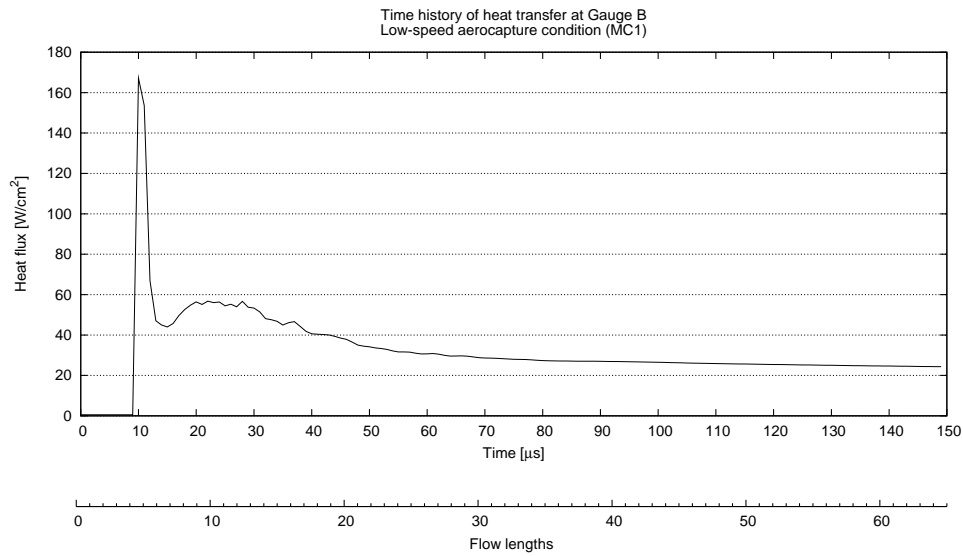


Figure C.2: Heat transfer time history for Gauge B for the low-speed aerocapture condition (free stream velocity $U_\infty = 6,500$ m/s).

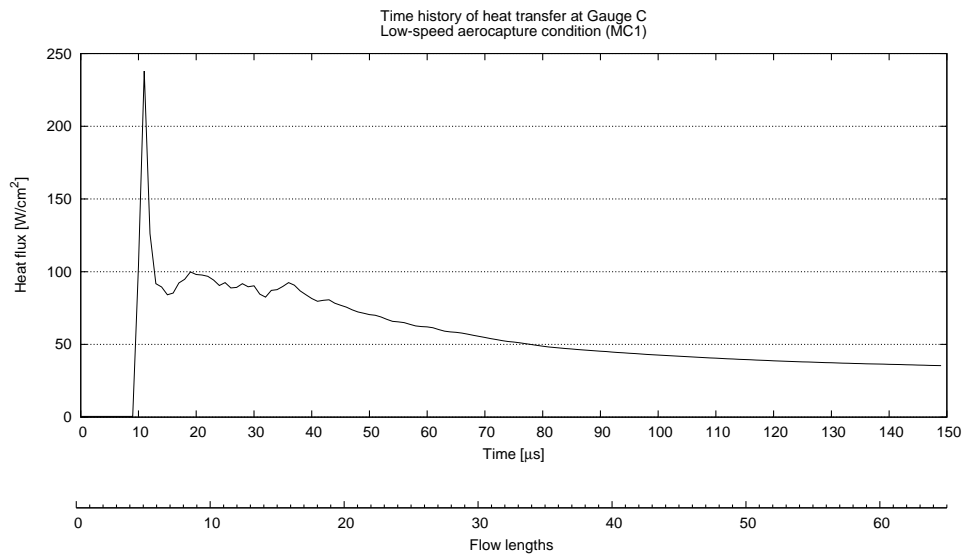


Figure C.3: Heat transfer time history for Gauge C for the low-speed aerocapture condition (free stream velocity $U_\infty = 6,500$ m/s).

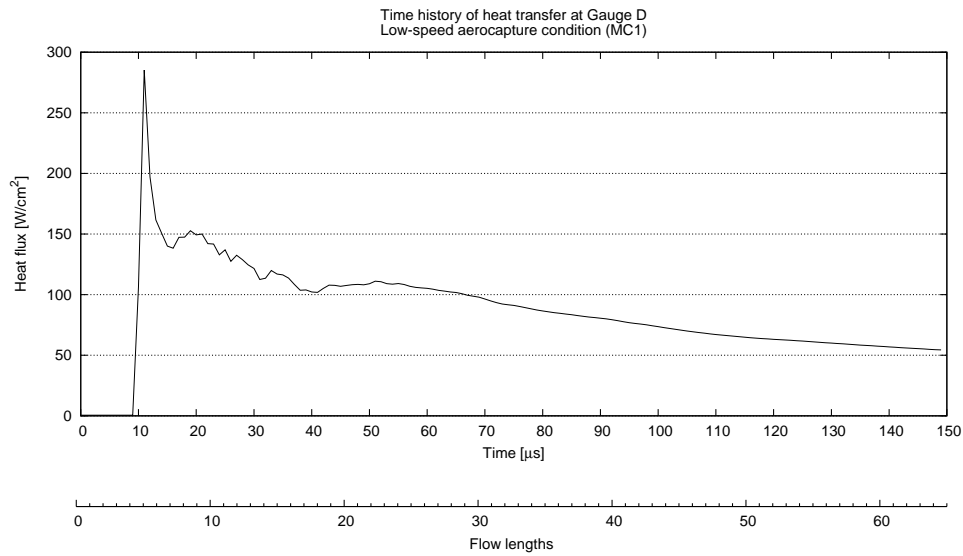


Figure C.4: Heat transfer time history for Gauge D for the low-speed aerocapture condition (free stream velocity $U_\infty = 6,500$ m/s).

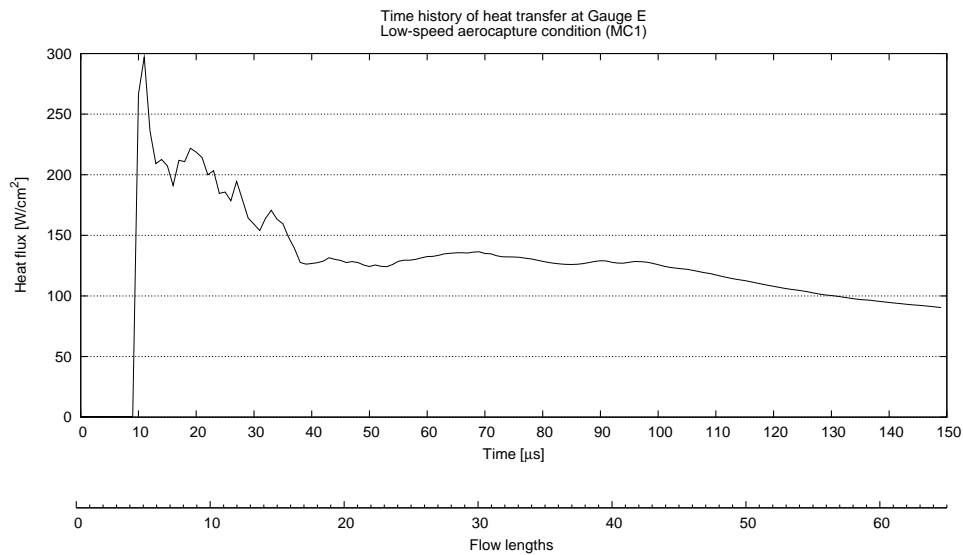


Figure C.5: Heat transfer time history for Gauge E for the low-speed aerocapture condition (free stream velocity $U_\infty = 6,500$ m/s).

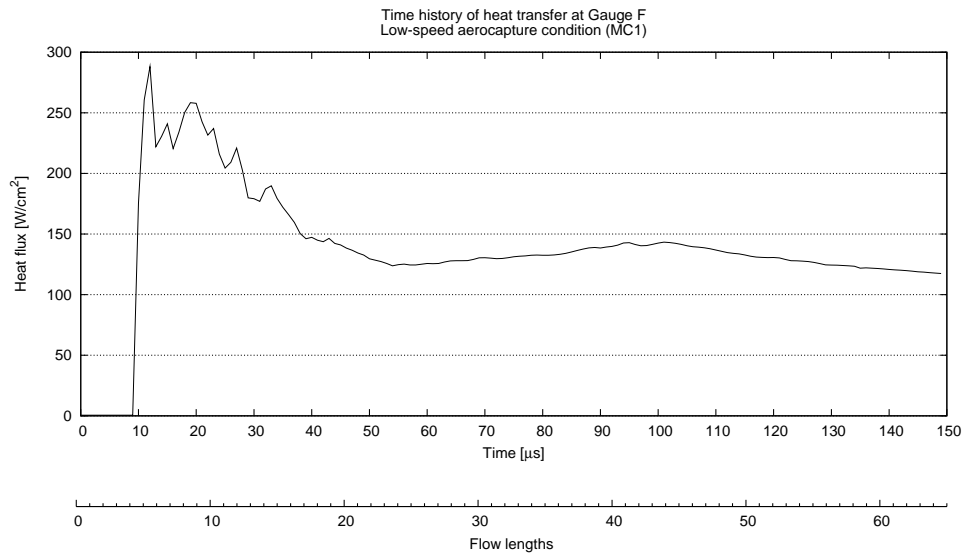


Figure C.6: Heat transfer time history for Gauge F for the low-speed aerocapture condition (free stream velocity $U_\infty = 6,500$ m/s).

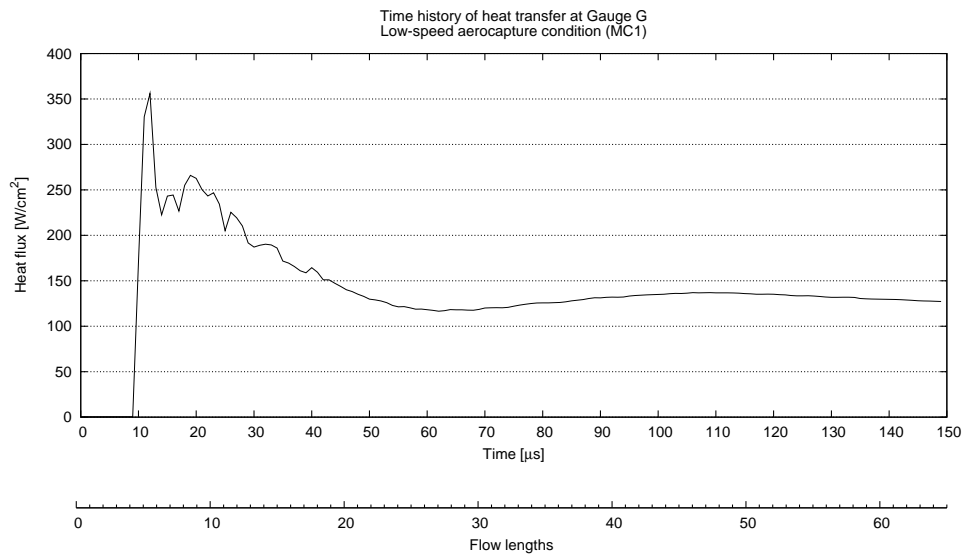


Figure C.7: Heat transfer time history for Gauge G for the low-speed aerocapture condition (free stream velocity $U_\infty = 6,500$ m/s).

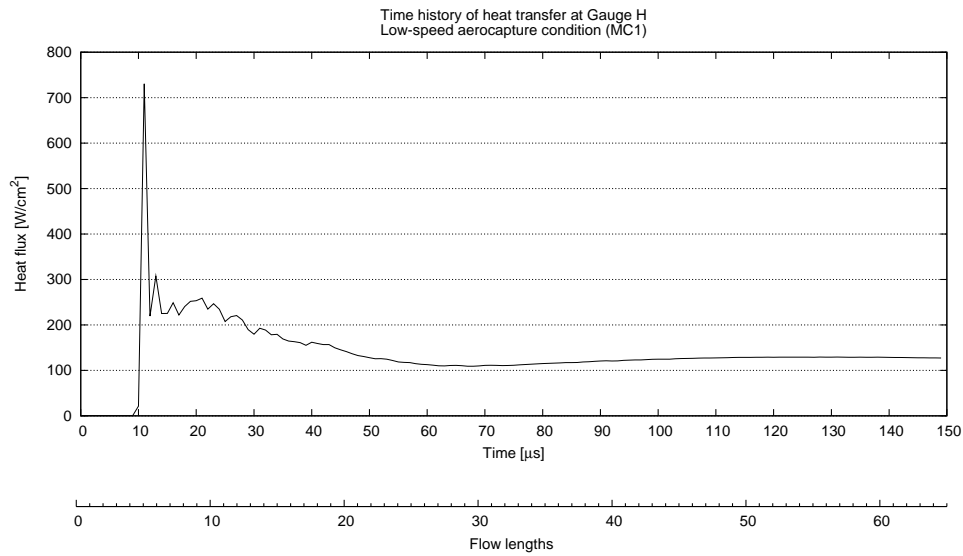


Figure C.8: Heat transfer time history for Gauge H for the low-speed aerocapture condition (free stream velocity $U_\infty = 6,500$ m/s).

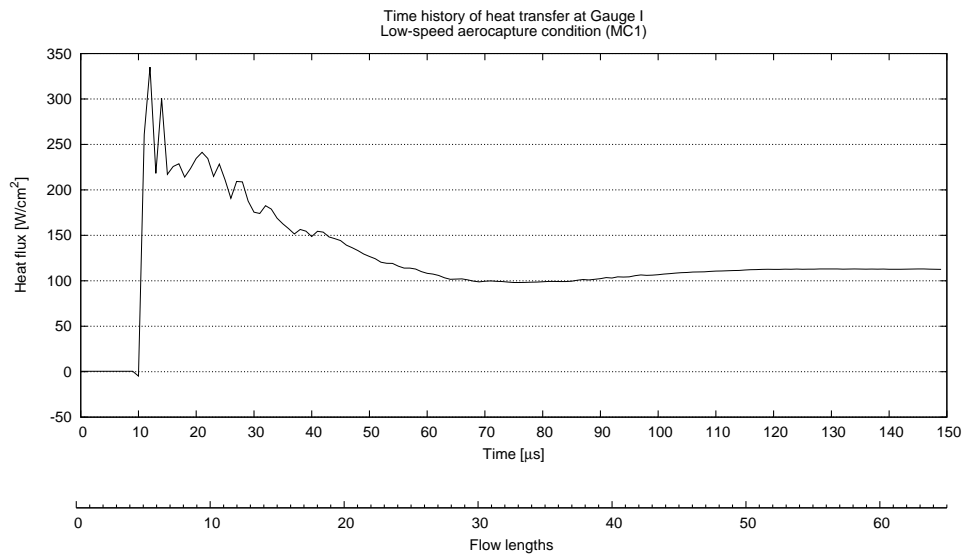


Figure C.9: Heat transfer time history for Gauge I for the low-speed aerocapture condition (free stream velocity $U_\infty = 6,500$ m/s).

C.1.2 Direct entry flow condition

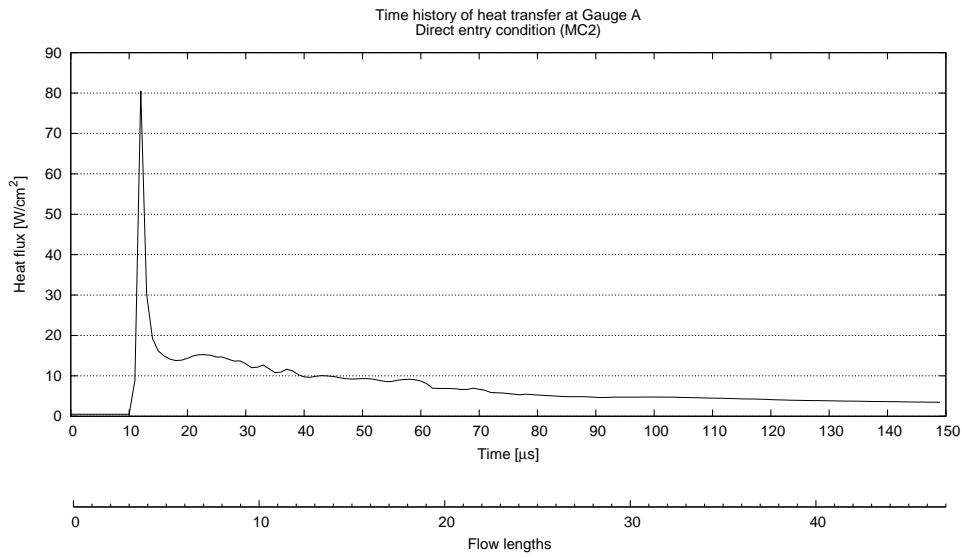


Figure C.10: Heat transfer time history for Gauge A for the direct entry condition (free stream velocity $U_\infty = 4,700$ m/s).

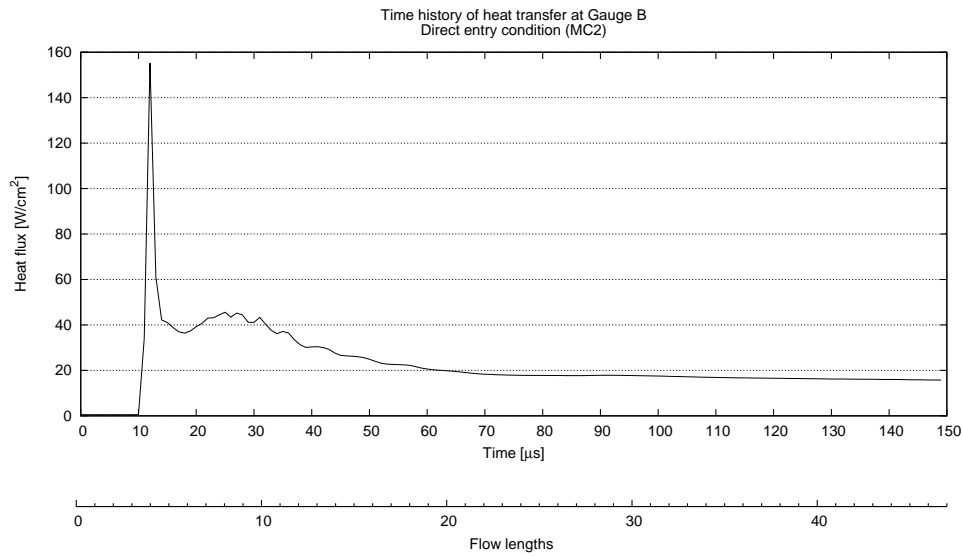


Figure C.11: Heat transfer time history for Gauge B for the direct entry condition (free stream velocity $U_\infty = 4,700$ m/s).

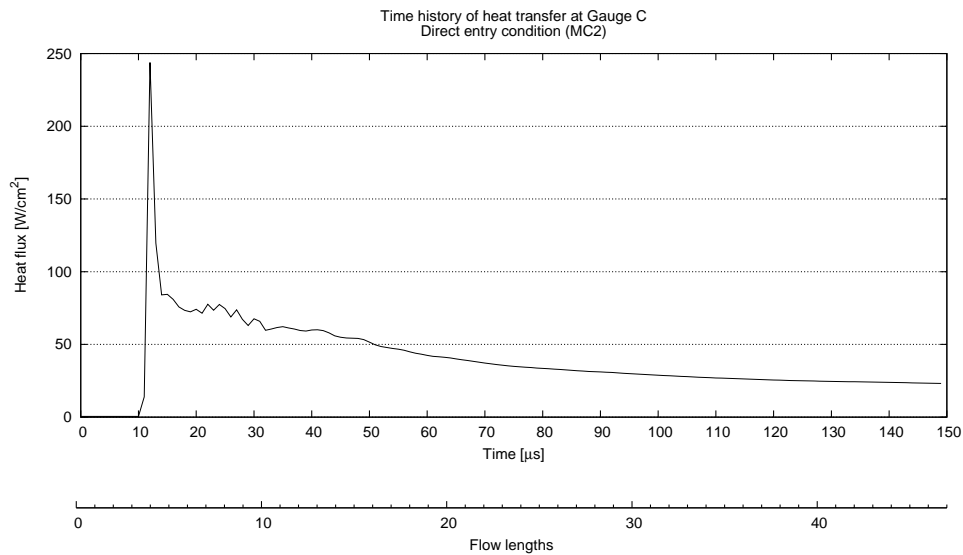


Figure C.12: Heat transfer time history for Gauge C for the direct entry condition (free stream velocity $U_\infty = 4,700$ m/s).

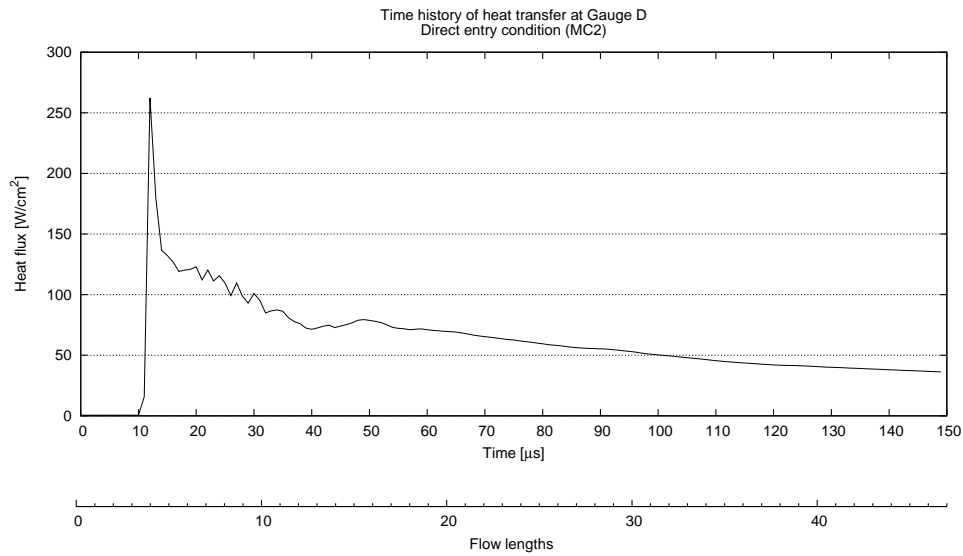


Figure C.13: Heat transfer time history for Gauge D for the direct entry condition (free stream velocity $U_\infty = 4,700$ m/s).

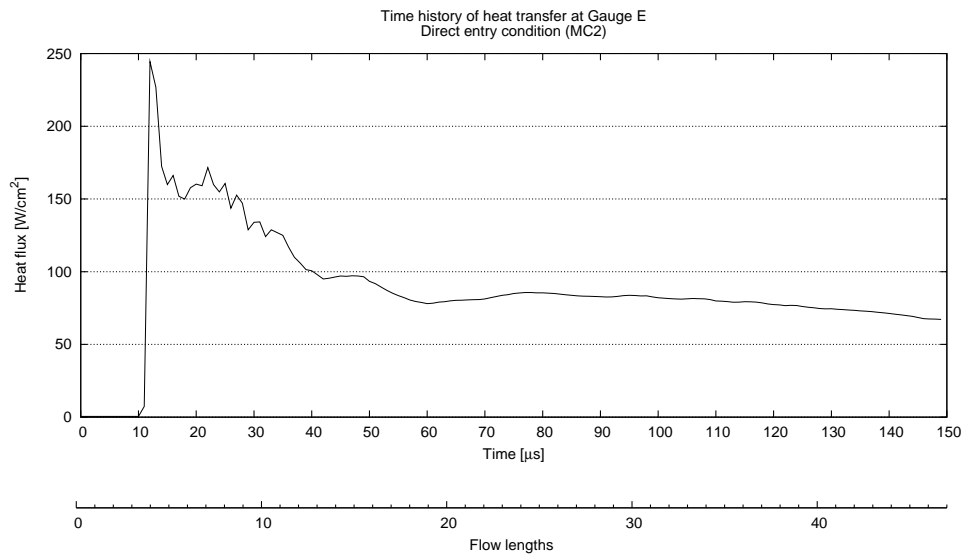


Figure C.14: Heat transfer time history for Gauge E for the direct entry condition (free stream velocity $U_\infty = 4,700$ m/s).

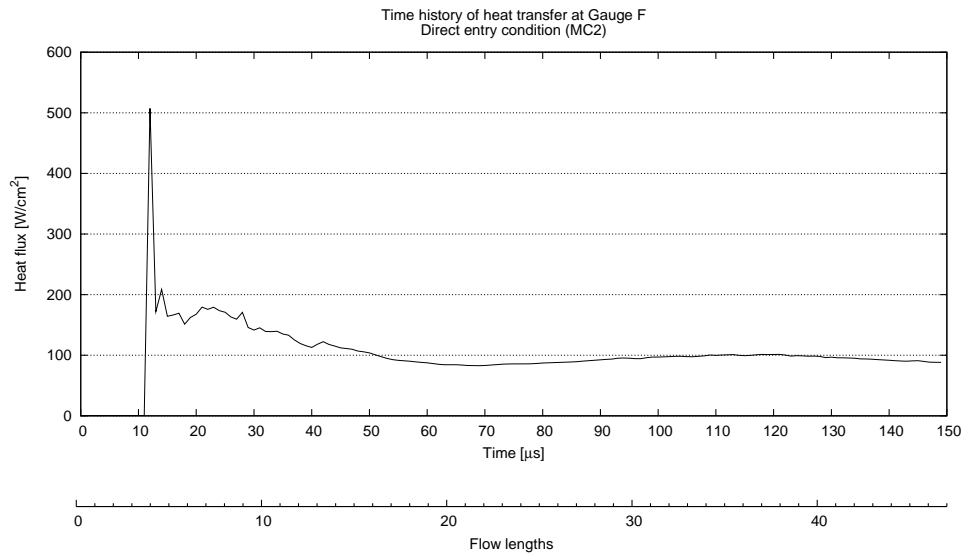


Figure C.15: Heat transfer time history for Gauge F for the direct entry condition (free stream velocity $U_{\infty} = 4,700$ m/s).

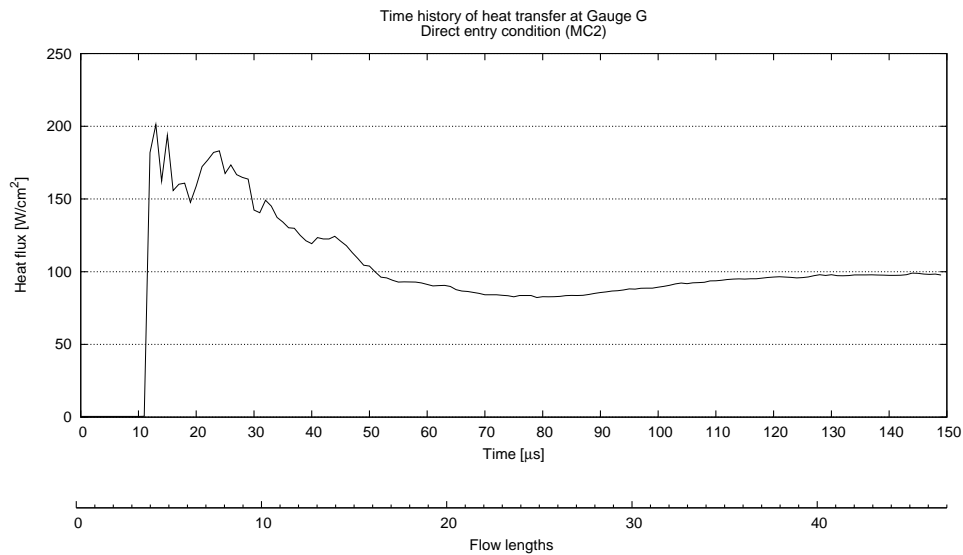


Figure C.16: Heat transfer time history for Gauge G for the direct entry condition (free stream velocity $U_{\infty} = 4,700$ m/s).

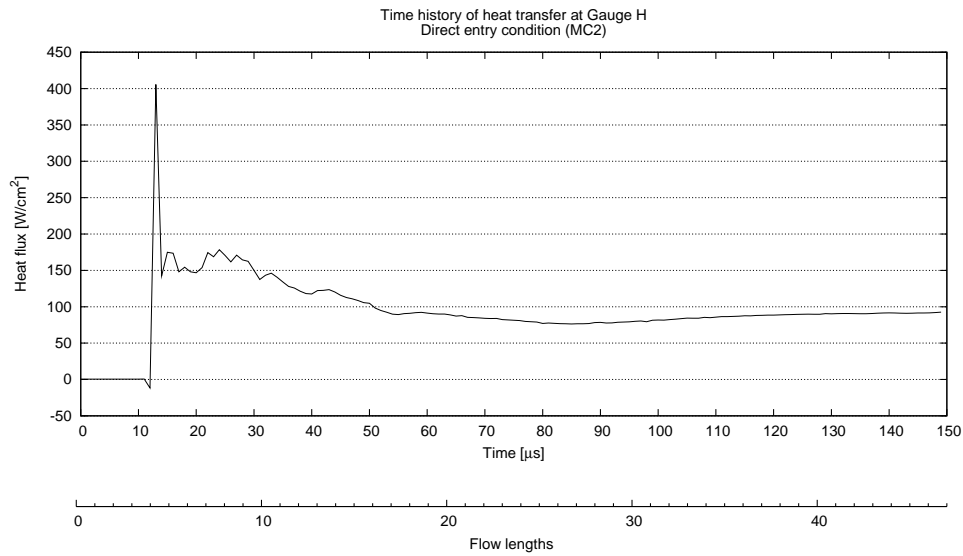


Figure C.17: Heat transfer time history for Gauge H for the direct entry condition (free stream velocity $U_{\infty} = 4,700$ m/s).

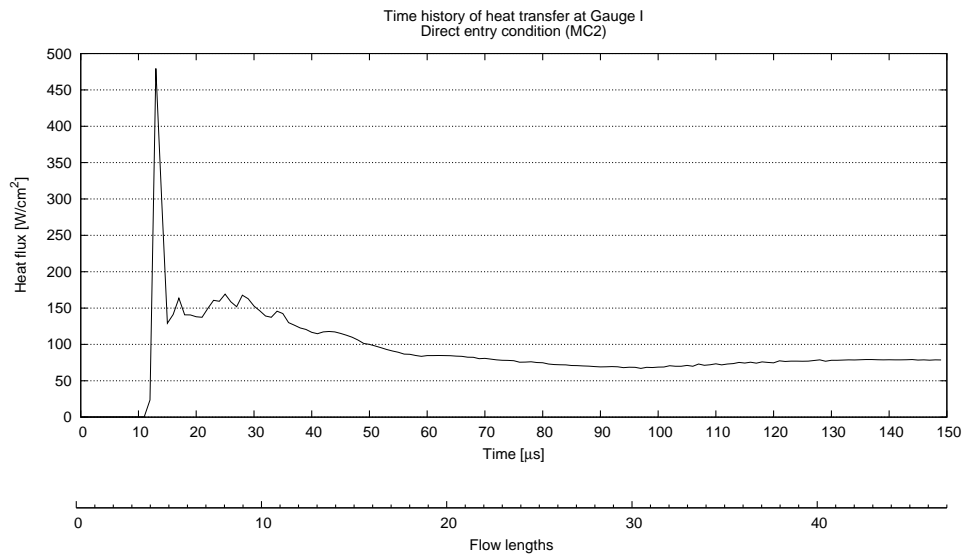


Figure C.18: Heat transfer time history for Gauge I for the direct entry condition (free stream velocity $U_{\infty} = 4,700$ m/s).

C.2 Instantaneous heat transfer plots along model sting

C.2.1 Low-speed aerocapture condition

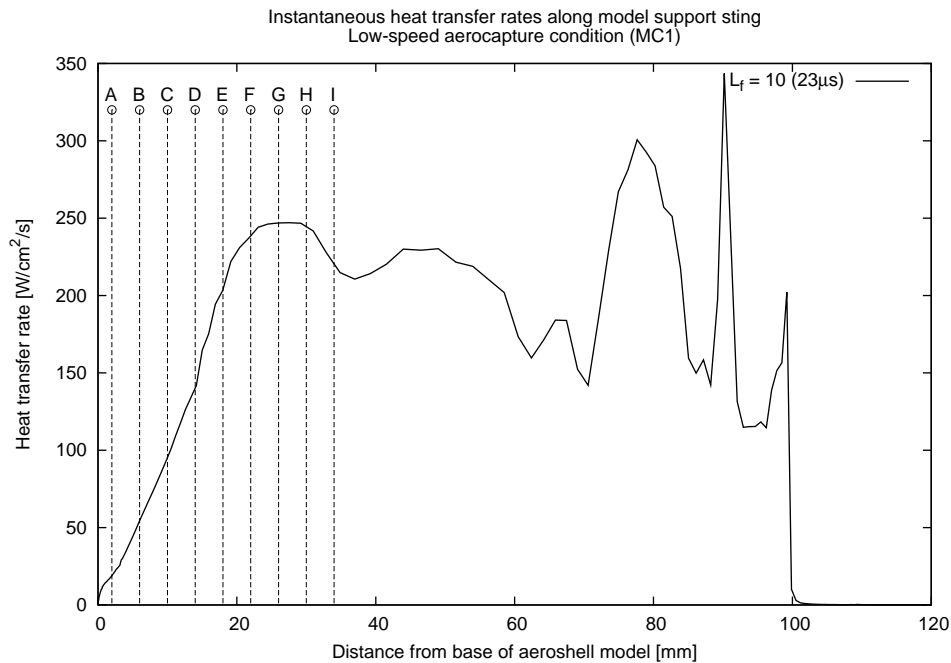


Figure C.19: Instantaneous heat transfer after 10 flow lengths for the low-speed aerocapture condition (free stream velocity $U_\infty = 6,500$ m/s).

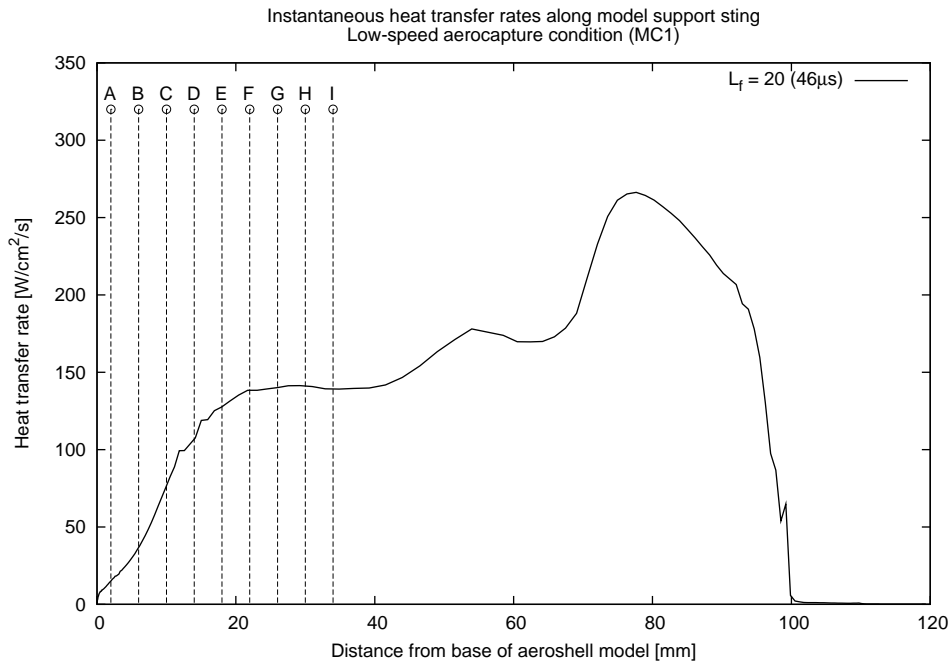


Figure C.20: Instantaneous heat transfer after 20 flow lengths for the low-speed aerocapture condition (free stream velocity $U_\infty = 6,500$ m/s).

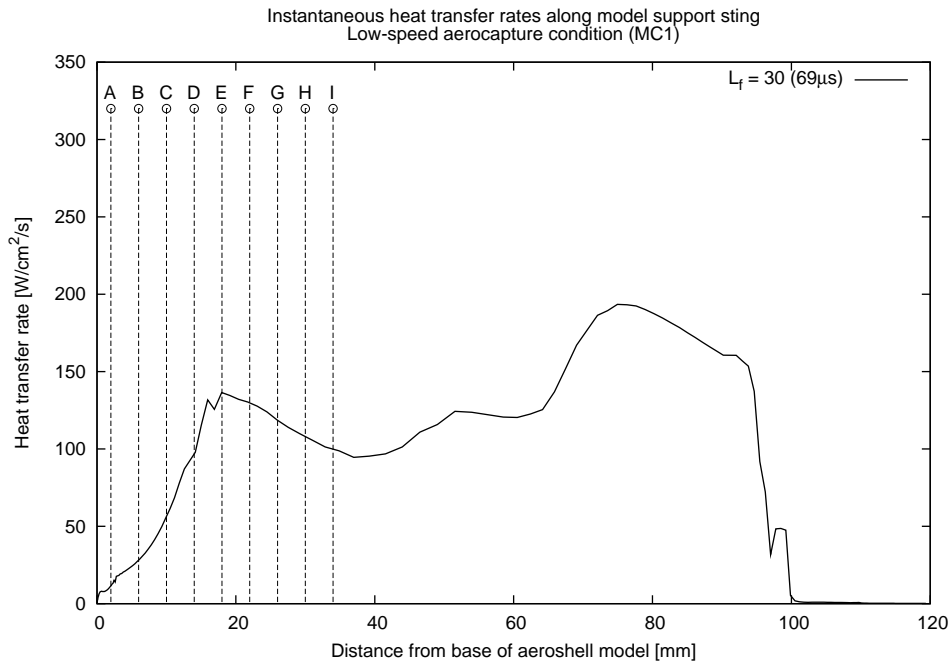


Figure C.21: Instantaneous heat transfer after 30 flow lengths for the low-speed aerocapture condition (free stream velocity $U_\infty = 6,500$ m/s).

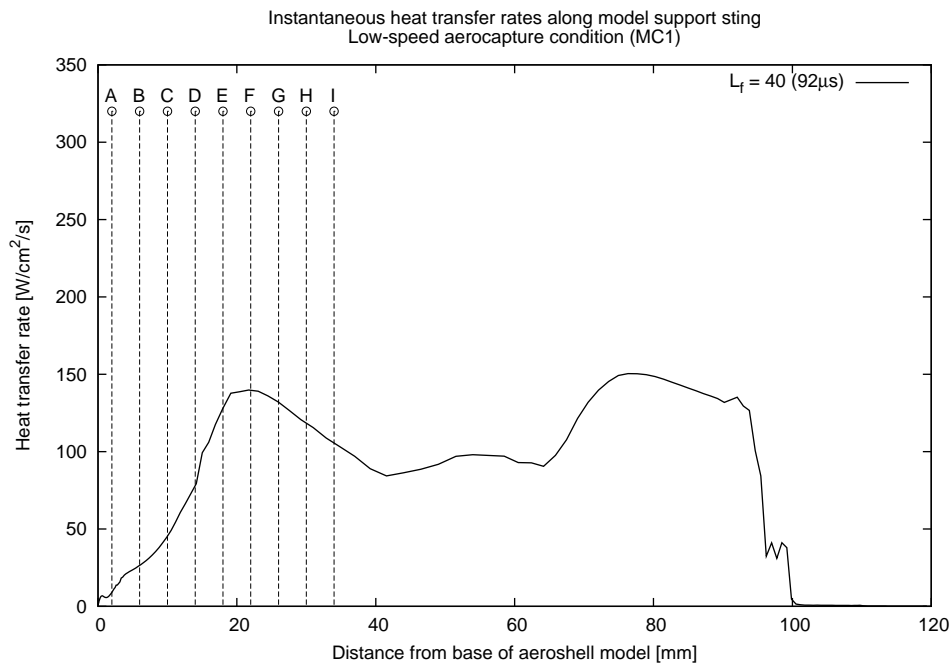


Figure C.22: Instantaneous heat transfer after 40 flow lengths for the low-speed aerocapture condition (free stream velocity $U_\infty = 6,500$ m/s).

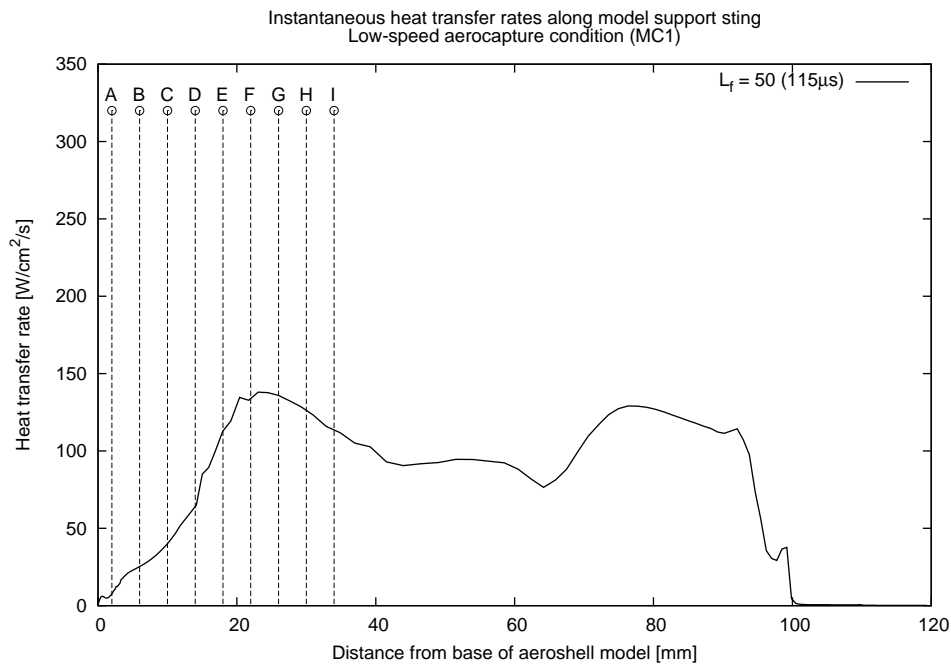


Figure C.23: Instantaneous heat transfer after 50 flow lengths for the low-speed aerocapture condition (free stream velocity $U_\infty = 6,500$ m/s).

C.2.2 Direct entry condition

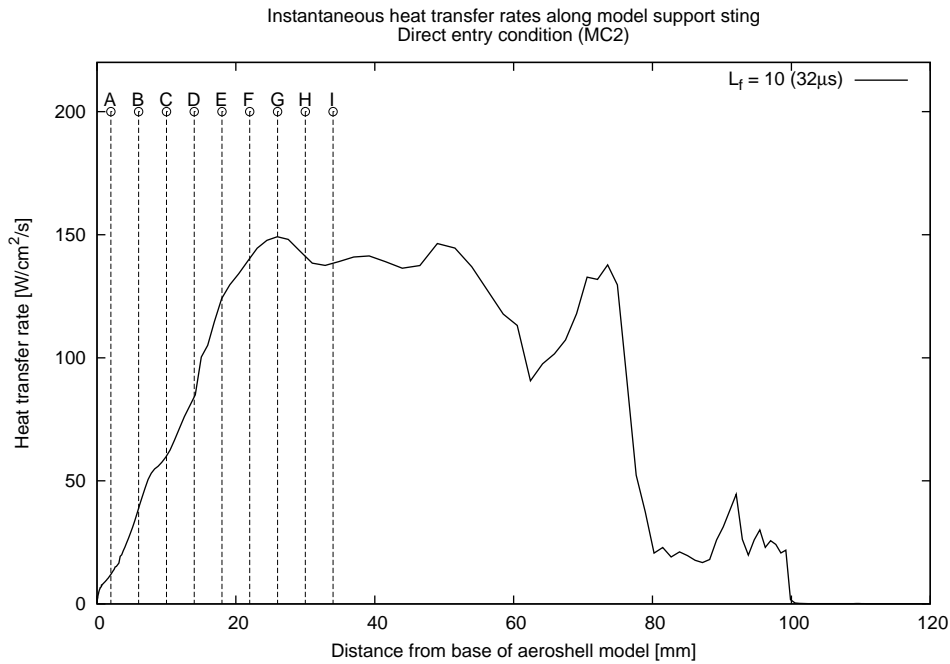


Figure C.24: Instantaneous heat transfer after 10 flow lengths for the direct entry condition (free stream velocity $U_\infty = 4,700$ m/s).

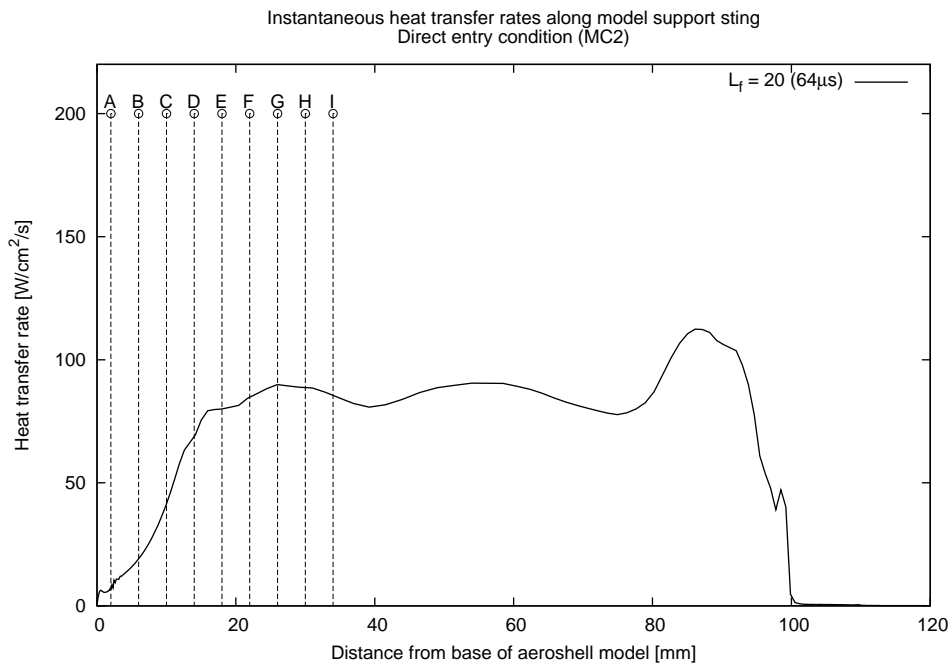


Figure C.25: Instantaneous heat transfer after 20 flow lengths for the direct entry condition (free stream velocity $U_\infty = 4,700$ m/s).

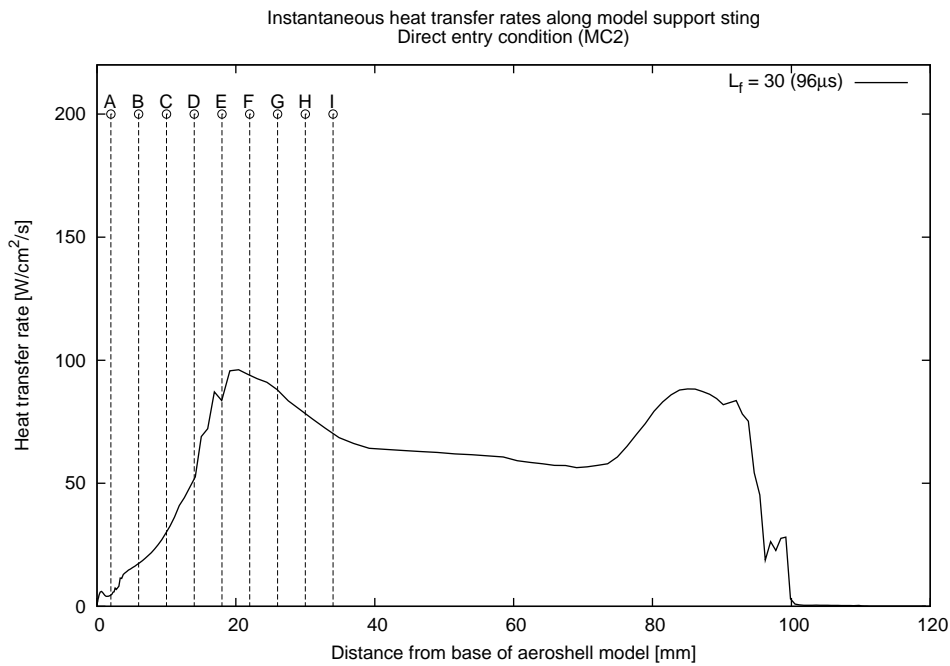


Figure C.26: Instantaneous heat transfer after 30 flow lengths for the direct entry condition (free stream velocity $U_\infty = 4,700$ m/s).

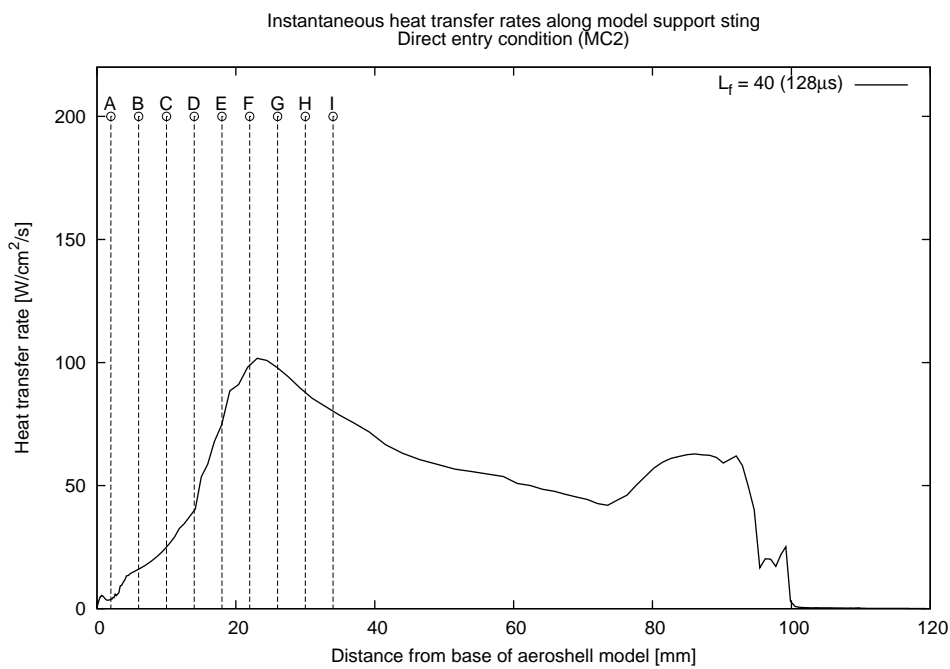


Figure C.27: Instantaneous heat transfer after 40 flow lengths for the direct entry condition (free stream velocity $U_\infty = 4,700$ m/s).

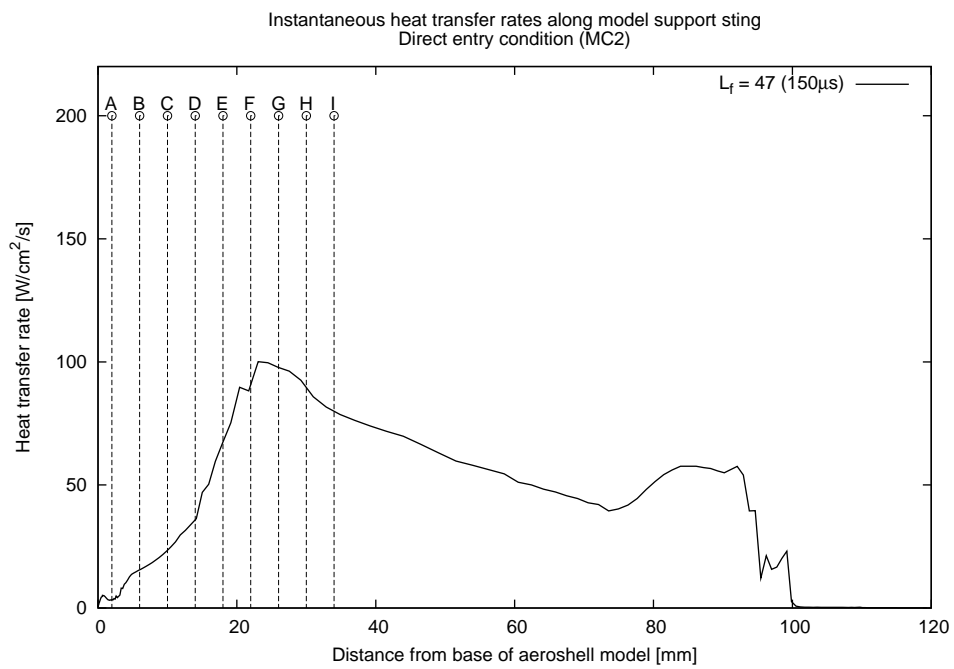


Figure C.28: Instantaneous heat transfer after 50 flow lengths for the direct entry condition (free stream velocity $U_\infty = 4,700$ m/s).

APPENDIX **D**

Model Schematics

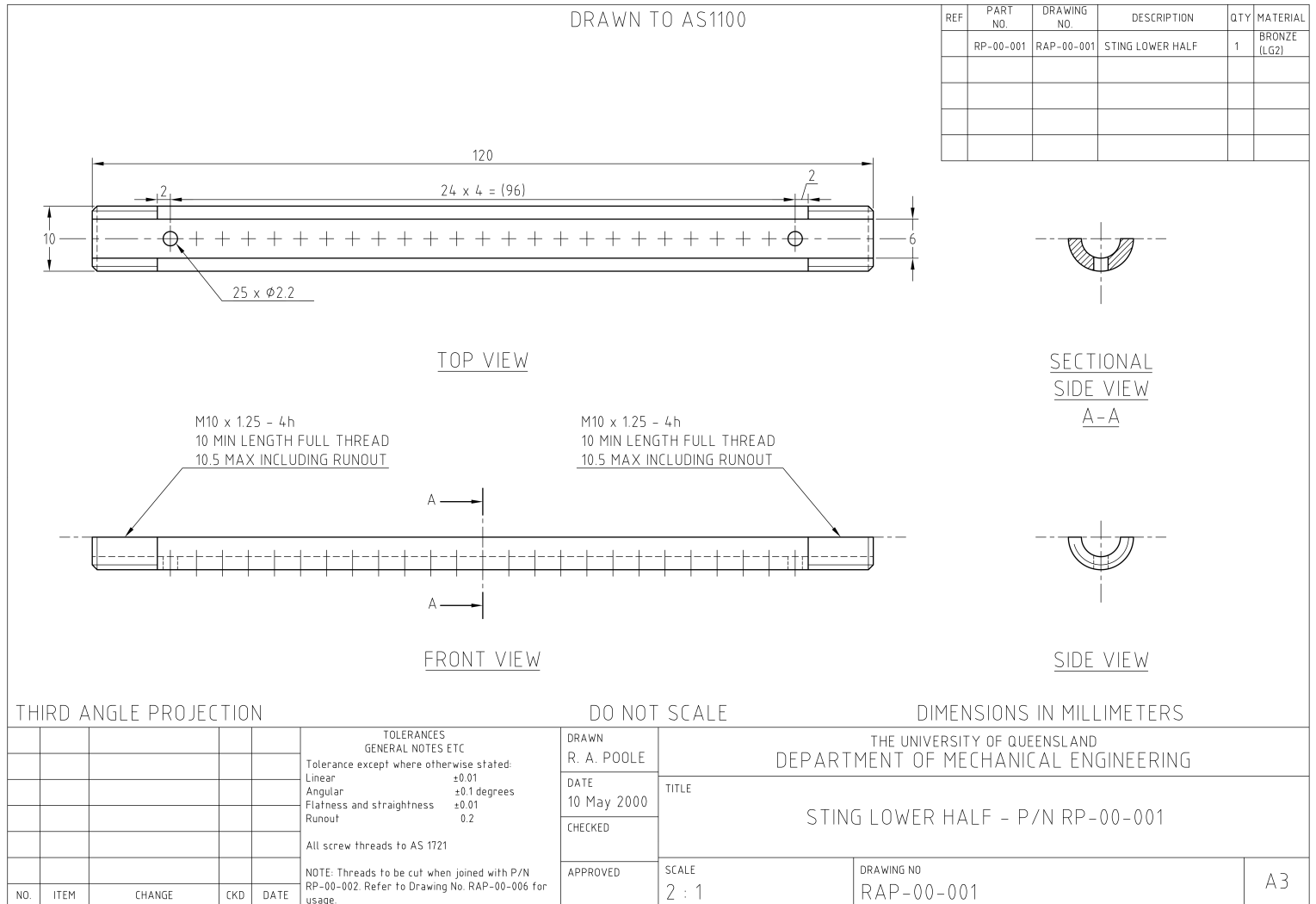


Figure D.1: Sting Lower Half.

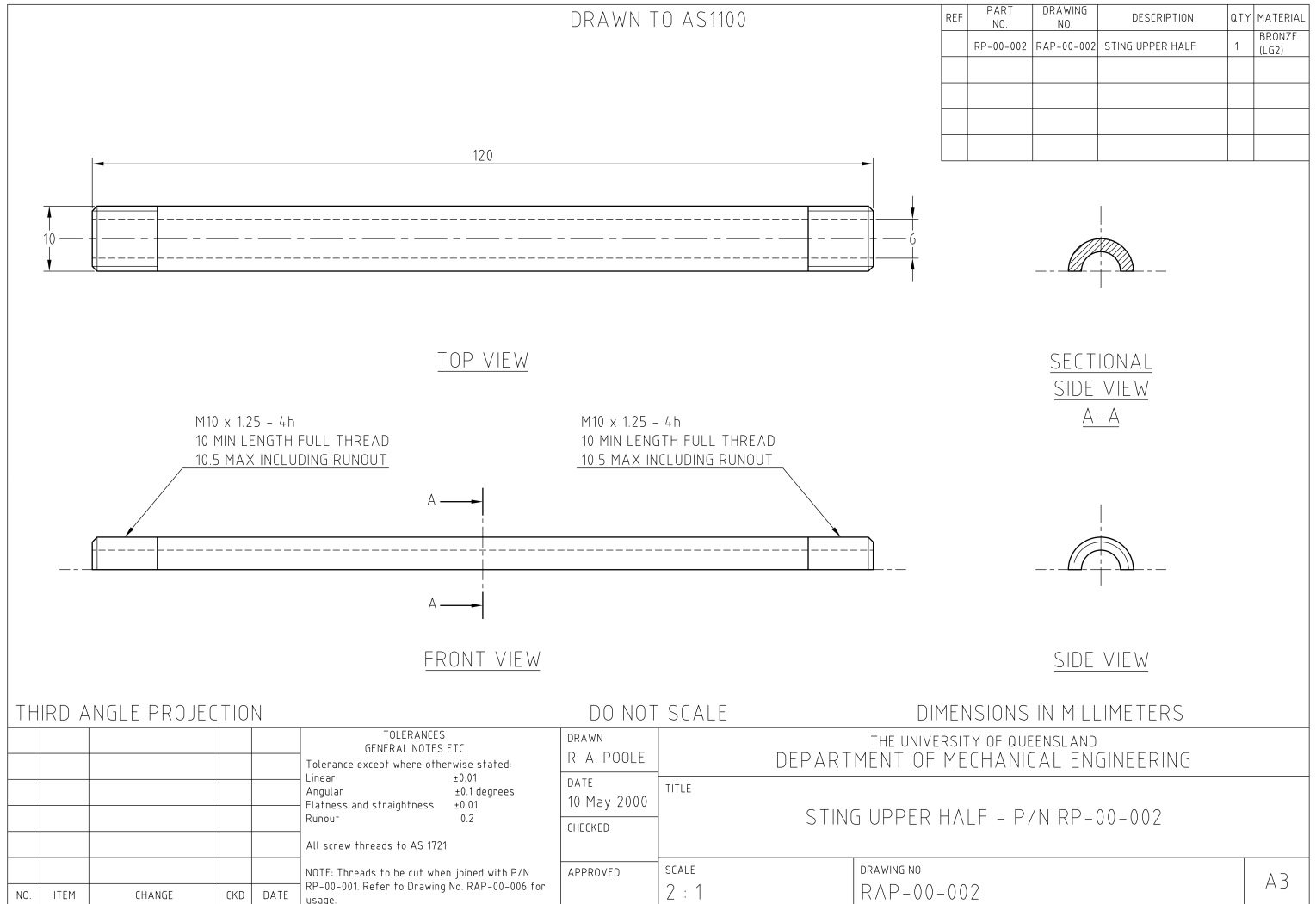


Figure D.2: Sting Upper Half.

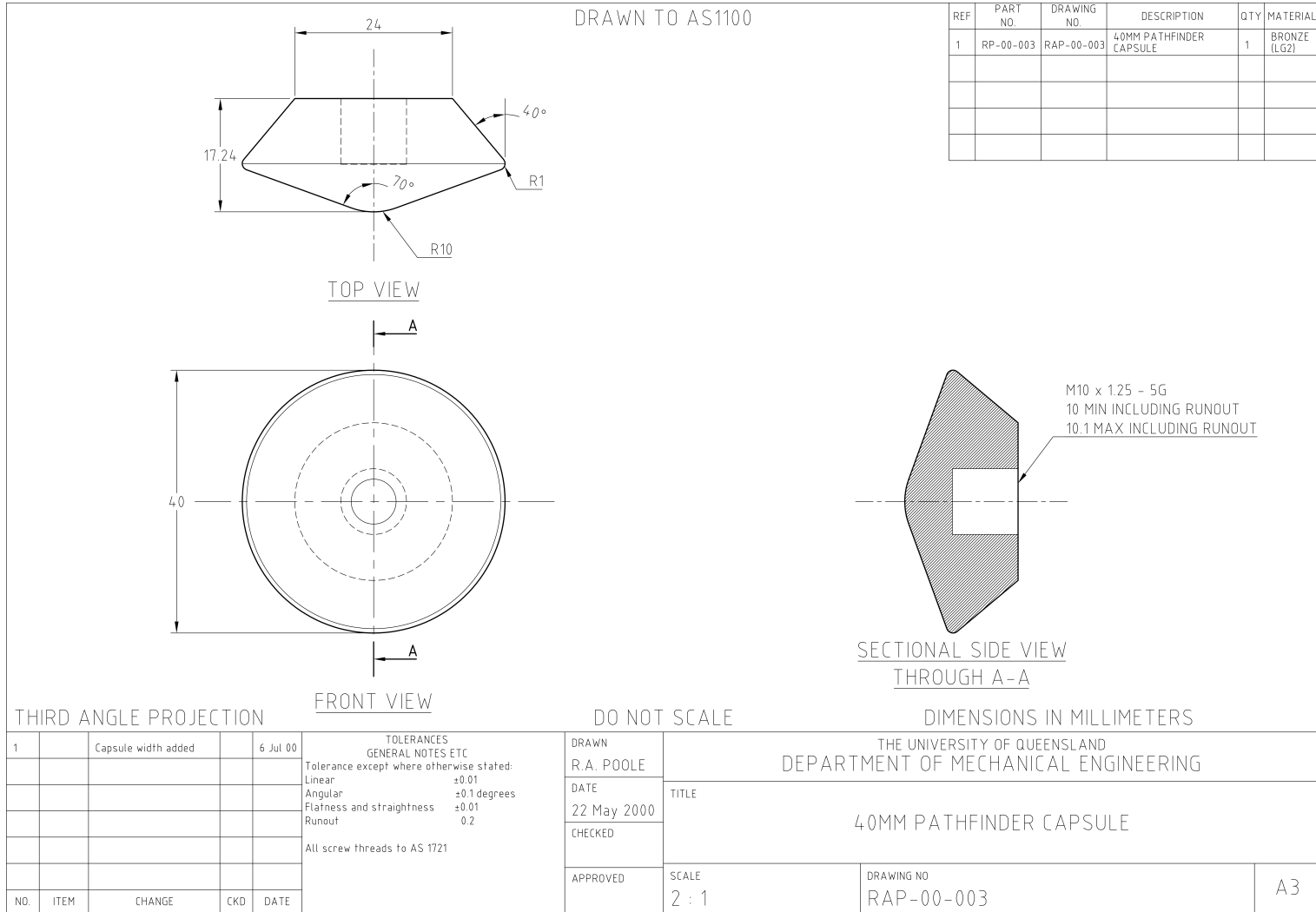


Figure D.3: 40mm Pathfinder Capsule.

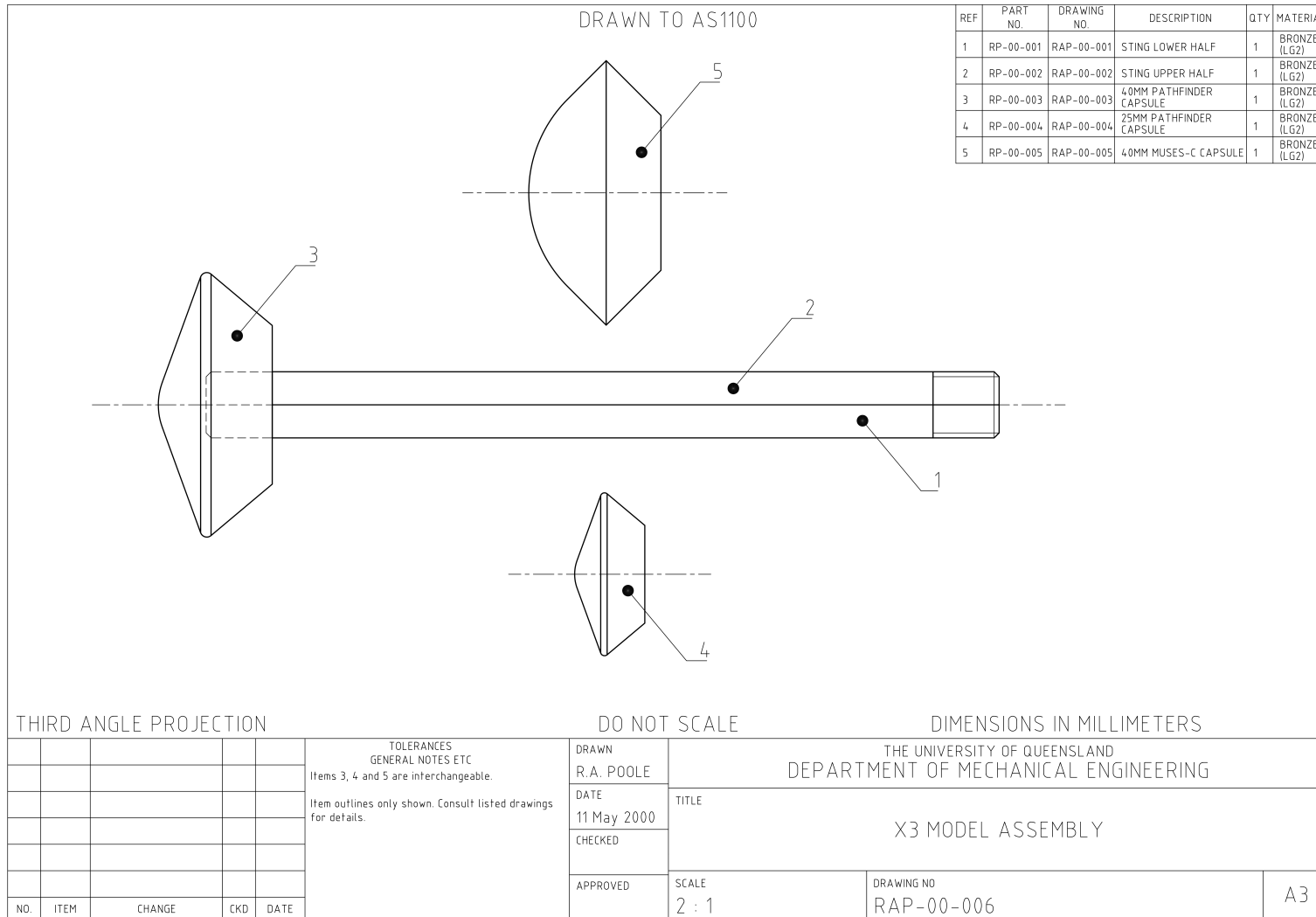


Figure D.4: Model assembly.

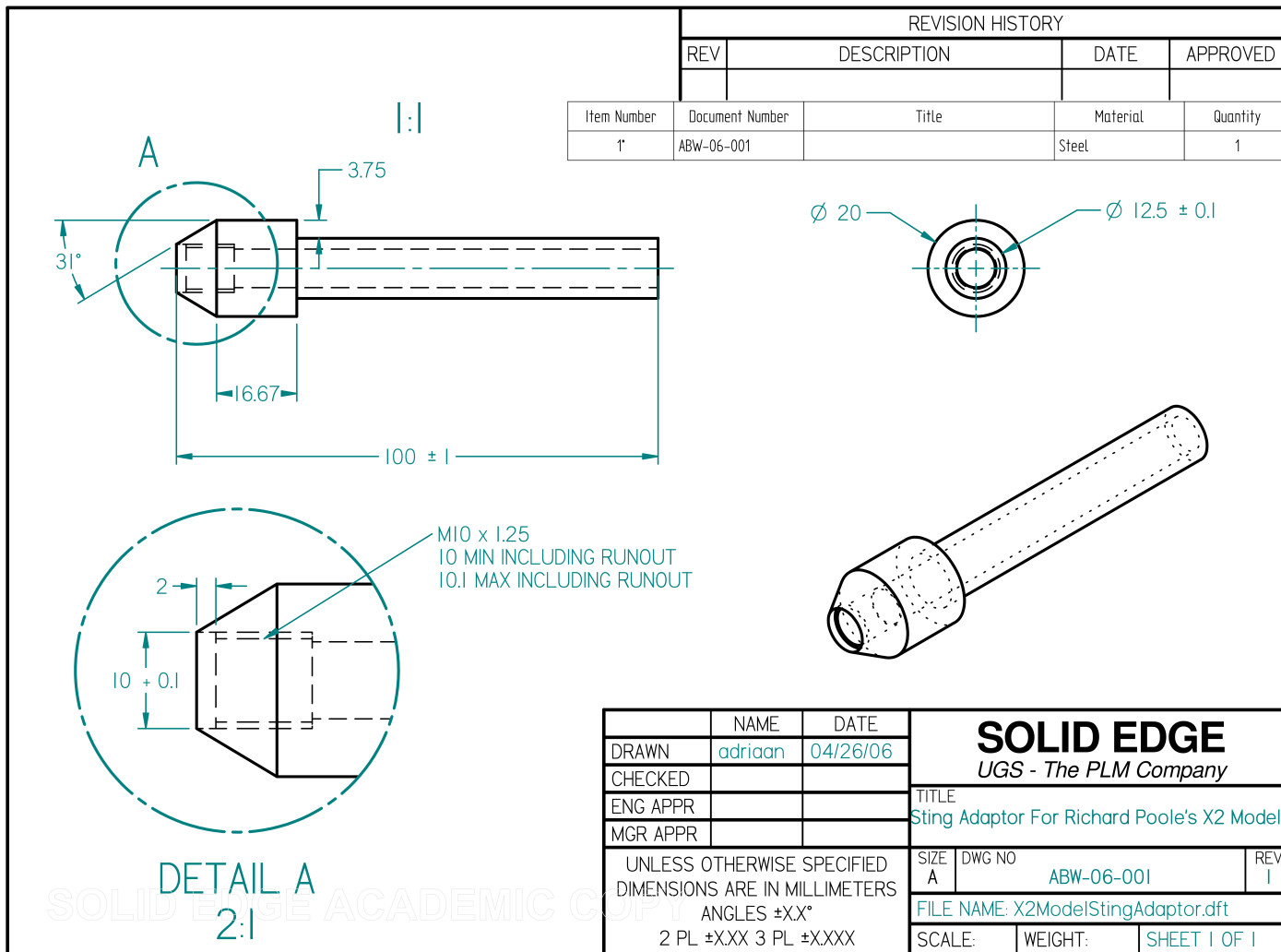


Figure D.5: Sting adaptor mount piece.

Gauge Calibration

E.1 Calibration Oven Settings

**START

Surname : WINDOW

Firstname : ADRIAAN

Phone Number :

Room Number :

Users Directory : \OVENUSER\WINDOW

Start Command For This User: WINDOW

Maximum Oven Temp. (minimum limit) : 35 Degrees

User Set Maximum Oven Temperature : 100 Degrees

Pre Set Oven Warm-Up Temperature : 30 Degrees

Duration Of Oven Warm-Up : 30 Minutes

Temperature Span Of Test : 70 Degrees

User Set Step Increment Temperature : 10 Degrees

User Set Increment Duration : 120 Minutes

Number Of Increment Steps : 7

Number Of Scans logged Each Step : 24

Number Of Increment Points Logged : 169

Number Of Inc. Step Points Averaged : 1 Point(s) / Step

User Set Step Decrement Temperature : 10 Degrees
User Set Decrement Duration : 120 Minutes
Number Of Decrement Steps : 6
Number Of Scans logged Each Step : 24
Number Of Decrement Points Logged : 144
Number Of Dec. Step Points Averaged : 1 Point(s) / Step

Total Number Of Data Lines Logged : 313

* TEST DURATION + OVEN WARM UP TIME *

Days : 1
Hours : 2
Minutes: 35

DATATAKER Averaging Every : 2 Seconds
Scanned DATATAKER Data Returns Every : 5 Minutes

Return Time Marker In Data String : OPTION INSTALLED
Report DATATAKER Errors To Screen : REPORT ERRORS
Build Printouts At End Of Test : NOT ENABELED
Shutdown Of System On Completion : NOT ENABELED
Delay 10 Second Then Backup : OPTION ENABELED
Record Up To 1000 DATAFILE.DAT(s) : NOT ENABELED

DATATAKER Pokes String : P34=23 P35=18 P22=44

DATATAKER Channel 1 : RESISTANCE
DATATAKER Channel 2 : RESISTANCE
DATATAKER Channel 3 : RESISTANCE
DATATAKER Channel 4 : RESISTANCE
DATATAKER Channel 5 : RESISTANCE

DATATAKER Channel 6 : RESISTANCE
DATATAKER Channel 7 : RESISTANCE
DATATAKER Channel 8 : RESISTANCE
DATATAKER Channel 9 : RESISTANCE
DATATAKER Channel 10 : RESISTANCE
DATATAKER Channel 11 : RESISTANCE
DATATAKER Channel 12 : RESISTANCE
DATATAKER Channel 13 : TK THERMOCOUPLE
DATATAKER Channel 14 : UNUSED
DATATAKER Channel 15 : UNUSED
DATATAKER Channel 16 : UNUSED
DATATAKER Channel 17 : UNUSED
DATATAKER Channel 18 : UNUSED
DATATAKER Channel 19 : UNUSED
DATATAKER Channel 20 : UNUSED
DATATAKER Channel 21 : UNUSED
DATATAKER Channel 22 : UNUSED
DATATAKER Channel 23 : UNUSED

--DATATAKER SWITCH STRING--

/a /C /d /E /f /g /K /l /M /n /o /p /R /S /t /u /x /z

* Refer To DATAKER Manual Before Altering This String *

**END

E.2 Calibration Data - Before model installation

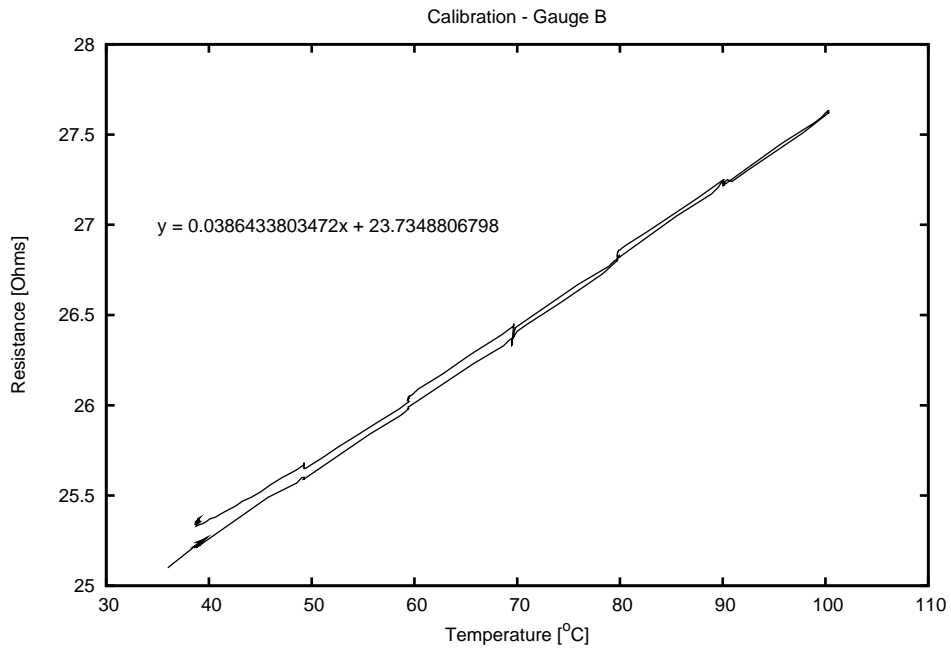


Figure E.1: Gauge B - Resistance as a function of temperature.

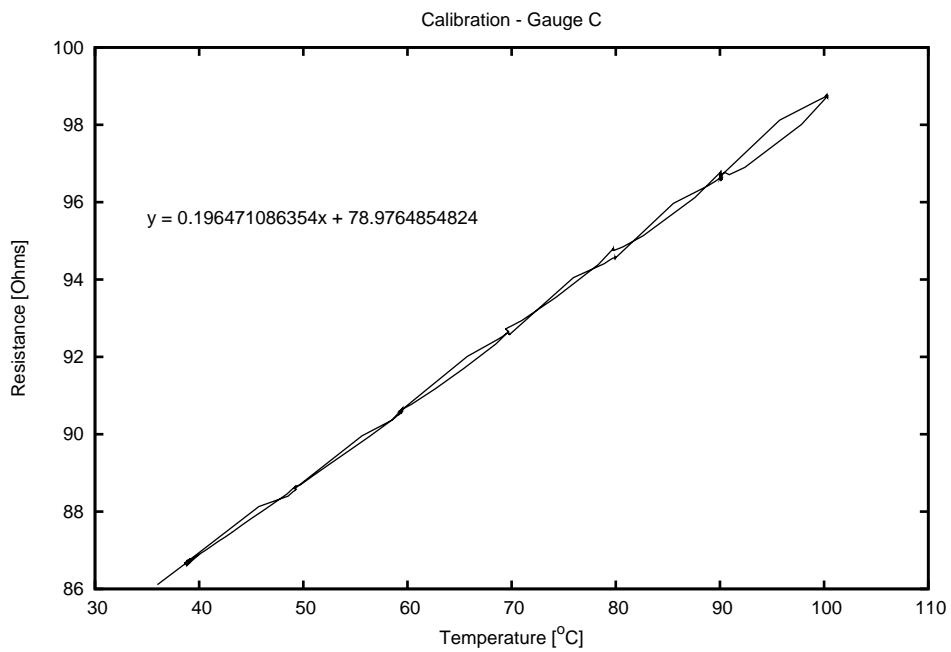


Figure E.2: Gauge C - Resistance as a function of temperature.

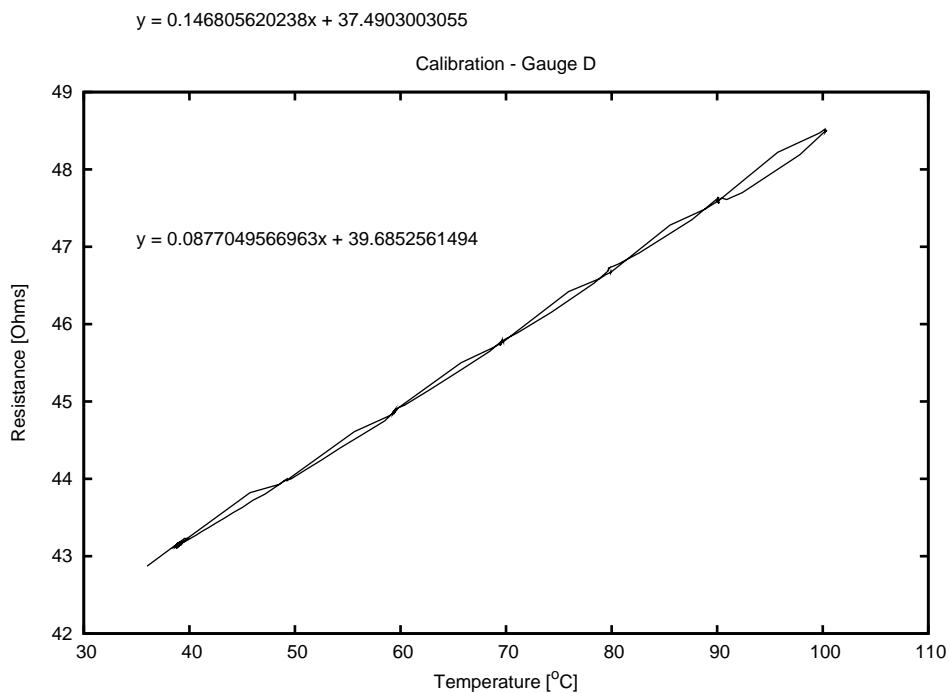


Figure E.3: Gauge D - Resistance as a function of temperature.

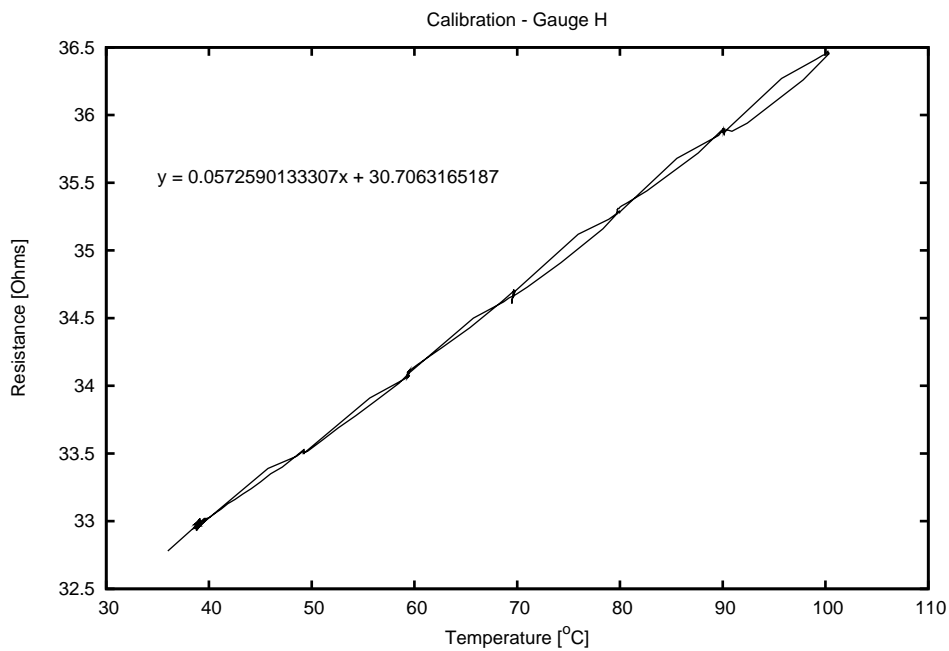


Figure E.4: Gauge H - Resistance as a function of temperature.

$y = 0.0386433803472x + 23.7348806798$

E.3 Calibration Data - After model installation

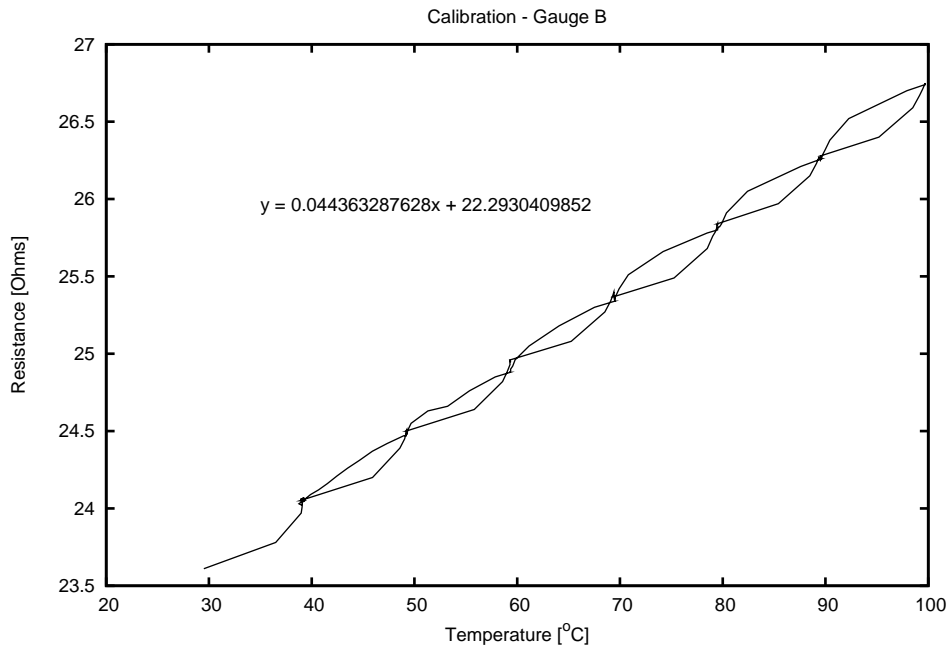


Figure E.5: Gauge B - Resistance as a function of temperature.

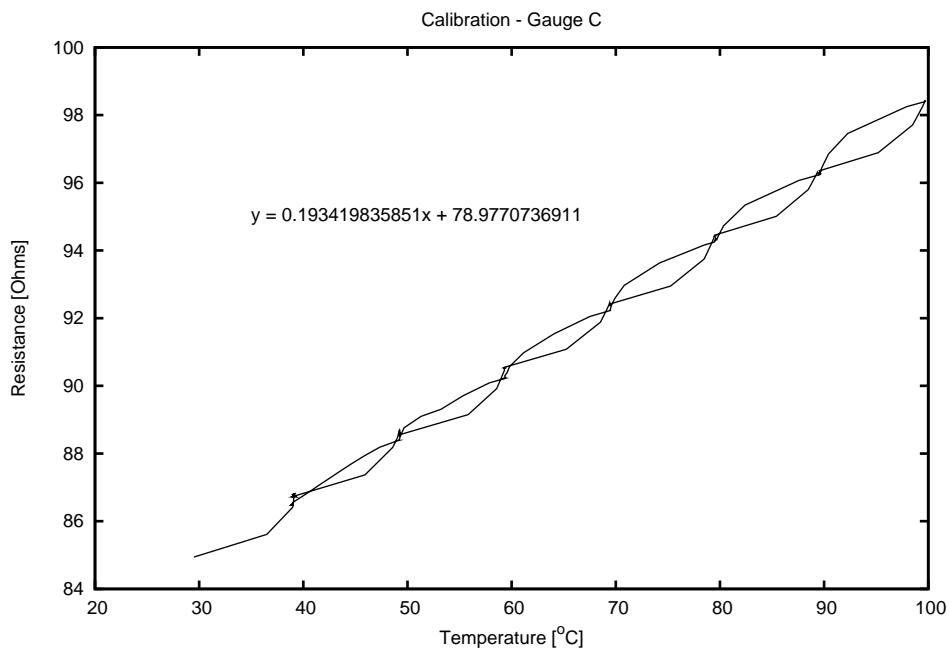


Figure E.6: Gauge C - Resistance as a function of temperature.

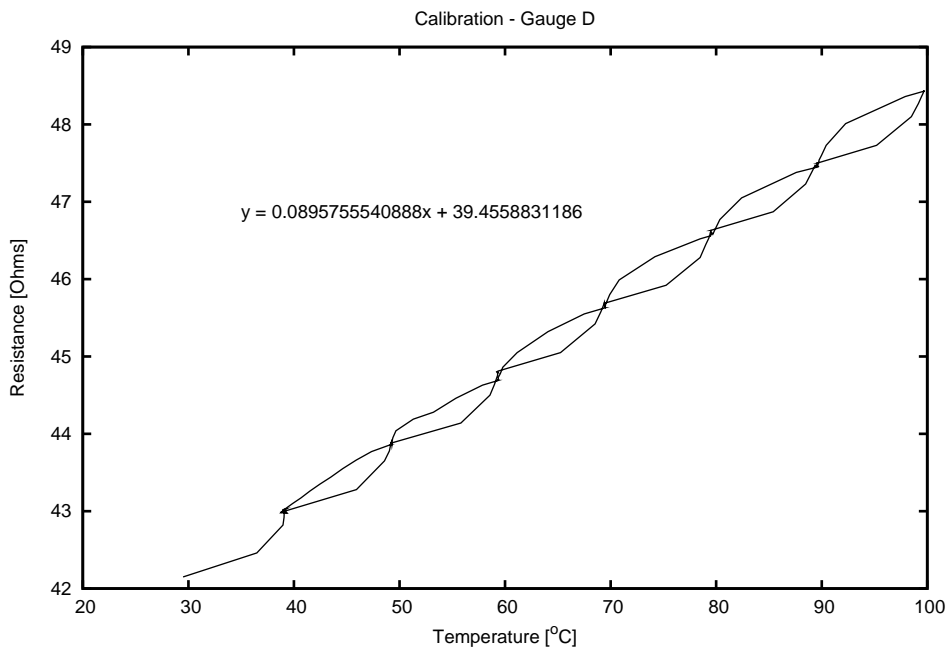


Figure E.7: Gauge D - Resistance as a function of temperature.

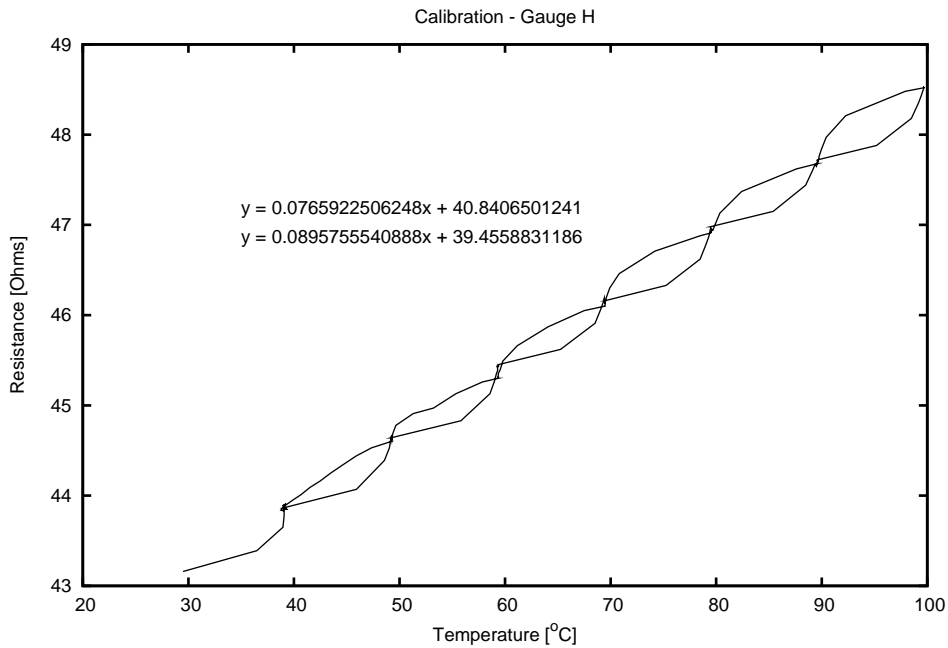


Figure E.8: Gauge H - Resistance as a function of temperature.

$y = 0.044363287628x + 22.2930409852$

APPENDIX **F**

Experimental Data

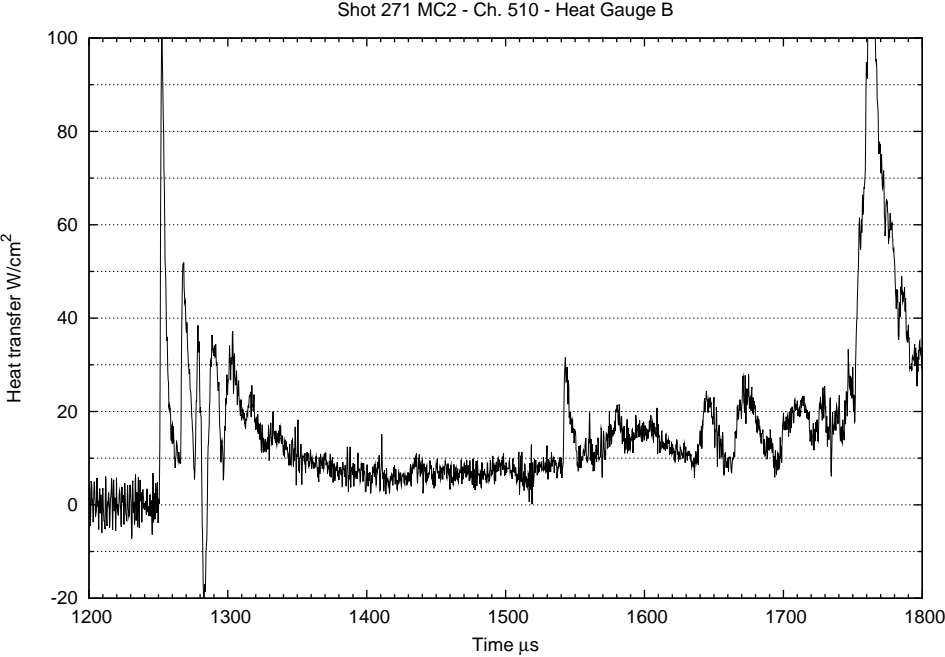


Figure F.1: Shot 271 heat gauge B data trace.

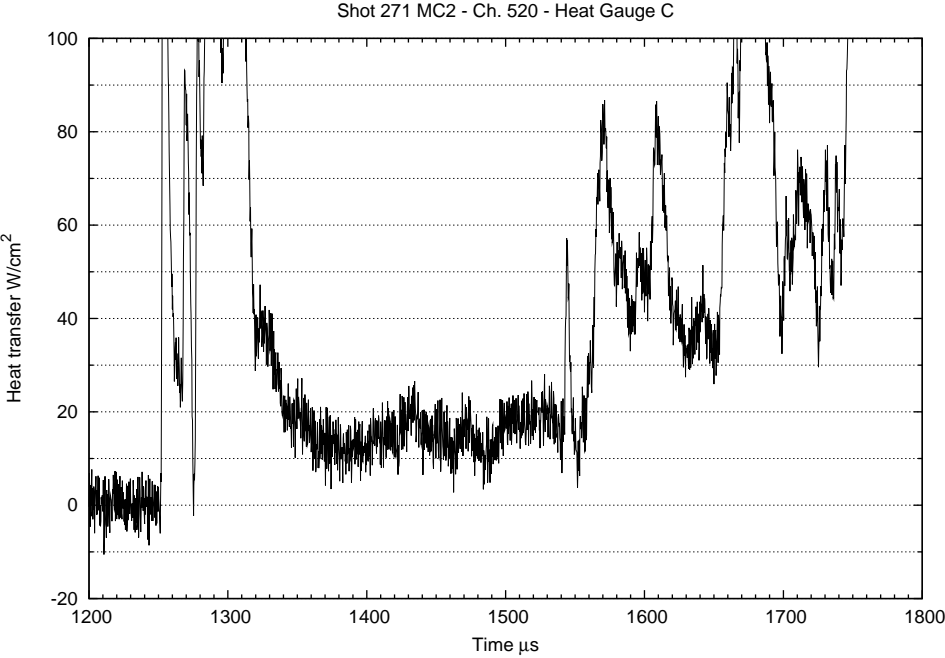


Figure F.2: Shot 271 heat gauge C data trace.

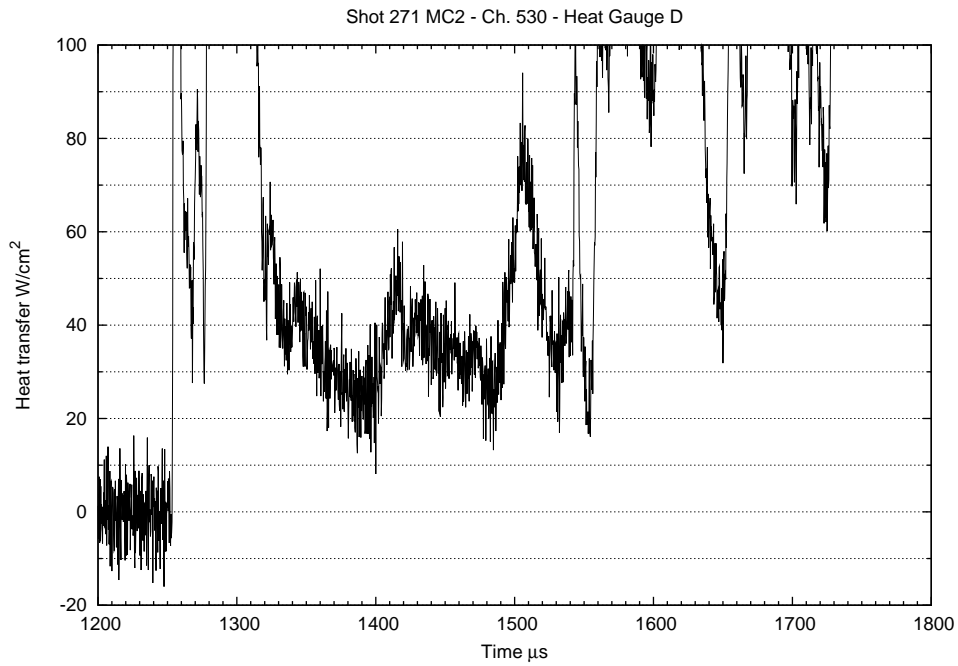


Figure F.3: Shot 271 heat gauge D data trace.

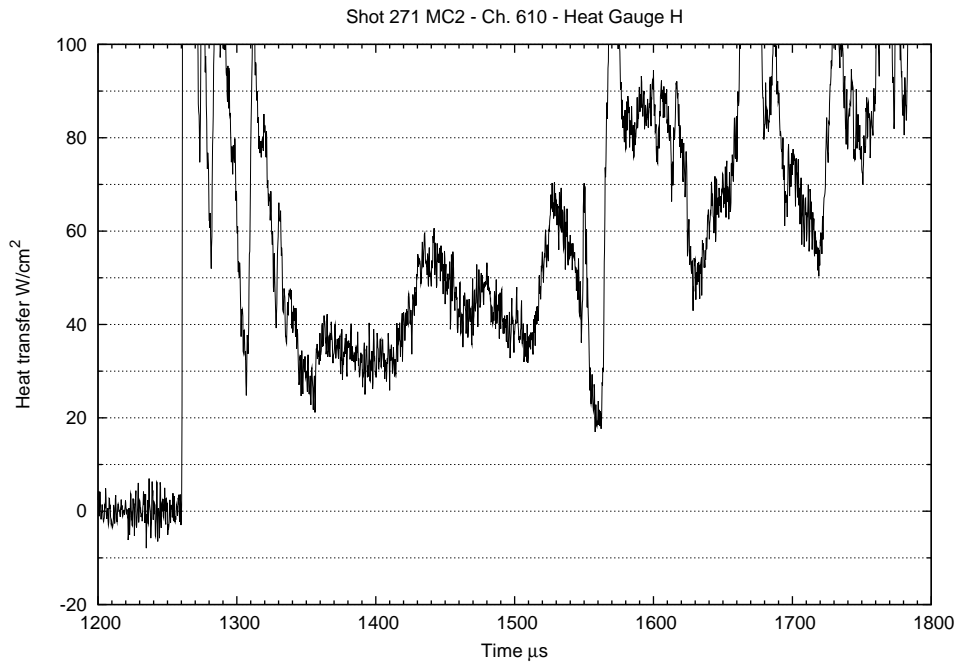


Figure F.4: Shot 271 heat gauge H data trace.

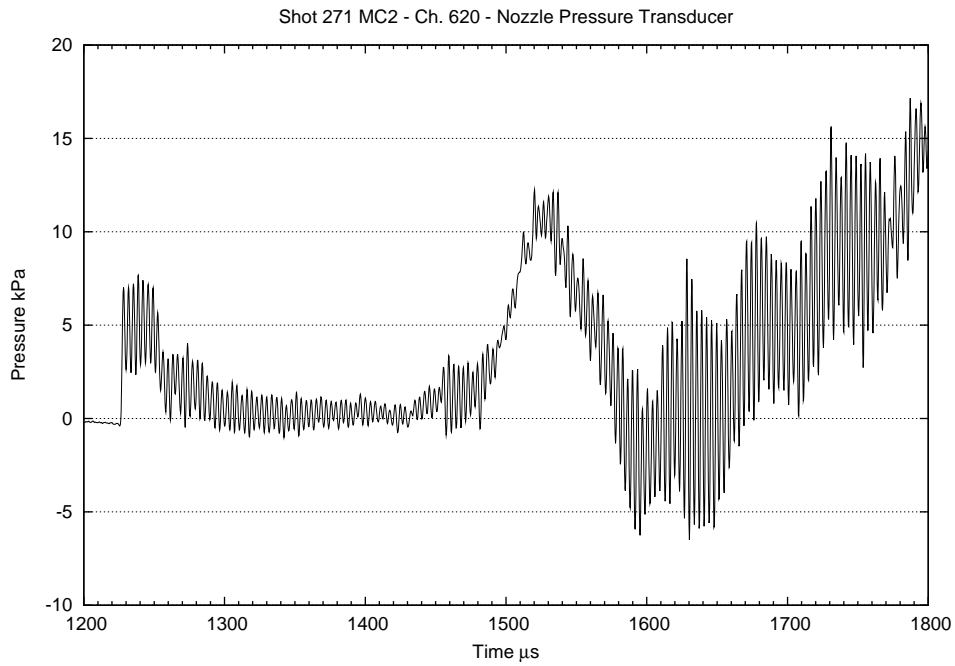


Figure F.5: Shot 271 nozzle pressure transducer data trace.

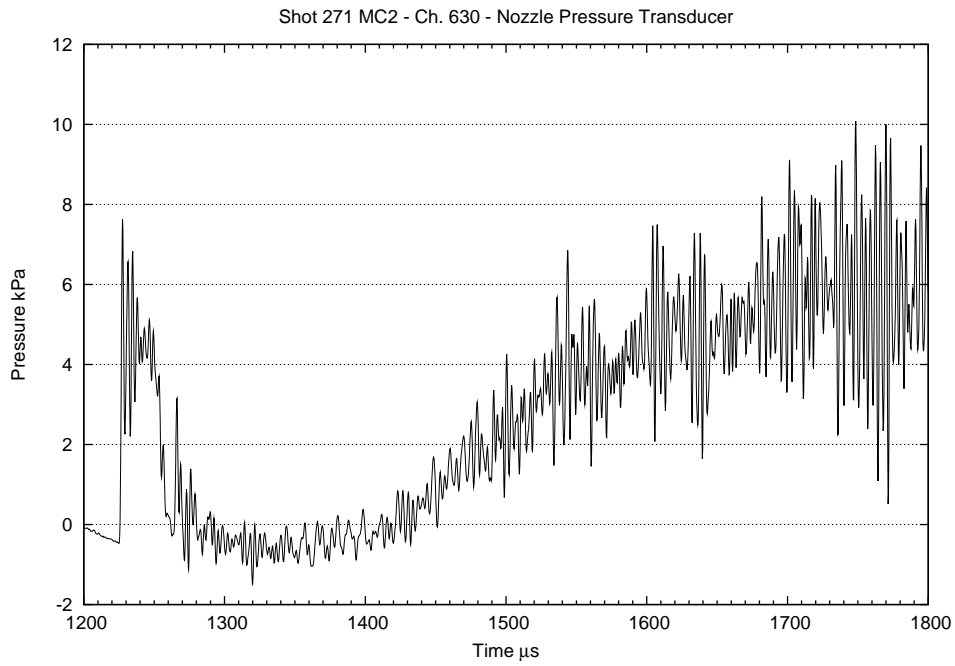


Figure F.6: Shot 271 nozzle pressure transducer data trace.

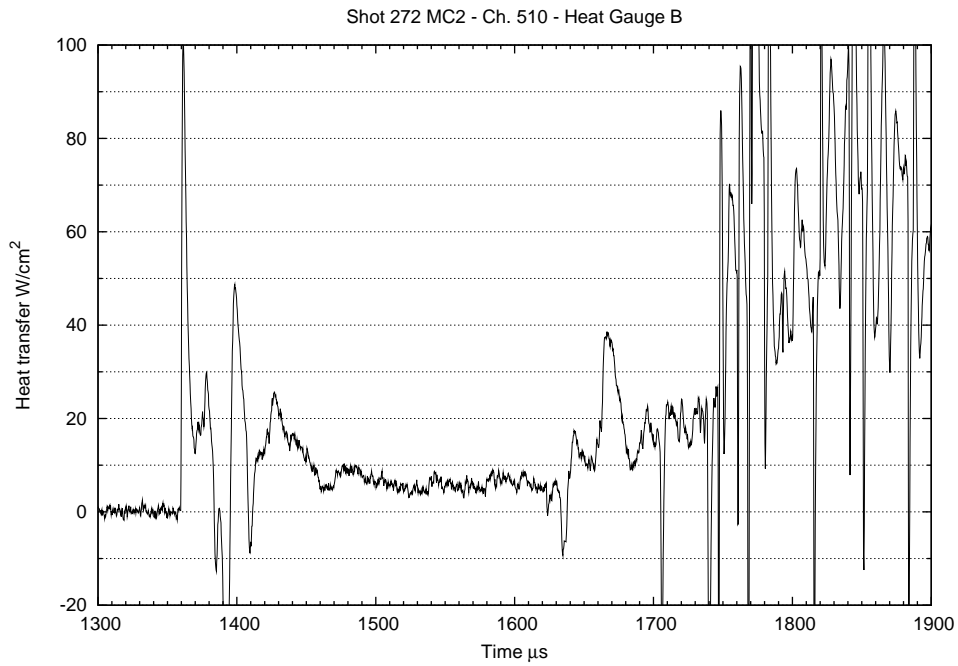


Figure F.7: Shot 272 heat gauge B data trace.

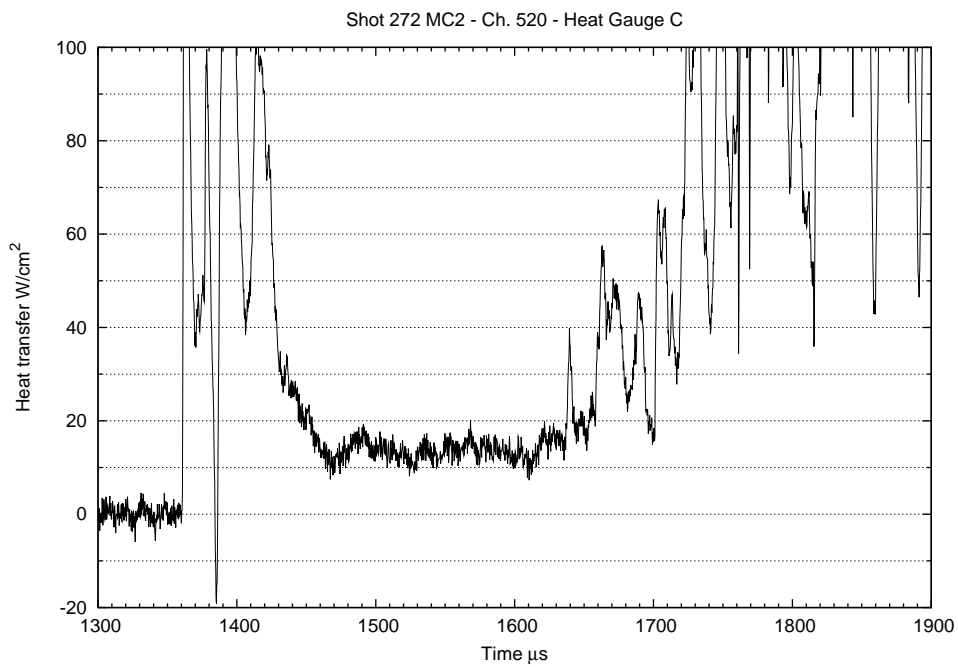


Figure F.8: Shot 272 heat gauge C data trace.

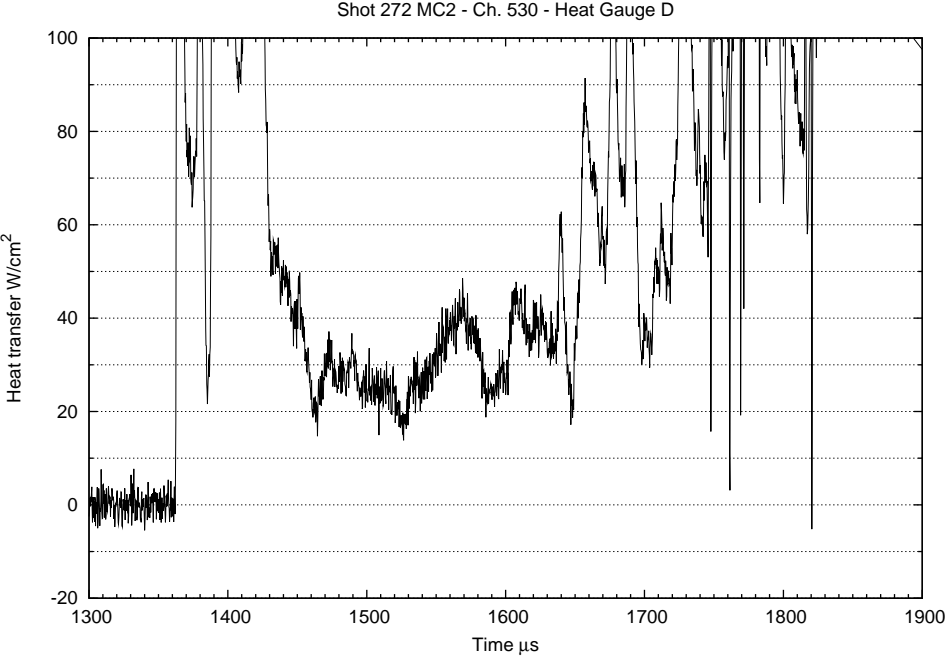


Figure F.9: Shot 272 heat gauge D data trace.

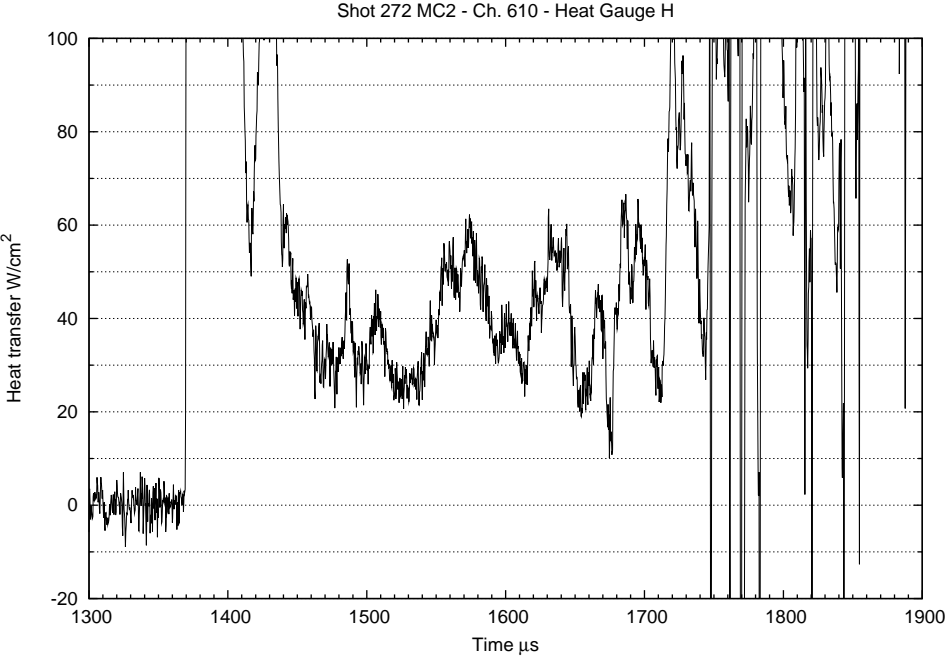


Figure F.10: Shot 272 heat gauge H data trace.

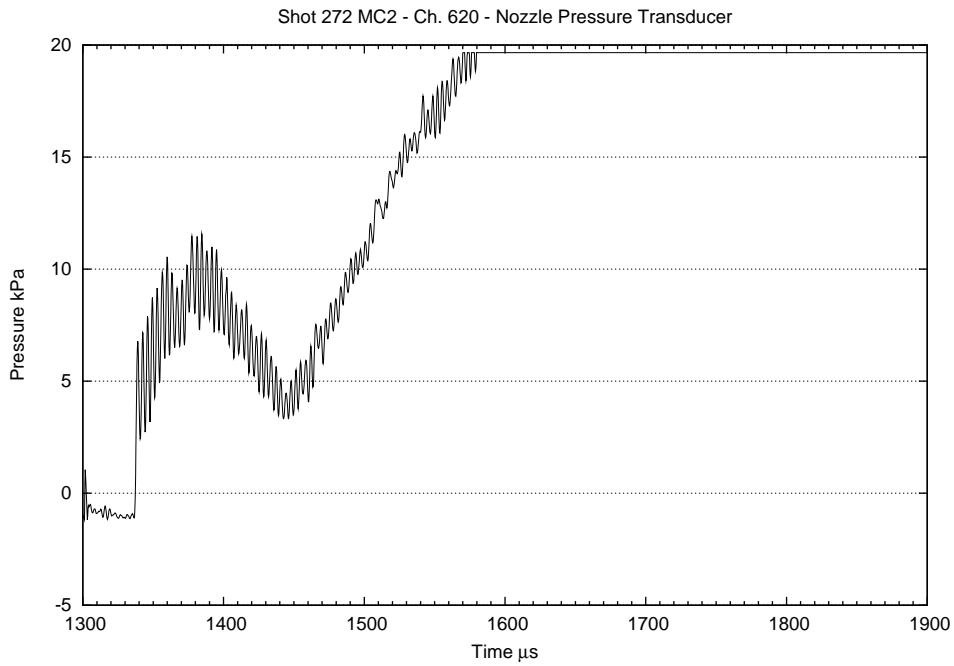


Figure F.11: Shot 272 nozzle pressure transducer data trace.

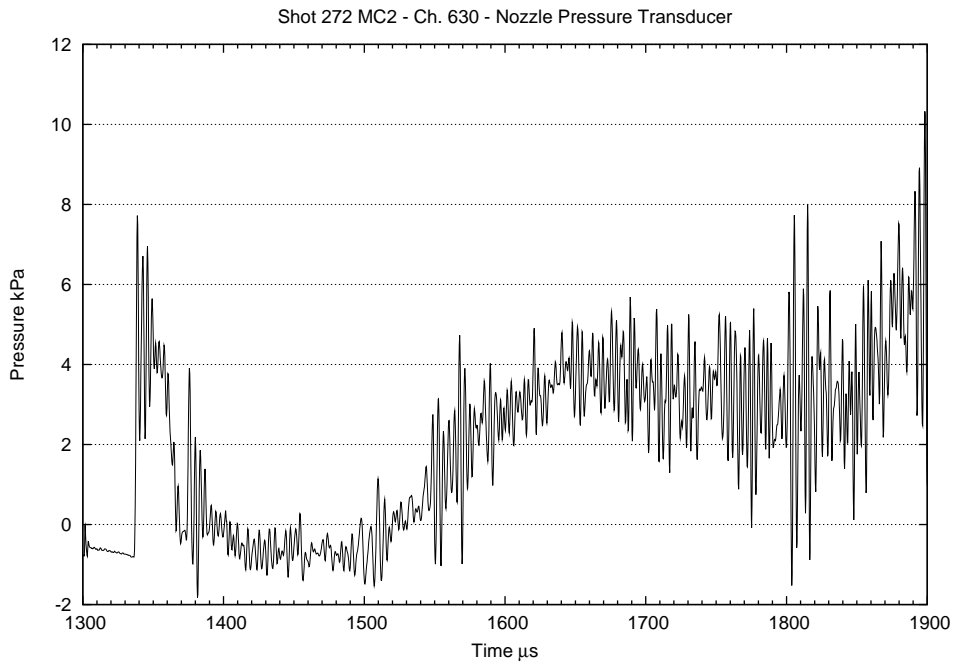


Figure F.12: Shot 272 nozzle pressure transducer data trace.

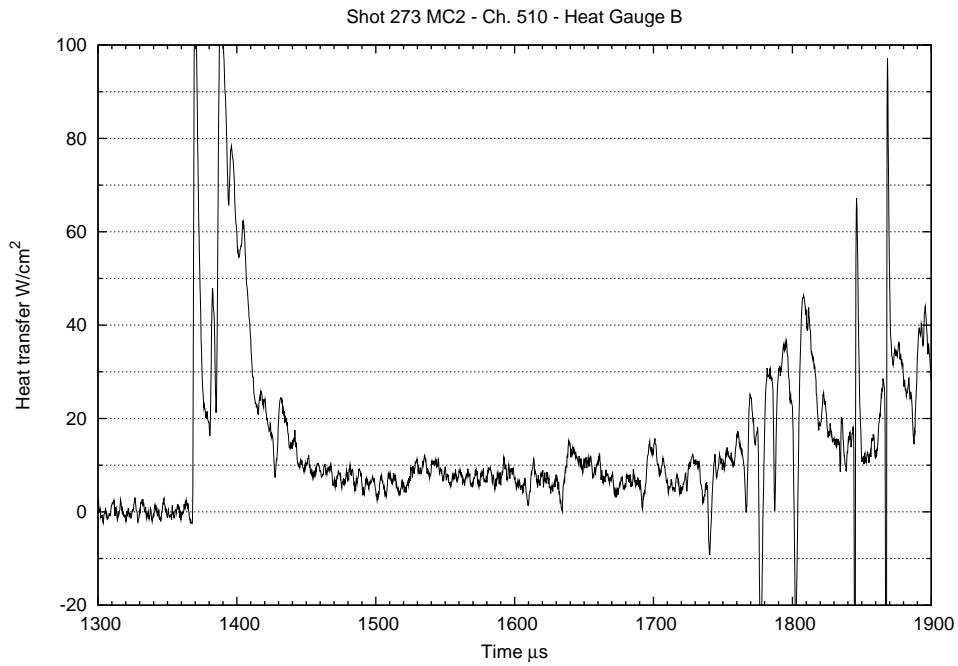


Figure F.13: Shot 273 heat gauge B data trace.

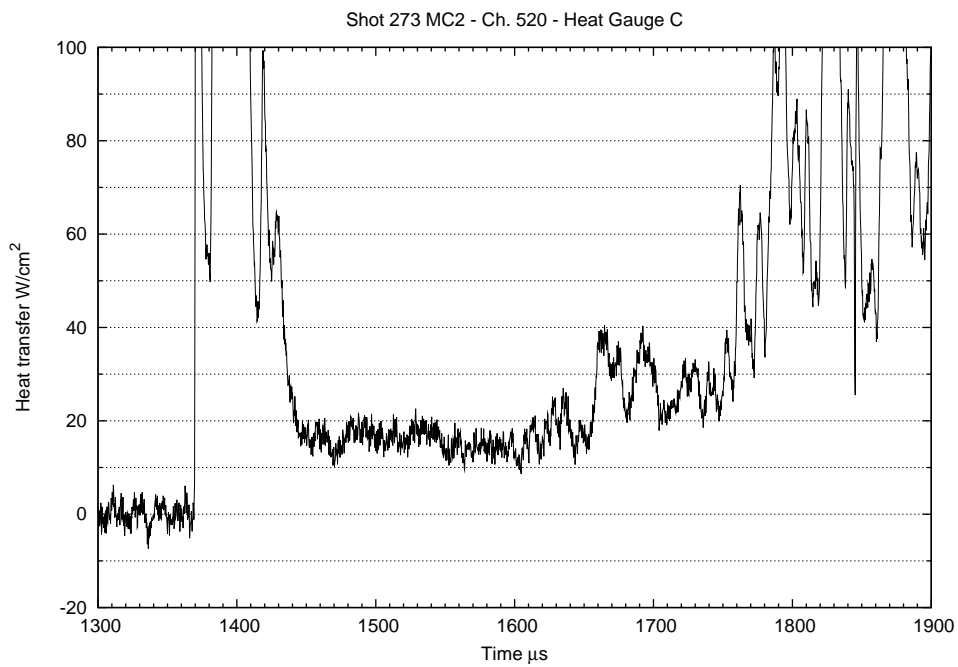


Figure F.14: Shot 273 heat gauge C data trace.

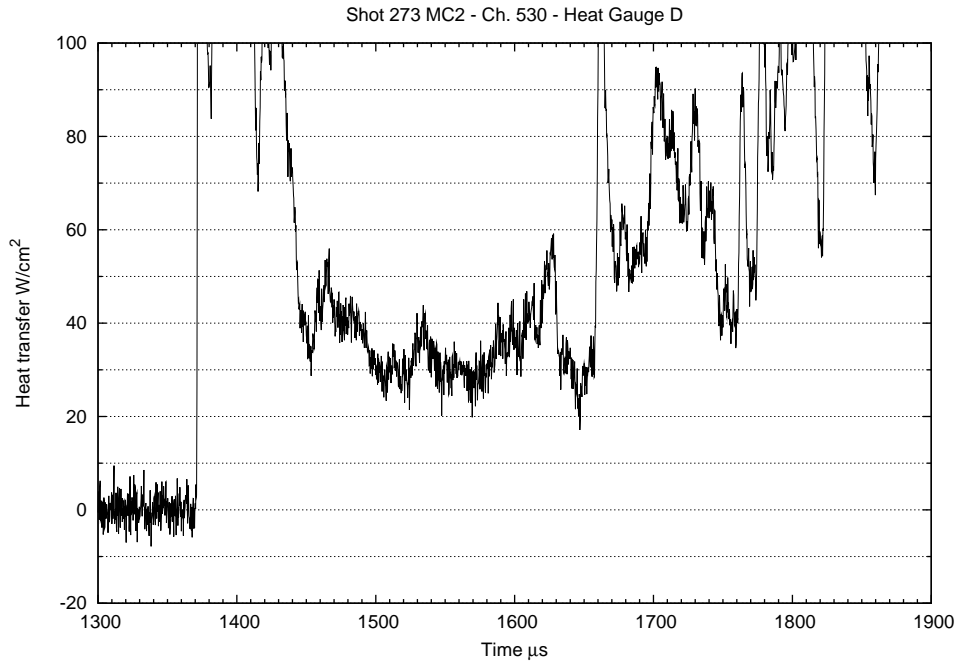


Figure F.15: Shot 273 heat gauge D data trace.

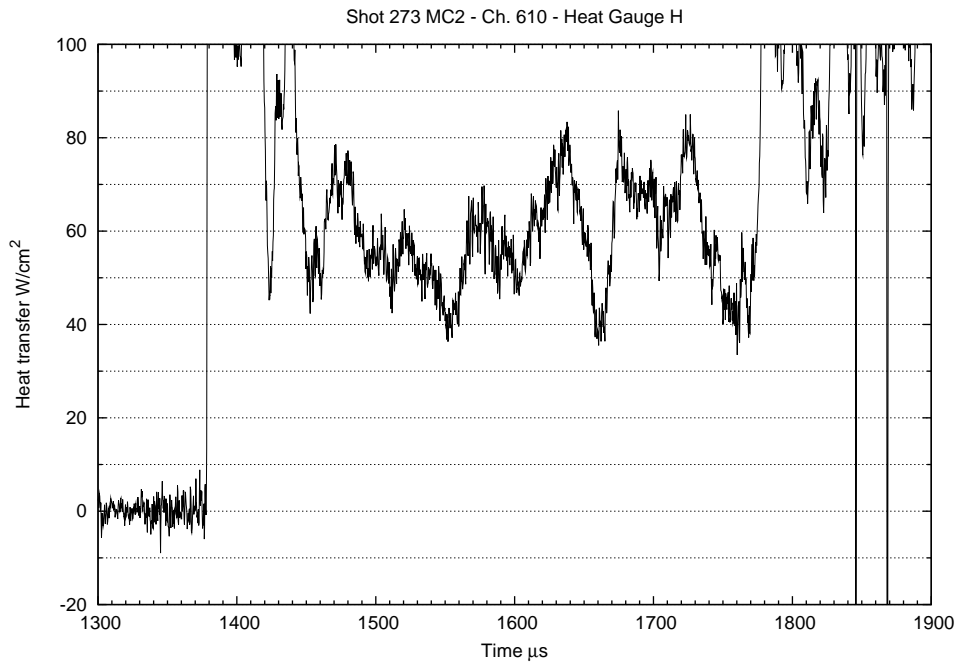


Figure F.16: Shot 273 heat gauge H data trace.

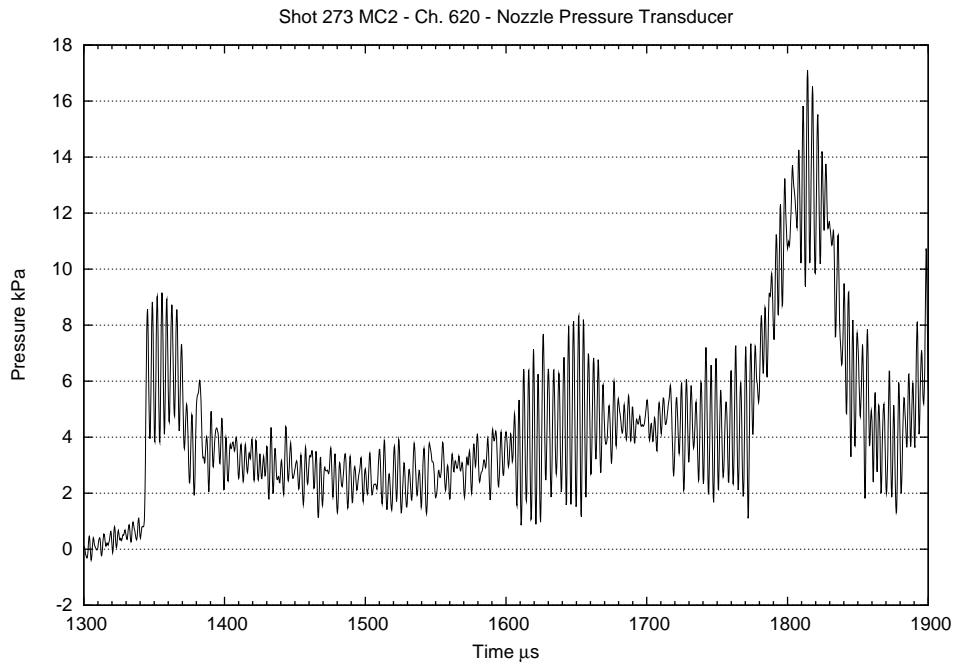


Figure F.17: Shot 273 nozzle pressure transducer data trace.

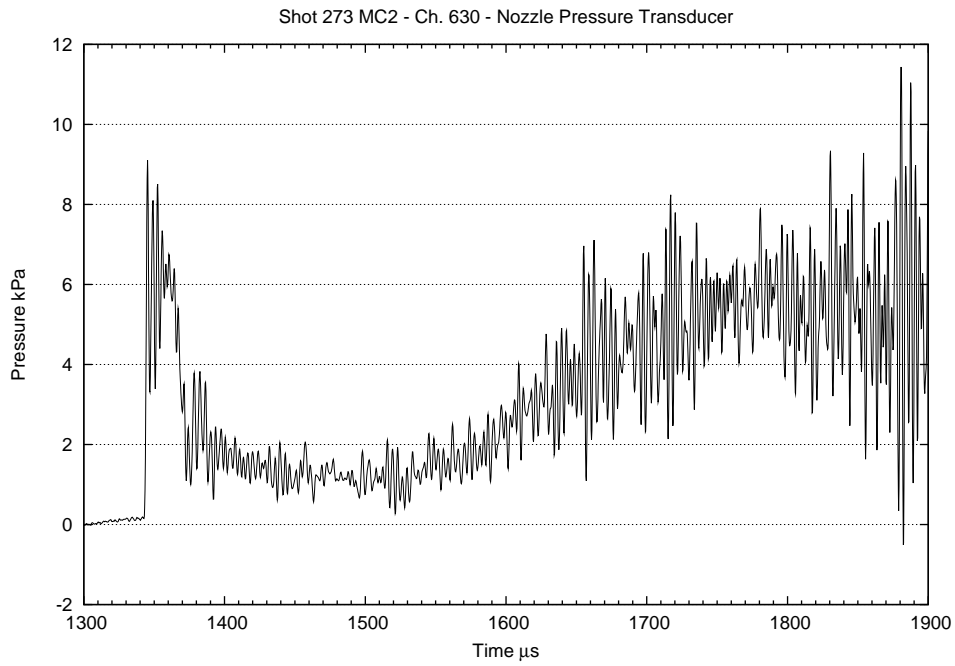


Figure F.18: Shot 273 nozzle pressure transducer data trace.

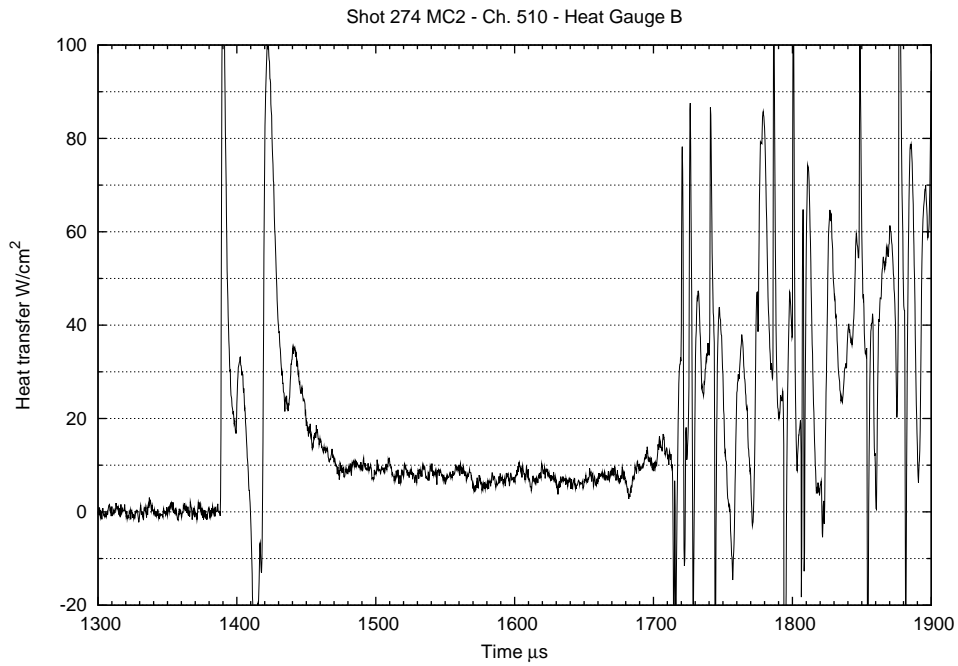


Figure F.19: Shot 274 heat gauge B data trace.

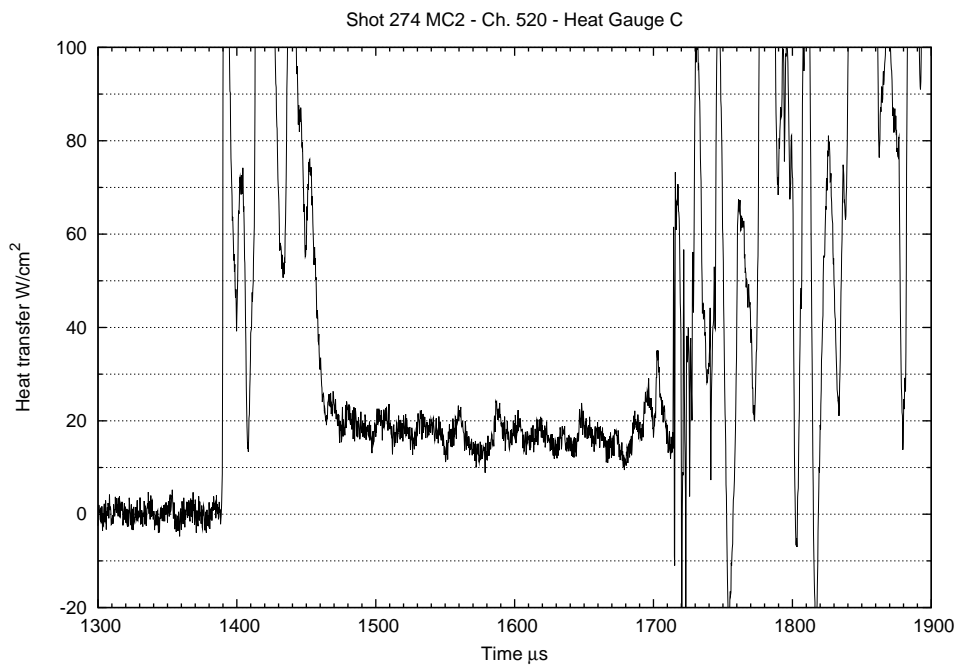


Figure F.20: Shot 274 heat gauge C data trace.

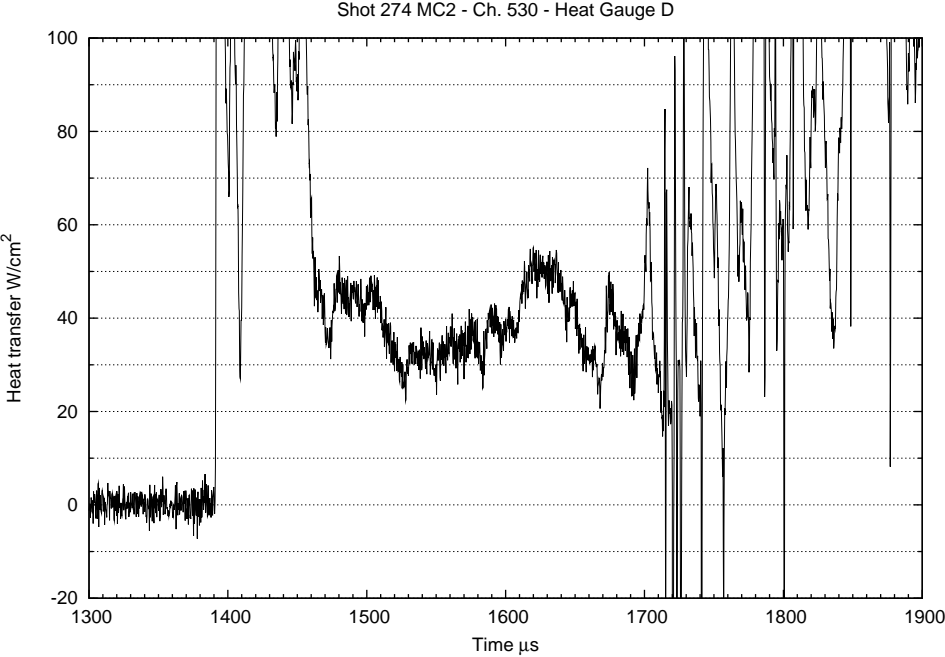


Figure F.21: Shot 274 heat gauge D data trace.

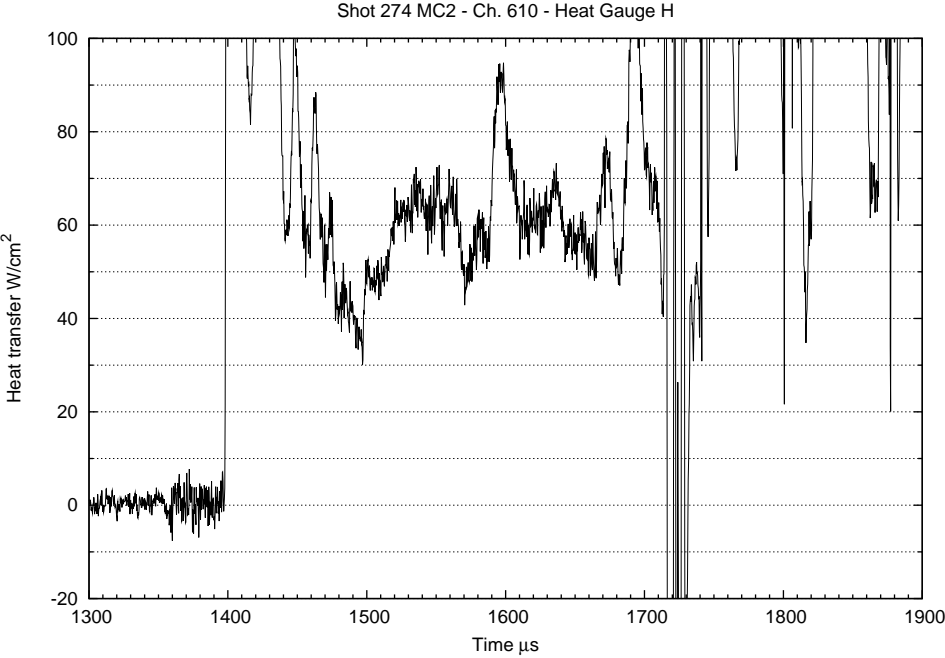


Figure F.22: Shot 274 heat gauge H data trace.

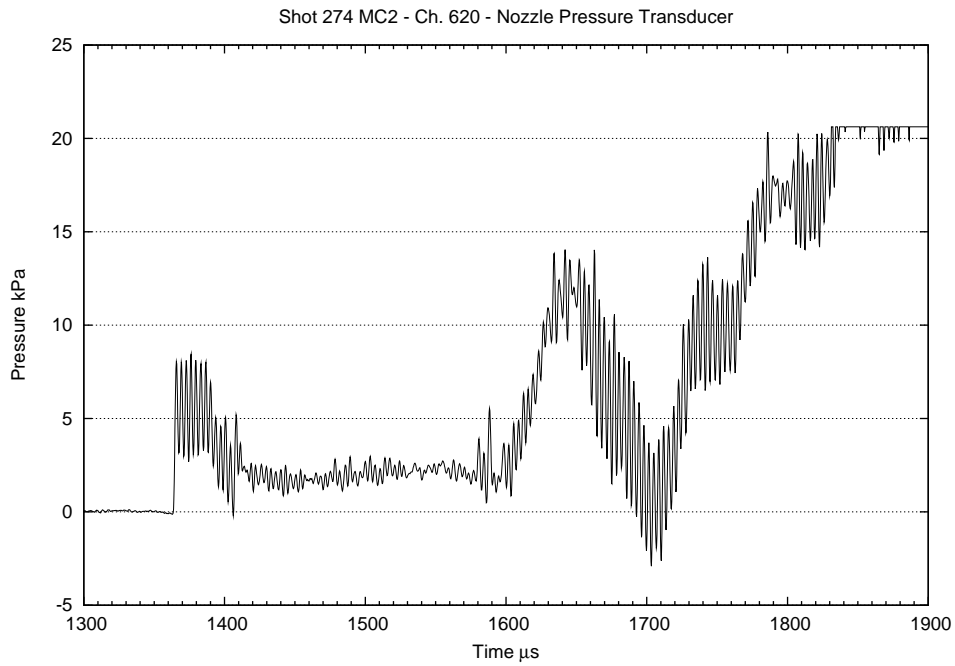


Figure F.23: Shot 274 nozzle pressure transducer data trace.

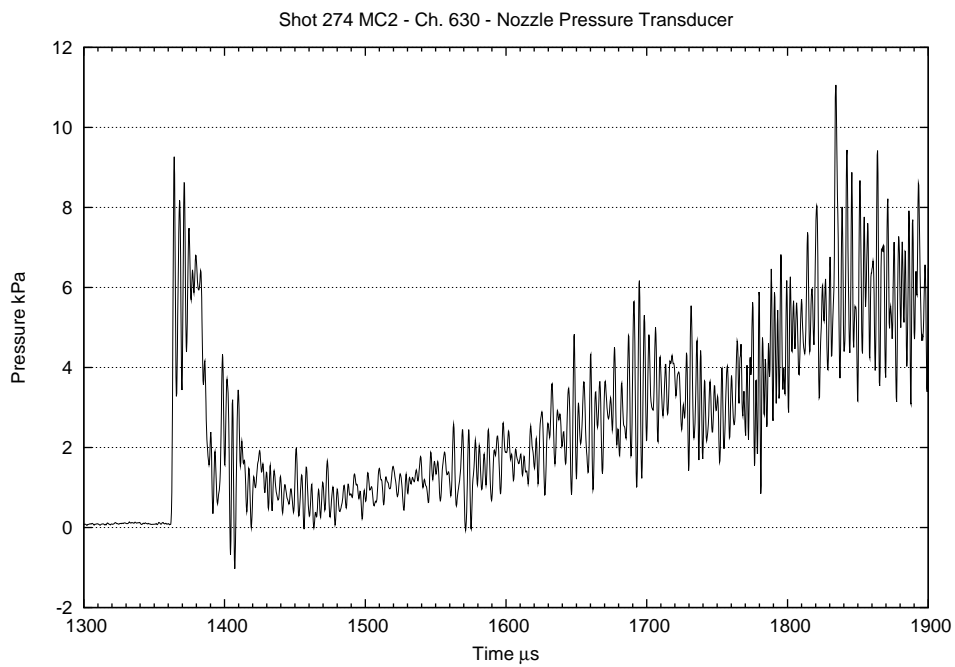


Figure F.24: Shot 274 nozzle pressure transducer data trace.

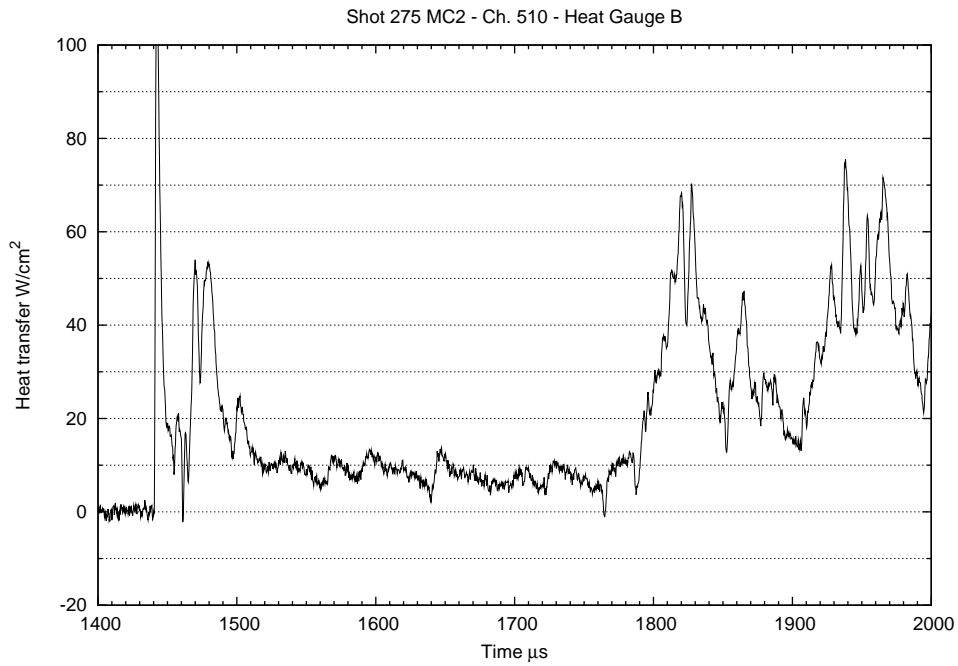


Figure F.25: Shot 275 heat gauge B data trace.

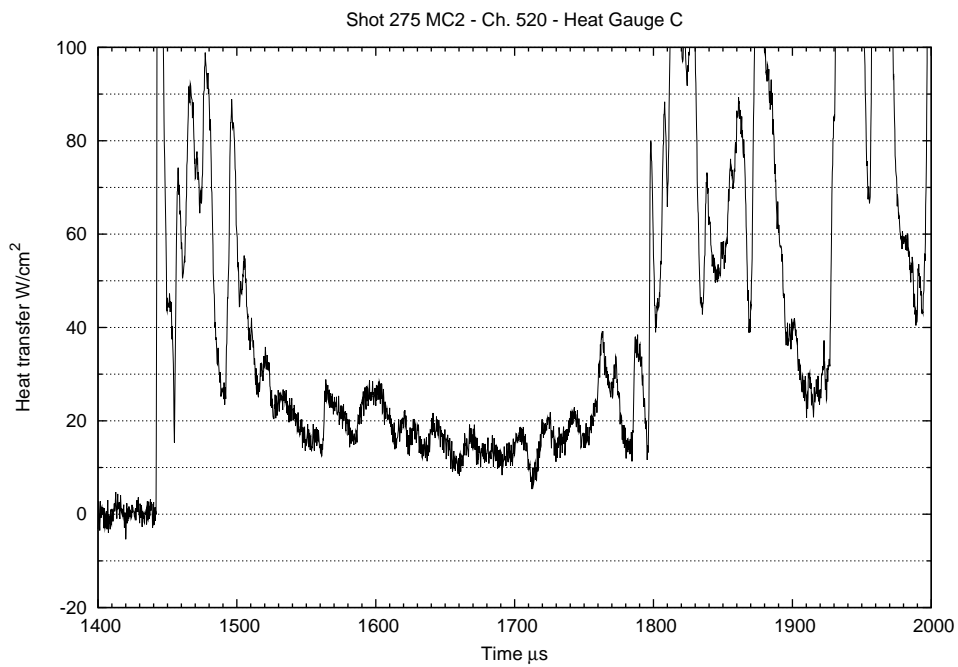


Figure F.26: Shot 275 heat gauge C data trace.

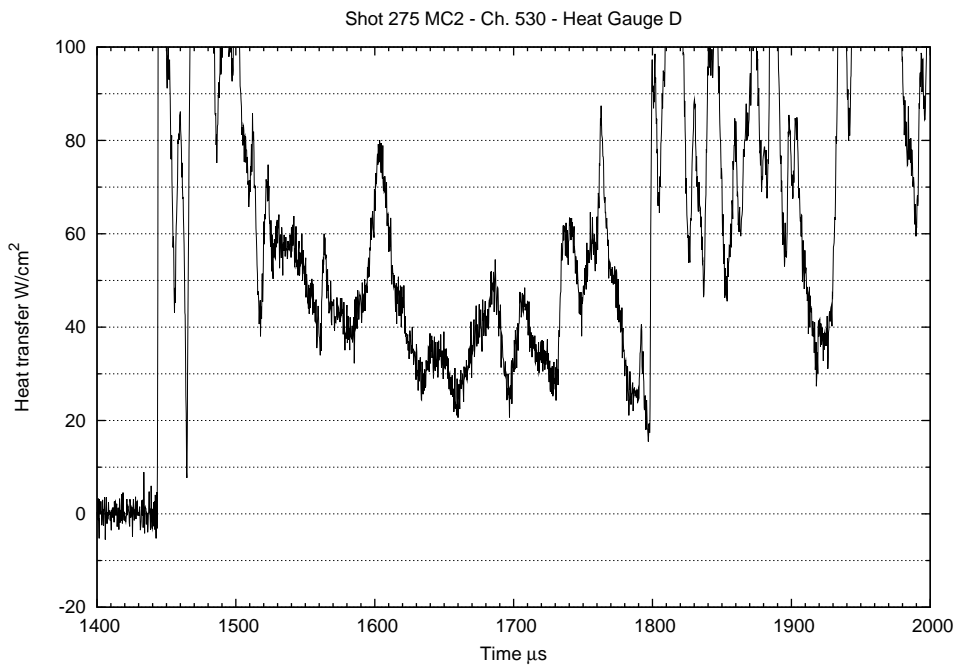


Figure F.27: Shot 275 heat gauge D data trace.

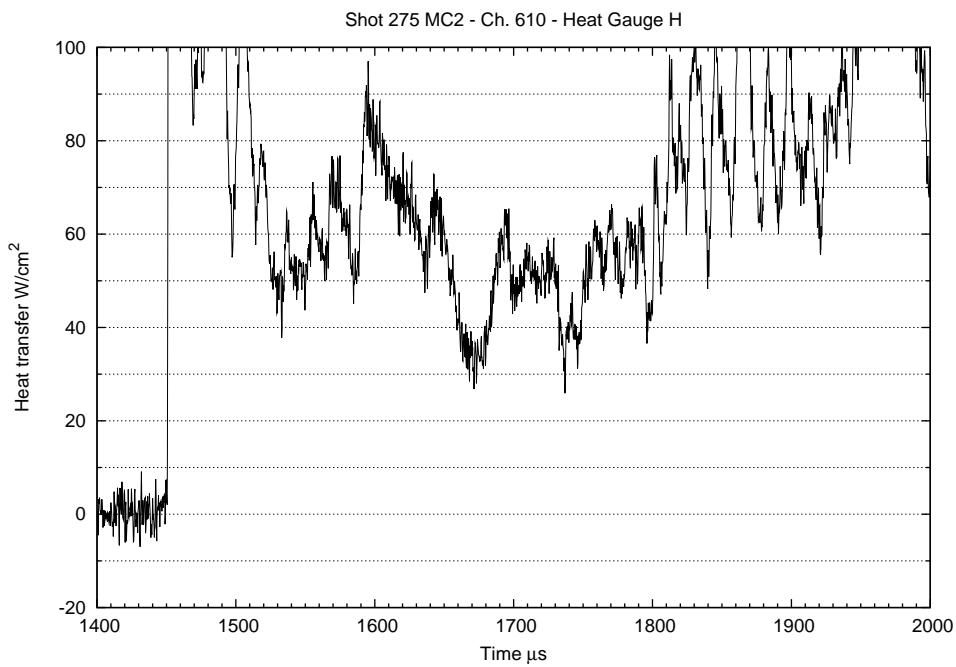


Figure F.28: Shot 275 heat gauge H data trace.

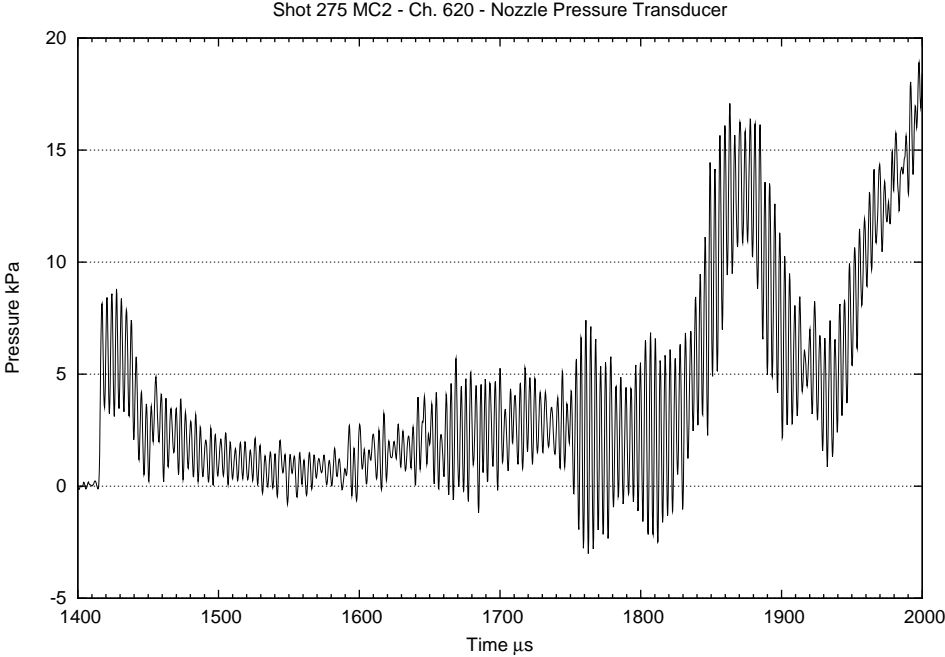


Figure F.29: Shot 275 nozzle pressure transducer data trace.

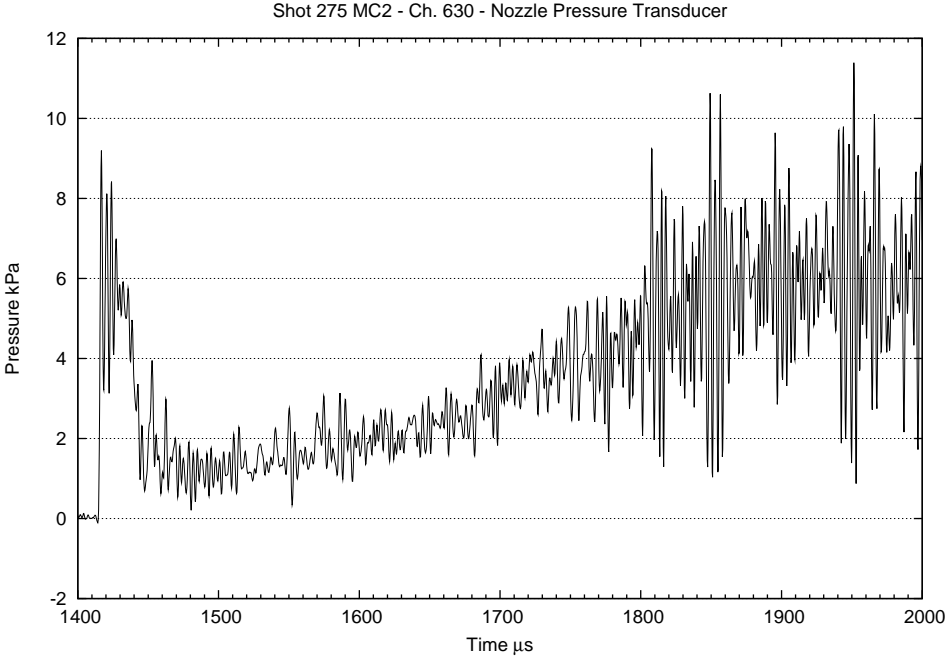


Figure F.30: Shot 275 nozzle pressure transducer data trace.

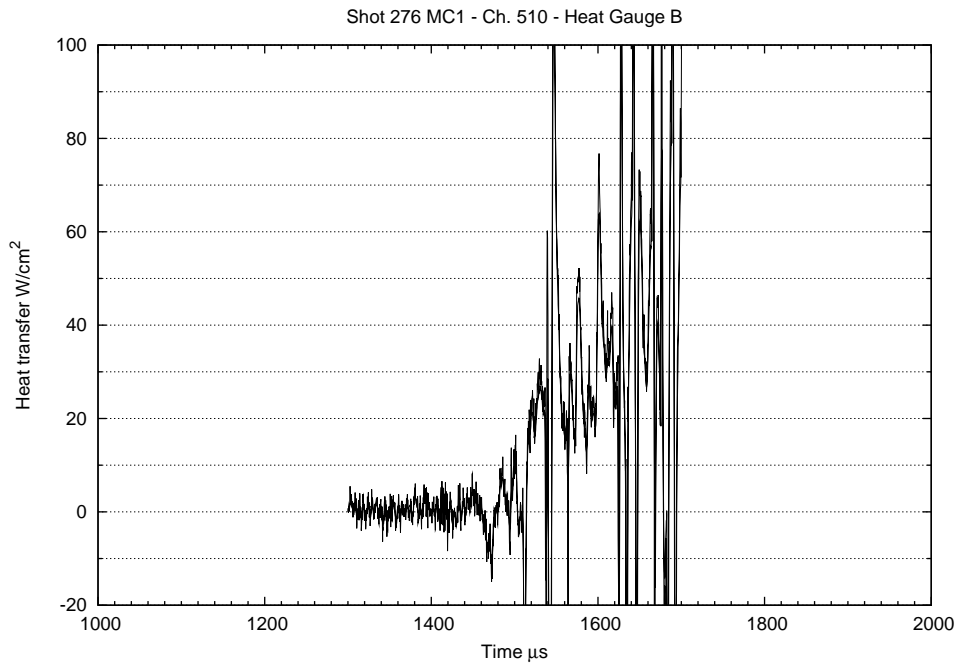


Figure F.31: Shot 276 heat gauge B data trace.

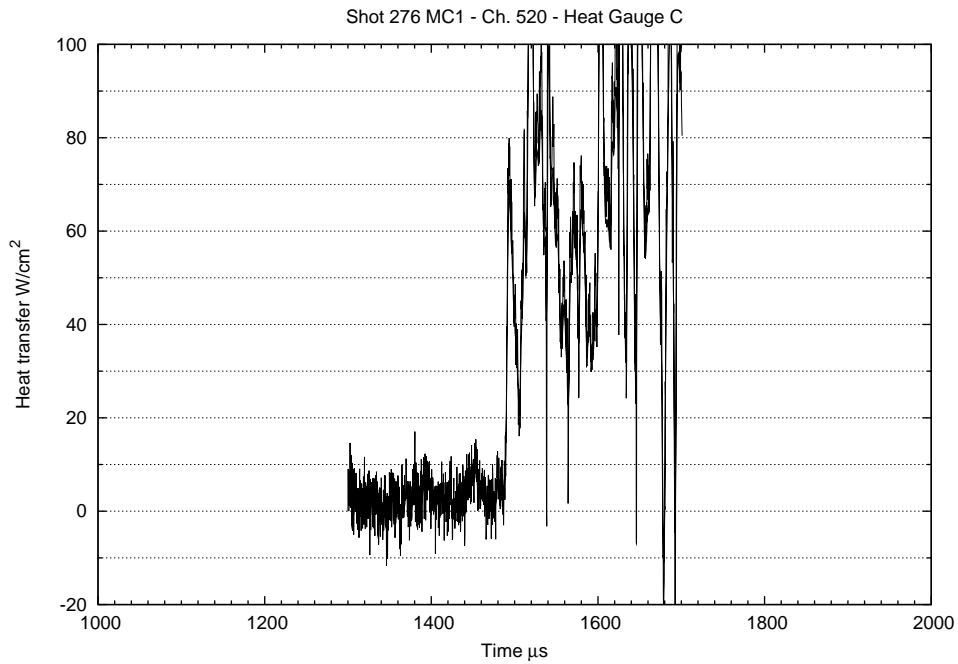


Figure F.32: Shot 276 heat gauge C data trace.

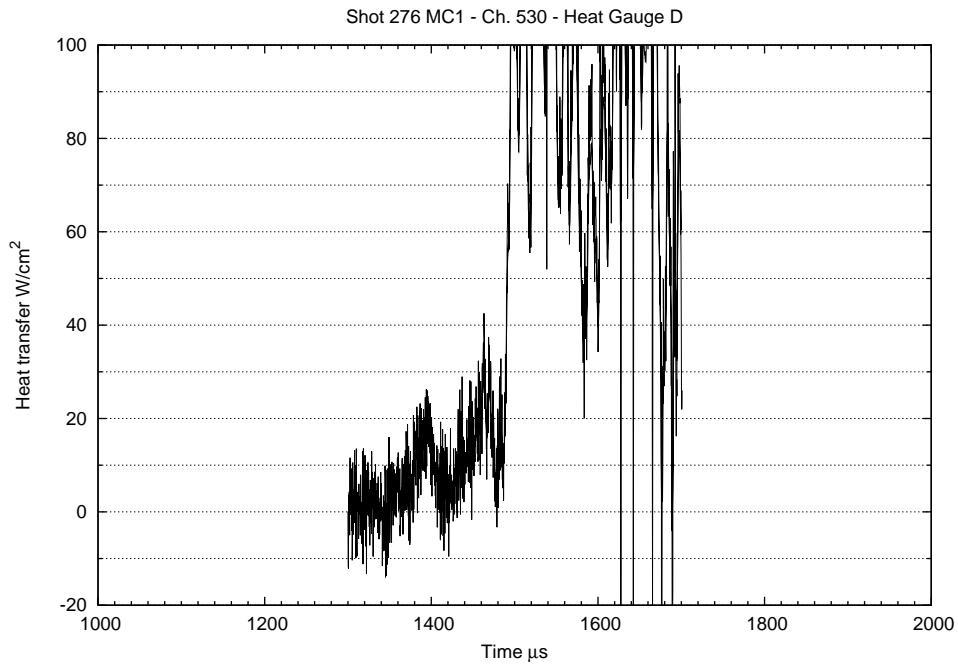


Figure F.33: Shot 276 heat gauge D data trace.

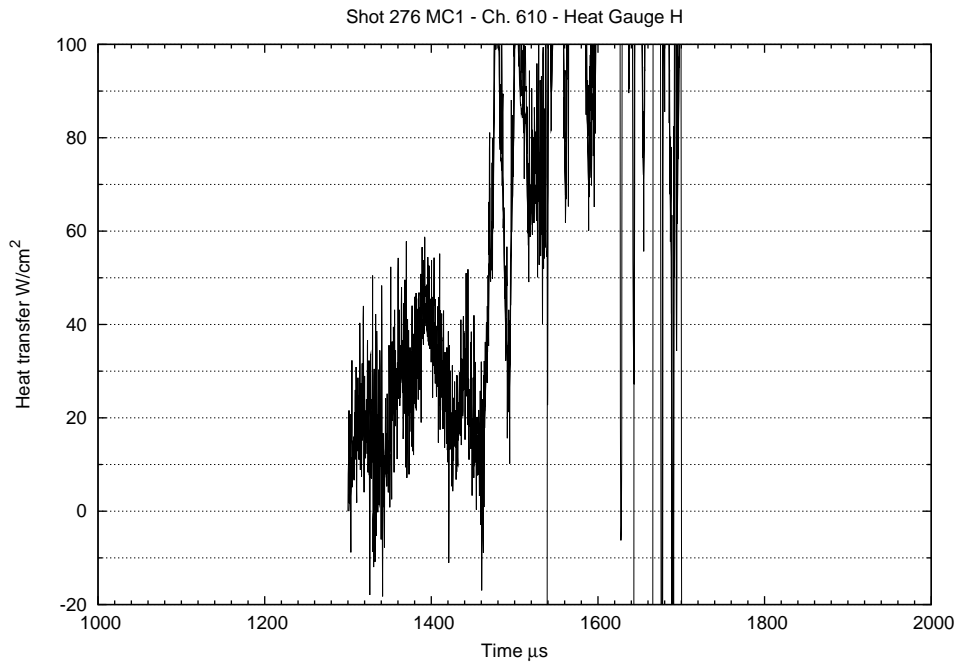


Figure F.34: Shot 276 heat gauge H data trace.

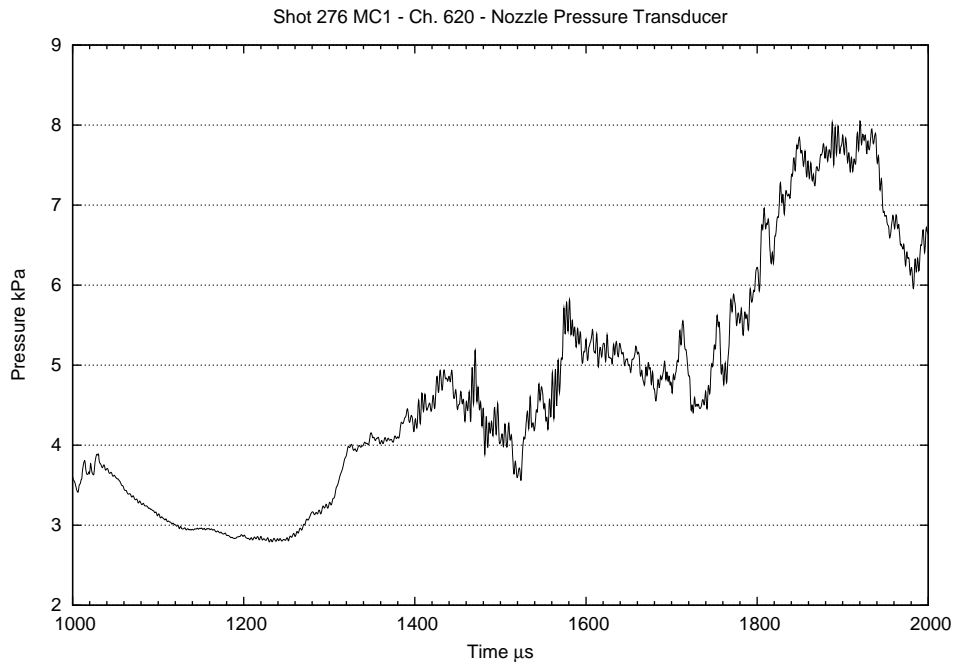


Figure F.35: Shot 276 nozzle pressure transducer data trace.

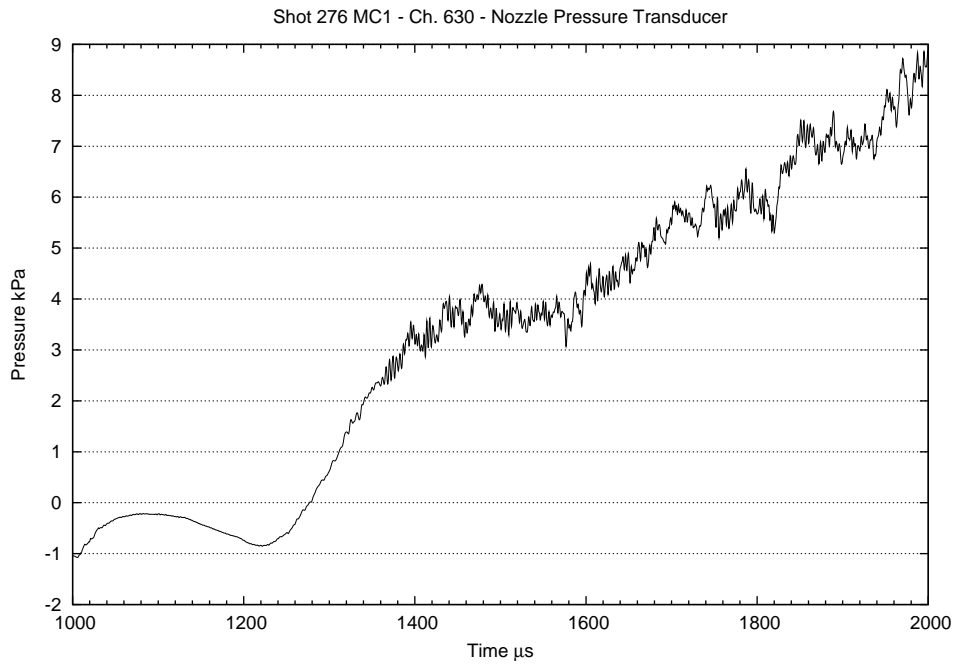


Figure F.36: Shot 276 nozzle pressure transducer data trace.

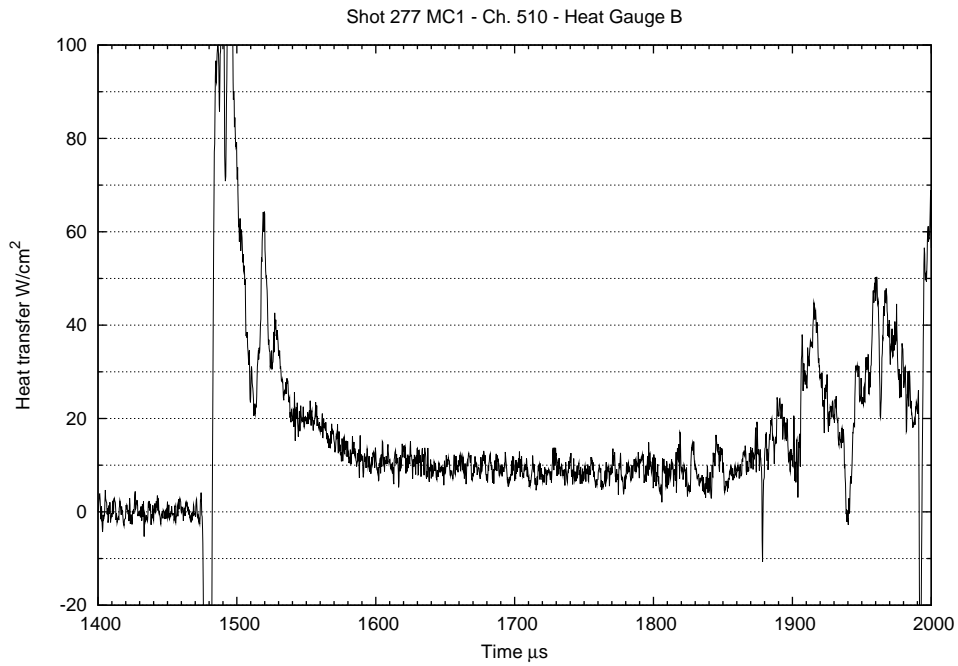


Figure F.37: Shot 277 heat gauge B data trace.

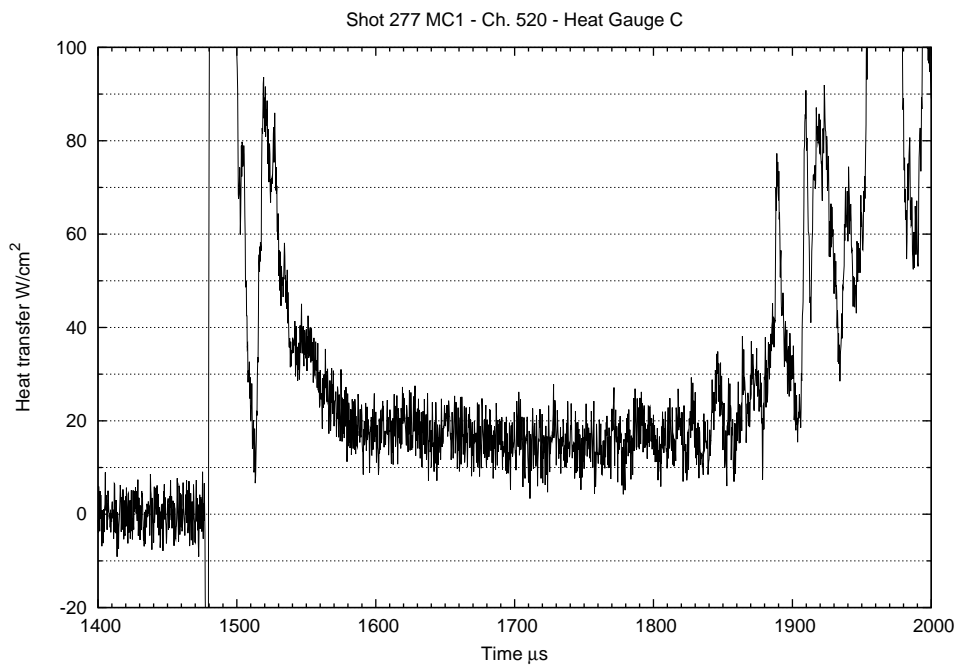


Figure F.38: Shot 277 heat gauge C data trace.

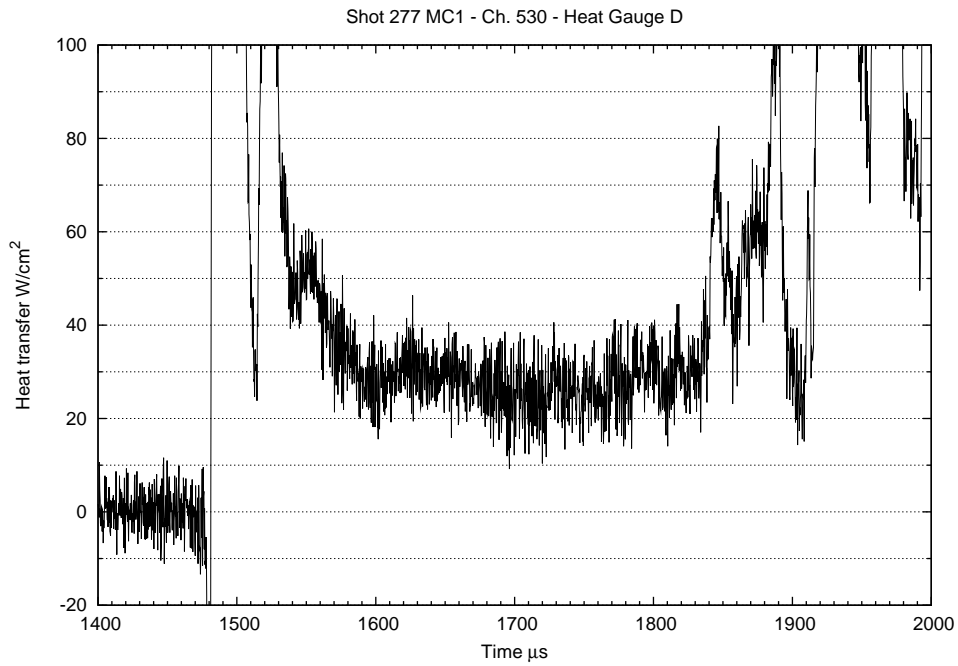


Figure F.39: Shot 277 heat gauge D data trace.

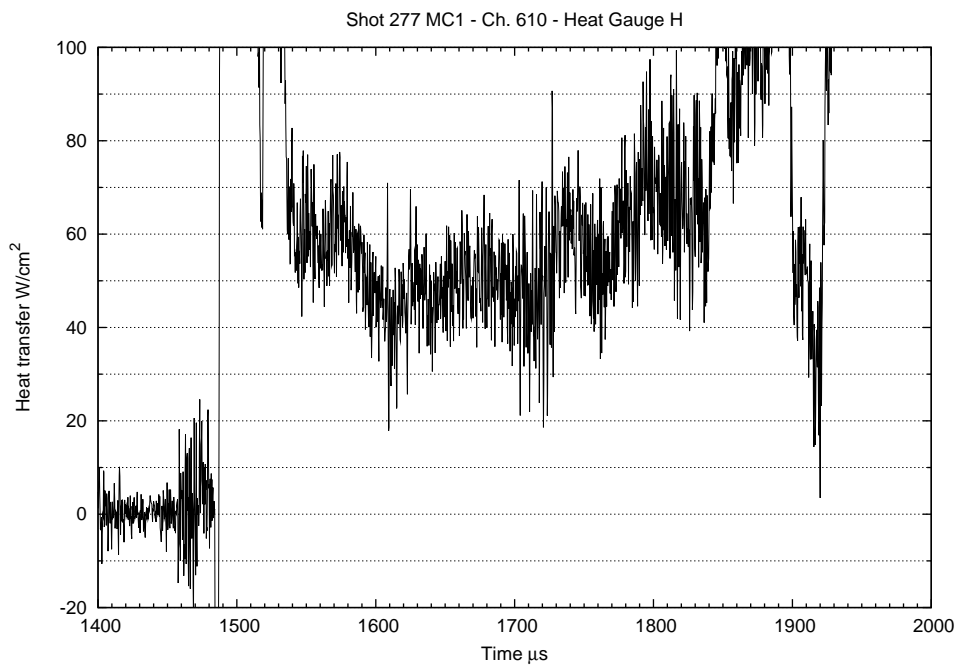


Figure F.40: Shot 277 heat gauge H data trace.

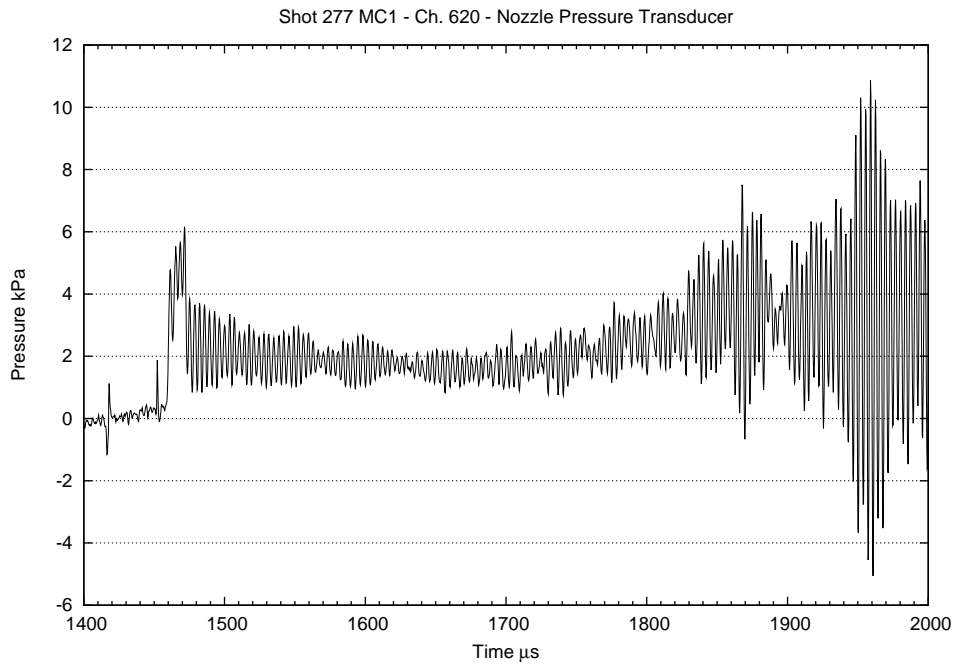


Figure F.41: Shot 277 nozzle pressure transducer data trace.

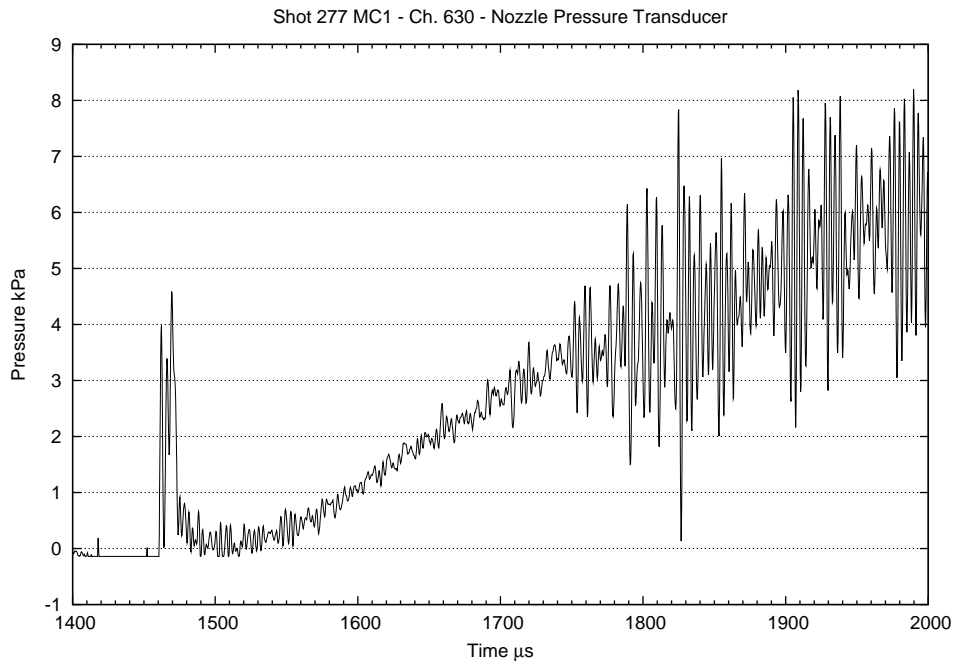


Figure F.42: Shot 277 nozzle pressure transducer data trace.

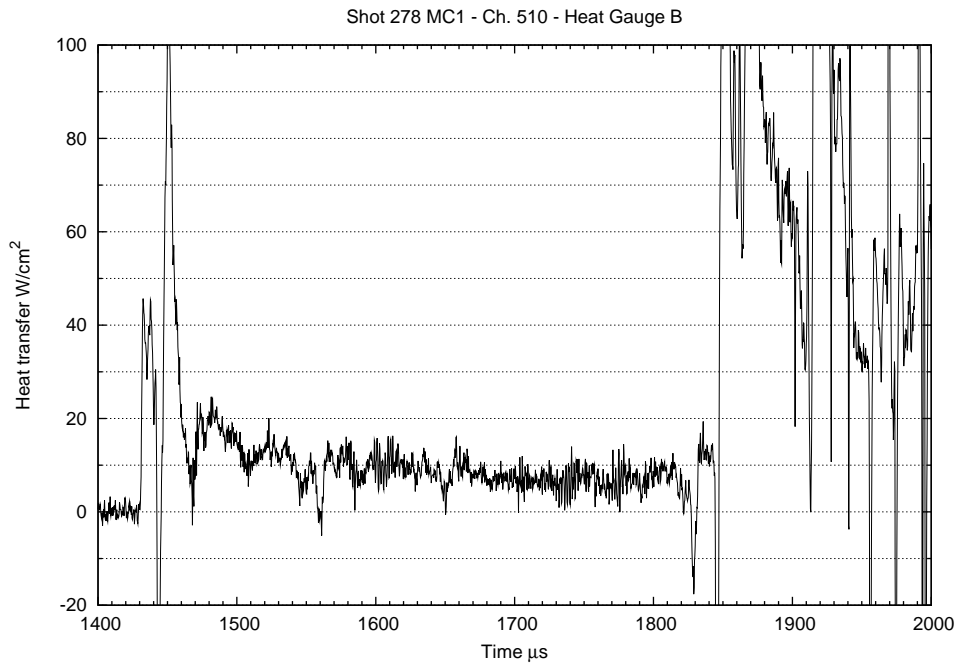


Figure F.43: Shot 278 heat gauge B data trace.

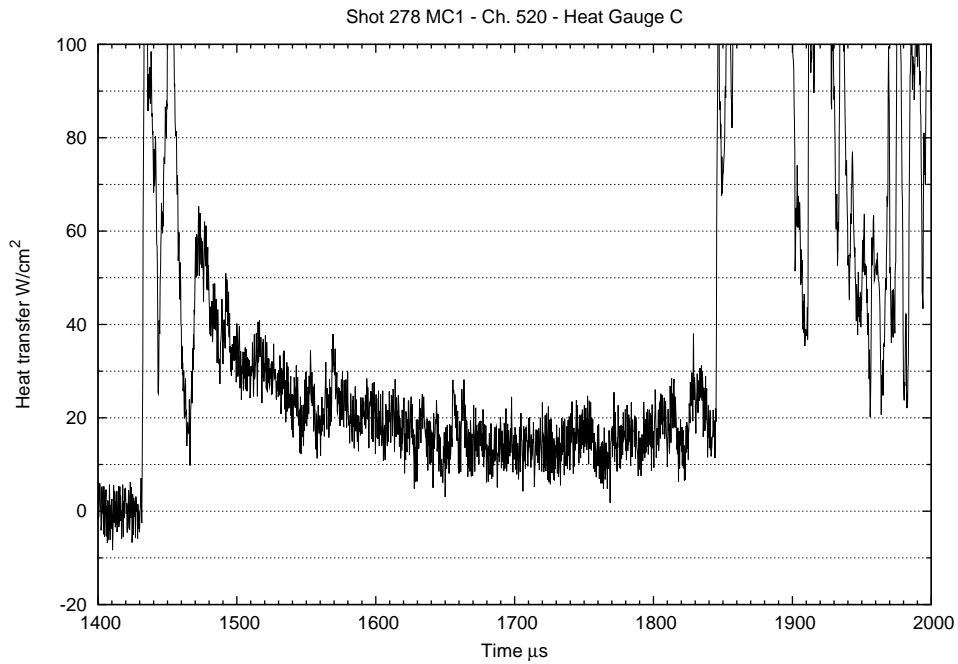


Figure F.44: Shot 278 heat gauge C data trace.

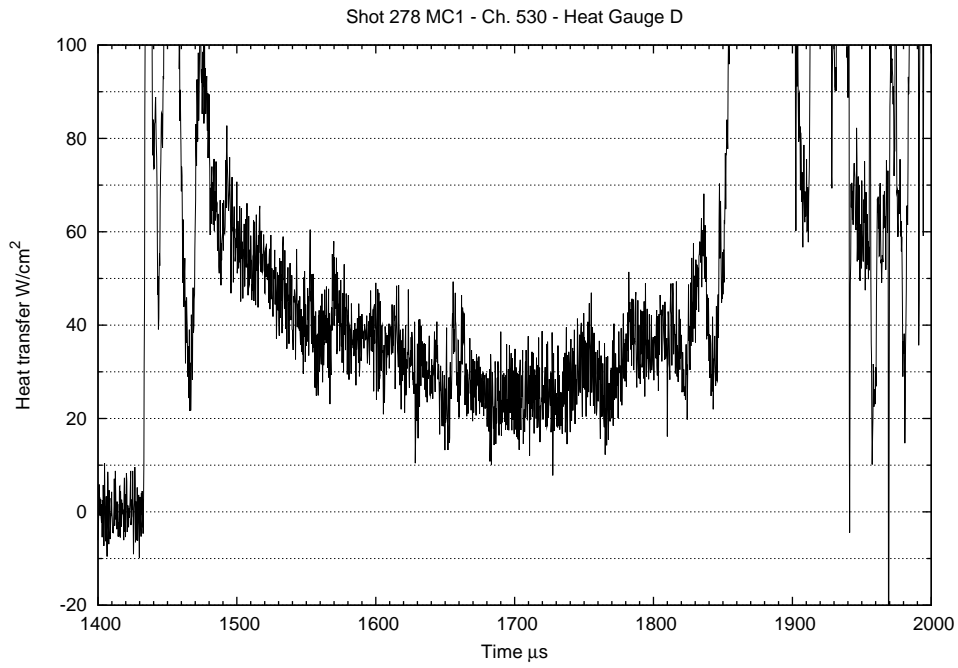


Figure F.45: Shot 278 heat gauge D data trace.

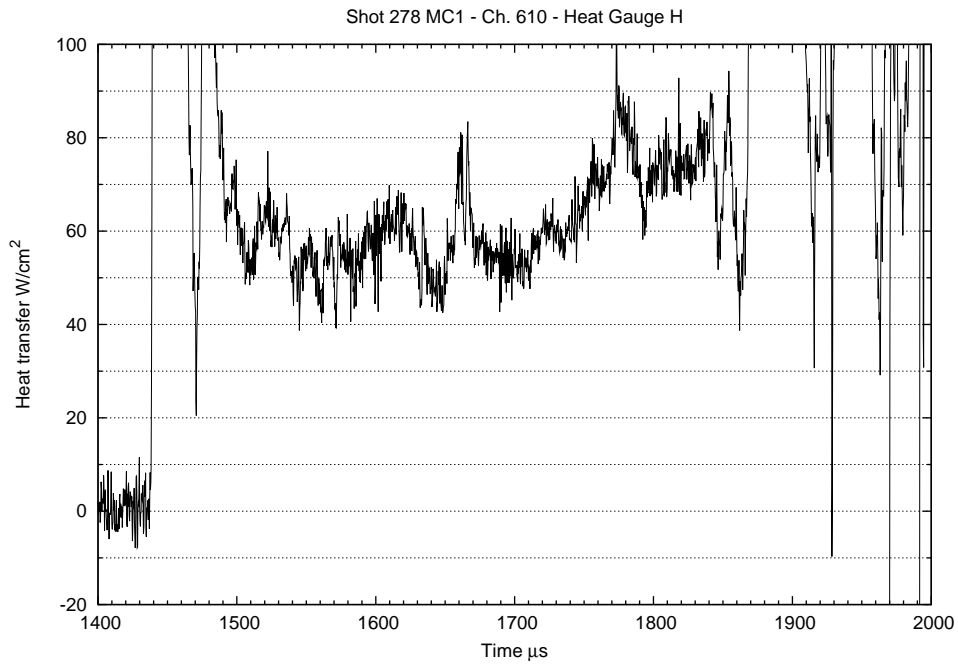


Figure F.46: Shot 278 heat gauge H data trace.

Data acquisition system failed to record data on this channel.

Figure F.47: Shot 278 nozzle pressure transducer data trace.

Data acquisition system failed to record data on this channel.

Figure F.48: Shot 278 nozzle pressure transducer data trace.

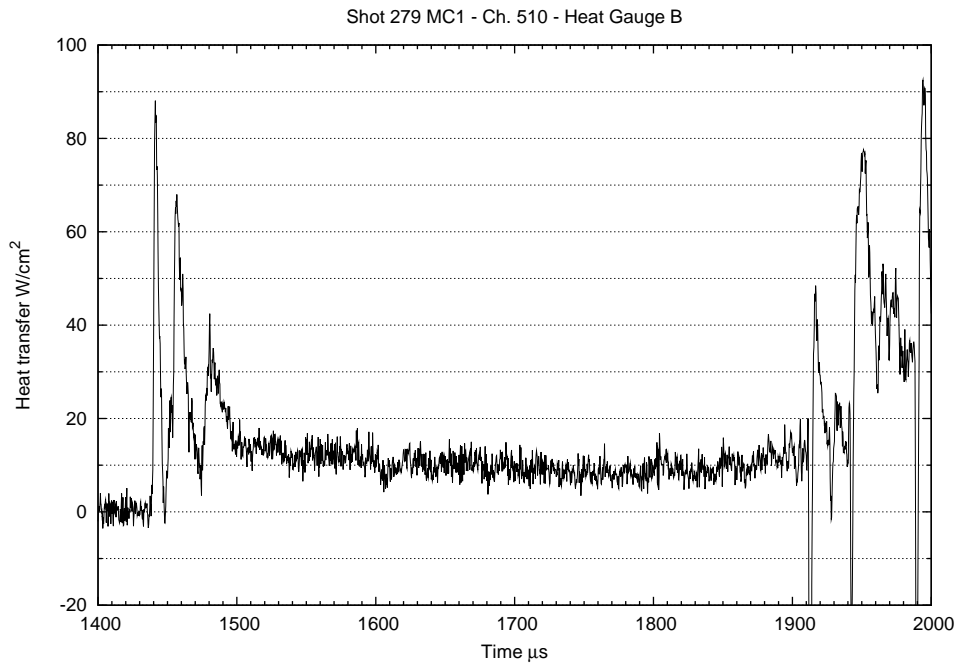


Figure F.49: Shot 279 heat gauge B data trace.

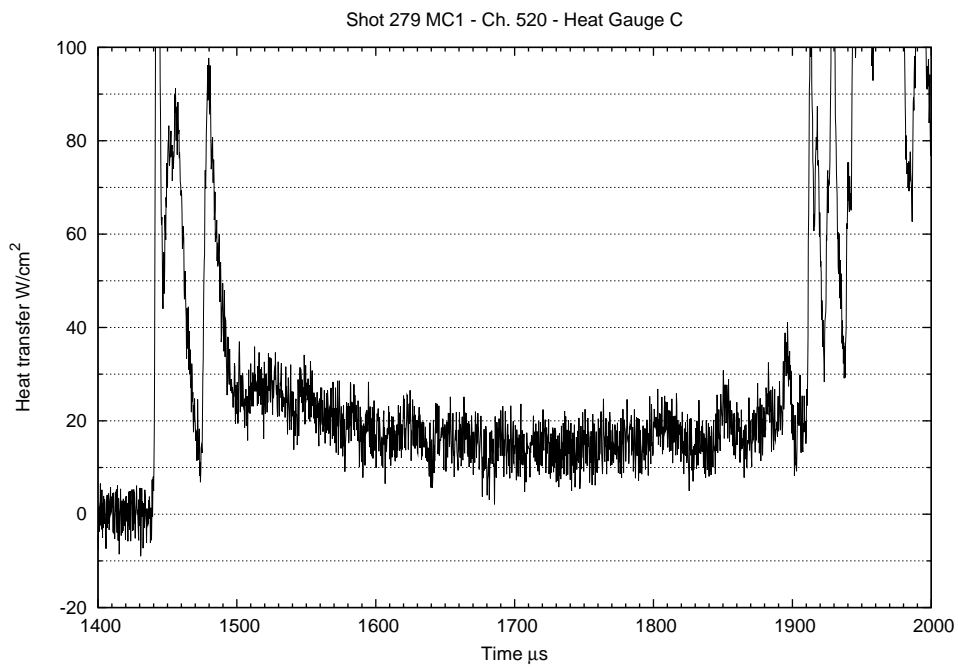


Figure F.50: Shot 279 heat gauge C data trace.

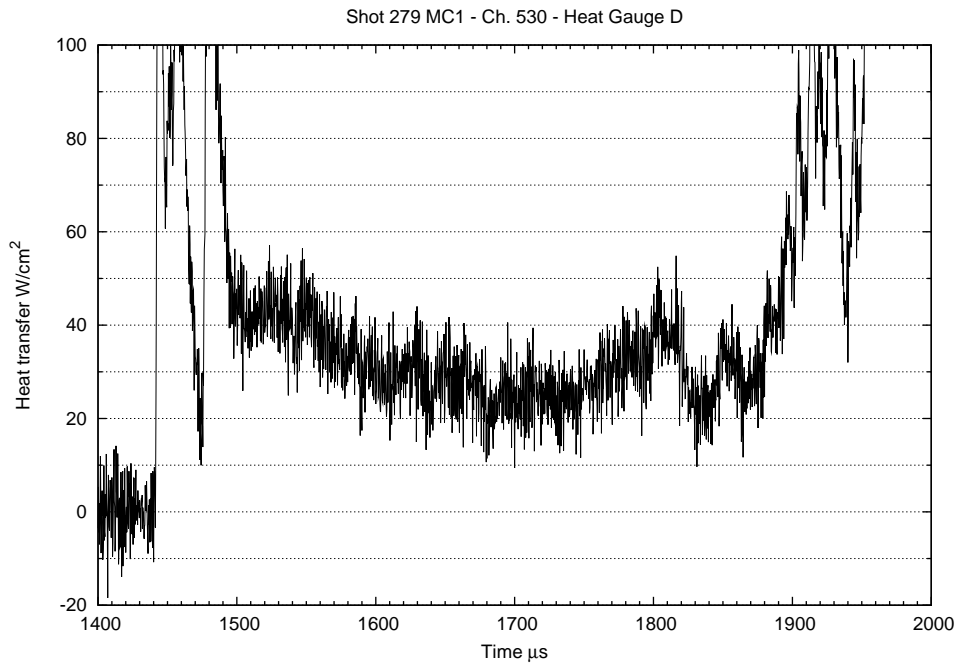


Figure F.51: Shot 279 heat gauge D data trace.

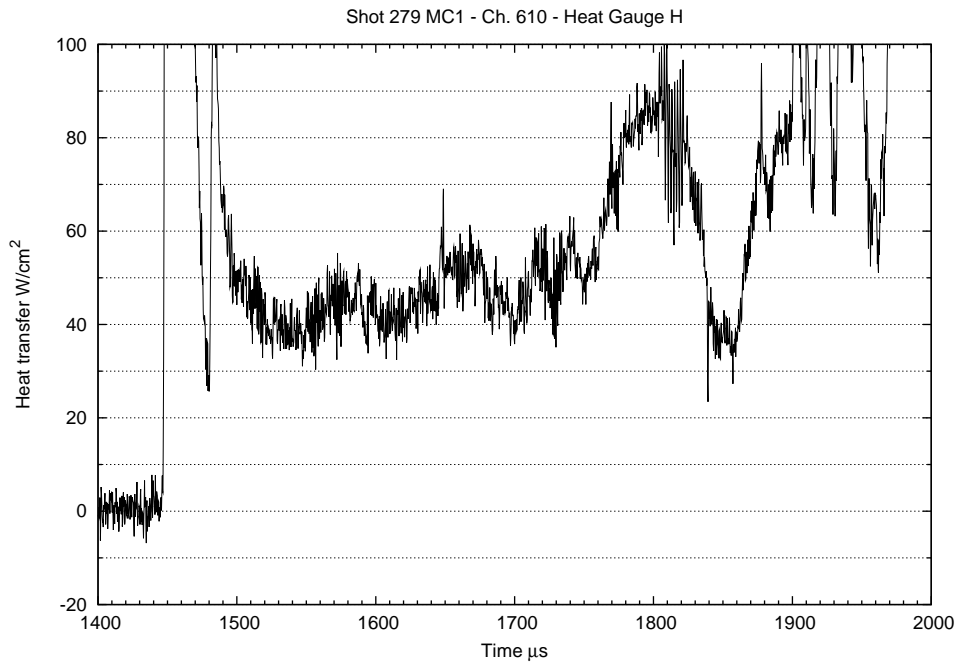


Figure F.52: Shot 279 heat gauge H data trace.

Data acquisition system failed to record data on this channel.

Figure F.53: Shot 279 nozzle pressure transducer data trace.

Data acquisition system failed to record data on this channel.

Figure F.54: Shot 279 nozzle pressure transducer data trace.

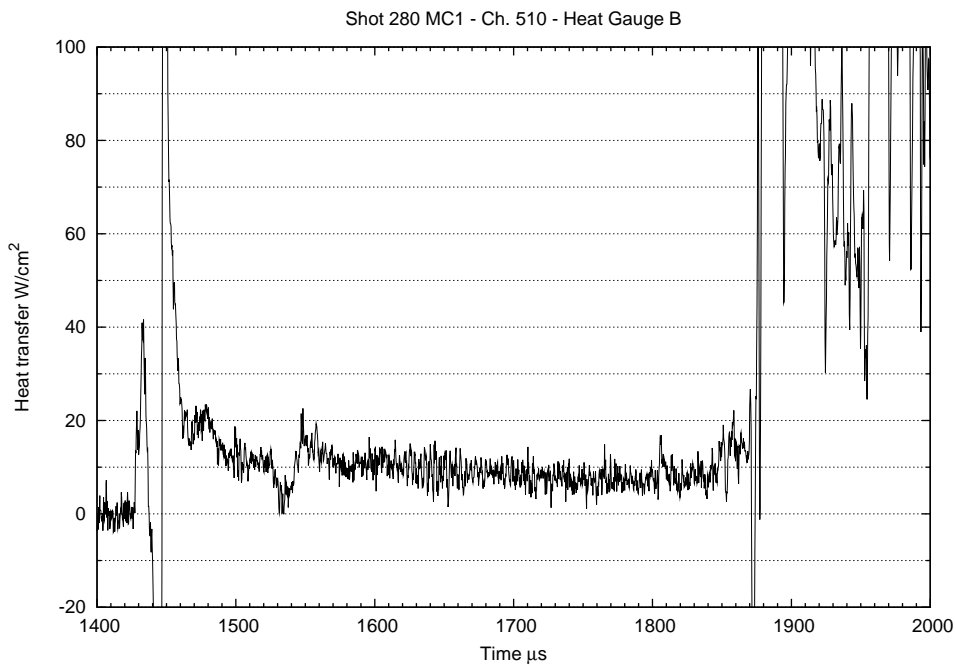


Figure F.55: Shot 280 heat gauge B data trace.

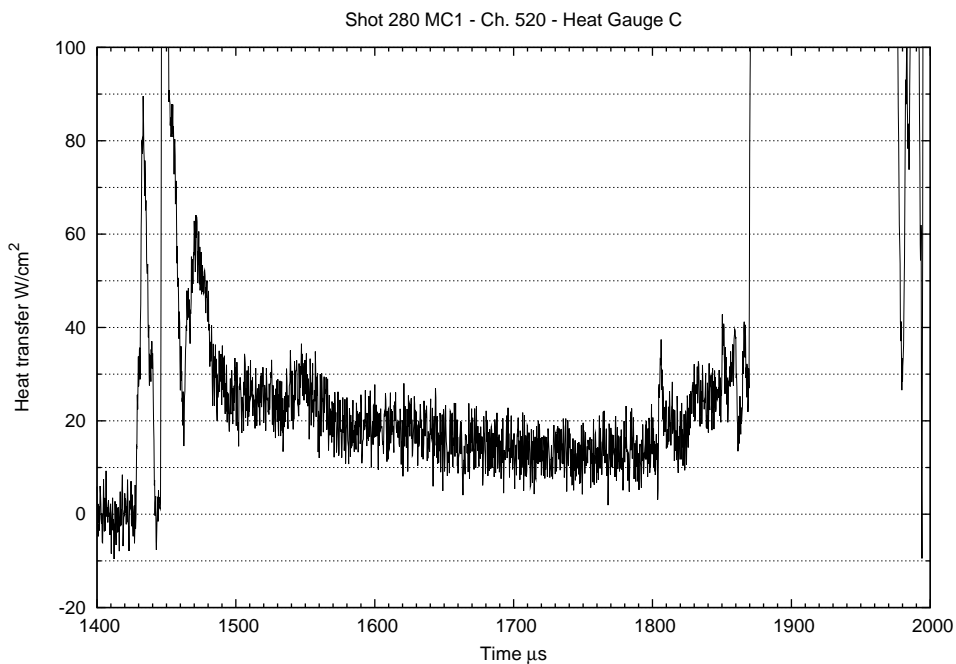


Figure F.56: Shot 280 heat gauge C data trace.

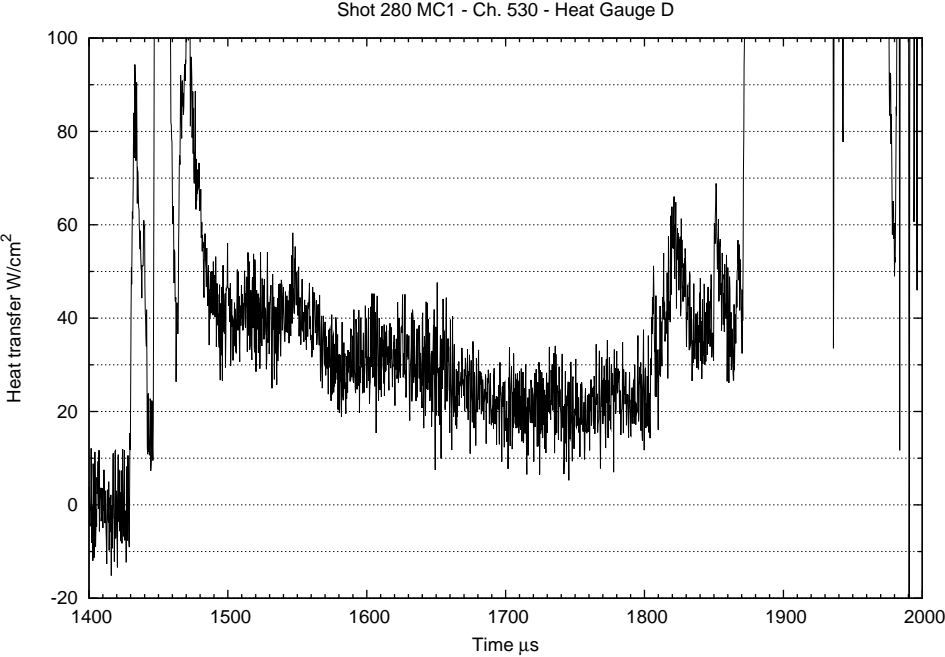


Figure F.57: Shot 280 heat gauge D data trace.

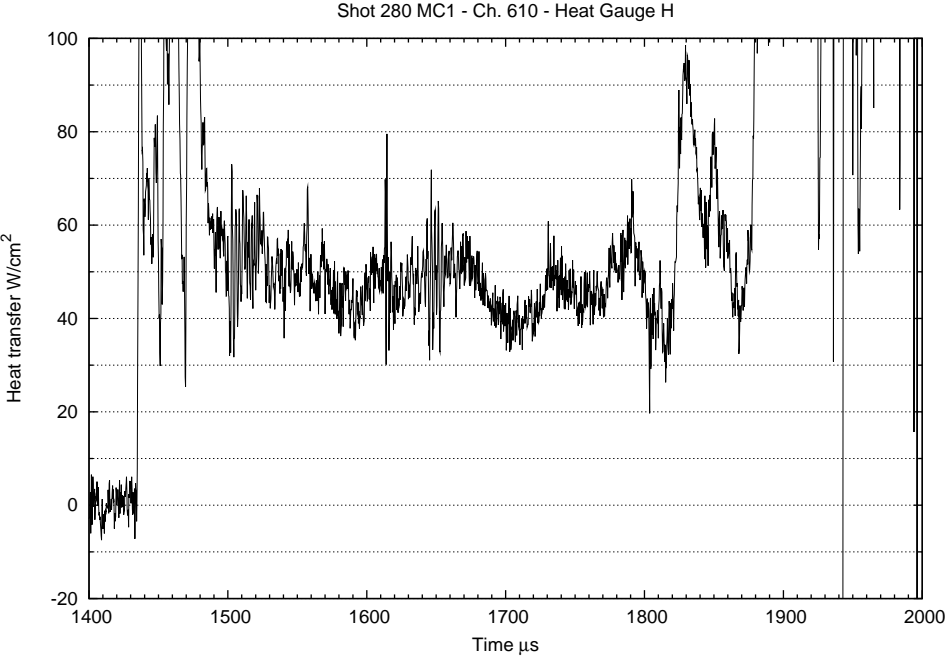


Figure F.58: Shot 280 heat gauge H data trace.

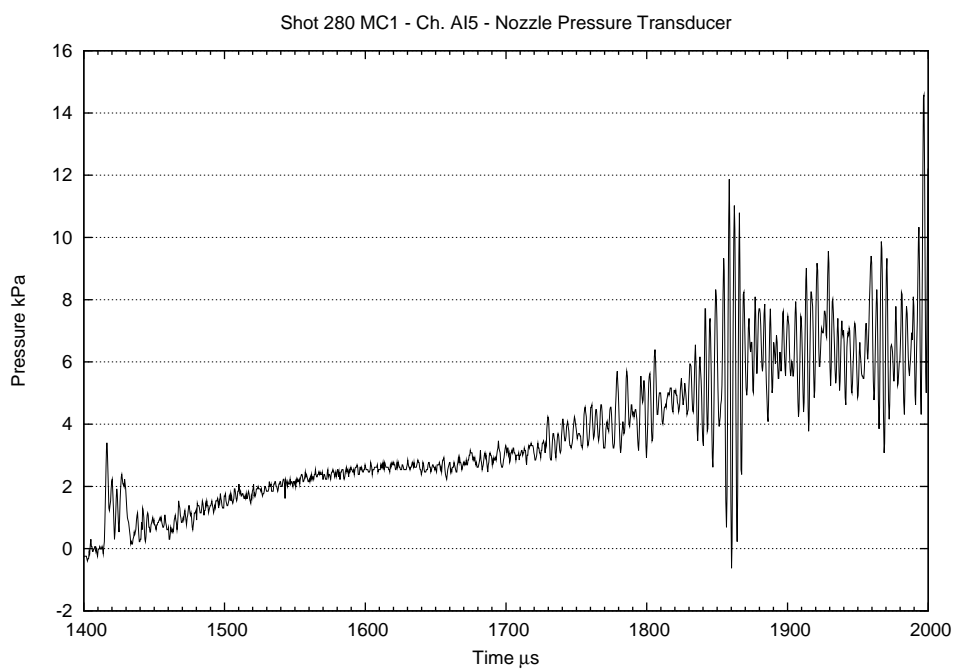


Figure F.59: Shot 280 nozzle pressure transducer data trace.

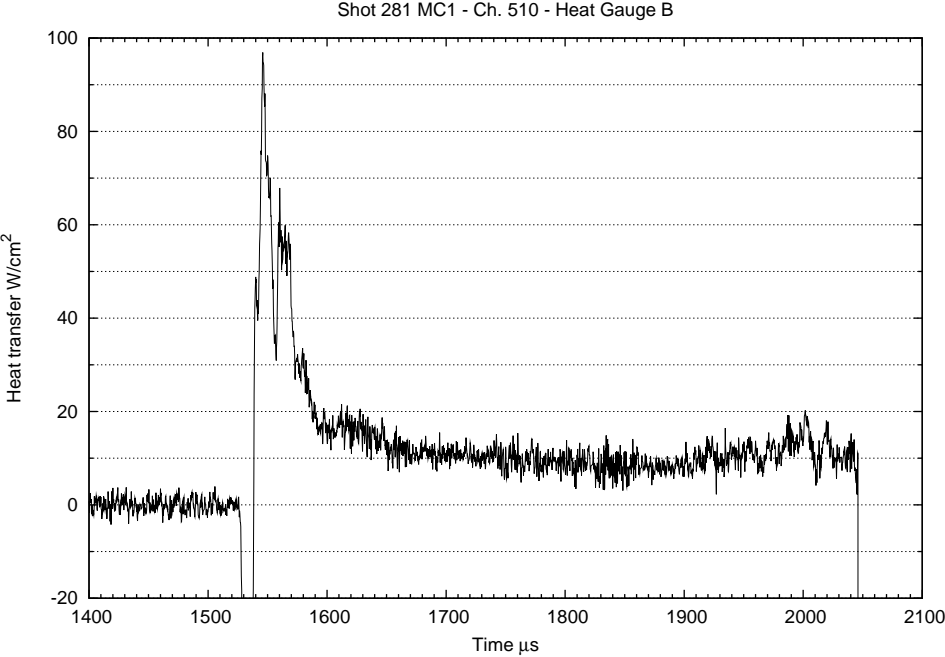


Figure F.60: Shot 281 heat gauge B data trace.

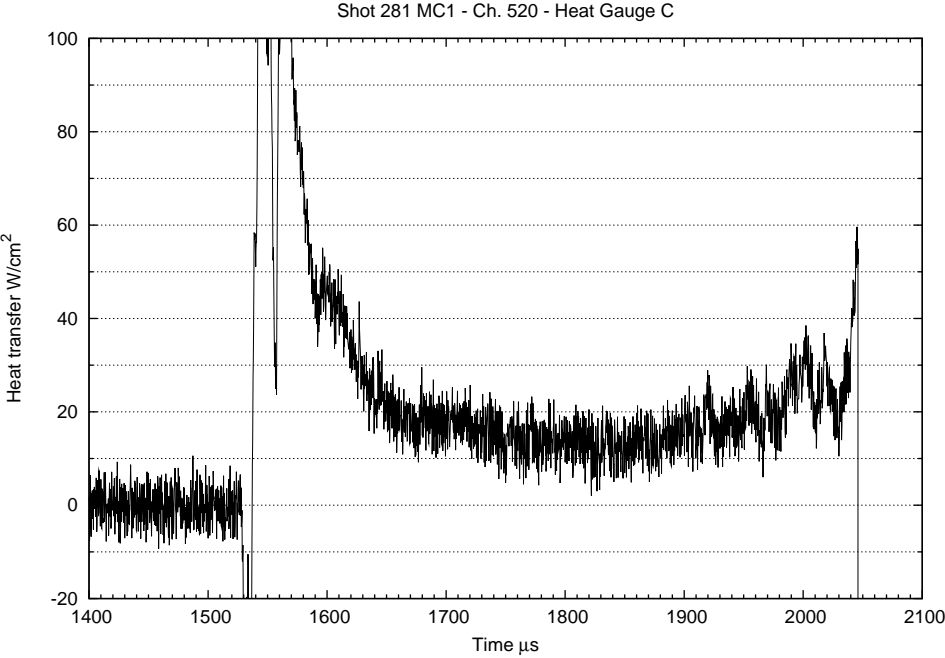


Figure F.61: Shot 281 heat gauge C data trace.

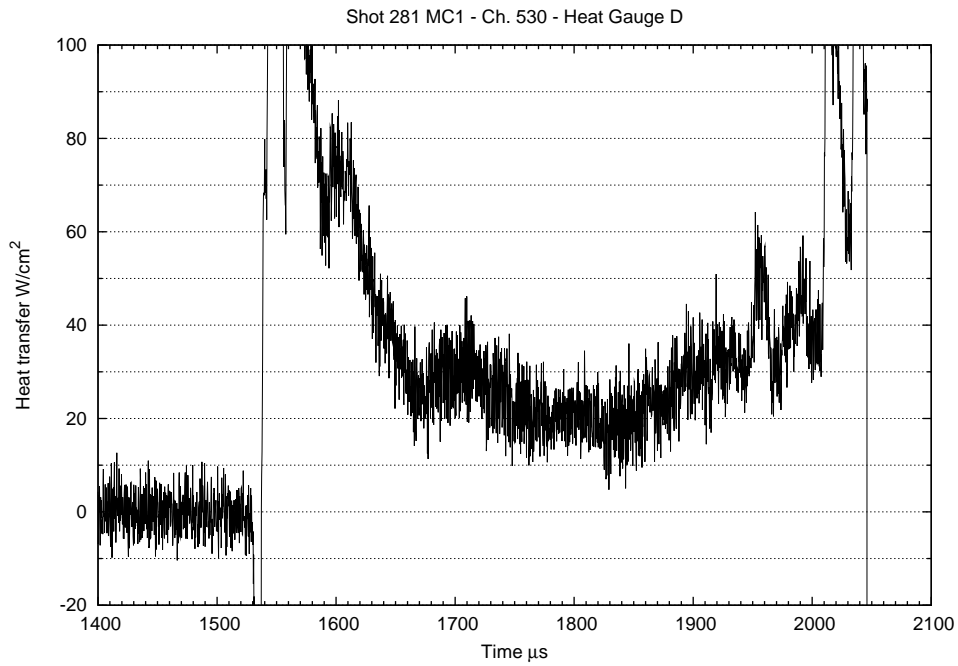


Figure F.62: Shot 281 heat gauge D data trace.

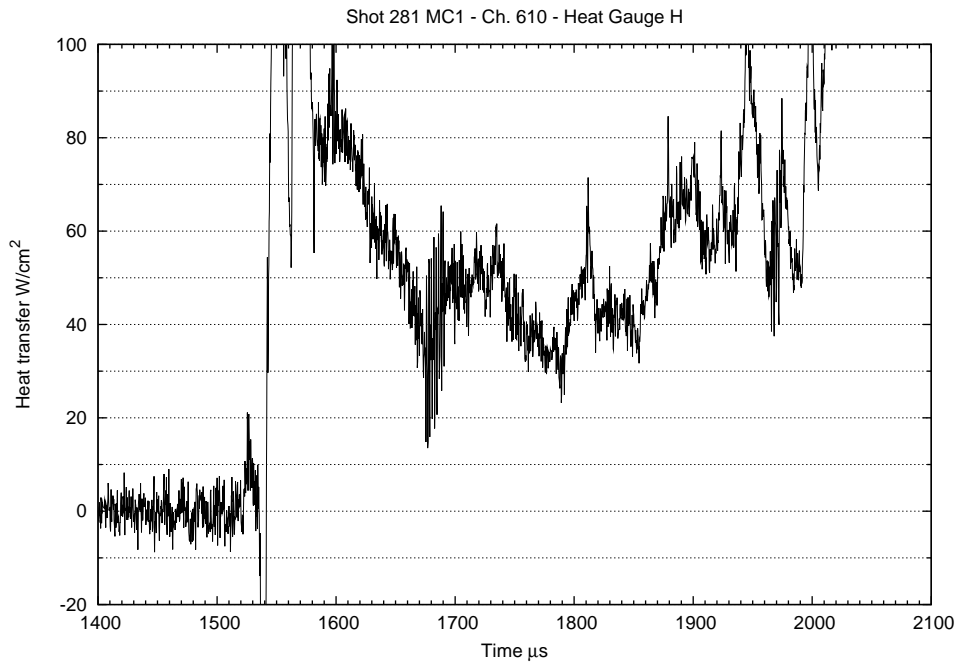


Figure F.63: Shot 281 heat gauge H data trace.

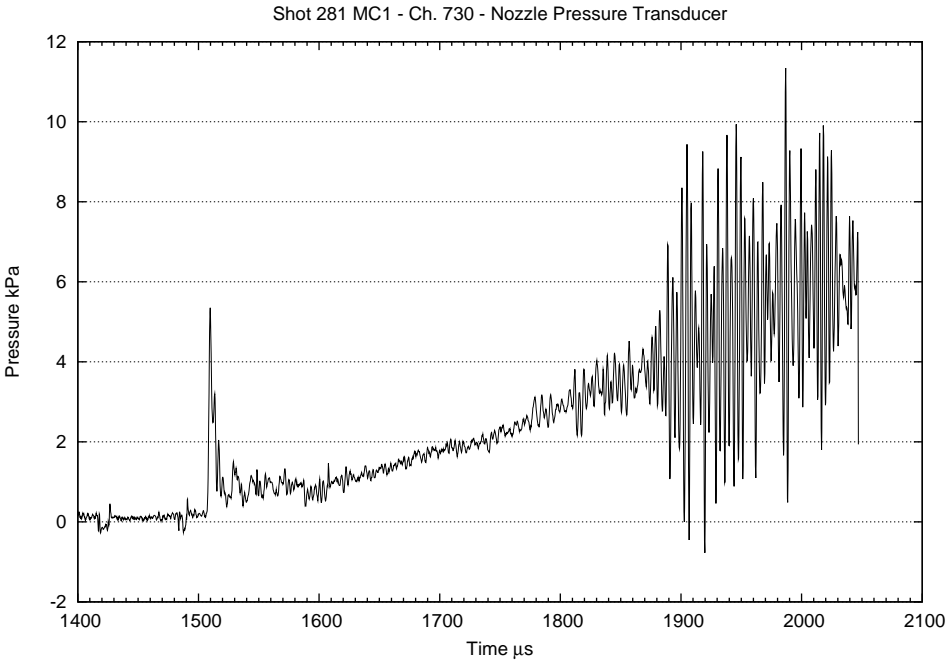


Figure F.64: Shot 281 nozzle pressure transducer data trace.

Bibliography

- [1] Anderson, J. D. J., *Hypersonic and High Temperature Gas Dynamics*, AIAA, Reston, Virginia, 2000.
- [2] Antonello, M., Masi, M., Fulchignoni, M., and Angrilli, F., “Turbulent flow around the Huygens probe: A comparison of algebraic Reynolds stress models,” Capua, Italy, March 2001.
- [3] Billig, F. S., “Shock-wave shapes around spherical and cylindrical-nosed bodies,” *Journal of Spacecraft and Rockets*, Vol. 4, No. 6, June 1967, pp. 822–23.
- [4] Doolan, C. and Morgan, R., “Hypervelocity simulation in a new large scale experimental facility,” *18th AIAA Aerospace Ground Testing Conference*, AIAA, Colorado Springs, Colorado, June 20-23 1994.
- [5] Gnoffo, P. and Braun, R., “Prediction and validation of Mars Pathfinder hypersonic aerodynamic data base,” AIAA, Albuquerque, NM, June 15-18 1998.
- [6] Hayne, M. J., *Hypersonics Flow Over Rearward-Facing Steps*, Ph.D. thesis, University of Queensland, 2004.
- [7] Holden, M. S., “Establishment time of laminar separated flows,” *AIAA Journal*, Vol. 9, No. 11, 1971, pp. 2296–2298.
- [8] Hollis, B. R., *Experimental and Computational Aerothermodynamics of a Mars Entry Vehicle*, Nasa contractor report 201633, North Carolina State University, Raleigh, North Carolina, 1996.
- [9] Jacobs, P., Silvester, T., Morgan, R., Scott, M., Gollan, R., and McIntyre, T., “Superorbital expansion tube operation: Estimates of flow conditions via numerical simulation,” AIAA, Reno, NV, January 2005.

- [10] Jacobs, P. A., "MB_CNS: A computer program for the simulation of transient compressible flows." Department of Mechanical Engineering Report 10/96, The University of Queensland, Brisbane, December 1996.
- [11] Jacobs, P. A., "MB_CNS: A computer program for the simulation of transient compressible flows; 1998 Update." Department of Mechanical Engineering Report 7/98, The University of Queensland, Brisbane, June 1998, <http://www.mech.uq.edu.au/cfcfd/>.
- [12] Lee, J. and Lewis, M., "A numerical study of the flow establishment time in hypersonic shock tunnels," *AIAA 22nd Fluid Dynamics, Plasmadynamics & Lasers Conference*, AIAA, Honolulu, Hawaii, June 1991.
- [13] Lees, L., "Hypersonic wakes and trails," *AIAA Journal*, Vol. 2, No. 3, March 1964, pp. 417–428.
- [14] Menter, F., "Two-equation eddy-viscosity turbulence models for engineering applications," *AIAA Journal*, Vol. 32, No. 8, August 1994, pp. 1598–1605.
- [15] Mitchelltree, R. A. and Gnoffo, P. A., "Wake flow about the mars pathfinder entry vehicle," *Journal of Spacecraft and Rockets*, Vol. 32, No. 5, September-October 1995, pp. 771–76.
- [16] Morgan, R., "A review of the use of expansion tubes for creating superorbital flows," *35th Aerospace Sciences Meeting & Exhibit*, AIAA, Reno, NV, January 6-10 1997.
- [17] Morgan, R., "Development of X3, a superorbital expansion tube," *38th Aerospace Sciences Meeting & Exhibit*, AIAA, Reno, NV, January 10-13 2000.
- [18] Poole, R., "Schematics of experimental models," Email communication, April 2005.
- [19] Potter, D., "Mars based flow conditions for the X2 expansion tube," Personal communication, April 2007.

- [20] Potter, D. F., Gollan, R. J., Eichmann, T., McIntyre, T. J., Morgan, R. G., and Jacobs, P. A., "Simulation of CO₂-N₂ expansion tunnel flows for the study of radiating shock layers." AIAA, Reno, Nevada, Jan. 7-10 2008.
- [21] Roberts, G. O., "Computational meshes for boundary layer problems." *Lecture Notes in Physics*, 8, Springer-Verlag, 1971, pp. 171–177.
- [22] Schultz, D. L. and Jones, T. V., "Heat-transfer measurements in short-duration hypersonic facilities," Monograph AGARDograph No. 165, Advisory Group For Aerospace Research and Development, North Atlantic Treaty Organization, February 1973.
- [23] Scott, M., *Development and Modelling of Expansion Tubes*, Ph.D. thesis, University of Queensland, 2006.
- [24] Teramoto, S., Fujii, K., and Hiraki, K., "Numerical analysis of dynamic instability at transonic speeds," *ISAS Report SP No. 17: Aerodynamics, Thermophysics, Thermal Protection, Flight System Analysis and Design of Asteroid Sample Return Capsule*, edited by Y. Inatani, The Institute of Space and Astronautical Science, Sagamihara, Japan, March 2003.
- [25] Valliammai, V., Gogoi, A., Uthup, B., and Singh, K. P., "Grid quality improvement using multi-block smoothing," *Computational Fluid Dynamics*, Vol. 10, No. 2, July 2001, pp. 169–174.
- [26] Wright, M., editor, *Tutorial on Ablative TPS: Entry Convective Heating (CFD)*, NASA Ames Conference Center, Moffett Field, California, August 21-22 2004, NASA.
- [27] Wright, M. J., Brown, J., Sinha, K., Candler, G., Milos, F., and Prabhu, D., "Validation of afterbody aeroheating predictions for planetary probes: Status and future work," NASA, Moffet Field, California, 2004, pp. 275–286.